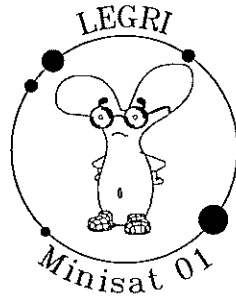
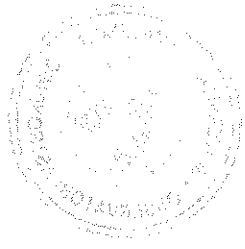




DEVELOPMENT OF IMAGING TECHNIQUES
IN γ -RAY ASTRONOMY USING
CODED MASK SYSTEMS.
APPLICATION TO THE TELESCOPE
LEGRI



Doctoral Thesis Report
D. FERNANDO JESÚS BALLESTEROS ROSELLÓ
November 1996
INSTITUTO DE FÍSICA CORPUSCULAR
MIXED CENTRE C.S.I.C.
UNIVERSIDAD DE VALENCIA

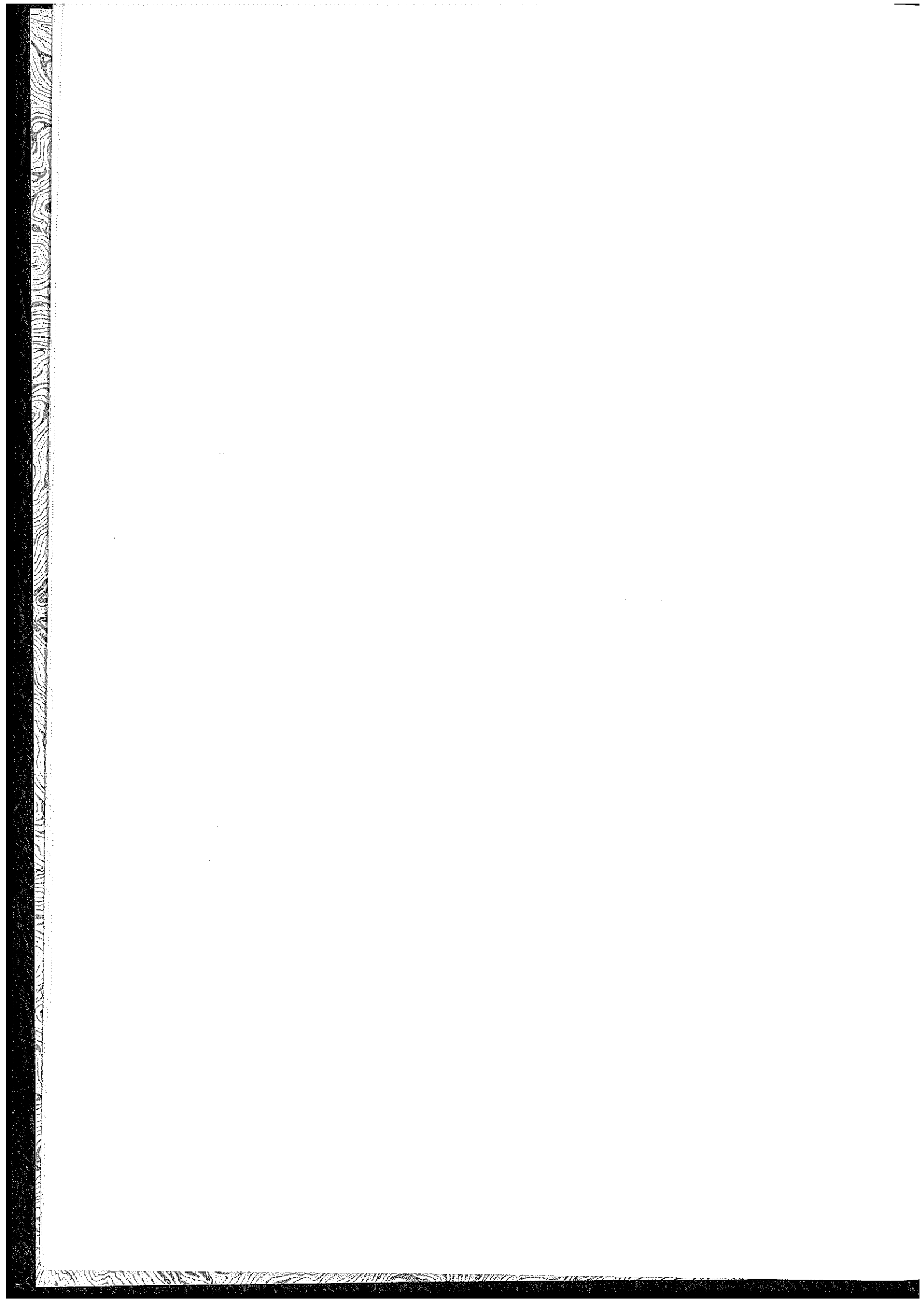


Index

Introduction	1
Chapter 1: The mision	5
1.1 Introduction	5
1.2 El Minisat program	6
1.3 Scientific objectives of LEGRI	10
1.4 Technological objectives of LEGRI	12
1.5 LEGRI description	14
1.6 LEGRI orbit	19
1.6.1 Induced background in LEGRI	20
1.6.2 Telemetry	22
1.7 The scientific team	23
1.7.1 The <i>Science Operation Center</i> (S.O.C.) of LEGRI	23
1.7.2 The LEGRI collaboration	24
Chapter 2: Masks theory. Foundations	27
2.1 Introduction	27
2.2 Co-ordinates systems	28
2.3 The coded masks	32
2.4 The Fresnel zone plates	34
2.5 Systematization	36
2.6 Raiders of the lost reconstruction	40
2.7 Cyclic systems	45
2.8 Choice of the mask pattern	49
2.8.1 Random masks	49
2.8.2 Non-Redundant Arrays (NRA)	49
2.8.3 Uniformly Redundant Arrays (URA)	50
2.8.4 Modified Uniform Redundant Arrays (MURA)	55
2.8.5 New patterns	56

2.9 Choice of G	56
2.9.1 Balanced correlation	57
2.9.2 Finely sampled balanced correlation (FSBC)	61
2.9.3 δ -decoding	63
2.10 Fourier transforms	65
2.11 Shields and collimators	67
2.11.1 Collimators	67
2.11.2 Shields	70
2.12 Other reconstruction methods	71
2.12.1 Inversion of functions	72
2.12.2 Maximum entropy	73
2.12.3 The EM algorithm	76
2.12.4 Maximization methods versus inversion of functions	82
Chapter 3: Other considerations	83
3.1 Introduction	83
3.2 Errors criterion	83
3.2.1 In reconstructions based on the correlation	83
3.2.2 In iterative methods	86
3.3 Sky mapping	87
3.4 Simulators	90
Chapter 4: Results. Study of the reconstruction methods	95
4.1 Introduction	95
4.2 Convergency criteria	95
4.2.1 EM algorithm convergency	95
4.2.2 Maximum entropy method convergency	98
4.3 Reconstruction of a point source	109
4.3.1 Study of the simulators	109
4.3.2 Reconstruction	111
4.4 Source movement	116
4.5 Angular resolution	119
4.6 Ghosts	123

4.7 Collimator effect	127
4.8 Noise effect	130
4.8.1 Constant noise	130
4.8.2 Noise with structure	134
4.8.3 Extending the source space	135
4.8.4 Improving the results	140
4.9 Extended sources	147
4.9.1 Multiple pointing	149
4.10 Non-cyclic patterns	154
4.11 Damaged detector plane	156
Chapter 5: Results. Real response of LEGRI	161
5.1 Introduction	161
5.2 Detector response	162
5.3 Correcting the data	166
5.4 Noise and sensitivity	169
5.4.1 Noise	169
5.4.2 Sensitivity	170
5.5 Imaging	176
5.6 Errors	183
Conclusions	187
Acknowledgements	193
Appendices	195
Appendix I: Relation between an area and its orthogonal projection	195
Appendix II: Errors	200
References	205



Introduction

By the fact of looking at the sky, we are already involved in astronomy. Perhaps there are very few people that have never seen the stars and thought a little about the mysteries of the Universe, and about the place of man in it. Astronomy tells us a fascinating story that began thousands of years ago, when our hominid ancestors looked at the sky and were puzzled when they saw those disconcerting fires.

The science of astronomy has discovered unexpected horizons, and due to it we have improved our knowledge of our place in the Universe. The Earth (on which surface we live) is simply a member of a planet family that turns around the Sun, which is just a star as others in the enormous stellar system that is our galaxy. In its turn, the Milky Way is just a light spot in the middle of the infinity of galaxies and galaxy clusters, extended all over the observed universe, some of them so far that their light takes millions of years to reach us; the observed universe has an expanse of the order of 10^{23} kilometres. In the middle of this vastness, the Earth and the man seem, indeed, insignificant.

Nevertheless, if we look at the other extreme of the scale, the man does not seem so small. The atom has a diameter of the order of 10^{-10} metres, while the nucleus, formed by protons and neutrons, is ten thousand times smaller (10^{-14} m). But precisely the explanation of the gigantic and surprising phenomena observed in the astronomical stage comes from here, from the physics of the microcosmos. This fact has allowed to open new observation windows to the Cosmos, besides the classical window of the optical astronomy. This is the case of radio astronomy (that started at the beginning of the thirties), or the high energy astronomy (X and γ -rays); the last one is, without any doubt, the branch of the astronomy that has contributed the most to our present knowledge of the Universe during the last 30 years.

The development of detection techniques for X and γ -rays coming from sky sources started after the II World War, when the developing of the needed technologies began, and afterwards it was possible to put instrumentation outside of the atmosphere (mainly balloons and satellites). It is impossible to

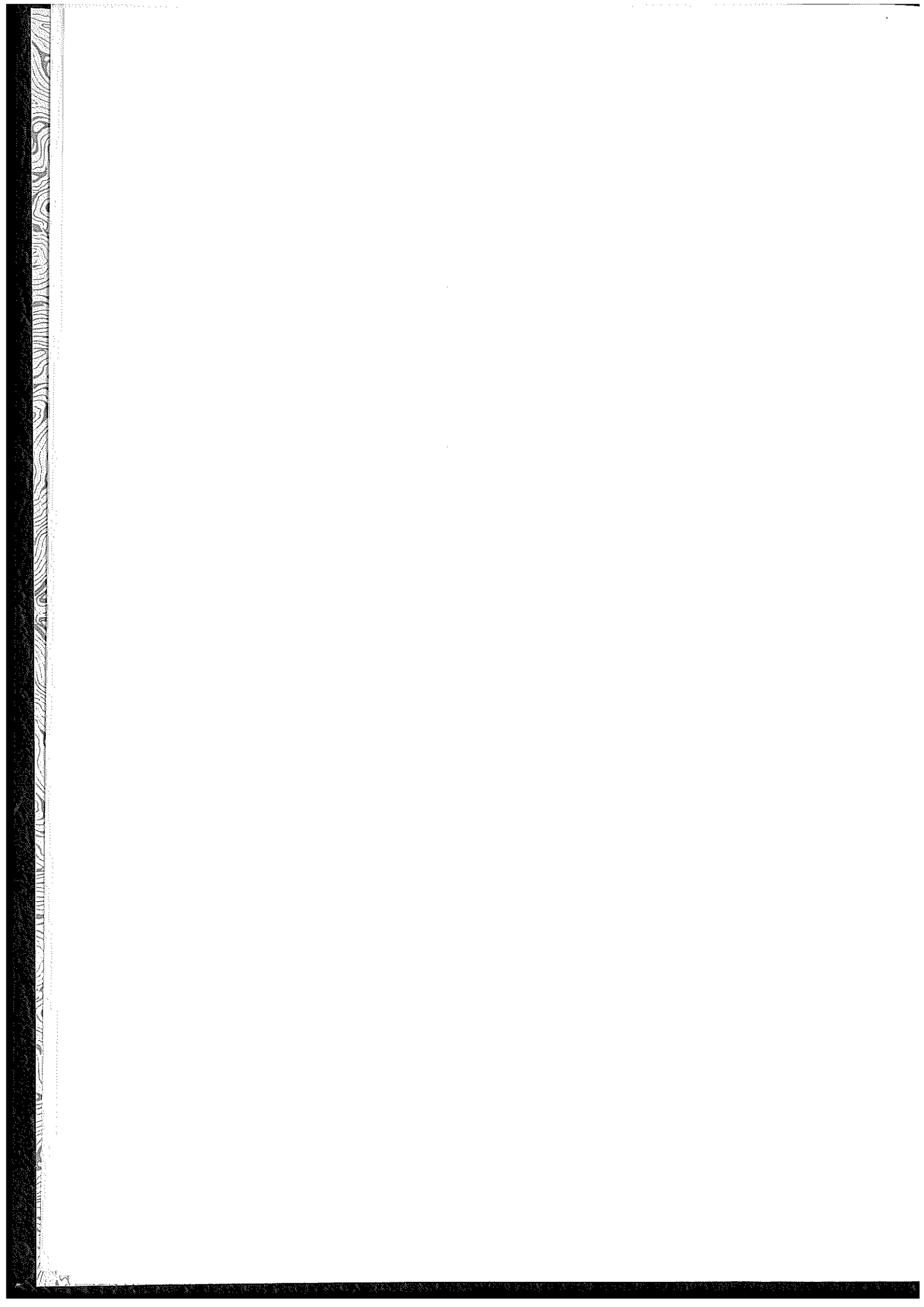
work in high energy astronomy on ground because, for not very high energies, photons interact significantly with the highest part of the atmosphere, being unable to reach the Earth surface; for instance, at a height of about 40 (the typical working height of balloons), photons of 100 keV are absorbed by a factor of $1/e$.

The first X-ray detectors were launched on board of balloons and rockets in the sixties. They measured high energy radiation fluxes of extraterrestrial origin and discovered that the Sun emits X radiation. In 1962, Scorpio X-1 was discovered: the brightest X-ray source in the sky. In 1970 the first satellite dedicated to the X-ray astronomy was launched: the Uhuru, which discovered the existence of a great number of high energy sources, so far unknown, and it was possible to do the first catalogues and sky maps in these frequencies. This discovery changed totally the conception of the Universe; it was more violent than what it was supposed to.

Due to the very energetic nature of γ and hard X-rays, the conventional focussing techniques based on lenses or mirrors are useless. This fact delayed the appearance of the γ -ray astronomy, because it was needed to develop new imaging techniques for this range of the spectrum. These techniques arised finally when the concept of coded mask was developed, which gave us a new tool for imaging and doing astronomy.

Thus, new γ -ray missions that use coded mask theory have recently appeared, such as the French SIGMA mission (on board of the Russian platform GRANAT) which was put into orbit in 1989 and was the first γ -ray mission working in the space, or the GRO (Gamma Ray Observatory). These missions have significantly improved our knowledgement of the Universe in that energy range and have led to the development of new missions. The same spirit animates the LEGRI project (Low Energy Gamma Ray Imager) whose objective is the soft γ -ray astronomy (20 - 100 keV). LEGRI will fly on board the Minisat 01 platform which will be the first mission of the Minisat program by the *Instituto Nacional de Técnica Aeroespacial "Esteban Terradas"* (I.N.T.A.). It will be launched in 1996.

In this work we describe the LEGRI project and summarily the Minisat program. We make an in-depth study of the mask theory and analyse and develop **image reconstruction techniques** (the main objective of this work), applying them to the specific case of the LEGRI telescope, and also studying other associated effects that affect the image reconstruction.



Chapter 1: The mission

1.1 Introduction



he results obtained during the last years by γ -ray missions have made possible a great advance in our knowledge of the Universe in the field of high energy astronomy [1]. It is interesting to briefly summarize the main points that can have important consequences on the development of future high energy missions:

- a) The hard X-ray and γ -ray sky sources show a great variability in number and intensities.

- b) Although the number of γ sources is relatively small, there are sky regions (for instance the Galactic Centre) where the relatively high density of γ emitters makes difficult to identify the sources and to relate them to their counterparts in the other wavelength.

- c) The spectrum of each well-known sky γ source shows characteristic features, and also a great variability on intensities.

Taking all that into account, there are three basic requirements for future missions devoted to the study of X and γ rays sky sources:

- 1) Imaging capability with good angular resolution.

- 2) Good energetic resolution, to allow a good study of the spectra emitted by the sky sources.

- 3) Improvement of the sensitivity with respect to former missions, in order to detect unknown sources.

The **LEGRI** project is a collaboration among different English and Spanish institutions. It arises as a mission which tries to cover part of those objectives, working in the range from 20 to 100 keV (just on the frontier between X and γ -rays). One of the main objectives of the LEGRI project is to test the behaviour of the new HgI₂ detectors and the CdZnTe detectors in space conditions, in order to study their viability for future missions. Thus, the project has a clear component of technical study.

Therefore, the LEGRI collaboration proposed to the I.N.T.A. a γ -ray telescope which uses a coded mask as imaging system, and a 10x10 array of HgI₂ and CdZnTe detectors as position detector, for the payload on board the first **Minisat** mission. It is planned that LEGRI will fly on board Minisat 01 in 1996, on a two-year mission.

1.2 The Minisat program

The conventional satellites are composed of two parts, forming an inseparable set: the service module (or platform) and the payload. Each part of the service module has been exclusively made for the mission the satellite has to carry out, and this procedure puts up building costs and the price of the mission. Consequently, putting a satellite in the space is beyond the means of many countries and it is only possible by working together different institutions and countries and, in most cases, by obtaining also state funding. This provokes unstable situations, because if a funding source disappears or a member of the collaboration retires, the whole project will run the risk of disappearing, and then it will need readjustments and concessions in order to maintain the project.

The I.N.T.A., which is the official Spanish institution in charge of research and development in the aerospace field, thought up the Minisat program in order to avoid this situation. Instead of having developed a different platform for each mission, a single and standard platform will be developed and the payload must fit to it. This will imply that the building cost,

as the platform is mass produced, will be smaller than that of a conventional satellite. With this program, Spain is the first country which offers minisatellites cheaper and with more features, that will be easily accessible to universities and companies, since the payload is not intrinsic to the platform.

Minisat is a multipurpose platform that is included in the minisatellite range (masses from 100 to 500 kg). Minisat and its subsystems are designed modularly and have standard interfaces with the payload module. Furthermore, as it is mass produced, Minisat will reduce the time necessary to prepare a mission: 2 years (typically, a conventional mission requires a preparation time of about 10 years).

In figure 1.1 we can see a drawing of the Minisat platform.

- 1) Upper platform
- 2) Solar sensor
- 3) Power control unit
- 4) Power distribution unit
- 5) Battery
- 6) Magnetic coil
- 7) Wheel electronics
- 8) Inertial wheel
- 9) Computerr
- 10) Transponder
- 11) Lower platform
- 12) Magnetometers
- 13) External panels
- 14) Supports

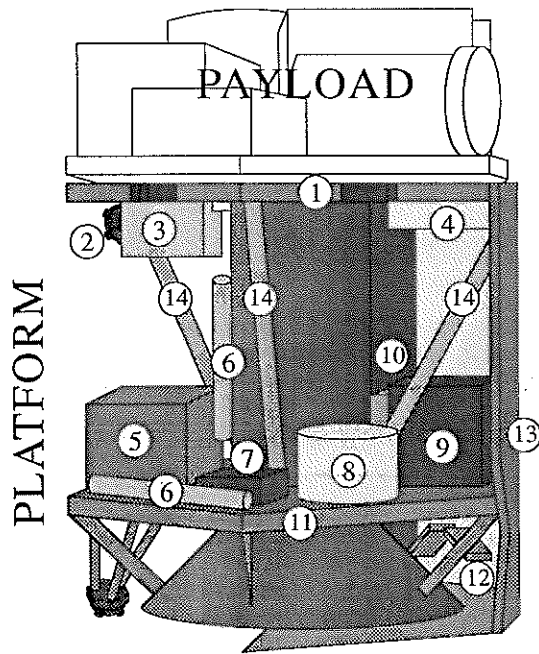


Figure 1.1: Minisat 01 Platform.

Minisat is also innovative and cheap in its launching system (taking advantage of the fact that it is a minisatellite and thus, light). Instead of being put into orbit with a conventional launcher taking off from ground (such as: Ariane, Protón, Space Shuttle, etc...), it will be put into orbit with a ballistic missile launched from a cargo aircraft (the process is shown in figure 1.2). The launcher for this first mission will be a Pegasus XL rocket, but for the following missions, I.N.T.A. has developed a new launcher: the Capricornio.

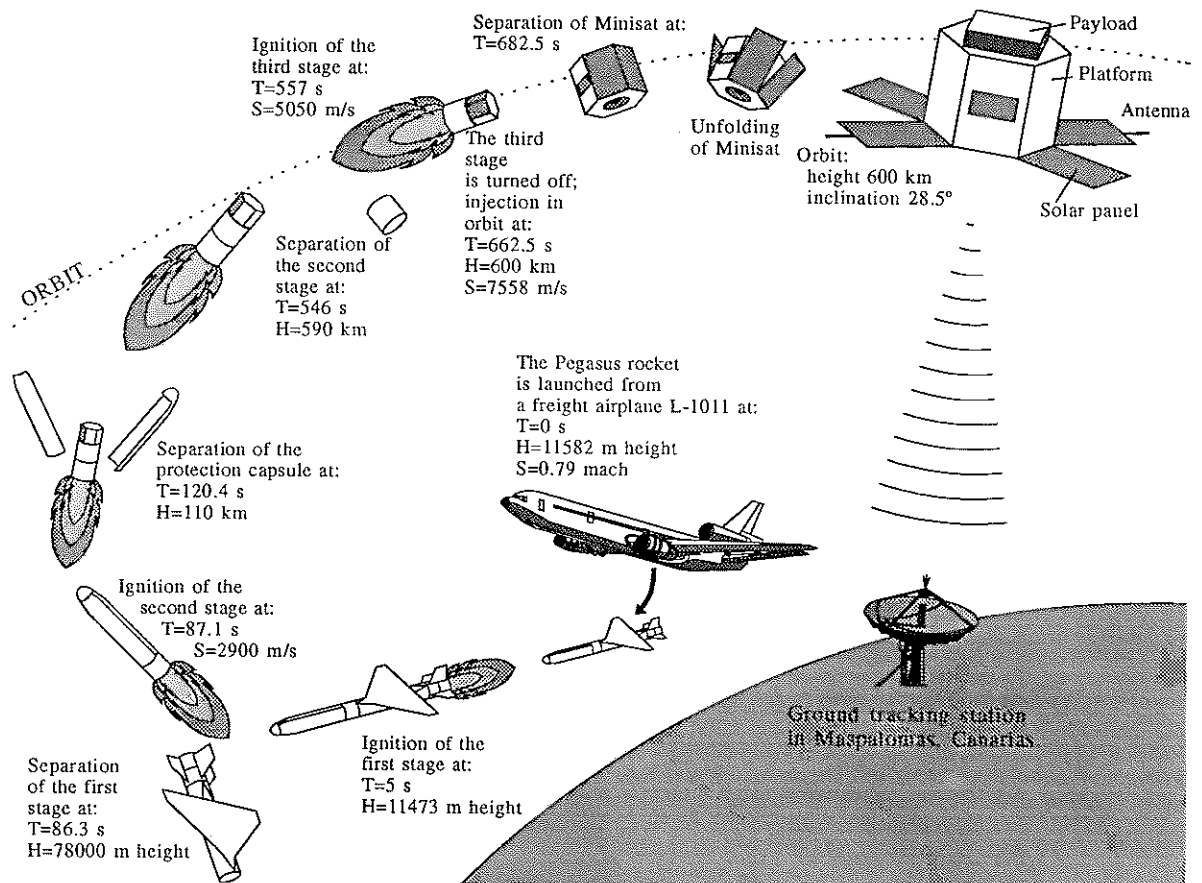


Figure 1.2: Minisat 01 launching

The general features of the Minisat 01 mission are the following:

Mass

- Base Module: 100 kg.
- Payload: 100 kg.
- Total: 200 kg.

Power

- Non-regulated Bus: 28 V.
- Power per panel: 45 W.
- Number of solar panels: 4
- Base module consumption: 60 W.
- Payload consumption: 40 W.

Data

- Memory modules: 32 Mb.
- Total memory: 32 Mb.
- Transmission velocity to ground: 1 Mbps.
- Telemetry band: S
- Transponder power: 5 W.

Attitude

- Stabilization: 3 axis.
- Pointing error: 3°

Orbit

- Altitude: 600 km
- Inclination: 28.5°
- Periode: 96 min.

The Payload of Minisat 01 will be:

- **EURD:** It studies the diffuse radiation of the interstellar environment in the ultraviolet extreme. It is being developed by an international scientific team made up of I.N.T.A. (Spain) and the Berkeley University, California (U.S.A.)
- **CPLM:** It studies the behaviour of liquid bridges in microgravity and it is being developed by the Universidad Politecnica of Madrid.

- **LEGRI (Low Energy Gamma Ray Imager):** It studies the low energy γ radiation (20 - 100 keV) of different sources. It will use HgI₂ and CdZnTe detectors.

1.3 Scientific objectives of LEGRI

As we have said in section 1.1, an accurate imaging capability and a better sensitivity are two important requirements in γ -ray astronomy. The precise location of γ emitters is very important in order to identify its counterparts in other wave longitudes [2].

There are a lot of interesting topics [3] to be studied by hard X-ray soft γ -ray astronomy. Therefore, they are scientific objectives of LEGRI:

- Pulsars, such as the one in the Crab nebulae.
- Binaries containing a star and a compact object (a neutron star or a black hole) whose emissions come from the accretion disk, formed when the mass from the star falls rotating fast on the compact object.
- Novas or supernovas, which produce γ -ray jets.
- γ -ray bursts, perhaps coming from neutron stars of our galaxy, or with an extragalactic origin. It is also interesting to know if there are also emissions in the visible range.
- The galactic centre, a place where it seems that there is a very massive compact object, since there are strong 511 keV lines, perhaps coming from a single source. The galactic centre is a specially interesting place, because in its closeness (in some few degrees around it) we can find X and γ -ray sources, whose intensity varies in a factor of 2 or 3 times,

although from the GRANAT data it seems that maybe even bigger.

- Diffuse background γ radiation, of unknown origin.
- The diffuse galactic emission and extended sources, which give us a way to know the composition of the interstellar environment, through:

i) γ lines, coming from the disintegration of radio isotopes produced during the stellar nucleosynthesis (see table I).

Disintegration chain	Half life (years)	Emission (keV)
$^{57}\text{Co} \Rightarrow ^{57}\text{Fe}$	0.742	14, 122, 136
$^{44}\text{Ti} \Rightarrow ^{44}\text{Sc} \Rightarrow ^{44}\text{Ca}$	47.3	68, 78, 511, 1157
$^{60}\text{Fe} \Rightarrow ^{60}\text{Co} \Rightarrow ^{60}\text{Ni}$	$1.44 \cdot 10^5$	59, 1173, 1332

Table I: γ emissions of the interstellar environment

ii) γ lines, coming from the nuclear disexcitations after the interaction of the interstellar material with cosmic rays.

iii) Injection of heavy elements due to the explosion of supernovas.

- Active Galactic Nuclei.

In this context, the region between 20 and 100 keV has a particular importance [4]. Unique astrophysical information related to nuclear excitation, radioactivity, cyclotron emission and line formation is included in this region of the electromagnetic spectrum. For many astronomical objects, it is very important to determine the end of its tails in X-rays, together with the possible

extension in X-rays of well known γ -emitters. The extension of the active galactic nuclei from the X-ray region to bigger energies is essential for understanding these so powerful emitters.

Anyway, despite the importance of this energetic range, there is a significant lack of data in this region. The efficiency of the present X detectors and new generations of CCD (Charged Coupled Device) that work in this region, fall abruptly when they arrive at 20 keV. On the other hand, many instruments based on scintillators are limited to work over 100 keV. LEGRI tries to fill this gap.

1.4 Technological objectives of LEGRI

An efficient detection of radiation requires materials with a high effective atomic number (i.e. high stopping power), as big as more energetical is the radiation (as it is the case of the γ radiation). The search of semiconductor detectors efficient on these energies, with high effective atomic number, good energetical resolution and working at room temperature (this means that they have a wide gap, of the order of some eV) has shown that the HgI_2 and the CdZnTe (in fact $\text{Cd}_{0.9}\text{Zn}_{0.1}\text{Te}$, a crystal of CdTe in which a 10% of the Cd atoms have been substituted by Zn atoms) are some of the best materials [5]; due to the achieved compromise between detection properties and technological possibilities, they are nowadays one of the most interesting options.

If we compare these new materials with the classical semiconductors Ge or Si we find **i)** they have a great effective atomic number (bigger in the case of the HgI_2); **ii)** they do not need cryogenic systems, because they work efficiently at room temperature (the gap energy is 2.2 eV for HgI_2 and 1.5 eV for CdZnTe); **iii)** they have a great resistivity ($>10^9 \Omega \text{ cm}$) and small capacity, and thus the leak current is quite low to have a good signal to noise ratio and therefore its energy resolution is also quite good, between the NaI scintillators and the Ge semiconductors ($\sim 0.38 \text{ keV}$ for HgI_2 and $\sim 0.5 \text{ keV}$ for CdZnTe , for an energy of 5.9 keV at room temperature).

These detectors show a great endurance to radiation damages, bigger than the endurance of their competitors (even bigger in the case of HgI_2); this is very useful for a detector working in space conditions. In the case of HgI_2 [5], they have been tested under doses of 40 keV photons with intensities bigger than 10^{12} photons $\text{cm}^{-2} \text{s}^{-1}$ without any damage; it has also been demonstrated that they support, without damages, doses of 10^{14} protons cm^{-2} at an energy of 10 MeV. The HgI_2 detectors have been worked efficiently during seven years at room temperature without any worsening; as the polarization is not a phenomenon intrinsic to this kind of detectors, they have a useful life very long. About the CdZnTe [6], they do not present drift phenomena as time goes by, and have been exposed to neutron fluxes (with energies of many MeV) of the order of 10^{10} neutrons/ cm^2 , finding a small activation, but without degradation in the response. Besides, the growth of this material is easier than the growth of HgI_2 crystals.

Thus, the main technological objective of the LEGRI project is to test the behaviour in space conditions of a γ -ray telescope based on this kind of detectors, with imaging capability in the range 20-100 keV, and to do a comparative study in equal conditions for both kind of detectors. The study has a clear character of technological demonstration in view of future missions of γ -ray astronomy.

In short, LEGRI tries to:

- Demonstrate the technological feasibility of γ -ray telescopes, optimized for the energetic zone from 20 to 100 keV, using HgI_2 or CdZnTe detectors.
- Test the capability of these detectors to operate efficiently in space conditions.

- Study their survival capacity in space conditions and evaluate the degrading and worsening of the response versus the time.
- Carry out a comparative study of endurance and features in the same conditions for both materials.

1.5 LEGRI description

The LEGRI telescope is composed of the following units:

- A position sensitive γ -rays detector, made up of an array of 10x10 detector units (80 HgI₂ and 20 CdZnTe), with a distance between detector centres of 1.2 cm, a collimator and a pasive shielding.
- A coded mask, made up of tungsten elements, in front of the detector plane and parallel to it, at 54 cm from the detector plane.
- A stellar sensor that indicates accurately and continuously the pointing direction of the system.
- A digital process and extra power unit, which will be an interface with the platform for the transmission of power and data.
- A high voltage source.
- The ground support and tracking team (the Science Operation Centre or S.O.C.), located in Valencia (see section 1.7).

The position of the instrumentation of the LEGRI project on board of the Minisat platform can be seen in figure 1.3.

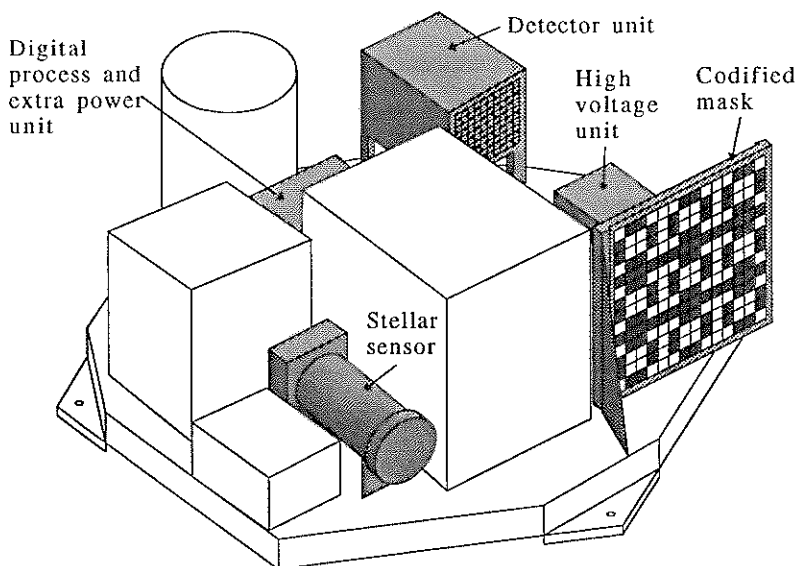


Figure 1.3: LEGRI system units on board of Minisat 01

The position of the Payload will be in such a way that the pointing direction of both the telescope and the stellar sensor will **always** be orthogonal to the direction where the Sun is (the solar axis).

The basic system is made up of the detector unit and the coded mask; they form the γ -ray telescope (see fig. 1.4).

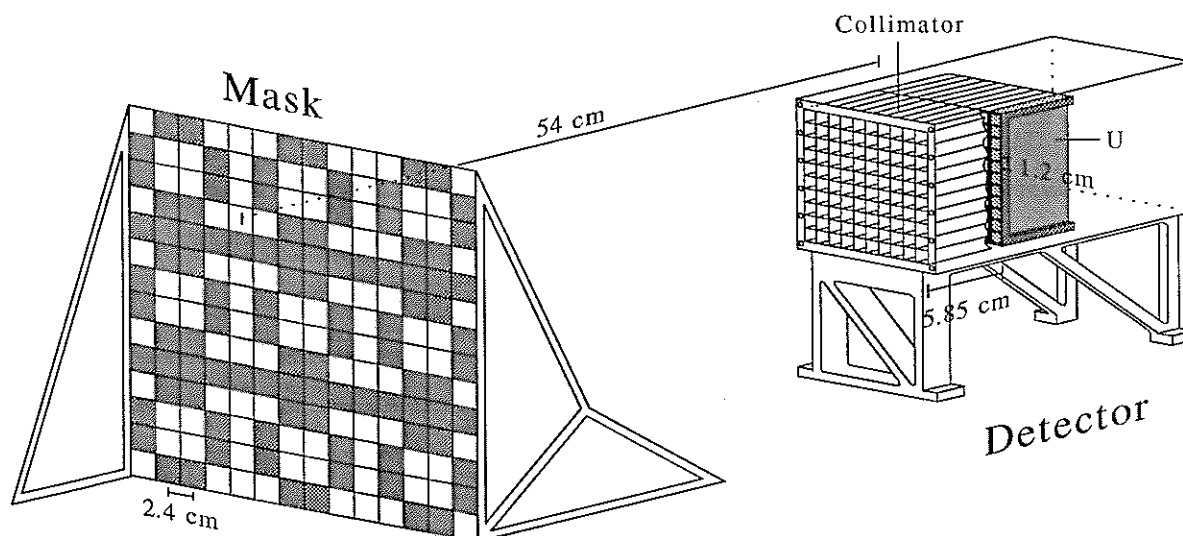


Figure 1.4: Mask and detector unit

The detector is a rectangular box joined to the platform by four aluminium supports. The detector consists of:

- A passive shielding (the walls of the box) to prevent that the radiation reaches the detectors, except that coming from the pointing direction. The shielding consists of several layers (from inside to outside, 1 mm of iron, 0.5 mm of tin, 0.25 mm of tantalum and 2 mm of lead) and prevents that γ radiation beneath 100 keV arrives to the detector plane. It also protects the electronics against electromagnetic interferences coming from other electronic systems on board the satellite.
- A tantalum collimator 5.85 cm long and with walls with a thickness of 0.25 mm (see fig. 1.4) placed over the detector plane, limiting the field of view so that the detector plane will only receive the radiation that has previously passed through the mask. To protect the detectors against the visible light, at the bottom of the collimator there is a thick window of *kapton* of 50 μm , transparent to the γ radiation.
- The detector plane comprises 80 crystals of HgI_2 with a thickness of 0.5 mm and a useful area of $\sim 0.25 \text{ cm}^2$; and 20 detectors of CdZnTe with a thickness of 1 mm and a useful area of 1 cm^2 . They are placed in a regular grid of 10×10 elements, with a distance between detector centres of $1.2 \times 1.2 \text{ cm}$. The grid is made up of 10 support structures with the shape of an U, each one carrying 10 detectors (see fig. 1.4, one of the U's is shaded). Each U has incorporated an analogical electronic card that checks the ten detectors. Therefore, each U (each group of ten detectors) has the same electronics and is an independent unit. This gives modularity and flexibility. Given that the electronics for groups of 10 detectors is the same one, those 10 detectors should have similar electronic properties. The U's are placed in vertical position to avoid distortions during the launching.
- The electronics associated to the detectors. As we have already said, the analogical electronics is incorporated to the structures with the shape of an U. But a digital electronics is needed as an interface between

the analogical signals in the detectors and the digital process unit. This digital electronics is not shown in the figure, but is placed at the bottom of the detector box.

The coded mask is the unit that allows the telescope to form images (see chapter 2) and it consists of a set of elements opaque to the radiation, made of tungsten, and placed in a honeycomb structure (see fig. 1.5). The honeycomb is a hexagonal structure made of *Nomex* (a kind of synthetic resin) with a shape similar to a honeycomb with a great endurance to distortion and traction and also with great transparency to the radiation if we compare it to other supporting materials. The tungsten elements are placed in hollows dug in the honeycomb and its two sides are covered with a thin carbon fibre skin, as it can be seen in fig. 1.5.

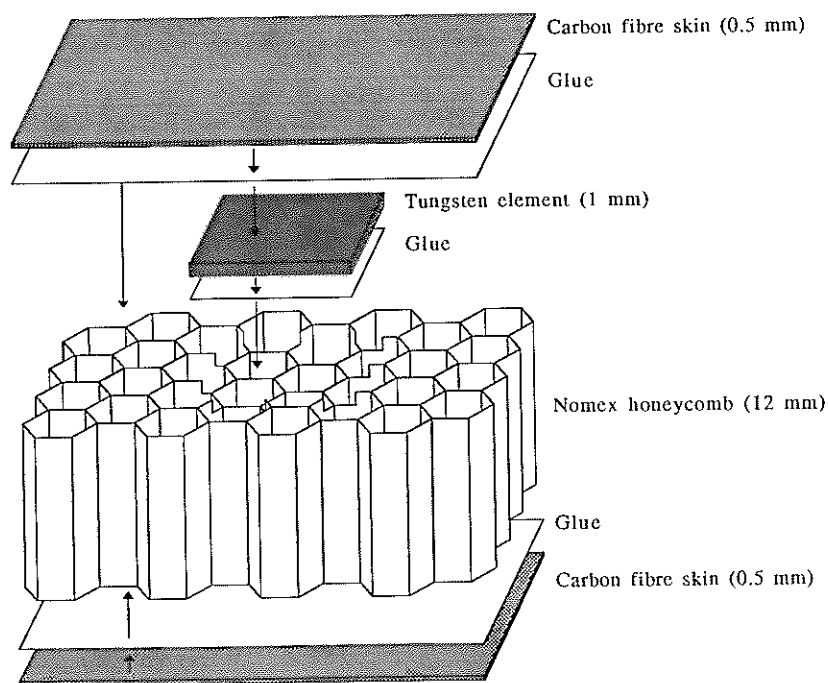


Figure 1.5: Structure of the coded mask

The size of the tungsten elements is $2.4 \times 2.4 \times 0.1 \text{ cm}^3$, and they are positioned forming a grid of 14x14 opaque (where there are tungstens) and transparent (where there are not) elements (see fig. 1.4); their centres are

equidistant a distance of 2.4×2.4 cm, that is just the double of the distance between the centres of the detector units in the detector plane.

The pattern of the transparent and opaque mask elements is a 5×5 MURA (Modified Uniform Redundant Array, see section 2.8.4 and figures 1.4 and 2.23) pattern, placed in mosaic to fill the 14×14 mask elements. Since the gap between centres of the mask elements is twice the one between centres of the detector plane elements, then 2×2 detector plane elements are equivalent to one mask element; that is to say, the size of the 5×5 MURA pattern has the same size as the 10×10 detector plane.

About the stellar sensor, we can say that it is a camera made up of a 310×287 photodiodes array and a common lense system; it has a field of view of 7° with a resolution of $1'$. It periodically gives an optical image of the brightest pixels (stars) in the field of view, so that the S.O.C. can exactly know the pointing direction of the telescope (comparing this image with stellar tables).

In table II we show the main features of the LEGRI system.

Energy range	20-100 keV
Continuum sensitivity	10 mCrab at 10^5 s (3σ)
Point source location capability	$20'$
Field of view	21°
Mass	30 kg
Power	20 W

Table II: LEGRI characteristics

1.6 LEGRI orbit

LEGRI is the only instrument on board Minisat 01 that needs a pointing direction. Therefore LEGRI is supposed to be, in principle, the instrument that will decide the orientation of Minisat 01. Since the pointing direction of LEGRI will be orthogonal to the solar axis (and the satellite will work under this constraint), the pointing will be achieved rotating the satellite around the solar axis. Then, a given sky zone will only be accessible during a few days at intervals of six months (see fig. 1.6; in fact, although it is not depicted in the figure, the solar axis is perpendicular to the platform plane, in such a way that the solar planes will get the maximum light).

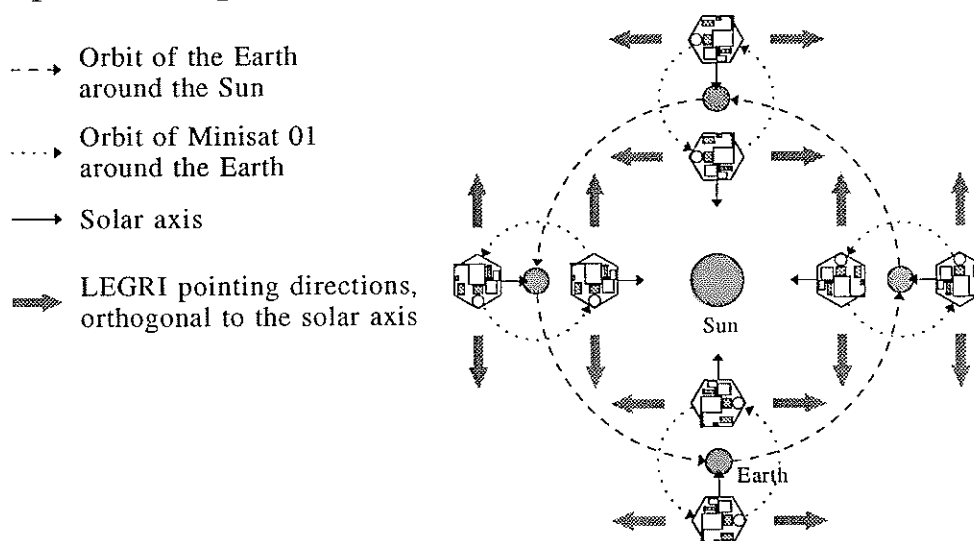


Figure 1.6: Minisat 01 orbit around the Sun and Earth

The parameters of the Minisat 01 orbit are shown in table III:

Eccentricity	0
Altitude	600 km (injection error ± 50 km at 3σ)
Inclination	28.5° (injection error $\pm 0.2^\circ$ at 3σ)
Periode	96.69 min.
Speed	7558 m/s
Orbits per day	14.89

Tabla III: Parámetros orbitales de Minisat 01

1.6.1 Induced background in LEGRI

Since the Van Allen belts begin at an altitude of 1000 km, the Minisat 01 orbit avoids them and so LEGRI will not be affected by such an important noise source. However, there is an important anomaly in the terrestrial magnetic field in altitudes beneath the Van Allen belts that LEGRI will cross through; it is the South Atlantic Anomaly (SAA) where there is radiation trapped (mainly electrons and protons) with energies over 30 keV. The Minisat orbit crosses it, as it can be seen in figures 1.7, 1.8 and 1.9.

When LEGRI passes through the SAA, the protons will induce a radioactivity in the LEGRI material that will be increasing each time it passes until it reaches a maximum saturation level, due to the long life isotopes desintegrations; the short life isotopes will produce a stronger radiation, but because it has a short duration, and given that during the passing through the SAA the sent data will not be taken into account, it will have no influence and its effect will disappear when LEGRI takes again useful data.

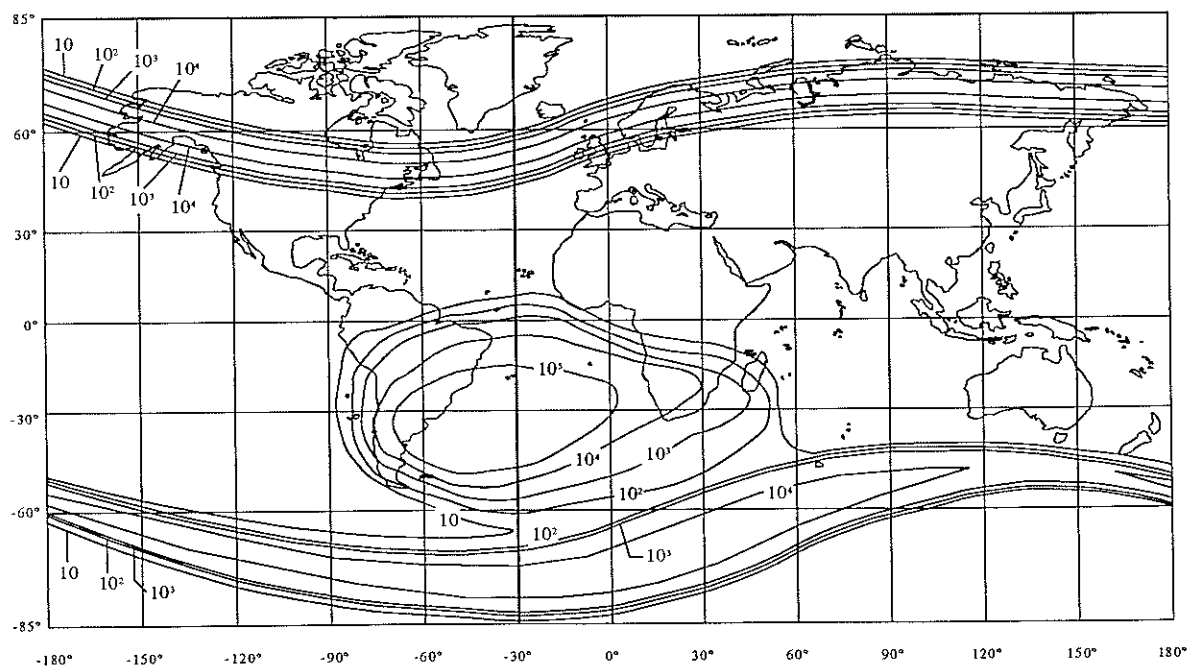


Figure 1.7: South Atlantic Anomaly. Omnidirectional flux contours in electrons $\text{cm}^{-2} \text{s}^{-1}$. $E > 1 \text{ MeV}$. Altitude 500 km.

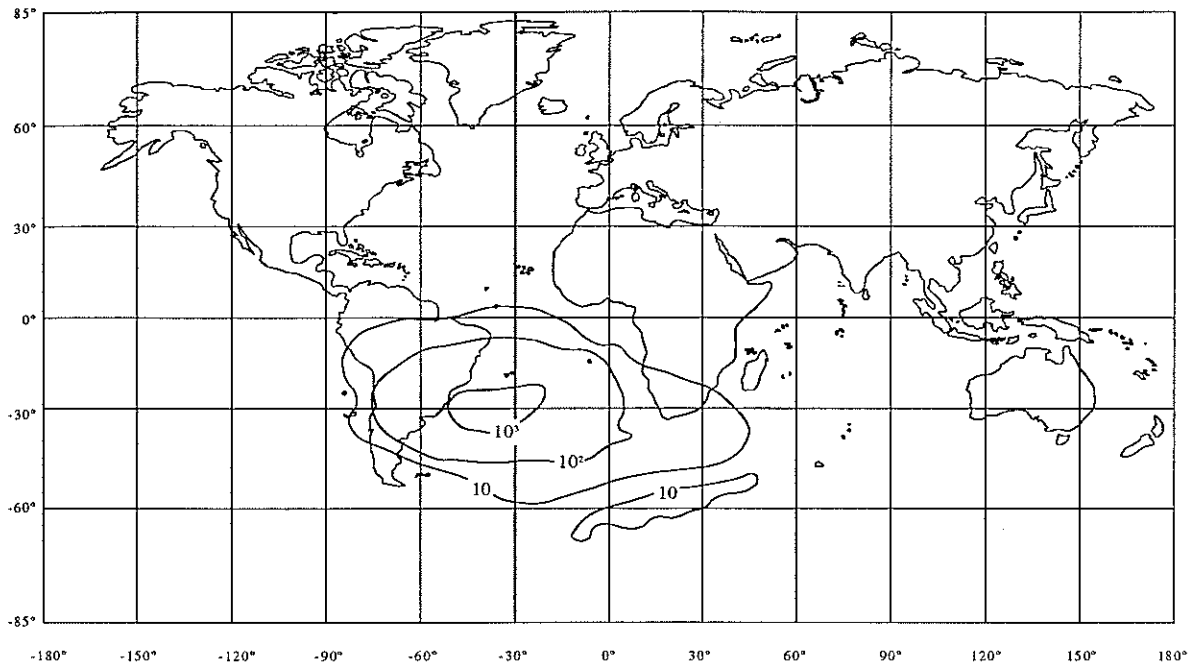


Figure 1.8: South Atlantic Anomaly. Omnidirectional flux contours in protons $\text{cm}^{-2} \text{s}^{-1}$. $E > 30 \text{ MeV}$. Altitude 500 km.

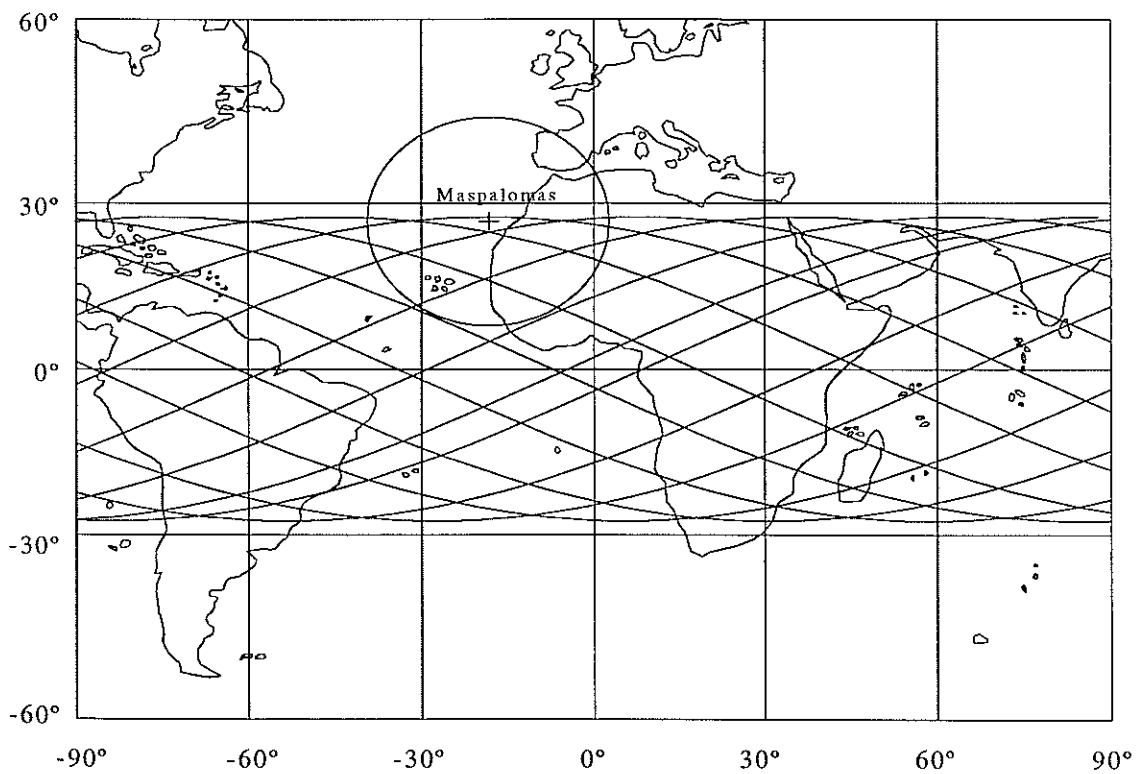


Figure 1.9: Orbital track of Minisat 01 in a day. Altitude 600 km.

The radiation produced by this long life isotopes [7] (induced in turns for the protons trapped in the SAA) produces in LEGRI a background noise of the order of $5 \cdot 10^{-3}$ counts $\text{cm}^{-2} \text{s}^{-1} \text{keV}^{-1}$. There are also other noise sources such as the cosmic protons which leave some signals in the detectors and which also induce isotopes (although its contribution is not considerable compared to the trapped protons); and also the diffuse γ -ray background which we mentioned in section 1.3 and which follows the law [8]:

$$\frac{dN}{dE} = 1.098 \cdot 10^3 \cdot E^{-2.3} \text{ fotones } s^{-1} \text{ keV}^{-1} \text{ cm}^{-2}$$

Anyhow, the main contribution to the noise is without any doubt the radioactivity induced by protons trapped in the SAA.

1.6.2 Telemetry

In table IV we show the visibility analysis of Minisat 01. We say that Minisat is visible when it can be detected from the tracking ground station in Maspalomas and information can be exchanged between them.

Passings per day (elevation over the horizon $> 20^\circ$)	5 (49% of times) 4 (51% of times)
Duration of the contact	max. 8.5 min min. 6.5 min average 8.1 min
Zenital passings (elevation over the horizon $> 85^\circ$)	17% of the passings

Table IV: Visibility results

Given that the EURD experiment on board Minisat 01 (because of the experiment conditions) only can work in eclipse conditions (the Earth is covering the Sun) and due to a lack of power in Minisat 01, EURD and LEGRI

can not work at the same time, then LEGRI will only work in insolation (except for the cases when EURD does not work at all). In this 96.69 min. orbit, an average eclipse takes 33.75 minutes, and an average insolation 62.94 minutes; therefore, about 2/3 parts of the observing time will be available for LEGRI.

The memory capacity available for the experiments on board Minisat 01 is 15.5 Mbytes. The memory need of LEGRI is 0.83 Mbytes/hour, that is to say 0.87 Mbytes/orbit. The EURD memory need is 0.71 Mbytes/hour (0.40 Mbytes/orbit -the third experiment, CPLM, will only work once per month-). This is a total of 1.27 Mbytes/orbit; then the 15.5 Mbytes memory of Minisat will be emptied out each 12.2 orbits. This is more or less once per day.

The scientific data that the detector unit of the LEGRI system will send to the ground are:

- X and Y co-ordinates of the detected signal (that is, detector unit).
- Deposited energy (in fact peak height).
- Impact time (in "clicks" of the internal clock).

The data that the stellar sensor will send are:

- x and y co-ordinates of the 12 brightest pixels in the field of view, or the 6 brightest stars, depending on if the stellar recognition software is working or not.
- Intensity of those pixels.

1.7 The scientific team

1.7.1 The *Science Operation Center* (S.O.C.) of LEGRI

The scientific operations of LEGRI will be monitored by the S.O.C., that will be located on the Burjassot campus of the Universidad de Valencia. The S.O.C. will act as an interface between Minisat and the six scientific teams of

the LEGRI collaboration. The main tasks of the S.O.C. are:

- Carrying out the in flight calibrations (pre-operational and operational).
- Developing a standard software, needed for the data analysis.
- Designing the Observing Programme from the suggestions of the scientific teams.
- Carrying out a quick analysis of the detector data (quick look) in order to take fast decisions about pointing changes or programme modifications, with reaction times smaller than 24 hours.
- Sending to each research team the detector data.
- Maintaining the main LEGRI files (pointing files -from the stellar sensor data-, raw data files, calibration files, historical image files, etc...).

The S.O.C. will receive from the Minisat 01 control centre the detector and stellar sensor data once per day. Besides, the S.O.C. commands for LEGRI will also be sent to the Minisat 01 control centre once per day.

1.7.2 The LEGRI collaboration

LEGRI has been designed and developed by a consortium of laboratories and universities, including:

- Universidad de Valencia/CSIC
Global project control; detector integration and assembling; responsible for the CdZnTe detectors; design and building of the coded mask and the mechanical detector structure; S.O.C.

-
- CIEMAT
Manufacturing and testing the HgI₂; assembling the detector array with the electronics.

 - INTA
Direction; thermal control; integration and test.

 - RAL
Electronics; high voltage unit; stellar sensor.


 - University of Birmingham
Digital process and extra power unit; on ground calibration.

 - University of Southampton
EGSE.

Chapter 2: Masks theory.

Foundations

2.1 Introduction

he possibility of imaging in X and γ -rays is very useful in different research fields. For instance, it can be needed in medicine to know the distribution inside the patient body of the emitter isotopes that the doctor has previously introduced, in order to diagnose or cure a cancer. In nuclear physics, for example, it can be useful in an experimental nuclear fusion reactor to know the plasma distribution and movements inside the container. In astronomy (the scope of this work), the motivations have been profusely explained in the previous chapter.

In each case it is needed to obtain an image of the zone emitting X or γ radiation, but this is a complicated problem, as we have already pointed out, because the classical telescopes based on lenses or mirrors are useless due to the high energy of the radiation [9]; the soft X-ray photons, unlike visible photons, have enough energy to pull out electrons from the atoms of the mirrors and lenses, being therefore absorbed. On the other hand, the hard X-ray photons and γ -ray photons are so energetic that can pass through the lens without suffering any significant deviation; therefore it is useless to use a lens for focussing them and forming an image.

Grazing-incident reflection [10] is a method that allows to focus the low energy X-rays by striking the photons in multiple reflectant surfaces (in a position almost tangential to the arriving photons). This technique implies surfaces whose normal is at great incidence angles with regard to the arriving direction of the photons, bigger than the critical angle of the reflecting surface material (therefore, the arriving radiation will not penetrate inside the reflecting material but will be reflected). This diverts the X-rays towards a focus, where the detecting surface is. Thus, we can form an image of the X source in an almost "classical" way.

However, this technique is more inefficient as the arriving radiation energy increases, because the needed incidence angles become too near to 90° , requiring therefore enormous surfaces in order to have a reasonable aperture, and place them with a great precision; this is too expensive. As a result, this technique is unfeasible for energies bigger than 10 keV.

Thus we need a completely different imaging technique for energies over 10 keV. This system is a coded mask.

2.2 Co-ordinates systems

Before introducing the foundations of imaging by means of coded mask, we are going to explain the co-ordinates system that we use in the following descriptions.

As each co-ordinates system in astronomy, the system we use is mainly a **direction** system. Astronomical objects are so far away that it is not worth considering a radius. Therefore, we will only consider the angular co-ordinates. In astronomy, when working in spheric co-ordinate systems, it is very useful to define a position in the sky by using only two angles (usually labelled θ and ϕ), which can be called right ascension and declination or altitude and azimuth, depending on the system we are working with.

In our case, the reference system is defined by the telescope (the set detector plane - mask), being the z axis of the system, the telescope symmetry axis (and x and y axis parallel to the detector plane borders, and its centre equal to the origin of the co-ordinate system -see fig. 2.3-). Therefore, any object in the centre of the telescope field of view will have the angular co-ordinates (0,0). These will be, of course, independent of which are the real sky co-ordinates of the object, because we are referring to something intrinsic to the telescope and the telescope can change its pointing direction without varying its own reference system.

The co-ordinates of any object inside the telescope field of view with regard to its centre will be given by two angles, α and β (see fig. 2.1).

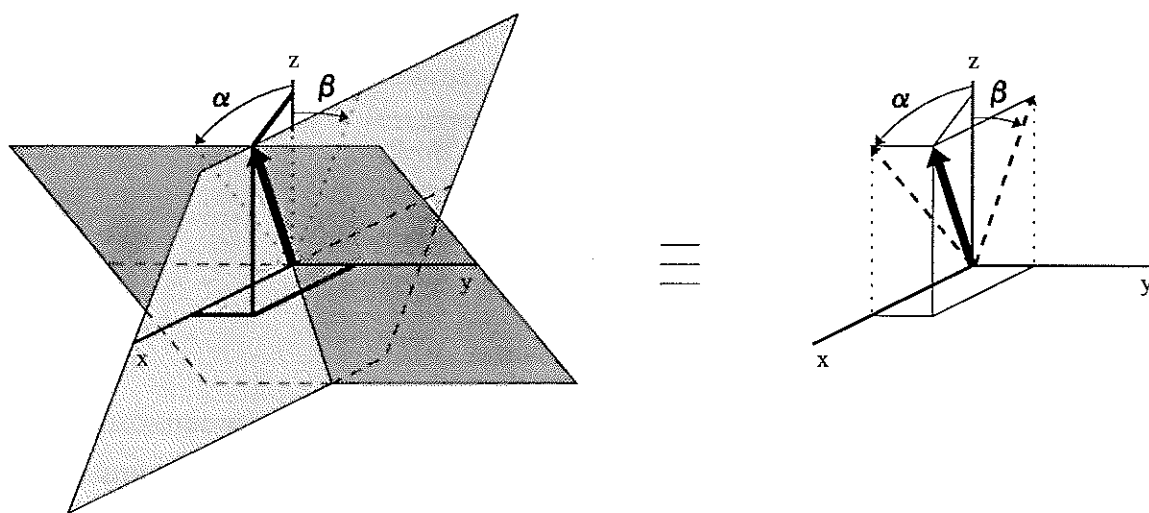


Figure 2.1: Definition of the co-ordinates of an object respect to the telescope system

The α angle defines a plane that passes through the y axis and that forms an angle α with the z axis. Similarly the β angle defines a plane that passes through the x axis and that forms an angle β with the z axis. The intersection of both planes is a straight line whose vector indicates the position of the sky object. Another way of interpreting it is that given a direction vector that points to the sky object, its projection on the xz plane forms an angle α with the z axis and similarly its projection on the yz plane forms an angle β with the z axis. This α and β angles are the co-ordinates of the object. Therefore we define a bidimensional square grid of angles that is centred in the telescope field of view centre.

The transformation laws between this co-ordinates system, the cartesian co-ordinates system and the spheric co-ordinates system are easy to be deduced from figure 2.1 (cf. appendix I, eq. A.2), and are given by:

$$\begin{aligned}
 u_x &= \text{sen}\theta \cos\phi = \frac{\text{tg}\alpha}{\sqrt{\text{tg}^2\alpha + \text{tg}^2\beta + 1}} \\
 u_y &= \text{sen}\theta \text{sen}\phi = \frac{\text{tg}\beta}{\sqrt{\text{tg}^2\alpha + \text{tg}^2\beta + 1}} \\
 u_z &= \cos\theta = \frac{1}{\sqrt{\text{tg}^2\alpha + \text{tg}^2\beta + 1}}
 \end{aligned}
 \tag{2.1}$$

or also by:

$$\begin{aligned}
 \text{tg}\alpha &= \text{tg}\theta \cos\phi \\
 \text{tg}\beta &= \text{tg}\theta \text{sen}\phi
 \end{aligned}
 \tag{2.2}$$

In figure 2.2 we have depicted the curves $\theta=\text{constant}$ y $\phi=\text{constant}$ in the co-ordinates system (α, β) to compare both. The curve $\theta=90^\circ$ corresponds to the (square) border of the co-ordinates system, and the curves $\phi=0^\circ$, $\phi=90^\circ$, $\phi=180^\circ$ and $\phi=270^\circ$ correspond to the α and β axis. As each representation of a sphere in a plane, there is a distortion of the image that grows as we move away from the centre. Nevertheless, for the fields of view of this kind of telescopes (typically smaller than $\pm 20^\circ$) the distortion is very small, as we can see looking at the central zone of fig. 2.2.

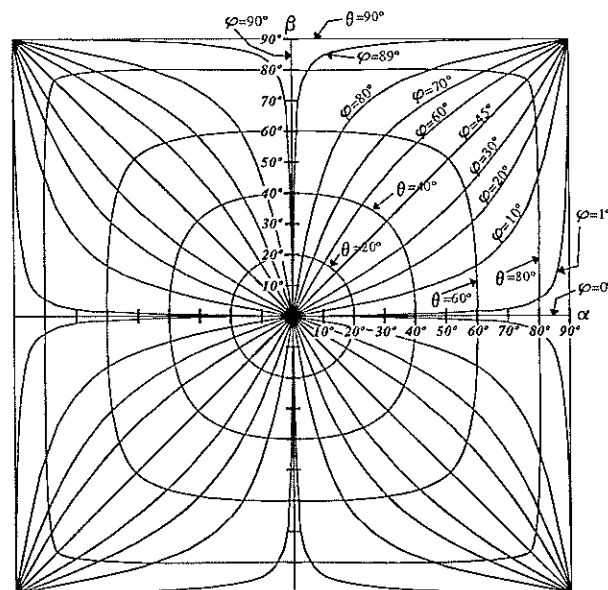


Figure 2.2: Co-ordinates (α, β) versus co-ordinates (θ, ϕ) .

In fact, for angles smaller than 20° , these angular co-ordinates behave very similarly to cartesian co-ordinates (for example: $\beta/\alpha \approx \text{tg}(\phi)$, $\alpha^2 + \beta^2 \approx \theta^2$) and we can employ with them the cartesian transformation laws (rotation, translation, etc...). One must also realize that if we represent an image following the signs criterium for the α and β axis shown in figure 2.2 (which may seem the most logical criterium) we obtain an image that is mirror-reversed, as we can see looking at figure 2.3.

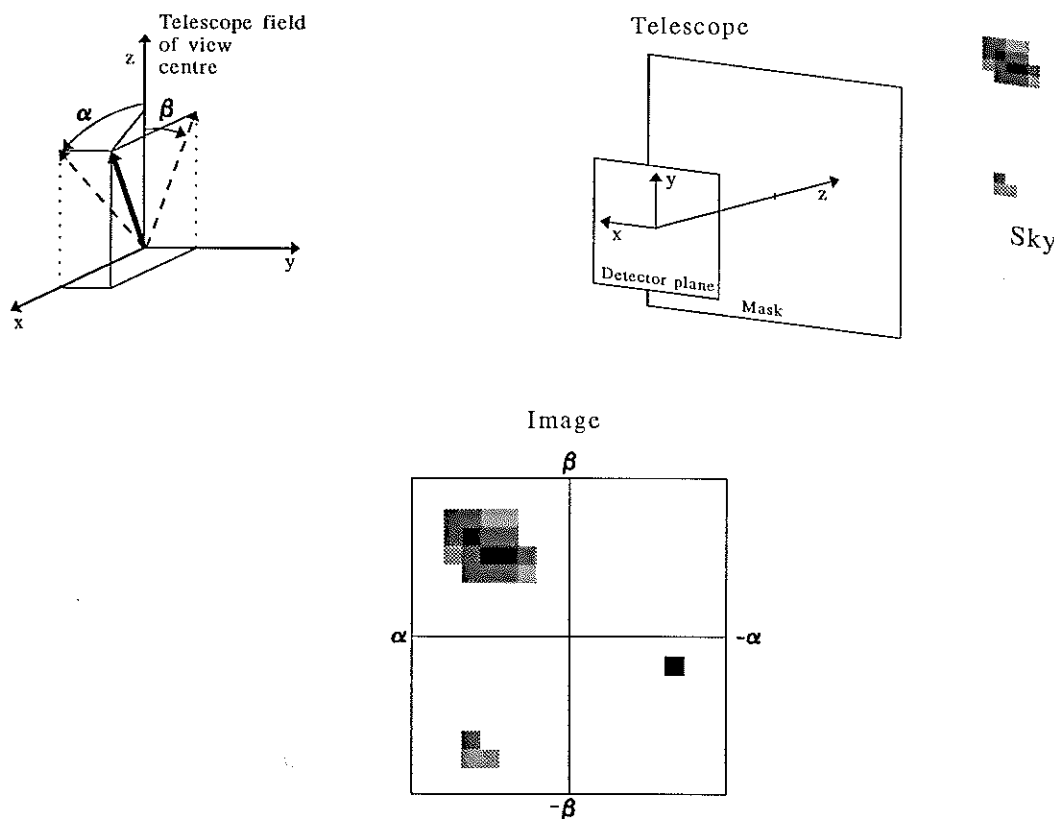


Figure 2.3: When we represent an image using a "logical" signs criterium for the angle, the image is mirror-reversed

An image with the signs criterium of fig. 2.2 is equivalent to look at the source from *outside* the vault of heaven. Therefore we have to reverse the α axis (for example) to obtain the real image (as seen from *inside* the vault of heaven). The same thing happens in the ordinary stellar maps; if we look at the map of a sky region we can see that the Right Ascension increases from right to left and not on the contrary. Anyway, since we already know this phenomenon, we will use the signs criteria of fig. 2.2, for simplicity in the software.

2.3 Coded masks

The idea behind the concept of coded mask is in fact the same as behind the pin hole camera (see figure 2.4); it is an opaque plate that allows the pass of radiation through certain zones, placed in front of the detector plane between it and the source; therefore, it modulates (codifies) the signal arriving from the source. In fact, the pin hole camera can be considered as the simplest case of coded mask.

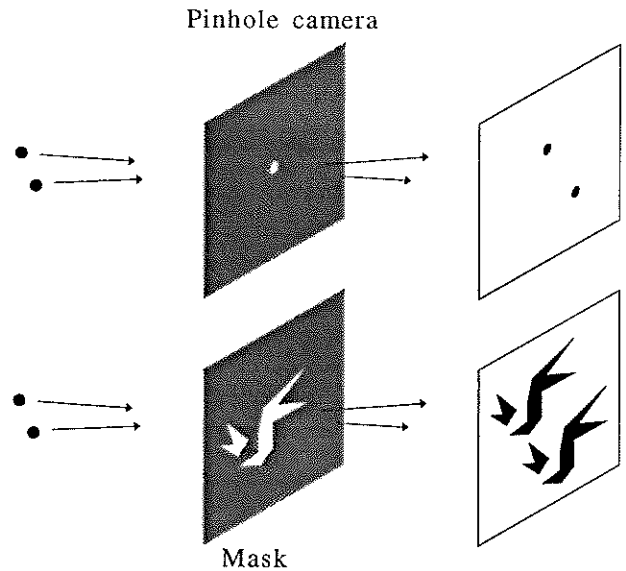


Figure 2.4: Comparison of the pin hole camera with a coded mask system

But the pin hole camera, which immediately gives us an image (inversed and slightly blurred) of the studied object, has the great disadvantage of a very low transmittivity since all the radiation arriving at the opaque plate can only pass through a very small hole, which is a very small percentage of the arriving light. The smaller the hole, the sharper (and weaker) the image, and since the sky sources are very weak, this is a great disadvantage; coming from a typical sky source, in an hour will only pass one photon through a hole of 1 mm^2 [9] (see table VII). Given that the background noise due to cosmic rays that arrives at the detector plane is bigger than 1 count per hour, we have a really bad signal to noise ratio (SNR) and thus, this simple system can not be used in astronomy.

The solution to this problem is obvious: to increase the transmittivity increasing the number and/or size of the holes. As a result, we obtain the concept of coded mask: an opaque body with a *certain transparent pattern* interposed between the detector plane and the source, which codifies the received signal, allows a bigger radiation passage and has a SNR better than the pinhole camera.

Unfortunately (apparently) as it can be seen in figure 2.4, when using a coded mask we do not have a direct image of the source, as happened when using a pin hole camera, but a distortion of it which depends directly on the mask pattern (in fact, it is its shadow). **Here** we have the key to reconstruct the image: given a mask pattern and knowing the detected distorted image, we can in principle reconstruct the source image.

Broadly speaking we can say that we look for the shadow of the mask pattern in the detector plan and from it we deduce where the sky source is (and which is its intensity). We can deduce from this description that our detector plane must be sensitive to the position where the photons arrive; that is to say, the detector plane must be a position sensitive detector, such as an Anger camera, a multiwires camera, a discrete detector array (scintillators, semiconductors, etc...) or even a photographic film. The choice mainly depends on the energy range involved.

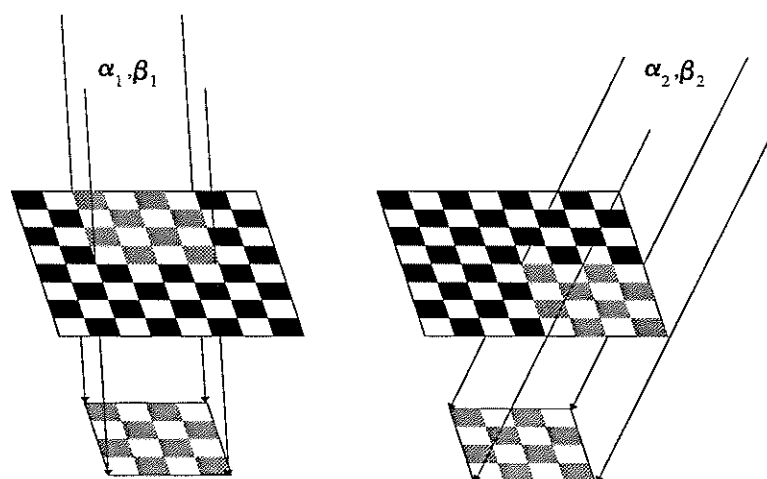


Figure 2.5: Projection of two identical shadows coming from two different directions on the detector plane, using a chess-like mask pattern

The choice of a suitable mask pattern is an important factor for imaging, because not all the possible patterns are equally suitable; the trick lies on choosing the correct one. Since the image reconstruction methods look for the mask shadow(s) projected on the detector plane by the source(s) and therefore deduce where the source(s) is (are), these shadows must be as distinguishable as possible. For instance, a mask as the one shown in figure 2.5 is not a good

choice and will be useless, because it casts the same pattern (the same shadow) over the detector plane for many different sky positions; in figure 2.5 we can see how two different directions, called (α_1, β_1) and (α_2, β_2) , produce exactly the same shadow on the detector plane. With this mask we have a great uncertainty about which is the true position of the source. There are plenty of possible (degenerated) directions that will appear as possible source positions in the reconstructed image, regardless of the reconstruction method used, because all the possible directions are equally good while we do not have additional information. Therefore we have a multiplicity of reconstructed sources where there is just a single real source, as we can see in figure 2.6.

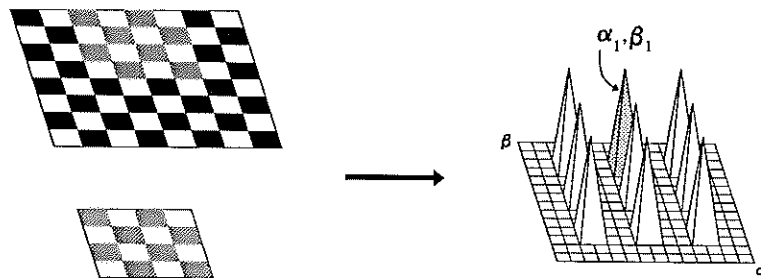


Figure 2.6: Reconstruction from the shadow detected when using a chess-like mask pattern

Therefore our pattern must be as distinguishable as possible. That is to say, the shadow produced by a sky source placed in some direction must be different of the shadow produced if it were in any other direction.

2.4 The Fresnel zone plates

The first imaging method that used a kind of mask was proposed by Mertz and Young [11], and we mention it here for historical purposes. The device recorded the shadows projected for a field of sources illuminating a Fresnel zone plate [12] which was used as mask pattern (figure 2.7).

The Huygens-Fresnel principle says that the intensity of a wave front in a point P can be obtained from the contribution of all the secondary waves generated from the points of a former surface H that the wave crossed. This former surface (that may not correspond to any physical surface and can be just a mathematical concept -for example, a previous wave front-) can be subdivided in zones (the Fresnel zones) each one of them at a distance

$r_0 + n \cdot (\lambda/2)$ from the point P, being n an integer; or what amounts to the same thing, the secondary waves emitted from these zones arrive at the point P with a phase difference of π , that is to say, in constructive interference. Choosing a different r_0 we have a different Fresnel zones set (except for the case when $r_0' = r_0 + m \cdot (\lambda/2)$ -m integer-, because in this case we have again the same set!). If we integrate the contribution of the whole surface H (that is, all the possible Fresnel zones) the different Fresnel zones will balance among them and the total in P coincides with what the wave propagation law foretells.

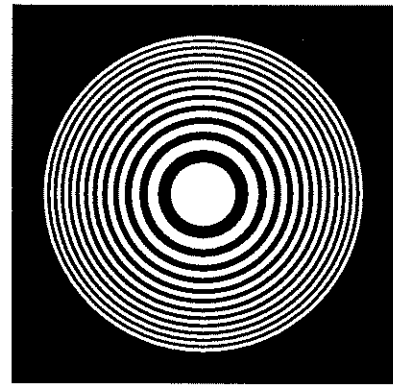


Figure 2.7: Fresnel zone plate

But what will it happen if we impede this integration over the whole surface H in some way? that is, if we select that only some Fresnel zones will contribute in P but not the other. Basically this is what we do if we use a Fresnel zone plate as the one shown in figure 2.7. In the zone plate, the zones where the difference of paths between the source that produces the wave and the point P are of the form of $x + n \cdot (\lambda/2)$ are the only transparent; that is to say, all the light coming from the source that arrives at the point P is in constructive interference. As an amazing consequence we have that the Fresnel zone plate works like a lens! (in fact the Fresnel zone plate is also called zonal lens) and it can directly generate images of small objects without any kind of reconstruction method.

However, this imaging system has two problems. First, the zonal lens is optimised for a certain wave length λ , as it can be easily deduced from its definition. Second, the zonal lens uses the diffraction phenomena of the light, which are a consequence of the interaction of the light with the matter, and therefore, for the same reasons that we can not use mirrors or lenses with X

and γ -rays, we can not either use directly a zonal lens as imaging system for these energies.

Therefore, if we use a zonal lens as a mask, each γ source in the field of view will produce a shadow of the Fresnel zone plate on the detector plane, overlapped and shifted. The reconstruction method is very peculiar; it generates a reproduction of the detected image in a transparent material (for example, in a photographic film) and illuminates the reproduction with a monochromatic light, whose wave length λ is the one of the Fresnel zone plate used (and hence we finally use the diffraction properties of the zonal lens). Then, as by magic, we get directly an image of the sky sources.

Unfortunately, although correct in theory, this system has the great disadvantage of generating a great amount of noise in the reconstruction, and other kind of mask are more useful for astronomy, for their better results and smaller SNR.

2.5 Systematization

Opposite to the Fresnel zone plates, where an optical reconstruction method is used, most of the used masks need to use a computer for the image reconstruction. Such reconstruction methods are the main subject of this work. That is why first of all we are going to systematize how the projected shadow is detected in the detector plane [13]. We will mainly consider rectangular masks with square patterns (that is to say, made up of square elements, as the mask in figure 2.8, where we show a random pattern).

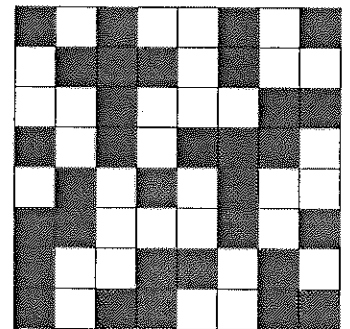


Figura 2.8: Máscara de patrón cuadrado aleatorio.

Let us explicitly explain how the detector plane detects a set of sky sources. Given a sky plane with emitting sources (see fig. 2.9), defined by the intensity function $O(\alpha, \beta)$ (photons received per cm^2 and time unit) coming from the sky position (α, β) (therefore, α and β are the angular co-ordinates of the sky source); let $D(x, y)$ be the number of photons received on the detector plane at the position (x, y) ; let $M(x', y')$ be the pattern of the mask, that is the mask transmittivity in the position (x', y') (1 if there is a hole and 0 if there is an opaque element). Both (x, y) and (x', y') have dimensions of length. Finally, let f be the distance detector plane-mask, b the distance mask-source (in astronomy equal to infinite) and c the size of a mask element side.

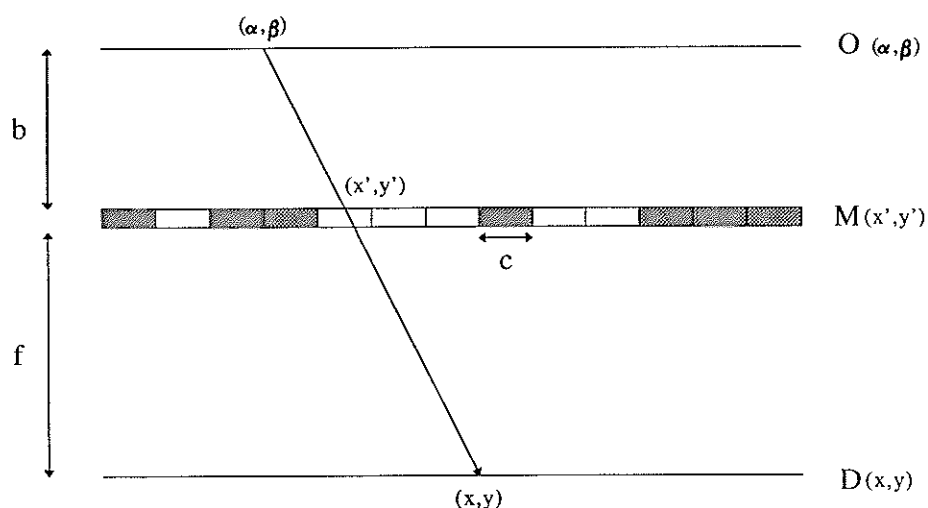


Figure 2.9: Effect of the mask in the detection process

As it can be deduced from figure 2.9, x' and y' are a function of x , y , α , β and f . Since in this kind of telescopes the field of view is usually smaller than $\pm 20^\circ$ (that is to say, 0.35 rad; and $\text{tg}(0.35) = 0.365 \approx 0.35$), we have:

$$\begin{aligned} x' &= x + f \cdot \text{tg}\alpha \approx x + f \cdot \alpha \\ y' &= y + f \cdot \text{tg}\beta \approx y + f \cdot \beta \end{aligned} \quad (2.3)$$

Therefore, the detected counts in the (x, y) position on the detector plane are given by:

$$D(x,y) = \int O(\alpha,\beta) M(x',y') d\alpha d\beta = \int O(\alpha,\beta) M(f\cdot\alpha+x, f\cdot\beta+y) d\alpha d\beta \quad (2.4)$$

This has the mathematical form of a correlation. This last equation can be discretized following the literature (for example, [13]) on the following way (this will make easier to operate with it and to implement it in a computer): we turn the sky plane and the detector plane into discrete fractions, and if we follow [13], also the mask. This is specially suitable for masks with square pattern but it is a little limited and inaccurate. But it is the most usual description found in the literature, and it is also the base of the traditional reconstruction methods based on discrete correlations.

Following [13] we have to divide the sky plane $O(\alpha,\beta)$ into pixels with a size of $\Delta\alpha \times \Delta\beta$, being $\Delta\alpha (= \Delta\beta \text{ usually}) = \text{arctg}(c/f) \approx c/f$, that is, the angle that subtends a mask element seen from the detector plane; the mask plane is also divided into pixels with a size $c \times c$ (it is already done by construction) and also the detector plane is divided into pixels with a size $c \times c$ (one can deduce, then, that the detector plane *must* be divisible in elements of that size). Then, we have:

$$\begin{aligned} O(\alpha,\beta) &\Rightarrow O_{ij} \\ D(x,y) &\Rightarrow D_{kl} \\ M(f\alpha+x, f\beta+y) &\Rightarrow M_{i+k, j+l} \end{aligned} \quad (2.5)$$

where M is a bidimensional array whose elements are 1's or 0's, depending on if it is a transparent element or an opaque element. Therefore, equation 2.4 will be now:

$$D_{kl} = \sum_{ij} O_{ij} M_{i+k, j+l} \equiv O * M \quad (2.6)$$

which is the discrete form of the correlation.

We can include a background noise term that is not codified (is not modulated by the mask):

$$D_{kl} = \sum_{ij} O_{ij} M_{i+k, j+l} + B_{kl} \Rightarrow D = O * M + B \quad (2.7)$$

This equation is the starting point of the classic reconstruction methods based on the correlation, and it is also useful for simulating the behaviour of a given telescope; this means that given a mask M and a (discrete) sky O , using this equation we can find out what the detector plane will detect. Anyway for this purpose the following discretization is more accurate, that is in fact the one we use for simulating. Similarly to the previous case, we do:

$$\begin{aligned} O(\alpha, \beta) &\Rightarrow O_{\alpha\beta} \\ D(x, y) &\Rightarrow D_{ij} \end{aligned} \quad (2.8)$$

$$M(x + f \operatorname{tg}(\alpha), y + f \operatorname{tg}(\beta)) \Rightarrow \Phi_{ij}^{\alpha\beta}$$

where $O_{\alpha\beta}$ is a discrete array giving the intensity of the source in the sky pixel (α, β) ; now we have the small advantage that the index (α, β) (non-integer) gives us explicitly which are the sky co-ordinates of the pixel. Besides, the size of the sky pixels can be now **any**, not just the angle that a mask element subtends from the detector plane. Φ is a function that gives us the flux (in fact the fraction) arriving at the detector plane pixel ij coming from the sky pixel (α, β) . Φ has values between 0 and 1 (not only 0 or 1 as it happened with the discrete array M) and can take into account other factors besides the mask, such as shieldings, collimators, efficiencies, etc... On the other hand, since Φ is a function, there is not necessity of discretizing the mask and also it does not need to be of square pattern (although the calculation of Φ is easier if it has a square pattern), allowing to handle a more general case and more exactly.

Therefore we will have that the detected signal in D_{ij} is given now by:

$$D_{ij} = \sum_{\alpha\beta} O_{\alpha\beta} \Phi_{ij}^{\alpha\beta} + B_{ij} \quad (2.9)$$

We will speak about this equation later on section 2.12.

2.6 Raiders of the lost reconstruction

Once we have understood how our telescope detects a field of sources, our objective is to reconstruct this unknown field from the obtained experimental data. Let us see now the keys for this reconstruction.

As we have seen in equation 2.7 (that we repeat here for convenience of the argument), we can systematize the detection process by:

$$D = O * M + B \quad (2.10)$$

where M , B , D and O are bidimensional arrays, which are supposed to have different sizes, except D and B that must have the same size.

The reconstruction method will be based on the search of a reconstruction array G that when correlating it with the D array (our experimental data) will give the original source O [13]. That is, we are looking for a G such that:

$$D * G = O \quad (2.11)$$

In general, what we have for a given G is:

$$\tilde{O} = D * G = O * M * G + B * G \quad (2.12)$$

where \tilde{O} stands for the reconstructed source, which in a general case should be the same as O .

Therefore, the requirements that G must fulfil are that M^*G should be a delta function, in such a way that $O^*(M^*G) = O$, and B^*G should be as close to 0 as possible. In the first condition we have the possibility of imaging and in the second, the possibility of subtracting (or reducing) the noise in order to improve the SNR. Indeed, for the first condition (the most important) G must fulfil the following requirement:

$$(M^*G)_{ij} = \delta_{0i} \delta_{0j} \quad (2.13)$$

that is, when we have $i=0$ and $j=0$ the correlation is equal to 1 and otherwise is equal to 0. Therefore we have:

$$\begin{aligned} \tilde{O}_{ij} &= \sum_{kl} D_{kl} G_{k+i \ l+j} = \sum_{i'j'} \sum_{kl} O_{i'j'} M_{i'+k \ j'+l} G_{k+i \ l+j} = \\ &= \sum_{i'j'} O_{i'j'} \sum_{kl} M_{k+i' \ l+j'} G_{k+i \ l+j} = \left\| \begin{array}{l} a \equiv k+i' \\ b \equiv l+j' \end{array} \right\| = \\ &= \sum_{i'j'} O_{i'j'} \sum_{ab} M_{ab} G_{a+(i-i') \ b+(j-j')} = \sum_{i'j'} O_{i'j'} \delta_{0 \ i-i'} \delta_{0 \ j-j'} = O_{ij} \end{aligned} \quad (2.14)$$

that is to say, a perfect reconstruction of our sky (see fig. 2.10).

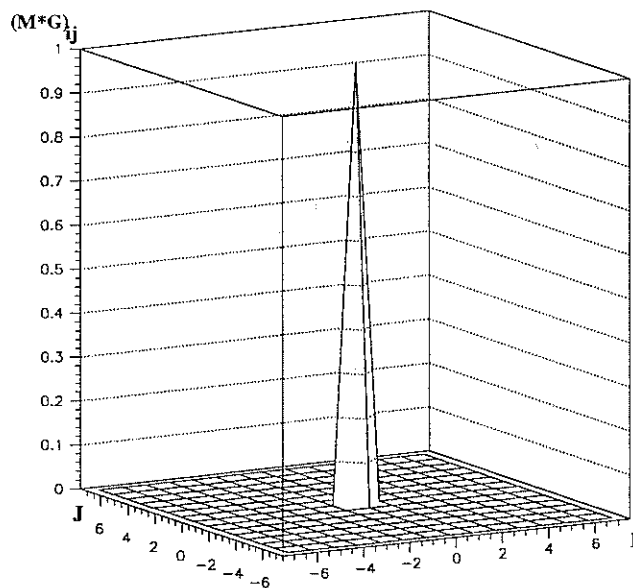


Figure 2.10: Ideal case. $(M^*G)_{ij} = \delta_{0i} \delta_{0j}$

As we look for a G with the property defined by eq. 2.13 (which it is depicted in figure 2.10) it seems clear that G will be very related to the pattern of M . Indeed, generally G will be a modification of M . In fact, M can be used as reconstruction array, obtaining quite good results. We will use M as a starting point for our search of the reconstruction array G .

If we self-correlate a mask with itself (for example, the one shown in figure 2.8) we obtain a *delta-like* function: let A_{ij} be the M self-correlation, that is:

$$A_{ij} = \sum_{kl} M_{kl} M_{k+i, l+j} \quad (2.15)$$

When $i=0$ and $j=0$ there is a full coincidence between both patterns; i.e., the correlation is maximum (see fig. 2.11) and therefore A_{00} coincides with the number of holes in the mask. In the remaining cases the patterns are shifted and the coincidence between holes (1's) is smaller, decreasing (roughly) the number of coincidences as i and j move away from the 0 value, until they reach a point where the patterns are not overlapped and there are no coincidences, being the value of the self-correlation equal to 0.

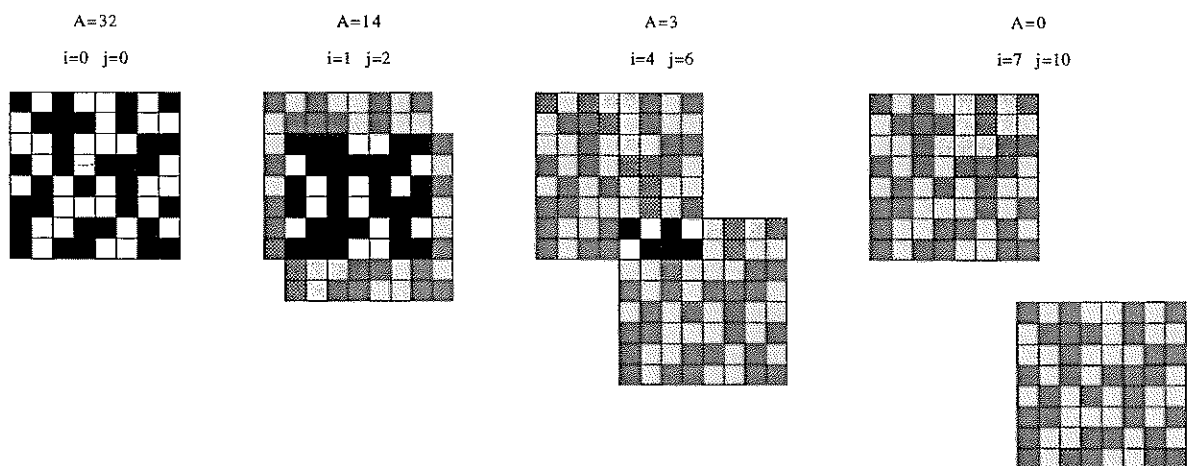


Figure 2.11: Self-correlation of the mask in figure 2.8

What we get is something similar to the image we showed in figure 2.10. In figure 2.12 we show the result of the self-correlation of the random mask

pattern shown in fig. 2.8.

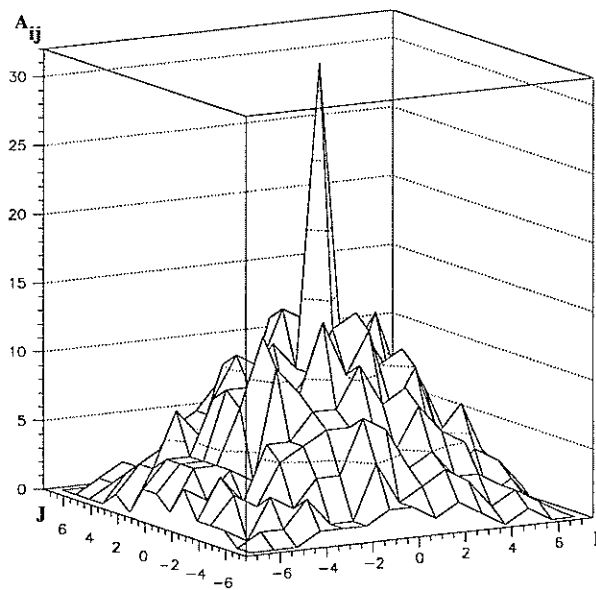


Figure 2.12: Self-correlation of the mask in figure 2.8. Result

As it can be seen, we have a peak for the case $i=0$ and $j=0$ (equal to 32, the number of holes in our mask) and a background that is not flat but decreases as i and j move away from 0.

If we consider a detector plane with the same size as the mask pattern, the described self-correlation will be the reconstruction of a source with intensity 1 placed in the centre of the field of view (and without any noise): if M and D have the same dimensions and we have a source with intensity 1 placed at $(\alpha=0, \beta=0)$, the projected shadow in D will be exactly the mask pattern (and, in absence of noise, that will be what we will detect). If we consider that M is also our reconstruction array G , then we have:

$$M * M = D * G \quad (2.16)$$

That is, its reconstruction. Therefore, a point source with intensity I in absence of noise will be reconstructed as a source with intensity $I \cdot (\text{no. of holes})$

plus a non-flat background that will distort the signal and that has nothing to do with the background noise. This is a "noise" due only to the reconstruction process and it will be called **reconstruction noise**.

We could improve a little the result if the reconstruction noise were more or less flat, because it would be easier to handle. Let us now consider a new type of correlation, different to the previous one; it is the cyclic correlation [14]. Using this correlation, when we calculate M^*M we do not calculate the product $M_{kl} \cdot M_{k+i, l+j}$ only in the overlapping zone, as it was illustrated in figure 2.11, but as we shift both patterns a quantity ij , one of them will be permuted cyclically, and therefore the product $M_{kl} \cdot M_{k+i, l+j}$ will be worked out for all the mask. That is to say, for a given ij , we multiply the mask pattern by a version of it cyclically permuted (see figure 2.13).

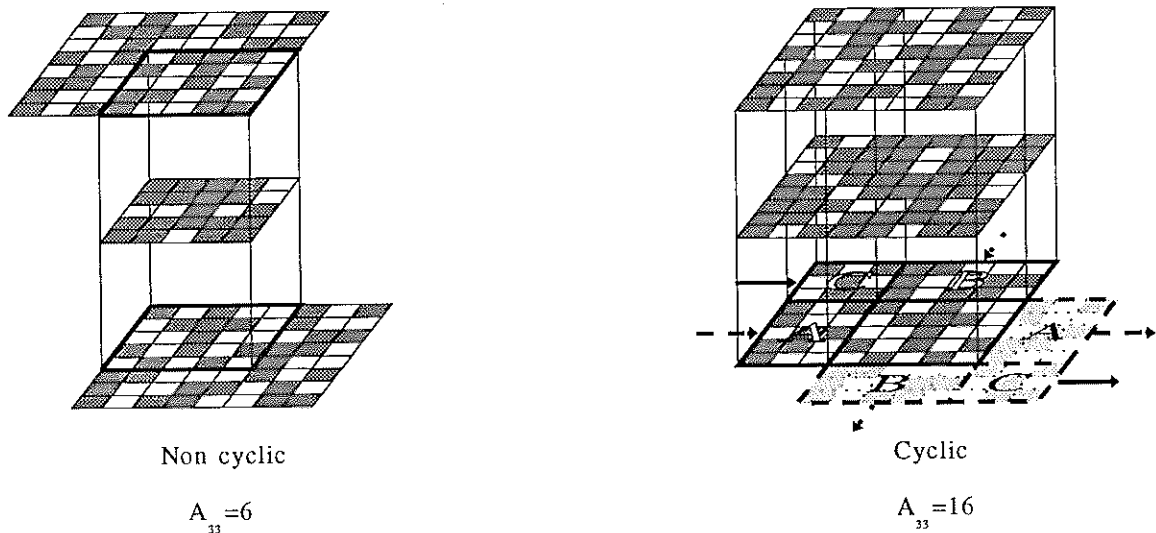


Figure 2.13: Non-cyclic correlation versus cyclic correlation

This can be expressed mathematically as:

$$A_{ij} = \sum_{k=0}^{m-1} \sum_{l=0}^{n-1} M_{kl} M_{(k+i) \bmod m, (l+j) \bmod n} \quad (2.17)$$

where $m \times n$ is the size of the mask pattern (8x8 in the example of fig. 2.8) and $i \bmod m$ is the **remainder** when dividing i by m . For example:

$$1 \bmod 3 = 1 ; \quad 2 \bmod 3 = 2 ; \quad 3 \bmod 3 = 0 ; \quad 4 \bmod 3 = 1$$

With this method we obtain a background flatter *on average* (although it is true that also higher and more chaotic) as it can be seen in figure 2.14. In this example where the mask in fig. 2.8 has been used, the background is more or less centred in a value of 16, and the peak has a value of 32. But do not worry, because this result will be improved soon.

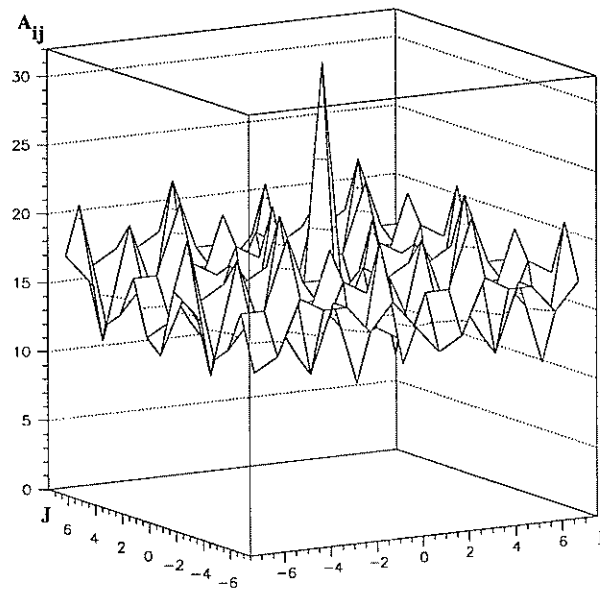


Figure 2.14: Cyclic self-correlation of a mask with random pattern

2.7 Cyclic systems

We could use one or another kind of correlation depending strictly on the physical structure of the telescope [15]. In figure 2.15 two different coded mask telescopes are shown; one of them is a simple (non-cyclic) system, with a mask with the same size of the detector plane. The other is a cyclic system where the mask, instead of a single pattern as in the other case, has a base pattern repeated in a mosaic (in the example of the figure, 2×2), having the base pattern the same size as the detector plane. All these systems are usually shielded and/or collimated in order to avoid that radiation not codified by the mask arrives to the detector plane.

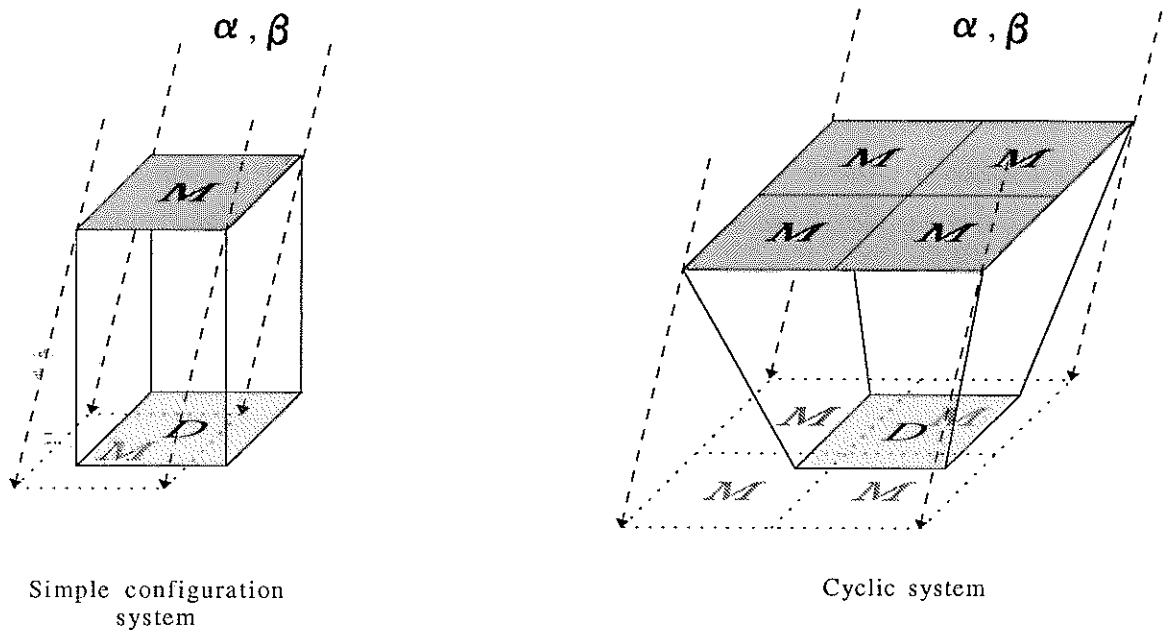


Figure 2.15: Simple configuration system versus cyclic system

As it can be seen in fig. 2.15, for a given direction (α, β) the first system produces a shadow of the mask that is in part outside the detector plane and therefore we will only detect a part of the shadow. In this case we have to use a non-cyclic correlation to reconstruct, because we can only correlate with the mask pattern the intersection of the shadow with the detector plane. However it does not happen the same thing in the second case. What we detect in the detector plane is a cyclically permuted *and complete* version of the basic mask pattern and therefore we can use in this case the cyclic correlation (we could also use the non-cyclic correlation, considering in this case the whole mask, but the final result would be exactly the same and it would take more time).

Although it was not obvious in section 2.6, the cyclic systems give the best results when using correlation-based reconstruction methods (also simply called correlation methods), when employing the correct mask pattern (as we will see in section 2.8). They also have a bigger illumination and a bigger field of view; that is why we are mainly going to refer to these systems (another reason is that LEGRI itself is a cyclic system, as it can be deduced from its description at section 1.5).

There is an intrinsic degeneration in the cyclic systems that arises from its construction, as we can see if we look to figure 2.16; for example, in the cyclic system shown in figure 2.15, just on the border of the field of view there is a degeneration in the directions:

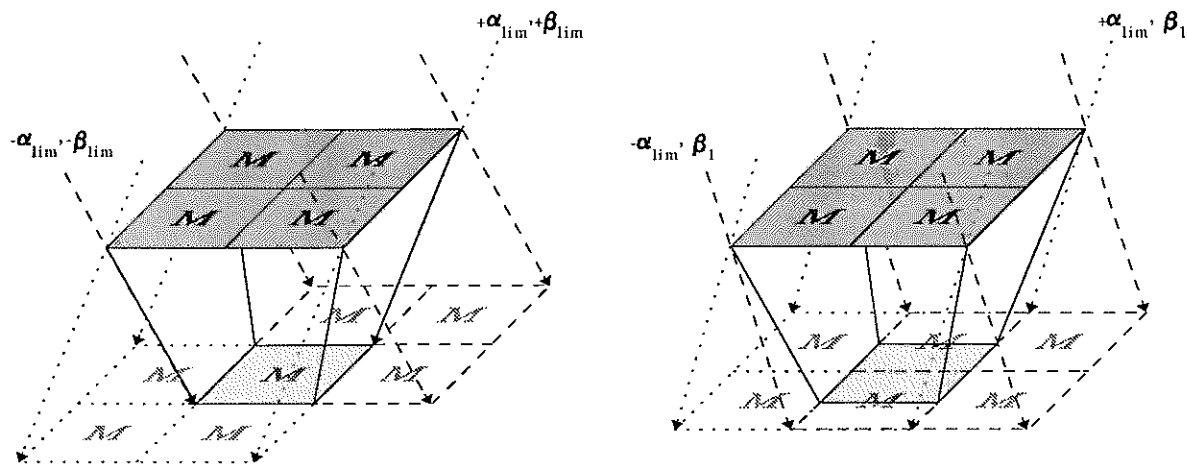


Figure 2.16: Degenerated directions in the border of the field of view in a cyclic system

If we define α_{lim} and β_{lim} as the limit angles of the field of view, so that $(\alpha_{lim}, \beta_{lim})$ will project over the detector the mask pattern without permutation, we have that the directions $(\alpha_{lim}, \beta_{lim})$, $(-\alpha_{lim}, \beta_{lim})$, $(\alpha_{lim}, -\beta_{lim})$ and $(-\alpha_{lim}, -\beta_{lim})$ project the same pattern in the detector plane. That is, the four corners of the field of view are degenerated, and if there is a source in any of those directions we will not distinguish in which direction it is. In the same way, the directions (α_{lim}, β_1) and $(-\alpha_{lim}, \beta_1)$ project the same pattern, and also the directions (α_1, β_{lim}) and $(\alpha_1, -\beta_{lim})$, being α_1 and β_1 two arbitrary angles.

But there is no reason to worry about. It is quite easy to handle this degeneration, as in the mentioned cyclic system the degeneration is restricted to the field of view borders, and there are different ways to break it. One of them is by physical procedures: we can reduce the field of view of the telescope and therefore we will not consider those pixels (for example using collimators or subtracting a part of the mask -the more external rows-). Another way is by operative procedures and it consists of varying the pointing direction of the

telescope in order to obtain more information about the real position of the source. This procedure is shown in figure 2.17.

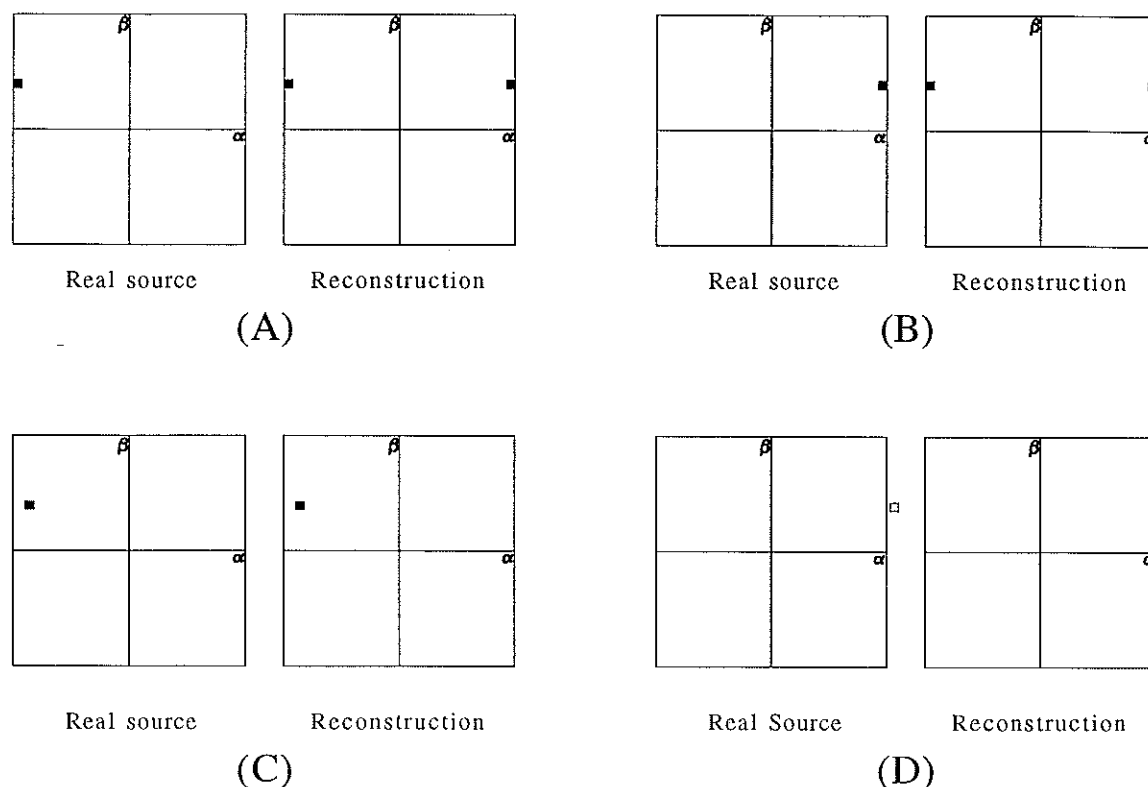


Figure 2.17: Elimination of the degeneration in the borders in a cyclic system by varying the pointing direction of the telescope (in this example, towards the left)

In cases (A) and (B) we have two sources in the field of view border, on the right and on the left respectively. Both produce the same pattern on the detector plane (as we saw in fig. 2.16) and therefore, since we can not distinguish them, the process will reconstruct both possibilities, and we have two sources where there is just a single source. To single out between both cases, we can slightly vary the pointing direction (towards the left in the example); then the (A) case becomes (C) and the source is not on the border but correctly reconstructed. But the (B) case becomes (D) and the source is now out of the field of view; we have now no signal in the detector plane and therefore we reconstruct an empty field.

2.8 Choice of the mask pattern

As we have already said several times, the use of the correct mask is very important. It must be as distinguishable as possible, and if it is possible it should not have shadow-direction degenerations: this means that two different directions should **not** project the same pattern in the detector plane.

The next step is, thus, the choice of a correct pattern. Since the cyclic systems will give better results, we want to find masks whose cyclic permutations will be perfectly distinguishable between them.

2.8.1 Random masks

Obviously, the first proposals for mask pattern was a random pattern. This case has already been seen when we spoke about cyclic and non-cyclic correlations; in fact this kind of masks gives quite good results, but the background that generates (the reconstruction noise, see fig. 2.14) is quite fluctuating.

2.8.2 Non-Redundant Arrays (NRA)

In 1971, Golay proposed a kind of mask whose properties were very similar to the desired properties for a perfect reconstruction [16]. This mathematical sets are obtained by imposing that there are not two pairs of holes in the mask with the same vector separation (horizontal and vertical distance between the holes); the only exception is 0 elements spacing. The (non-cyclic) self-correlation of this arrays is a single central peak and a flat background (until a certain separation where the two patterns are not overlapped and the self-correlation is 0). This flat background is due to the fact that the separation vector between hole pairs is unique (non-redundant).

Unfortunately, the mathematical constraints imposed to the NRA are too strong and therefore there are not many sets; and usually they do not have

many holes: one of the biggest NRA masks (with 30x30 elements) has only 27 holes. This gives a transparency (*open area/closed area*) of only 0.03. This gives a very bad SNR and so its interest in astronomy is reduced (although this kind of mask has found applications in medicine).

2.8.3 Uniformly Redundant Arrays (URA)

Considered in terms of cyclic self-correlation, we obtain the mathematical solution to our problems with the URA sets. The URA are non-random patterns whose vector separation between two holes is repeated a **constant number** of times, the same for any other vector separation (different of 0). This constraint is smaller than the one for the NRA, so we can dispose of more variety of patterns, and also with bigger transparency. The URA sets are based on the *cyclic difference sets* (CDS) [9]. We will explain those sets with the following example: given the integer numbers from 1 to 15, we are going to mark in a special way the numbers 1, 2, 3, 5, 6, 9 and 11. Those numbers have a strange relation; if we permute cyclically the set of numbers from 1 to 15 and bring them face to face with the original set, the number of coincidences between marked numbers will always be the same, independently of the permutation (see figure 2.18).

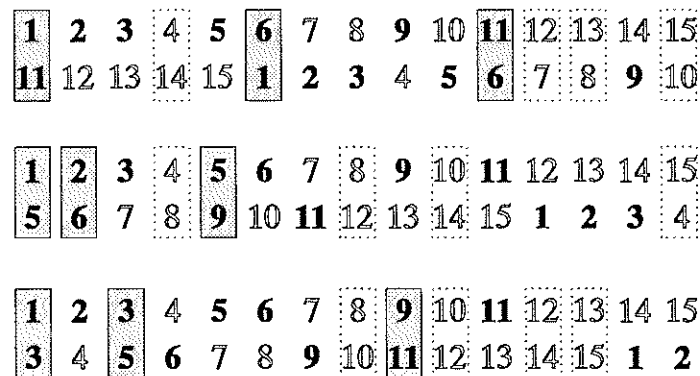


Figura 2.18: Cyclic difference set of base 15

As it can be seen in the picture, we always have three marked elements of the set of numbers in the permuted set that coincide with the marked elements of the original set (except when we do not permute, when 7 elements coincide). Besides, in the complementary set of numbers 4 elements coincide (except when we do not permute, coinciding 8). That is to say, the complementary set of a CDS is also a CDS.

comple. diff. set.

From a cyclic difference set we can build an URA mask by following this procedure [9]: 15 is the product of the prime numbers 3 and 5; therefore we create a rectangular array with size 3x5 and we place in it the numbers from 1 to 15 diagonally; afterwards we identify each element of the CDS (each marked element) for example with an opaque element, being the remaining transparent elements (it is better if we have an even number of holes, as we will see in section 2.9.1). That is:

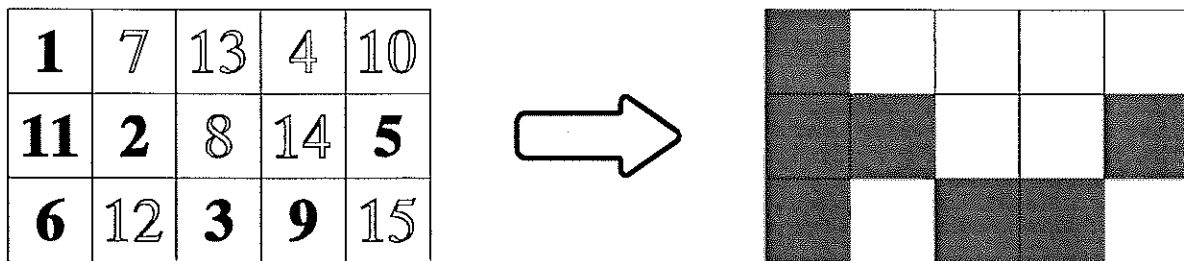


Figure 2.19: Generation of an URA pattern using a cyclic difference set

This layout maintains the characteristics of the CDS when we calculate its cyclic self-correlation; when $i=0$ and $j=0$, in this mask we have that the seven opaque elements coincide (that is, the eight holes) and then the self-correlation of this mask (when $i=0$ and $j=0$) is 8; in any other permutation only 3 opaque elements will coincide (and 4 holes); then, its self-correlation for **any** other permutation (different of $i=0, j=0$) is 4. This is valid for any URA array; the value of its cyclic self-correlation is a central peak (whose value is the number of mask holes) and a absolutely flat background.

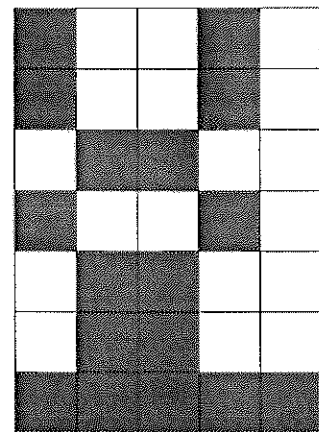


Figure 2.20: URA 5x7.

In figure 2.20 we can see a 5x7 URA pattern, and in figure 2.21 we can see its self-correlation.

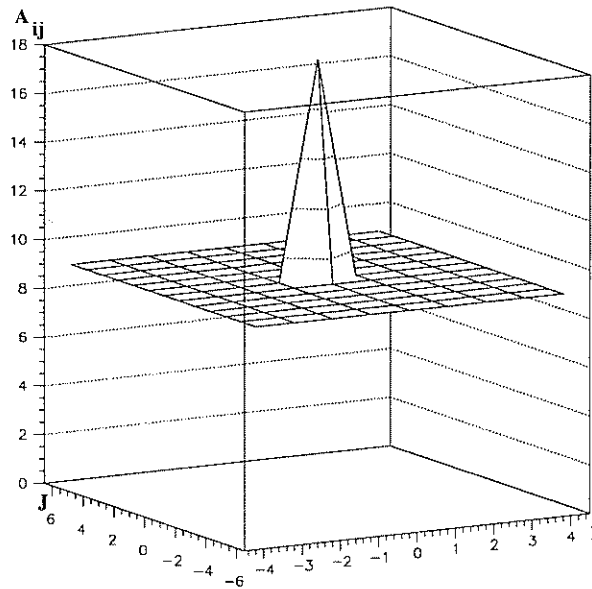


Figure 2.21: Self-correlation of the URA pattern in fig. 2.20.

There are different URA families, depending on the methods of generation and the CDS used. Besides, a given URA can belong to different classifications. If we consider a CDS of base N (15 in the previous example, shown in figure 2.18) containing K elements (7 elements in the previous example) and with λ solution pairs (the number of elements that coincide when we permute cyclically the set; 3 in the previous example) we have [17] the following relation:

$$\lambda = \frac{K(K-1)}{N-1} \quad (2.18)$$

and therefore we can characterize a CDS, and therefore also the URA generated with it, just with two numbers, N and K (N is the number of elements in the mask and H the number of opaque -or transparent, depending on our choice- elements).

In a simplistic way, we can identify K with the signal and λ with the reconstruction noise; thus we want the difference between K and λ to be as large as possible. This is achieved by the Hadamard difference sets, which fulfil the following conditions:

$$\begin{aligned} N &= 4m - 1 \\ K &= 2m - 1 \\ \lambda &= m - 1 \end{aligned} \tag{2.19}$$

being m an integer. These arrays can be classified in:

- Twin primes: $N = p \cdot (p+2)$ where both p as $p+2$ are prime numbers. This is the case of the examples in figure 2.19 (3x5) and 2.20 (5x7). The way of generating the pattern M_{ij} of this URA array [13] is:

$$\begin{aligned} M_{ij} &= 0 \text{ if } i=0 \\ M_{ij} &= 1 \text{ if } j=0, i \neq 0 \\ M_{ij} &= 1 \text{ if } C_i(p) \cdot C_j(p+2) = +1 \\ M_{ij} &= 0 \text{ if } C_i(p) \cdot C_j(p+2) = -1 \end{aligned}$$

Handwritten note: $C_3(5) = -1, C_4(5) = 1$

where $C_i(p) = 1$ if i is a quadratic residue mod p (that is, if exists an integer n such that $n^2 \text{ mod } p = i$), and equal to -1 otherwise. For $p = 5$, for instance, we have:

$$\begin{aligned} (1)^2 & & (2)^2 & & (3)^2 & & (4)^2 & & (5)^2 \\ 1 \text{ mod } 5 &= 1; & 4 \text{ mod } 5 &= 4; & 9 \text{ mod } 5 &= 4; & 16 \text{ mod } 5 &= 1; & 25 \text{ mod } 5 &= 0 \\ 36 \text{ mod } 5 &= 1; & 49 \text{ mod } 5 &= 4; & 64 \text{ mod } 5 &= 4; & 81 \text{ mod } 5 &= 1; & \text{etc...} \end{aligned}$$

In this example, 1 and 4 are the quadratic residue mod 5, that is, $C_1(5)=1, C_2(5)=-1, C_3(5)=-1$ and $C_4(5)=1$.

- Pseudo-noise sequences or m -sequences: $N = 2^m - 1$ (m an integer). The example of figure 2.19 also fulfils this case.
- Quadratic residues, where N is prime and the set is given by the squares of the first $((N+1)/2)$ integers, mod N . They are not applicable to

rectangular masks, but to hexagonal masks as the one in fig 2.22. This masks are called HURA (Hexagonal URA) and have the special feature that when we turn them 60° , we obtain the antipattern (except for the central element).

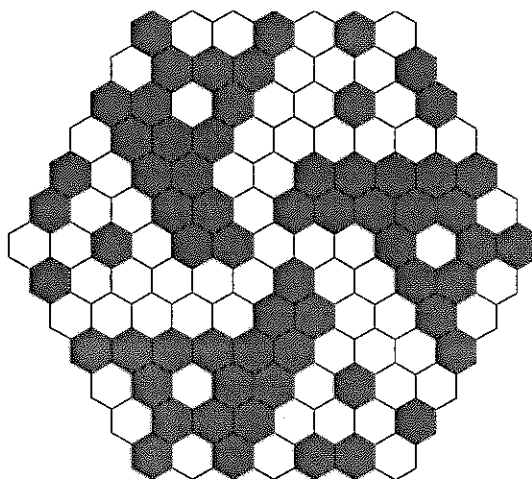


Figure 2.22: Hexagonal HURA pattern

The Singer sets are another CDS group that fulfils the following:

$$\begin{aligned}
 N &= \frac{t^{m+1} - 1}{t - 1} \\
 K &= \frac{t^m - 1}{t - 1} \\
 \lambda &= \frac{t^{m-1} - 1}{t - 1}
 \end{aligned} \tag{2.20}$$

where t is a prime number. When $t=2$, we obtain the m sequences.

The number of URA sets is limited for the "population" of prime numbers, so the choice of an URA mask appropriate to a given detector needs a carefully study. In general the contrary process it is easier: to choice an URA mask, and then to define the appropriate detector.

2.8.4 Modified Uniform Redundant Arrays (MURA)

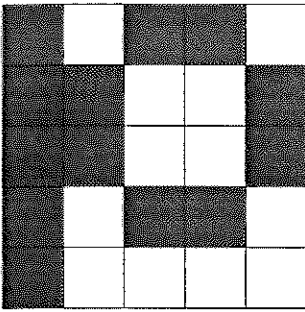


Figura 2.23: MURA 5x5.

Gottesman and Fenimore [18], proposed in 1989 another kind of coded mask which have some of the characteristics of the URA arrays, and that allow a bigger variety of patterns. These patterns are the MURA, and as their name says, they are a modification of the URA patterns.

As we have said, in the URA generated by twin primes we have that $N = p \cdot q$, where both p and q are prime numbers, and they fulfil $p - q = 2$. But the set given by $p - q = 0$ is also very interesting for imaging and allows square mask patterns. These are the MURA patterns. The generation procedure is the same as the one for twin primes (but now $N = p \cdot p$). That is:

$$\begin{aligned}
 M_{ij} &= 0 \text{ si } i=0 & \text{e} \\
 M_{ij} &= 1 \text{ si } j=0, i \neq 0 \\
 M_{ij} &= 1 \text{ si } C_i(p) \cdot C_j(p) = +1 \\
 M_{ij} &= 0 \text{ si } C_i(p) \cdot C_j(p) = -1
 \end{aligned}$$

As we have seen in section 2.8.3, for $p = 5$ the numbers **1** and **4** are the quadratic residues mod 5; then, following this procedure we obtain the pattern shown in figure 2.23. The element (0,0) is the one placed at the bottom left corner. This is the base pattern of the LEGRI mask (as we can see if we look again at fig. 1.3 and 1.4). In figure 2.24 we can see its cyclic self-correlation.

We can see in this figure that the background now is not flat, as it happened with the URA patterns but does not fluctuate chaotically as in the random mask case; in fact this odd fluctuation is very easy to correct as we will see in section 2.9.1.

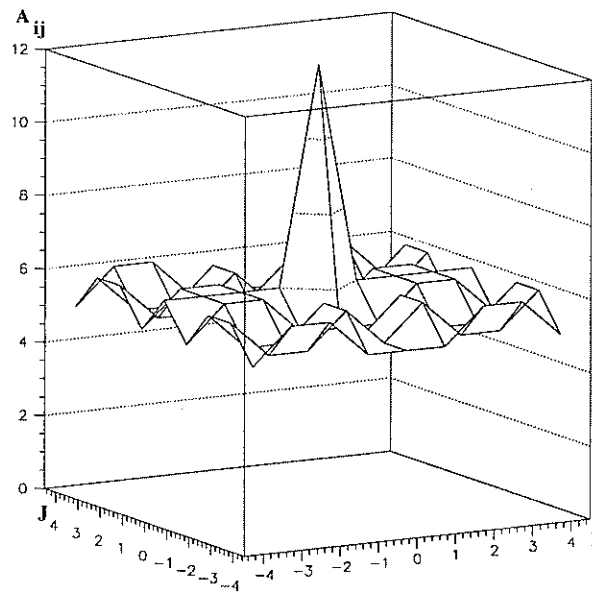


Figure 2.24: Self-correlation of the 5x5 MURA pattern shown in figure 2.23

2.8.5 New patterns

Recently the application in astronomy of a new kind of patterns with perfect self-correlative properties have been suggested. Generically they are called Perfect Binaries Arrays (PBA), and both the URA and MURA patterns can be considered as a particular case of them. Their imaging properties are very similar to the MURA and URA properties; its main advantage lies in their greater variety of possible patterns. To know more about them, we refer the reader to [19], [20], [21] and [22].

2.9 Choice of G

As it was explained in section 2.6 we are looking for a reconstruction array g which fulfils that M^*G is as similar as possible to a delta function; repeating equation 2.21, this means:

$$(M^*G)_{ij} = \delta_{0i} \delta_{0j} \quad (2.21)$$

We have also said that G is a modification of M . On the whole, we can consider we have a good result if:

$$(M * G)_{ij} = (\text{no. of holes}) \delta_{0i} \delta_{0j} \quad (2.22)$$

(which is a scale factor). We get this result when we have an URA or MURA (or PBA) array and we choose the proper G . By the way, we define [13] the *System Point Spread Function* (SPSF) as:

$$SPSF = M * G \quad (2.23)$$

that is the answer of the system for a point source in the middle of the field of view and without noise (as we have seen in section 2.6 for the particular case when $M=G$); it gives us an idea of how good the reconstruction is, given a mask M and a reconstruction array G .

2.9.1 Balanced correlation

The balanced correlation [23] is the most usual method used when reconstructing images by means of a correlation. It consists in defining the reconstruction array G_{ij} as:

$$\begin{aligned} G_{ij} &= 1 \text{ if } M_{ij} = 1 \\ G_{ij} &= -1 \text{ if } M_{ij} = 0 \end{aligned}$$

This makes up for quite a lot the existence of reconstruction noise (which appeared when reconstructing using M as reconstruction array). In fact, in the case of the URA arrays, this reconstructed noise is totally suppressed if the number of holes (the number of 1's in the M array) is even, since in that case the cyclic correlation of M and G is:

$$\tilde{O}_{ij} = \sum_{k=0}^{m-1} \sum_{l=0}^{n-1} M_{kl} G_{(k+i) \bmod m, (l+j) \bmod n} \quad (2.24)$$

For (i,j) different to $(0,0)$, $M * G$ is a sum of values 1 and -1; there are as many values as holes (1's) in M (if this number is odd, it would not be possible that

all the 1's balance totally the -1's in order to give a value of 0).

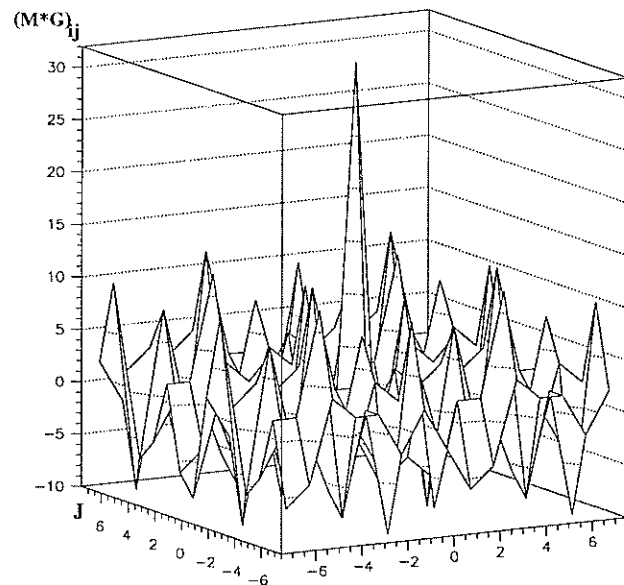


Figure 2.25: Balanced reconstruction of the random pattern shown in figure 2.8

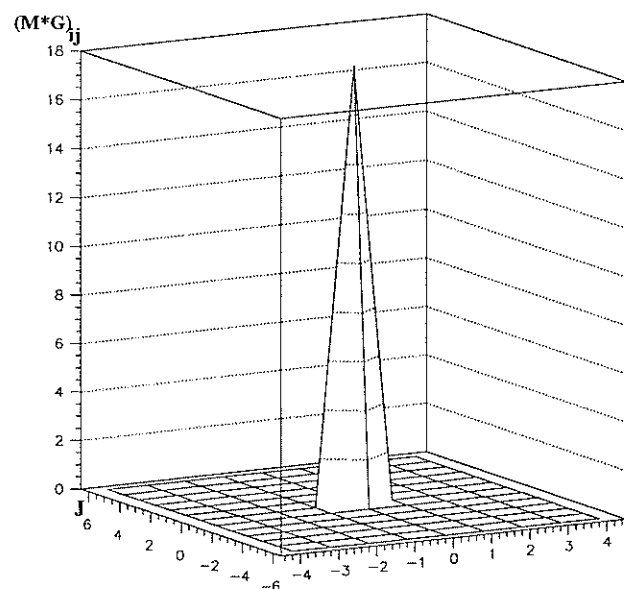


Figure 2.26: Balanced correlation of a 5x7 URA

In figure 2.25 we can see the effect of the balanced correlation applied to the random mask in figure 2.8, and in figure 2.26 we can see its effect on the URA patterns shown in fig. 2.20; if we compare these figures with those we got

when we only used the cyclic self-correlation as reconstruction method (that is to say, using the own M array as reconstruction array, see figures 2.14 and 2.21) we can see how in the case of the random mask the background has now been strongly suppressed, being now centred in 0 instead of 16 while the peak value is still the same; and how, in the case of the URA mask, the background is now absolutely flat and with a value of 0!

On the other hand, if we apply balanced reconstruction to our MURA pattern in fig. 2.23, although we greatly suppress the reconstruction noise (similarly to what it happened with the random mask) we do not obtain a flat background with value 0 as we would desire, but what we can see in figure 2.27.

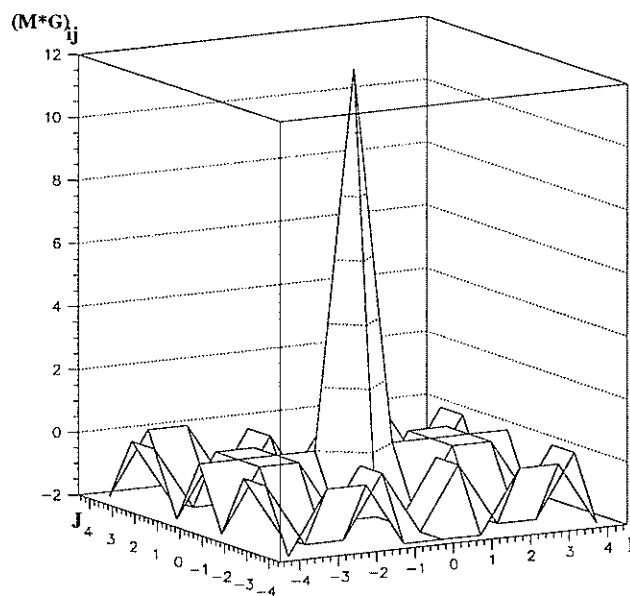


Figure 2.27: Balanced reconstruction of a 5x5 MURA

But there is not problem. As it was said in section 2.8.4, this is a problem that will be easily corrected. In order to have a flat background, we just have to do a small modification of our G array [18], which consists of changing its (0,0) element (the equivalent to the element at the bottom left corner in figure 2.23 for M) that is now a -1 (because in M is a 0) into a +1. Using this particular version of the balanced correlation for MURA mask, we have the following result:

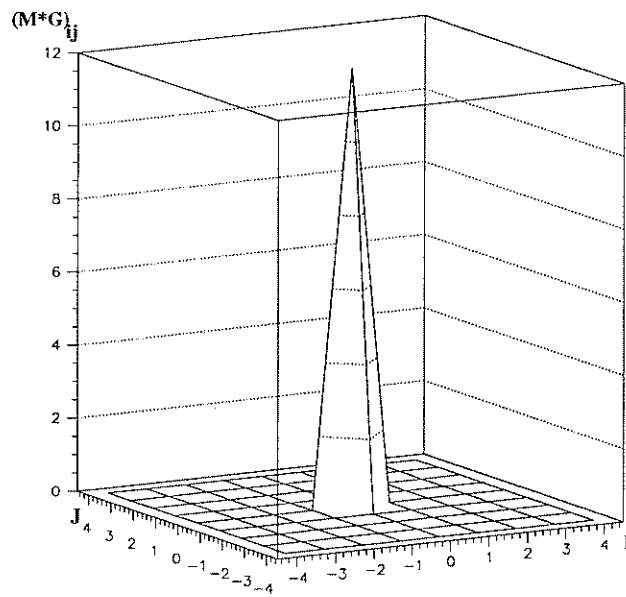


Figure 2.28: Balanced reconstruction of a 5x5 MURA, once the reconstruction array has been modified

That is, a flat plane with value 0, as we desired.

As it can be deduced from section 2.5, the angular resolution of these kind of telescopes (or what is the same, the size of the pixels in the reconstructed image) is given by:

$$\text{resolución} = \arctg\left(\frac{c}{f}\right) \quad (2.25)$$

where c is the size of a mask element and f is the mask - detector plane distance; therefore, the resolution is equal to the angle that a mask element subtends, seen from the detector plane.

From these results, if we use correlation methods, we can define the **optimum telescope** [14] as the coded mask system in which there are not codification errors; this means that it obtains an optimum reconstruction without reconstruction noise (the only noise is due to the data). This is achieved using cyclic mask designs based on MURA or URA (or PBA) patterns,

and making sure that the shadow projected on the detector plane is an integer number of cycles the basic mask pattern. Typically a mask with $(N_x+1) \cdot (N_y+1)$ cycles and a detector plane with a size equal to $N_x \cdot N_y$ cycles is used. A very usual case is $N_x=N_y=1$. LEGRI is close to this case, because the mask has $2.8 \cdot 2.8$ cycles of the basic MURA pattern, and the detector has a size of $1 \cdot 1$ cycles. This is because it was desired a field of view (see section 2.11) as big as possible and therefore the maximum mask and detector size allowed by the remaining devices in the Minisat 01 platform was used.

We have mentioned here the most used variety of balanced correlation. To round off, we say now that one can deal with a more general case [17] by defining the reconstruction array G as:

$$\begin{aligned} G_{ij} &= A \text{ if } M_{ij} = 1 \\ G_{ij} &= -\alpha \text{ if } M_{ij} = 0 \end{aligned}$$

Depending on the values of these two parameters we can favour some characteristics in the reconstructed image or others; flux conservation between the detected signal and the reconstructed image, noise elimination, etc... In practice, all these possibilities are incompatible, and if we favor some characteristic in the reconstruction, we worsen others (for example, if we remove the noise in the reconstructed image, we have a wrong value of the reconstructed intensities). We think that the most suitable values are $A=\alpha=1$, although we leave the choice to the reader's opinion. A detailed discussion of the effect of these parameters can be found in [17].

2.9.2 Finely sampled balanced correlation (FSBC)

In section 2.9.1 we have implicitly supposed that the detector plane can be subdivided into pixels with the same size of the mask elements. But it could happen that the detector plane had better spatial resolution and we could subdivide it more finely. This is what happens with the LEGRI detector plane, in which each mask element is equivalent to 2×2 detector plane elements, or what could happen in a continuous detector in which we could in principle subdivide the detector plane as finely as we wanted, and so each mask element

would be equivalent to $n \times n$ detector plane elements, being n the integer we want (in practice this subdivision would have a limit, because a *really* continuous detector does not exist). When this subdivision is possible, we can improve the reconstructed image using a modification of the balanced correlation called finely sampled balanced correlation [23]. We will explain this method using as an example the case of LEGRI.

Each mask element is equivalent to 2×2 detector plane elements; thus we will subdivide the mask array M (see fig. 2.29) and each mask element will correspond to a single detector plane element and the basic mask pattern will have the same size and element number as the detector plane (as a result, the pixels in the reconstructed image will be also subdivided).

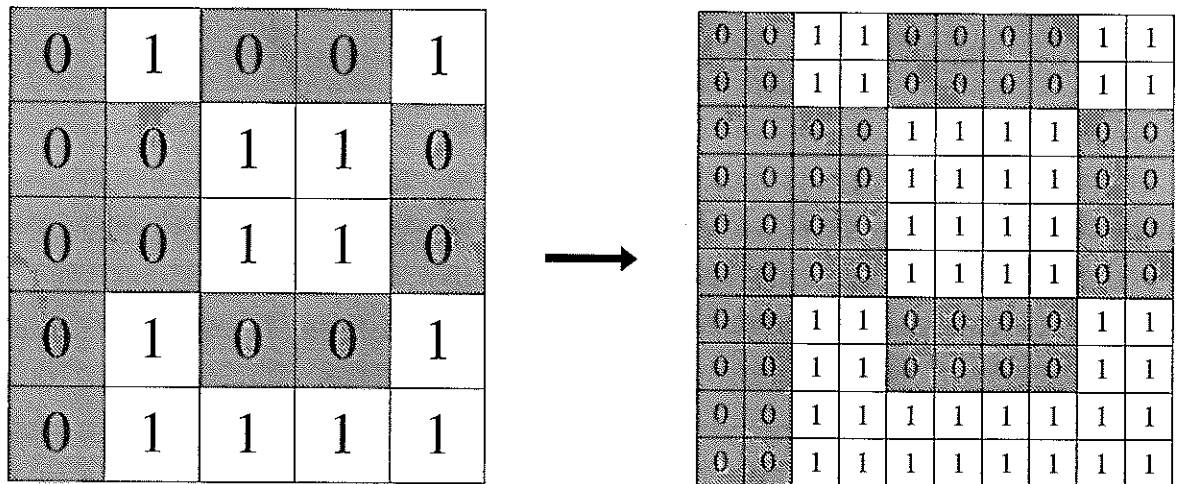


Figure 2.29: Subdivision of the M array in smaller elements with the same size as the elements in the detector plane

Once this subdivision is done, we generate the array G in the same way we did in section 2.9.1:

$$G_{ij} = 1 \text{ si } M_{ij} = 1$$

$$G_{ij} = -1 \text{ si } M_{ij} = 0$$

and in the case of MURA patterns, the subdivisions of its element (0,0) will be changed to 1 instead of -1, as we did in the previous section (see figure 2.31). Now both M and G will have a greater number of elements than in the

previous case (and thus the reconstructed image).

The response in this case will not be a delta function as it happened in the case of balanced correlation but it will have a pyramidal structure (see fig. 2.30 in two different representations), with a FWHM equal to:

$$\text{FWHM} = \arctg\left(\frac{c}{f}\right) \quad (2.26)$$

that is, equal to the resolution (equation 2.25). But although the angular resolution is still the same, due to the fact that now the pixels are smaller (a half of the size, in this case), we will be able to locate the sources more accurately (more finely) and have a better image.

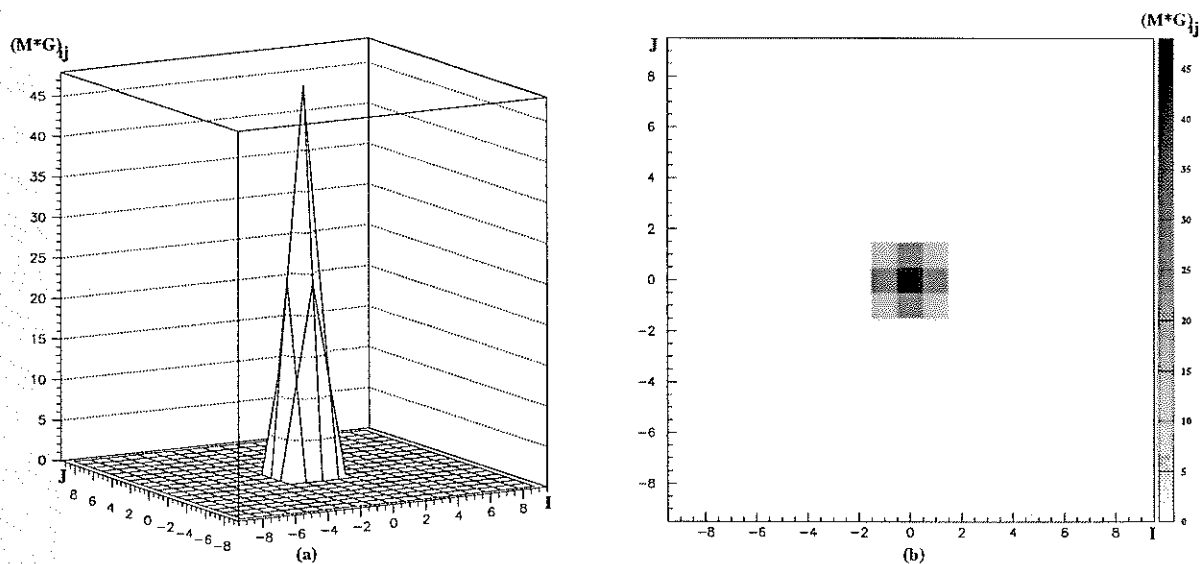


Figure 2.30: $M*G$ using finely sampled balanced correlation

2.9.3. δ -decoding

The δ -decoding method [23] is a method for minimizing the *non-delta* structure that appears with finely sampled balanced correlation (that is, it is a method to improve the contrast of the image). It is similar to FSBC, because it also subdivides the M array in order to have the same size of the elements as the detector plane. The difference is in the definition of the G array; now it is a bit different. We can see this difference more clearly in figure 2.31.

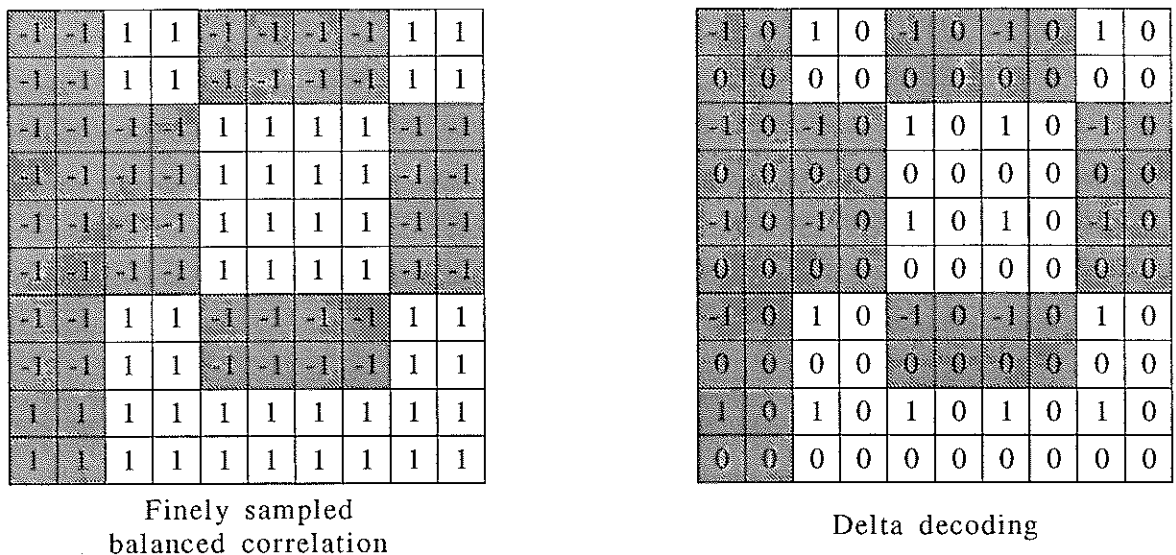


Figure 2.31: Comparison between the reconstruction arrays used in finely sampled balanced correlation and δ -decoding in the case of the pattern of LEGRI

This means that in each mask element, instead of converting all its subdivisions into values 1 or -1 (as we did in FSBC) we will only convert one of them (we can choose which one, but it must be the same in each mask element; in fig.2.31 we have chosen the top left subdivision) keeping 0 the remaining subdivisions. This procedure improves the contrast in the reconstructed image; now the response is not a pyramid but a (bidimensional) box function, which width is equal to the angular resolution given by eq. 2.25.

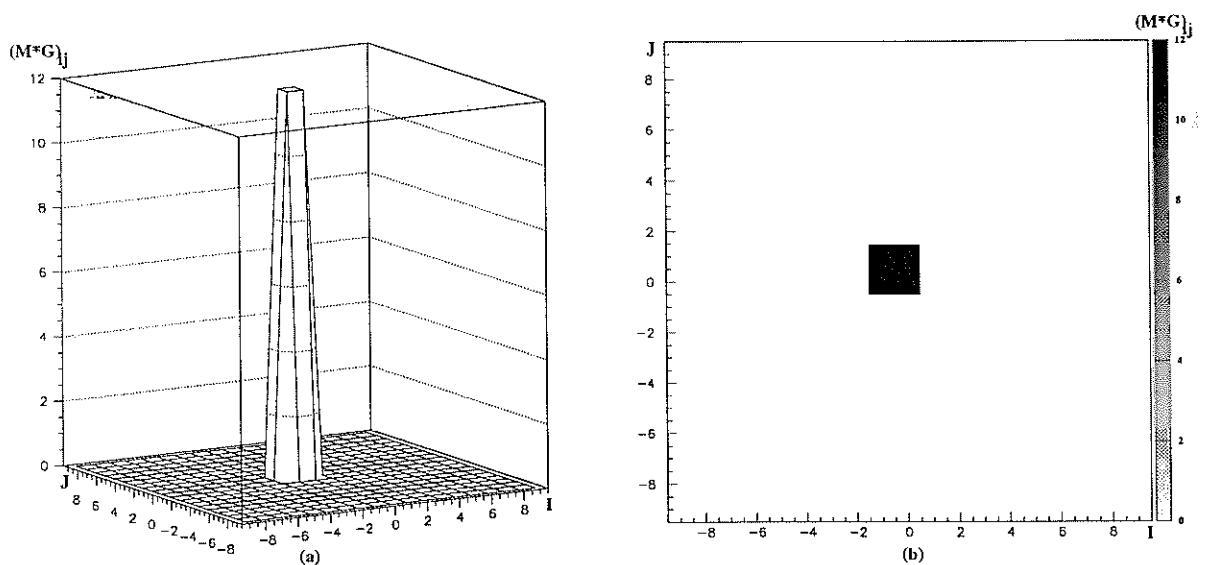


Figure 2.32: M^*G using δ -decoding

Like when using FSBC (since the pixel size is smaller), we can more finely locate the sources, although this method introduces an intrinsic shift, depending on where we put the 1's and -1's in G . If it were possible to subdivide each mask element in $n \times n$ pieces, being n an odd number (this is **not** the case of LEGRI), choosing the element different to 0 as the **central** one, we would obtain that there is not shift in the reconstructed sources.

2.10 Fourier transforms

As we have said before, the reconstruction method consists of obtaining the correlation of the D data array with a reconstruction array G . That is, $\tilde{O} = D * G$, which can be written in a more explicit way:

$$\tilde{O}_{ij} = \sum_{k=0}^{m-1} \sum_{l=0}^{n-1} D_{kl} G_{(k+i) \bmod m, (l+j) \bmod n} \quad (2.27)$$

Nevertheless, if we implement this equation in telescopes where m and n are big numbers (this means that both D and G have a great number of elements) we find that we need a great number of calculations: $m \cdot n$ multiplications for each ij sky pixel and depending on m and n , it can be impossible to do these calculations in a suitable time. This will not be the case of LEGRI, because $n=m=10$ and therefore we have to do 100 multiplications for each reconstructed image pixel; the reconstruction of the whole image is done in less than a second (in a SUN Sparc 20); but for completeness reasons we are going to explain an alternative and faster method to carry out the correlation of eq. 2.27. We will use in this method the Fourier transforms.

The Fourier transform of a function $h(t)$ is defined by:

$$H(v) = \mathcal{F}[h(t)] = \int_{-\infty}^{\infty} h(t) e^{2\pi i v t} dt \quad (2.28)$$

and its inverse by:

$$h(t) = \mathcal{F}^{-1}[H(v)] = \int_{-\infty}^{\infty} H(v) e^{-2\pi i v t} dv \quad (2.29)$$

Usually it is said that $h(t)$ is the representation in the space of times of the function, and $H(v)$ the representation in the space of frequencies. Similarly, if instead of a continuous function we have a discrete set of data h_k , we define its Fourier transform [24] by:

$$H_n = \sum_{k=0}^{N-1} h_k e^{2\pi i k n / N} \quad (2.30)$$

and its inverse by:

$$h_k = \frac{1}{N} \sum_{n=0}^{N-1} H_n e^{-2\pi i k n / N} \quad (2.31)$$

Let a and b be two discrete arrays of size m whose correlation, c (which is another array) we want to calculate (in equation 2.27, D and G are equivalent to a and b). Let $c_k = (a * b)_k$ be the k -th element of the correlation of both arrays. And let A and B be the Fourier transforms of a and b . The discrete correlation theorem [24] says:

$$\begin{aligned} a * b &= \mathcal{F}^{-1}[\mathcal{F}(a) \cdot \mathcal{F}(b)^*] \\ c_k = (a * b)_k &\leftrightarrow A_n \cdot B_n^* = C_n \end{aligned} \quad (2.32)$$

where * represents the conjugated complex; what in the space of times corresponds to a correlation (which implies m multiplications for each element) in the space of frequencies corresponds to a single multiplication. That is, in order to calculate the c_k element of the correlation we need to multiply the m elements of a and b (shifted between them k positions) while for calculating the C_n element of the Fourier transform of c , we only have to multiply the n -th elements of the A and B arrays.

On the other hand, we now have to calculate the Fourier transforms, which are additional operations; to minimize the number of calculations, there is an algorithm that obtains the Fourier transforms of discrete sets, called Fast

Fourier Transform (FFT) [24]. But, though fast, it has the limitation that it can only handle with sets of numbers having $N = 2^l$ elements, where l is an integer. If this is not the case, we have to pad the set with enough 0's until we have a number of elements equal to an integer power of 2 (or if it is possible, to subdivide the set -as we did with FSBC and δ -decoding- in order to have the required number of elements) [24] [14].

2.11 Shields and collimators

These kind of telescopes are usually shielded and/or collimated in order to avoid that radiation not codified by the mask arrives at the detector plane. Both systems have their advantages and disadvantages.

2.11.1 Collimators

When we use collimators (for instance the case of LEGRI) we limit the field of view of each detector unit in such a way that, for example, they can only see the mask (fig. 2.33). This arrangement has the advantage that all the detector plane elements have the same field of view, independently of the position they have in the detector plane. This means that if a collimator exists and it is rather high, it will define the telescope field of view.

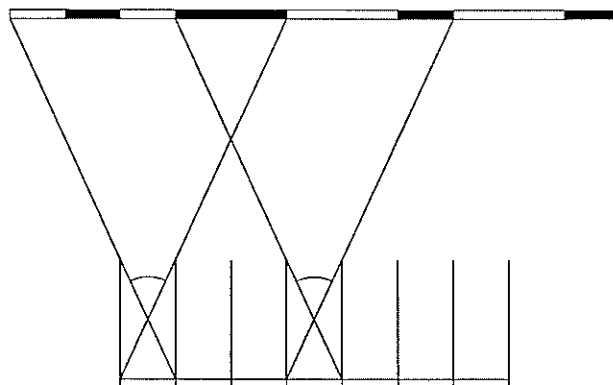


Figure 2.33: Limitation of the field of view of the detector plane units using a collimator

On the other hand, the collimator has an undesired effect on the detected signal; the farther from the field of view centre the source is, the smaller the detected flux will be, as the reader can see looking at figure 2.34.

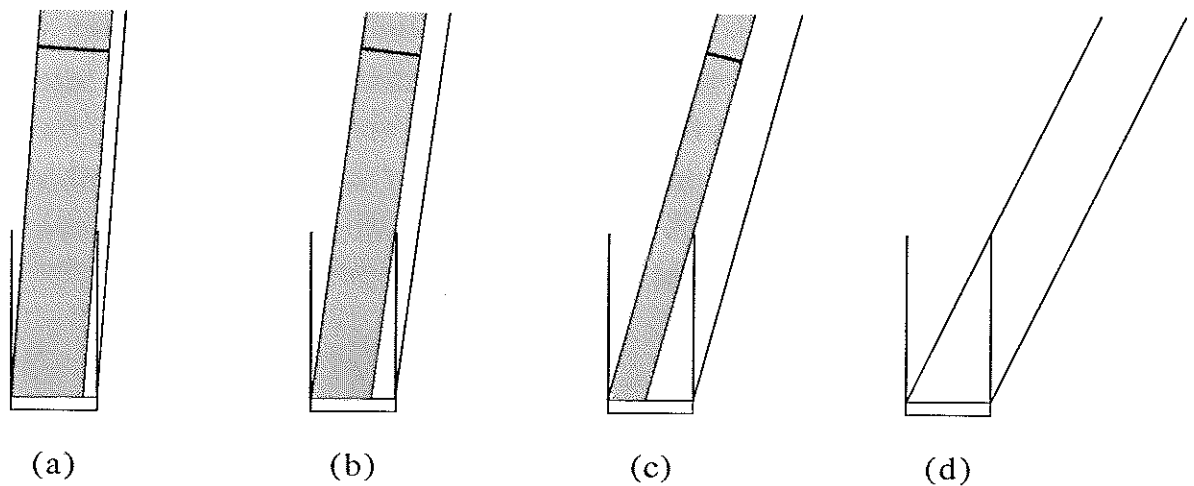


Figure 2.34: Effect of the collimator in the detected signal; the bigger the angle where the signal is received from, the bigger the signal absorption produced by the collimator

The response varies with the illumination angle, since the detector units receive a different flux depending on it. The response of the collimator is almost triangular, with a maximum value when the angle is equal to 0 and decreasing almost linearly until the angle reaches a maximum value (this is the case (d) shown in figure 2.34) and from it the response is equal to 0. Let H be the collimator height, $L \times L$ the detector unit area and α the angle where the source is, as we can see in figure 2.35 (a).

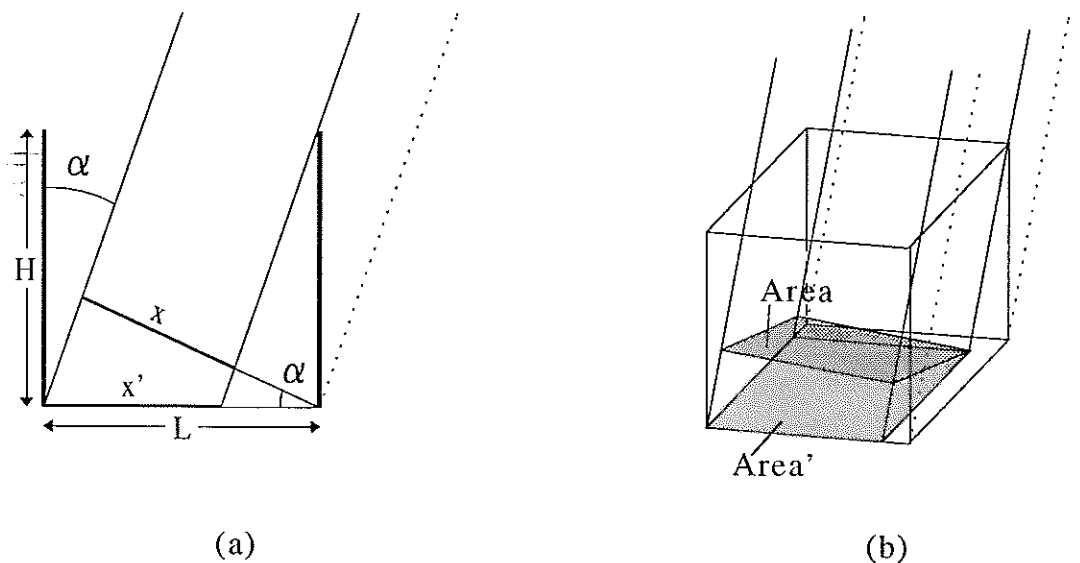


Figure 2.35: Effect of the collimator in the response of the detector, in (a) 2 and (b) 3 dimensions

We have that x' is the zone of the detector unit illuminated, given by:

$$x' = L - H \cdot \operatorname{tg}|\alpha| \quad (2.33)$$

and x is the projection orthogonal to the direction α , and it is equal to:

$$x = x' \cos\alpha = \frac{x'}{\sqrt{\operatorname{tg}^2\alpha + 1}} \quad (2.34)$$

(this is a geometrical effect, due to the fact that the detector is "rotated" with regard to the direction where the source light comes from; it always appears, independently of the presence or absence of a collimator). Therefore, we define the flux allowed by the detector (in fact, the fraction) as:

$$\Phi(\alpha) = \frac{x}{L} = \cos\alpha - \frac{H}{L} \operatorname{sen}|\alpha| \quad (2.35)$$

If we generalize this to the three-dimensional case (fig. 2.35 (b)), we have that $Area'$ is the zone of the detector unit that is illuminated, and it is given by:

$$\begin{aligned} x' &= L - H \cdot \operatorname{tg}|\alpha| \\ y' &= L - H \cdot \operatorname{tg}|\beta| \\ Area' &= x' \cdot y' \end{aligned} \quad (2.36)$$

and $Area$ is the projection orthogonal to the direction (α, β) ; generalizing equation 2.34 (see appendix I) it is:

$$Area = \frac{Area'}{\sqrt{\operatorname{tg}^2\alpha + \operatorname{tg}^2\beta + 1}} \quad (2.37)$$

The flux seen through the collimator, similarly to eq. 2.35, is:

$$\Phi(\alpha, \beta) = \frac{Area}{L^2} \quad (2.38)$$

These expressions have a physical meaning whenever x' and y' are bigger than 0 (that is, the source illuminates the detector, indeed). This will happen if:

$$\operatorname{tg}|\alpha| \leq \frac{L}{H} \quad \text{and} \quad \operatorname{tg}|\beta| \leq \frac{L}{H} \quad (2.39)$$

2.11.2 Shields

A shield is a structure opaque to the radiation that wraps the detector-mask set in such a way that any radiation that has not previously passed through the mask does not arrive to the detector plane (fig. 2.36). This system, when compared with a collimator, has the disadvantage that each detector has a different field of view depending on its position in the detector plane; but it has the great advantage of not suppressing the detected signal as its position moves away from the field of view centre; we have only a small decrease due to the fact that the detector is rotated with regard to the position of the source (and whose effect we have showed in equations 2.34 and 2.37 for two and three dimensions, respectively). But this is a very small effect when compared with the collimator effect.

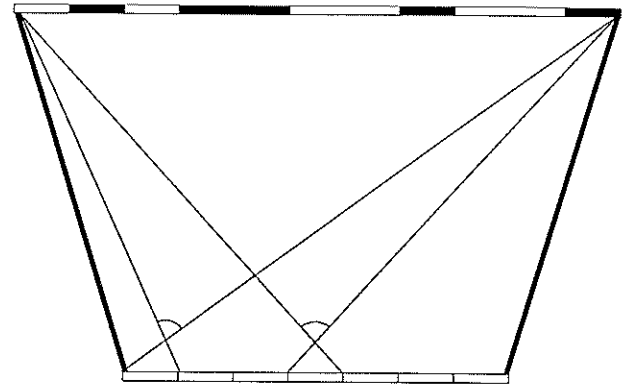


Figure 2.36: Limitation of the detector field of view using a shield

If the system does not have a collimator (or if it exist but it does not limit the field of view to the mask), we can define different fields of view [25], according to figure 2.37.

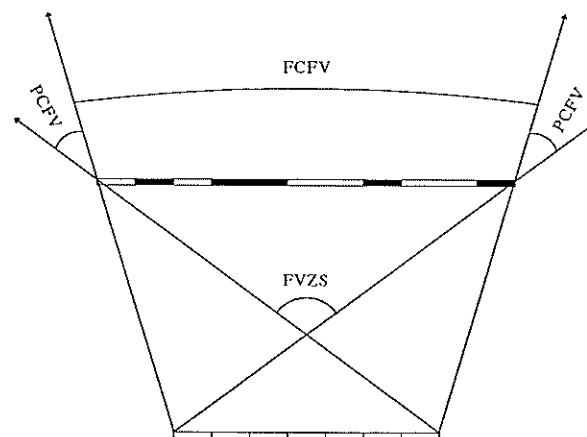


Figure 2.37: Different fields of view in a coded mask telescope

FCFV (*Fully Coded Field of View*) refers to the part of the sky where any source will project in the detector plane a whole cycle of the mask; FVZS (*Field of View at Zero Sensitivity*) is the sky zone where any source will project light in the detector plane (either a complete cycle or a part), i.e. the total field of view. PCFV (*Partly Coded Field of View*) is the complementary field of view of the other two (fig. 2.37).

2.12 Other reconstruction methods

Until now we have treated in detail the reconstruction methods based in the correlation; this means that they are based in equation 2.7. In some sense, what these methods do is to apply the inverse function (the array G) to the data space to obtain the source space, in the cases where this analytical inverse function exists (when we use a URA or MURA in a cyclic system) or a reasonable approximation of it when it does not (for example, if the mask is random). As we have said, even if equation 2.7 is an useful parametrization of the detection process, it is somewhat inexact because it does not take into account some factors, as the collimator effect or the efficiency of the detectors. We have also said that the detection process is better represented by equation 2.9 which we show here again:

$$D_{kl} = \sum_{\alpha\beta} O_{\alpha\beta} \Phi_{kl}^{\alpha\beta} + B_{kl} \quad (2.40)$$

where Φ can include all the effects that can alter the signal (mask, collimators, efficiencies, etc...).

We are now going to deal with reconstruction methods which take into account those effects (and therefore one can expect a more realistic reconstruction), not based on the correlation but on maximization techniques; these methods look for the estimators \tilde{O} , compatible with the data (by using equation 2.40) that maximize a certain magnitude. Unfortunately, we will find that these methods are slower than the correlation methods, and that they can be unapplicable for too complex telescopes.

2.12.1 Inversion of functions

Before describing these methods, some concepts related to the problem of inversion of functions should be clarified, since the reconstruction methods are directly related to them: we have a function that links the source space \mathbf{O} (we can include the noise \mathbf{B} as a part of the space source, although we will not do it now for clarity of exposition) with the data space \mathbf{D} , and we want to obtain the inverse function that gives us the source space from the known data space; but this inverse function might *not exist*. The problem is, besides, worsened by the incompleteness and inaccuracy of our data [26].

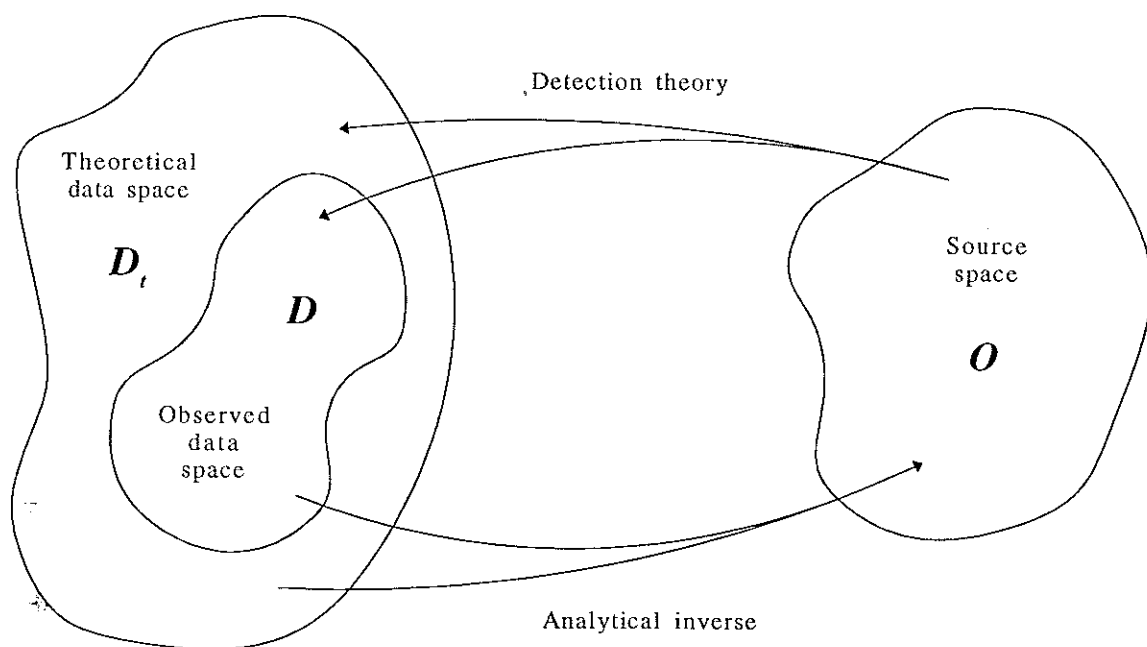


Figure 2.38: Relations between the source space and the theoretical and observed data spaces

In principle it is desirable that the source space we want to reconstruct has a pixel size as small as possible. In practice this pixel size will have a limit, due to the fact that our experimental data are finite. We will call our data the observed data space \mathbf{D} and we will call \mathbf{O} the source space. The data will not be as thorough as we would like, due to the intrinsic limitations of our detector

(for example, finite pixel size in the detector plane). Thus, we can think about a theoretical data space D_t made up of all the infinite number of observations we can conceive, without the limitations of a real detector (figure 2.38). We can only know a small fraction of D_t , which is D .

One must realize that *even when the analytical inverse function exists* and is univocally defined, it will carry us from D_t to O , not from the subset D to O . The passage from D to O is not univocally defined; if we apply the analytical inverse to D assuming values for the lost data, what we get is an estimation of the sources, \tilde{O} , which might not be the best estimation; because we can have a great number of possible estimations \tilde{O} **compatible** with our data D . Then we have to impose some criteria to \tilde{O} in order to select the preferred among all the compatible estimations.

2.12.2 Maximum entropy

This is one of the most successful image reconstruction methods used in astronomy [27] and it can be applied to any detection process parametrized by a equation with the form:

$$D_k = R_k(f) + B_k \quad (2.41)$$

[28] where D_k are the detected data, B_k is the noise, $\{f_i\}$ is the source of the signal (our unknowns) and $R_k(f)$ is the response function of the detection system. As it can be seen, the analogy with equation 2.40 is complete: we just have to identify f with O and $F(f)$ with $\Sigma O \Phi$. The only limitation we have is that the magnitudes f must be additive magnitudes [26].

To explain the maximum entropy method, we will use the *monkey argument* [29]: let us suppose a sky map divided into discrete cells, and a team of monkeys throwing balls (photons) at random inside those cells, generating in this way lots of trial sky maps; given that our monkeys are more patient than the "Maxwell devil", they will generate all the possible maps, repeating many maps. Afterwards we apply to all those maps the response function of the detector, $R_k(f)$ and we compare the result with our experimental data; almost all the trial maps f_i will be inconsistent with the data D_k , but there will be

some trial maps consistent with the data and the error; we will keep these and reject the others. Since we will have many repeated maps, we will sort them into piles (each different map in a different pile), and we will select the maps of the largest pile. That is, the map consistent with the data produced more often by the monkeys.

This procedure makes the map consistent with the data more uniform and soft. This means that it is the feasible maximum entropy map. This image represents the minimum quantity of structure imposed by the data. Or what is the same, any structure we see in the map must come exclusively from the real source.

As it is not possible to count on such a monkey team, we will formulate a definition of entropy and will maximize it, under the restriction that it must be compatible with the data. There are different entropy definitions (in [30] some of them can be seen), and the different authors have not agreed on which is the best. We will follow [29] and will use as entropy:

$$S = -\sum_{\alpha\beta} O_{\alpha\beta} \cdot \log O_{\alpha\beta} \quad (2.42)$$

If we calculate the $O_{\alpha\beta}$ that maximize 2.42, we will get an absolutely flat image, without any structure. Therefore we have to maximize it with the restriction that the $O_{\alpha\beta}$ estimations must be consistent with our data. We achieve this by defining a function Q as:

$$Q = -\sum_{\alpha\beta} O_{\alpha\beta} \cdot \log O_{\alpha\beta} - \lambda \sum_{ij} \frac{(\tilde{D}_{ij} - D_{ij})^2}{\sigma_{ij}^2} \quad (2.43)$$

where the second term, except for the value λ (that works as a Lagrange multiplier) is a χ^2 distribution of the data. When maximizing Q with respect to $O_{\alpha\beta}$, we have the estimation of O we were looking for:

$$\tilde{O}_{\alpha\beta} = e^{-1-2\lambda \sum_{ij} \Phi_{ij}^{\alpha\beta} \frac{(\tilde{D}_{ij} - D_{ij})}{\sigma_{ij}^2}} \quad (2.44)$$

One of the most obvious advantages of this estimation is that it compares the experimental data D_{ij} with its estimation, given by:

$$\tilde{D}_{ij} = \sum_{\alpha\beta} \tilde{O}_{\alpha\beta} \Phi_{ij}^{\alpha\beta} \quad (2.45)$$

[31] under the restriction of our experimental error σ_{ij} . The other great advantage is the non-negativity of the reconstructed image, assured by the exponential; therefore we do not need additional checks in order to assure that there are not pixels with negative intensities.

But due to eq. 2.45 our maximum entropy solution given by eq. 2.44 is a **transcendental** equation, without analytical solution, because \tilde{O} is on both sides of the equal sign and we can not solve it. Therefore we have to use numerical techniques to solve it. We could use equation 2.44 iteratively in order to find the solution, beginning with an initial uniform map \tilde{O}^0 , evaluating the right side of eq. 2.44 and obtaining a \tilde{O}^1 value that we will put again on the right side, etc...

Unfortunately the straight use of 2.44 does not give a convergent result. In order to solve this problem, in [31] it is suggested to use an average of two successive iterations on the form:

$$\tilde{O}_{\alpha\beta}^{n+1} = (1-\gamma)\tilde{O}_{\alpha\beta}^n + \gamma e^{-1-2\lambda \sum_{ij} \Phi_{ij}^{\alpha\beta} \frac{(\tilde{D}_{ij}^n - D_{ij})}{\sigma_{ij}^2}} \quad (2.46)$$

where γ controls the "memory" of the algorithm. The authors suggest that $\gamma=1/3$ should be used because of its good results. Even so, the use of 2.46 does not assure that if $\tilde{O}_{\alpha\beta}$ converges, it will converge to the correct solution. [29] suggests as a suitable procedure to average successive iterations in order to obtain convergence.

Anyhow, independently of which iterative method we use to solve equation 2.44, we have the extra problem of the free parameter λ , which is so

free that can change from iteration to iteration (and it changes!) (there are expressions of the maximum entropy method -for example in [31]- with even more free parameters!). To maintain the $O_{\alpha\beta}$ of each iteration in suitable values, following different authors, it is chosen a λ^n (the λ value in iteration n) in such a way that the generated O^{n+1} give us a χ^2 value of the order of the number of data.

2.12.3 The EM algorithm

The EM algorithm is an iterative algorithm of maximization that we found by sheer chance in a medical article [32], applied to emission tomography. Its formalism is analogous to ours, thus it could be totally exportable to the problem of imaging with coded masks and used as a new tool for our task of image reconstruction.

The EM algorithm (whose name arises from "Expected value" and "Maximization") is an algorithm to compute maximum likelihood estimators iteratively [33] from incomplete data. The idea is the following: let us suppose that the data observed in an experiment is a random vector y , with a conditioned probability function $g(y | \phi)$ where ϕ is a set of unknown parameters to be estimated; that is, g stands for the probability of obtaining the data y given the parameters ϕ . Our aim is to find the set of parameters ϕ^{\max} that maximizes $g(y | \phi)$ and that will be the best estimator of the real value of the parameters ϕ . Generally, it will be difficult to maximize $g(y | \phi)$ with respect to ϕ , so instead of working in the observed (and incomplete) data space, which following [33] we call \mathbf{Y} (it is equivalent to \mathbf{D} in section 2.12.1), we will work in the biggest space of theoretical complete data, called \mathbf{X} (we called it \mathbf{D}_t in section 2.12.1) where the optimization will be easier (following the analogy with section 2.12.1, our parameters to be estimated ϕ correspond to the O of the source space). The data of this theoretical space, x , can not be directly observed but only through the data y .

We assume that there is a (non-univocal) mapping $x \rightarrow s(x)$ from \mathbf{X} to \mathbf{Y} , and that the x values can be known only if they are included in $\mathbf{X}(y)$, i.e., the subset of \mathbf{X} determined by the equation $y=s(x)$. We postulate for the complete

data x a conditioned probability function $f(x|\phi)$. Under these assumptions, it is possible to obtain again $g(y|\phi)$ from $f(x|\phi)$ by means of the following relation:

$$g(y|\phi) = \int_{x(y)} f(x|\phi) dx \quad (2.47)$$

where the integral is converted in a sum if we are treating it with discrete variables (and hence the probability functions in just probabilities). Notice that in general there will be several specifications $f(x|\phi)$ that will be able to generate $g(y|\phi)$. In some cases there will be a natural choice of f that will be obvious and in other cases there will be different ways to define f .

Each iteration $n+1$ of the EM algorithm consists of two steps; to find out an expected value (**E** step) and maximize it (**M** step):

- **E** step: one forms the conditional expected value

$$E(\log f(x|\phi) | y, \phi^n) \quad (2.48)$$

where ϕ^n stands for the vector of parameters estimated in the iteration n (it is a known value, therefore).

- **M** step: to obtain the new parameters vector ϕ^{n+1} , one maximizes eq. 2.48 with respect to ϕ , keeping constant ϕ^n (which we have obtained in the previous iteration and is our current estimation).

The intuitive idea is that we would like to know the parameters ϕ that maximizes $\log f(x|\phi)$. Since we do not know $\log f(x|\phi)$, we maximize instead *its expected value* in the present iteration, given the data y and the current estimation of the parameters, ϕ^n .

Let us consider now the function:

$$H(\phi | \phi^n) = E(\log f(x|\phi) | y, \phi^n) - \log g(y|\phi) \quad (2.49)$$

This function [33] has the following oddity:

$$H(\phi' | \phi) \leq H(\phi | \phi) \quad (2.50)$$

From eq. 2.49 we have:

$$\begin{aligned} \log g(y | \phi^{n+1}) - \log g(y | \phi^n) = \\ [E(\log f(x | \phi^{n+1}) | y, \phi^n) - E(\log f(x | \phi^n) | y, \phi^n)] \\ + [H(\phi^n | \phi^n) - H(\phi^{n+1} | \phi^n)] \end{aligned} \quad (2.51)$$

Given that ϕ^{n+1} maximizes eq. 2.48, keeping ϕ^n constant, the first brackets on the right side of the equal sign in eq. 2.51 will be ≥ 0 . The same thing happens with the second brackets, thanks to the property 2.50. Therefore we have that:

$$\log g(y | \phi^{n+1}) \geq \log g(y | \phi^n) \quad \Leftrightarrow \quad g(y | \phi^{n+1}) \geq g(y | \phi^n) \quad (2.52)$$

being strictly bigger in many cases. That is, the EM algorithm is designed to increase the likelihood in each iteration.

Does the sequence of ϕ^n converge to the ϕ^{\max} which we are looking for and which maximizes $g(y | \phi)$? Unfortunately, the demonstration of convergence developed by Dempster *et al.* [33] is not correct because in one of the steps he uses incorrectly the triangular inequality. In [34] and [35] the authors try to remedy this situation although without covering all our needs.

Fortunately, Lange y Carson [32] demonstrate that in the concrete case studied by them (emission tomography -which is completely analogous to ours-) the required convergency to the correct solution **does** exist thanks to the *strict concavity* of the function $\log g(y | \phi)$ in the studied model, based on poissonian statistics.

The emission tomography works by changing the position of a single detector (focussed towards the patient) and measuring the radiation that the patient emits (because the doctor has previously supplied a radioactive substance) from different positions (projections). Following [32], it is defined:

- i : projection subscript
 j : pixel subscript in the reconstructed image
 I_i : pixels subset that contributes to projection i
 J_j : projections subset to which pixel j contributes
 λ_j : source intensity of pixel j (parameters to estimate)
 c_{ij} : probability that a photon leaving pixel j reaches the projection i
 Y_i : number of photons detected in projection i

We have, therefore:

$$Y_i = \sum_{j \in I_i} C_{ij} \lambda_j \quad (2.53)$$

that is an equation analogous to 2.40. Applying the EM algorithm [32], we obtain the iterative solution for the estimation of the λ parameters shown in equation 2.54:

$$\tilde{\lambda}_j^{n+1} = \frac{\tilde{\lambda}_j^n}{\sum_{i \in J_j} C_{ij}} \sum_{i \in J_j} \frac{C_{ij} Y_i}{\sum_{k \in I_i} C_{ik} \tilde{\lambda}_k^n} \quad (2.54)$$

Going now from tomography to coded masks, if we identify each detector projection in tomography with a different detector unit in our detector plane (or what is the same, placing a single detector in different positions -projections- and doing a measurement in each place it is equivalent to having many detectors in different places and doing a single measurement with each detector), then the analogy is clearer, and therefore we can conclude from equation 2.40 that the solution of the EM algorithm to the imaging problem when using coded masks is:

$$\tilde{O}_{\alpha\beta}^{n+1} = \frac{\tilde{O}_{\alpha\beta}^n}{\sum_{ij} \Phi_{ij}^{\alpha\beta}} \sum_{ij} \frac{\Phi_{ij}^{\alpha\beta} D_{ij}}{\sum_{\alpha'\beta'} \tilde{O}_{\alpha'\beta'}^n \Phi_{ij}^{\alpha'\beta'}} \quad (2.55)$$

or what is the same, in a more elegant way:

$$\tilde{O}_{\alpha\beta}^{n+1} = \tilde{O}_{\alpha\beta}^n \frac{\sum_{ij} \Phi_{ij}^{\alpha\beta} \left(\frac{D_{ij}}{\tilde{D}_{ij}^n} \right)}{\sum_{ij} \Phi_{ij}^{\alpha\beta}} \quad (2.56)$$

being:

$$\tilde{D}_{ij}^n = \sum_{\alpha\beta} \tilde{O}_{\alpha\beta}^n \Phi_{ij}^{\alpha\beta} \quad (2.57)$$

identically to ec. 2.45. This is the first time the EM algorithm is introduced in the context of coded mask telescopes.

The iterative equation 2.56 has a great advantage with respect to the equations we showed for the maximum entropy method: the total absence of free parameters; the equation is robust and does not require continuous and annoying checks in each iteration to adjust any parameter (or set of parameters) that slow down the process. Furthermore, given that the description of the probability function $g(y | \phi)$ is based on the random nature of the detection process (using Poisson statistics) one can expect a better and more natural reconstruction than when using the maximum entropy method. Another advantage is the non-negativity of the reconstructed image. As with the maximum entropy method, it is not necessary to impose additional constraints to assure it. The only thing we need to assure it, is that the initial parameters must be positive, that is $\tilde{O}^0 \geq 0$. This does not preclude the possibility

$$\lim_{n \rightarrow \infty} \tilde{O}_{\alpha\beta}^n = 0$$

Moreover, it converges to the proper maximum likelihood estimator, independently of the initial value of \tilde{O}^0 , as it is demonstrated in [32]. We will

get a uniform field of value 1 for all (α, β) as initial parameters, in order to avoid introducing any previous structure in the image.

Its excellent convergency can be felt by looking at equation 2.56; in the case when our estimated parameters \tilde{O}^n are the correct values, we will have that D and its estimation will coincide, and therefore the fraction between both which appears between parenthesis in eq. 2.56 will be 1 and thus also the fraction between sums, having, then, $\tilde{O}^n = \tilde{O}^{n+1}$.

Simply act of curiosity, and linking with the correlation methods, one can realize that after the first iteration, given that $\tilde{O}^0 = 1$, and due to eq. 2.56 and 2.57, what we have is:

$$\tilde{O}_{\alpha\beta}^1 = \frac{\sum_{ij} \Phi_{\alpha\beta}^{ij} \cdot \left(\frac{D_{ij}}{\sum_{\alpha\beta} \Phi_{\alpha\beta}^{ij}} \right)}{\sum_{ij} \Phi_{\alpha\beta}^{ij}} \quad (2.59)$$

if our definition of Φ is as the definition of the mask array M_{ij} (that is, $\Phi=1$ if the ij detector "looks" through a hole when looking at (α, β) , and $\Phi=0$ if it looks through an opaque element), then we have:

$$\sum_{\alpha\beta} \Phi_{\alpha\beta}^{ij} = N_A$$

$$\sum_{ij} \Phi_{\alpha\beta}^{ij} = N_C$$

where N_A =total number of holes in the mask and N_C =number of holes in a cycle of the mask. With it, we have that eq. 2.59 becomes:

$$\tilde{O}_{\alpha\beta}^1 = \frac{1}{N_A N_C} \sum_{ij} \Phi_{\alpha\beta}^{ij} D_{ij} \equiv \tilde{O}^1 = \frac{1}{N_A N_C} (D * M)$$


That is, the first iteration of the EM algorithm is something equivalent to the reconstruction methods based on the correlation.

2.12.4 Maximization methods versus inversion of functions

We have to say that both the maximum entropy method and the EM algorithm solve elegantly the problem of inverse functions (see 2.12.1). As we have already said, the response function of the detector (in our case Φ) relates the source space O to the data space D . The "obvious" way to obtain the parameters O from the data D would be applying the inverse function; but as we have said, perhaps it is not univocally defined (for the incompleteness of our data) or still worse, perhaps the inverse function does not exist. Both the EM algorithm and the maximum entropy method **only** use the detector response function Φ and **never** its inverse, to go from the trial maps in the source space to the data space and compare the result with the experimental data.

Chapter 3: Other considerations

3.1 Introduction

 In chapter 2 we have studied different image reconstruction methods, needed when using a coded mask system for imaging. We have called it *masks theory*. However, before getting inside the result chapters, it is suitable to explain in this chapter some additional points that are related to the mask theory and the γ ray telescopes, and which may be useful for a better understanding.

3.2 Errors criterion

3.2.1 In reconstructions based on the correlation

Following [36], and according to equation 2.10, given an O array that represents the source, given an M array that stands for the mask, and a background noise B array, then the detector plane, represented by the D array, will be given by:

$$D = O * M + B$$

and the reconstruction by:

$$\tilde{O} = D * G$$

or also by:

$$\tilde{O}_{ij} = \sum_{kl} D_{kl} G_{k+il+j} \quad (3.1)$$

As it can be seen in [37], by square error propagation, the estimated statistical error in a term with the form $d \cdot g$ is given by

$$\epsilon^2(dg) = d^2 \epsilon^2(g) + g^2 \epsilon^2(d) \quad (3.2)$$

where d and g correspond respectively to the elements of D and G in eq. 3.1. All the terms in the reconstruction array (G) are constants (for instance, with balanced correlation they are 1 or -1), therefore its associate error is $\varepsilon(g)=0$. This gives us:

$$\varepsilon^2(dg) = g^2 \varepsilon^2(d) \quad (3.3)$$

Using balanced correlation, we have $g^2=1$. This means that we can write the associate error in each reconstructed image pixel as:

$$\varepsilon^2(\tilde{O}_{ij}) = \sum_{kl} \varepsilon^2(D_{kl}) \quad (3.4)$$

And taking into account that the detected counts in D have poissonian character, the error of D_{kl} is given by

$$\varepsilon(D_{kl}) = \sqrt{D_{kl}} \quad (3.5)$$

therefore we have

$$\varepsilon^2(\tilde{O}_{ij}) = \sum_{kl} \left(\sqrt{D_{kl}} \right)^2 = \sum_{kl} D_{kl} = T_D \quad (3.6)$$

where T_D is the total detected counts number in the detector plane, and therefore **independent** of the considered ij detector element.

Using it in the particular case of LEGRI, let us consider the balanced correlation: we have a 5x5 pattern in the mask and a detector plane with the same size (we group the detectors in 2x2 groups in order to have the same elements size in both arrays). Let us suppose a source with an intensity of 100 photons/area unit (during an arbitrary Δt integration time). For simplicity let us suppose absence of noise, detecting in each illuminated detector ~100 photons (except for the statistical fluctuation); therefore we detect in each 2x2 group ~400 photons (and ~0 in those not illuminated). Since the mask pattern (fig. 2.23) has 12 transparent and 13 opaque elements, there will be 12 2x2 groups illuminated having $T_D \sim 4800$ detected counts, and an error of $\sqrt{4800} \approx 70$ in each reconstructed image pixel.

Considering the ij sky position where the source is, and using eq. 3.1, we have that each 1 in the G array will multiply an illuminated detector (those with ~ 400 counts), and each -1 will multiply a non-illuminated detector (with ~ 0 counts). This means, $12 \times 400 - 13 \times 0 = 4800$ counts in the reconstructed image peak, with an error of ± 70 , exactly what would correspond to its statistical error if it were a direct measurement. The rest of the reconstructed image will have a flat background with a value of ~ 0 (see fig. 2.28), and with an error of ± 70 in each image pixels. Nevertheless, if in the field of view there were two sources with an intensity of 100 each one, the detector would measure ~ 9600 counts (except for the collimator effect); in this case, the error for each reconstructed image pixel would be 100. This means that the same source of the previous case will be reconstructed with the same intensity (4800) (given the form of equation 2.14, since the intensity value of a pixel does not depend on the other image pixels) but with a *bigger error*, just because it has another source in the field of view.

If we use FSBC or δ -decoding (with pyramidal or square response respectively) we have a systematic error besides, because they reconstruct sources where there is nothing, even in the best case (ideal detector and absence of noise). If we look at figure 2.30 (where FSBC is used for a source with intensity 100), the real source is in the centre, but we see a structure surrounding the real signal that does not correspond to any true structure.

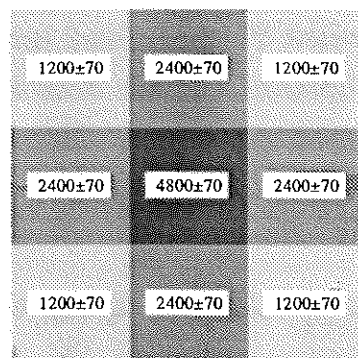


Figure 3.1: Reconstruction with FSBC (enlargement). It is showed the pixel intensity and its error.

The pixels in this structure should be ~ 0 , but they have quite a high value and a statistical error that it is too small, and thus the true value (0) is not included in the error interval. Therefore there is a systematic error when using FSBC and δ -decoding.

3.2.2 In iterative methods

It was really difficult to find an error criterion for iterative methods (as is the case of the EM algorithm and the maximum entropy method), because the bibliography related to statistics and probability issues usually does not consider iterative processes, and those books and articles that consider such processes used to be related to mathematical problems that do not consider experimental errors. Fortunately, we found a statistical book [38] where, in a pair of pages, an iterative process is considered and it is assigned an error to its result. Although in [38] it is studied a case that is different to ours, the analogy is complete and we have used their error criterion to assign an error to the result of our iterative methods.

This criterion consists in (once the algorithm has reached the desired convergency, let us say at the $n+1$ iteration) estimating the pixels error by square error propagation [37] from the iterative formula, estimated at the n iteration. If we consider as magnitudes with error the detected counts (D_{ij}) and the response detector array Φ (since we include in it magnitudes with error as detectors position, detector-mask distance, and optionally the transparency of the non-opaque telescope components, or the detectors efficiency), then we have that the (square) error assigned to the (α, β) sky pixel is given by:

$$\varepsilon^2(\tilde{O}_{\alpha\beta}^{n+1}) = \sum_{kl} \left[\left(\frac{\partial \tilde{O}_{\alpha\beta}^{n+1}}{\partial D_{kl}} \right)_n^2 \cdot \varepsilon^2(D_{kl}) + \left(\frac{\partial \tilde{O}_{\alpha\beta}^{n+1}}{\partial \Phi_{kl}^{\alpha\beta}} \right)_n^2 \cdot \varepsilon^2(\Phi_{kl}^{\alpha\beta}) + \sum_{\gamma\delta \neq \alpha\beta} \left(\frac{\partial \tilde{O}_{\alpha\beta}^{n+1}}{\partial \Phi_{kl}^{\gamma\delta}} \right)_n^2 \cdot \varepsilon^2(\Phi_{kl}^{\gamma\delta}) \right] \quad (3.7)$$

where the n subindex means that the partial derivatives must be estimated

with the values of the n -th iteration. For a more detailed study of the errors, see appendix II.

3.3 Sky mapping

The result of a single reconstruction operation is a pixels weft, an image or map, that represents the sky intensities in a particular sky zone, whose centre is the pointing telescope direction. As time passes, the pointing direction will change to study different sky zones. Each of our particular maps is an element of a mosaic, and uniting them we will carry out the sky mapping. But firstly we need to know how to pass from our (α, β) co-ordinates, which are related to the telescope pointing direction (or field of view centre), to the Right Ascension and declination (*r.a., dec.*) co-ordinates, the absolute co-ordinates used in astronomy.

Both systems are related by tridimensional rotations, defined by the Euler angles, ψ_1, ψ_2 y ψ_3 , which define three rotations that allow us to pass from the z_1 axis, parallel to the telescope pointing direction, to the z_3 axis, parallel to the Earth's rotation axis, as it can be seen in figure 3.2.

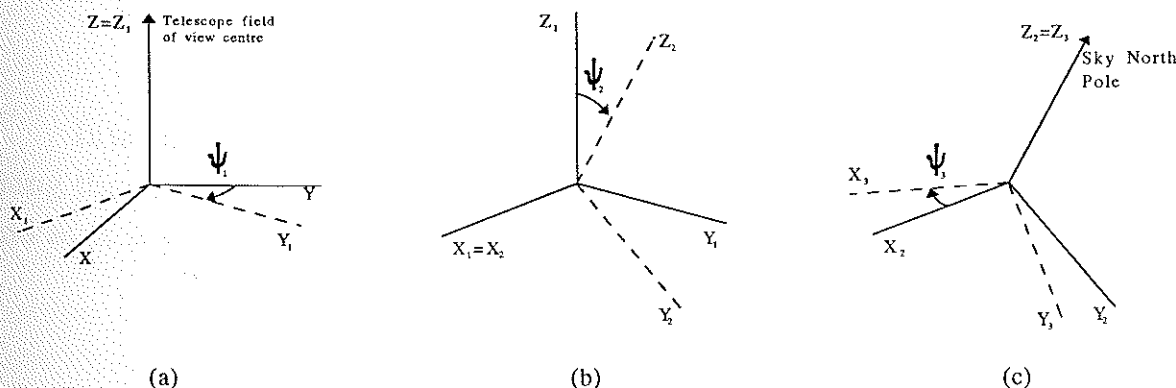


Figure 3.2: Euler angle definition

In our case, this Euler angles can be obtained from the stellar sensor data (see fig. 3.3), in the following way:

- ψ_1 is the angle between the α axis of the image and the celestial parallel that passes through the field of view centre (FVC).
- ψ_2 is the angle between the FVC and the celestial north, and it is related to the FVC declination by $\psi_2 = -(90^\circ - \text{dec.})$, since the sign of this rotation (as we have defined it) is negative.
- ψ_3 are the degrees needed to rotate the α axis to put it parallel to the right ascensions origin; it is given by $\psi_3 = 270^\circ - \text{r.a.}$ (in degrees, because the r.a. is measured in hours).

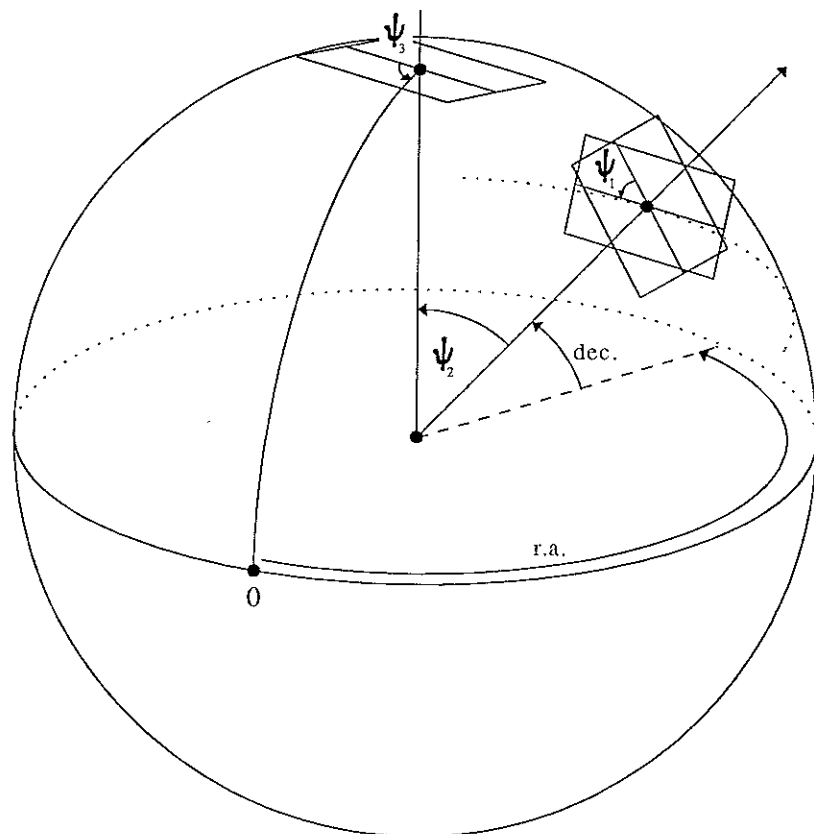


Figure 3.3: Euler angles that connect the co-ordinates system intrinsic to the telescope with the standard celestial co-ordinates system.

Therefore, given an object at the (α, β) position in the telescope co-ordinates system, we get its spheric co-ordinates (θ, ϕ) referred also to the FVC, by means of equation 2.2. It is trivial to calculate the new spheric co-ordinates (θ_1, ϕ_1) after the first rotation (a) (see fig. 3.2), and it is given by:

$$\theta_1 = \theta \tag{3.8}$$

$$\phi_1 = \phi - \psi_1$$

It will not be so trivial to calculate the new (θ_2, ϕ_2) after the second rotation (called (b) in figure 3.2), so we need to use the cartesian co-ordinates to help us:

$$\begin{aligned} x_2 &= x_1 \\ y_2 &= y_1 \cdot \cos(\psi_2) + z_1 \cdot \sin(\psi_2) \\ z_2 &= z_1 \cdot \cos(\psi_2) - y_1 \cdot \sin(\psi_2) \end{aligned}$$

and given that:

$$\begin{aligned} x_1 &= R \cdot \sin(\theta_1) \cdot \cos(\phi_1) & x_2 &= R \cdot \sin(\theta_2) \cdot \cos(\phi_2) \\ y_1 &= R \cdot \sin(\theta_1) \cdot \sin(\phi_1) & y_2 &= R \cdot \sin(\theta_2) \cdot \sin(\phi_2) \\ z_1 &= R \cdot \cos(\theta_1) & z_2 &= R \cdot \cos(\theta_2) \end{aligned}$$

we have the following relation among angles:

$$\begin{aligned} \sin(\theta_2) \cdot \cos(\phi_2) &= \sin(\theta_1) \cdot \cos(\phi_1) \\ \cos(\theta_2) &= \cos(\theta_1) \cdot \cos(\psi_2) - \sin(\theta_1) \cdot \sin(\phi_1) \cdot \sin(\psi_2) \\ \sin(\theta_2) \cdot \sin(\phi_2) &= \sin(\theta_1) \cdot \sin(\phi_1) \cdot \cos(\psi_2) + \cos(\theta_1) \cdot \sin(\psi_2) \end{aligned} \tag{3.9}$$

It is easy to calculate the new spheric co-ordinates after the (b) rotation using the relations shown at eq. 3.9. Rotation (c) is analogous to rotation (a), and so it is given by:

$$\theta_3 = \theta_2 \tag{3.10}$$

$$\phi_3 = \phi_2 - \psi_3$$

The co-ordinates (θ_3, ϕ_3) are basically the declination and right ascension (respectively) of our object; we have only to pass ϕ_3 from degrees to hours to get the **r.a.**, and the declination is given by **dec** = $90^\circ - \theta_3$. With this two changes we have finally the correct celestial co-ordinates.

3.4 Simulators

It has been necessary to create some programs to simulate the LEGRI response, as a first step to develop our image reconstruction software. Using these simulators we can create useful data from well-known synthetic "sources" that can be used as inputs for our reconstruction programmes, and so, we are able to compare among the different reconstruction methods.

In this chapter, the considered simulators have been two: a model of the whole detector based in the Monte Carlo method [39], with a comprehensive description of the component materials, and all the physical processes involved in the detection, using the GEANT-3 [40] simulation package; and a geometrical simulator that we will describe afterwards. The first is more accurate and similar to reality, but very much slower, while the second, although perhaps not so exact, is very much faster. When developing our software and studying the characteristics of the different reconstruction methods, we have mainly used the last one, using the first to check if the approximation we do using the geometrical simulator is good enough. Both methods try to obtain the detected image in the telescope detector plane, given a field of sources. The Monte Carlo method does it by launching photons (in a number proportional to the source intensity) coming from the (α, β) direction where the source is; those photons interact with the matter by means of the photoelectrical and Compton effect (in our energy range there are not pair production), being finally detected by the detector plane units. As one can see, this is a slow process, and still more if we consider many sources, or an extensive source. The geometrical simulator calculates analitically the Φ array of eq. 29, which gives us the detector response. Apart from being faster, this simulator has the advantage of obtaining *explicitly* the Φ flux factors, needed not only for simulation of the detector but also for reconstruction when using maximization methods (see eq. 2.44 and 2.56). With the Monte Carlo we can calculate them, but no explicitly; we have to do a different simulation for each (α, β) direction, and after that, divide the counts detected in each detector by the launched photons by area unit.

Let us shortly describe the algorithm used in the geometrical simulator to calculate the Φ flux factors. What we want to obtain is, given a source with intensity I at the arbitrary position (α, β) , which fraction of intensity the detector ij will see, taking into account the tungstens position in the mask and the collimator. To calculate it, we project in the mask plane the square defined by the detector ij and the one defined by its collimator towards the (α, β) position, as it can be seen in figure 3.4, and we find the rectangle given by their intersection.

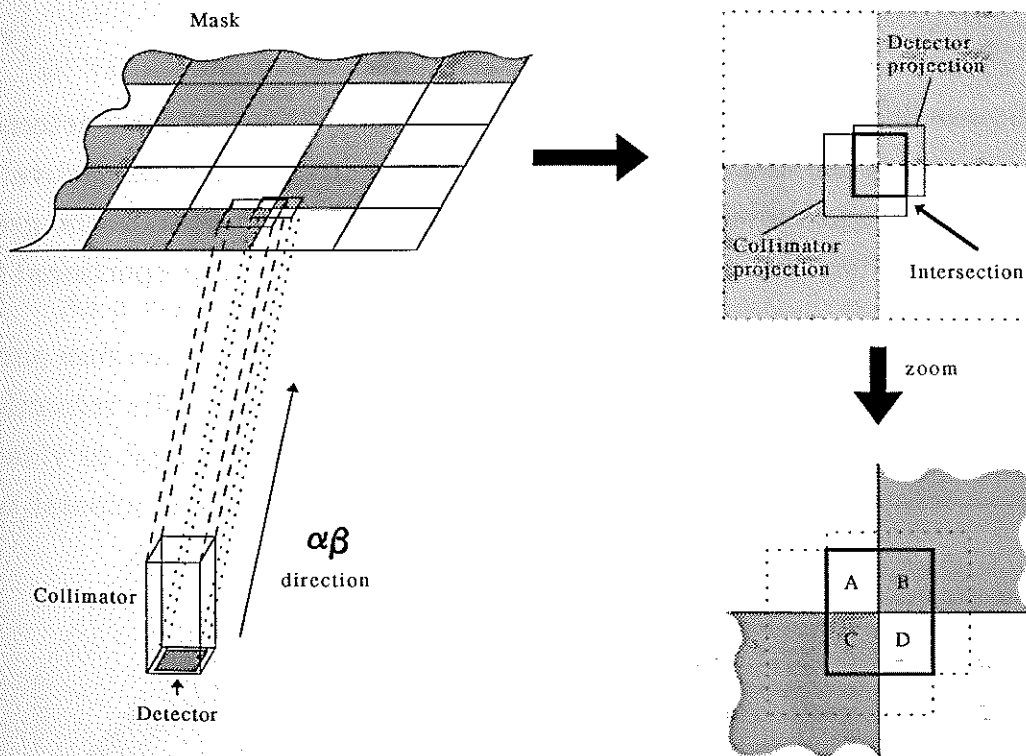


Figure 3.4: Calculation of the flux coming from the (α, β) direction that is seen by a detector plane unit, taking into account the effect of the collimator and the mask.

Afterwards, we calculate the intersection of *this* rectangle with the mask pattern: we have four possible cases: the rectangle is inside a mask element (either transparent or opaque), between two mask elements, or among four elements (this last case is the one shown in figure 3.4), defining, respectively, one, two or four subareas. Multiplying each subarea by 1 if it is a hole or 0 if it is a tungsten, and obtaining the total sum, we obtain the detector unit area that is illuminated by the source in (α, β) . Intuition tells us that, to obtain our

flux, we only need to divide this area by the total area of our detector unit. This is almost true, but we have also to divide by the geometrical factor as the detector is rotated with respect to the coming direction of the radiation, as we have seen in equation 2.37 (in section 2.11.1). Then, the flux seen by the detector ij , coming from the direction (α, β) is given by:

$$\Phi_{ij}^{\alpha\beta} = \frac{\sum_{n=1}^{n^{\circ} \text{ subáreas}} M_n \cdot A_n^{\text{subdiv}}}{A_{ij}^{\text{total}} \cdot \sqrt{1 + \text{tg}^2 \alpha + \text{tg}^2 \beta}} \quad (3.11)$$

In figures 3.5 and 3.6 we have shown graphically this flux, for a detector unit in the centre of the detector plane and for other in a corner, respectively. Each of the graphics is shown in two different representations: in (a) the grey tone is proportional to the flux value, and in (b) the height is proportional to the flux value.

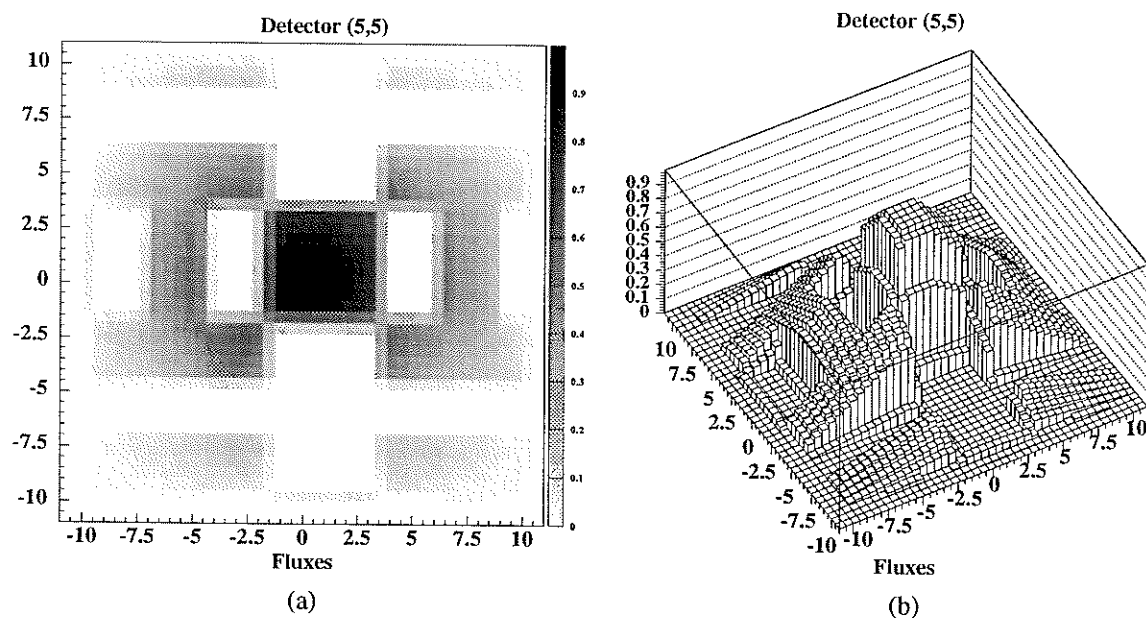


Figure 3.5: Flux factors of the detector (5,5)

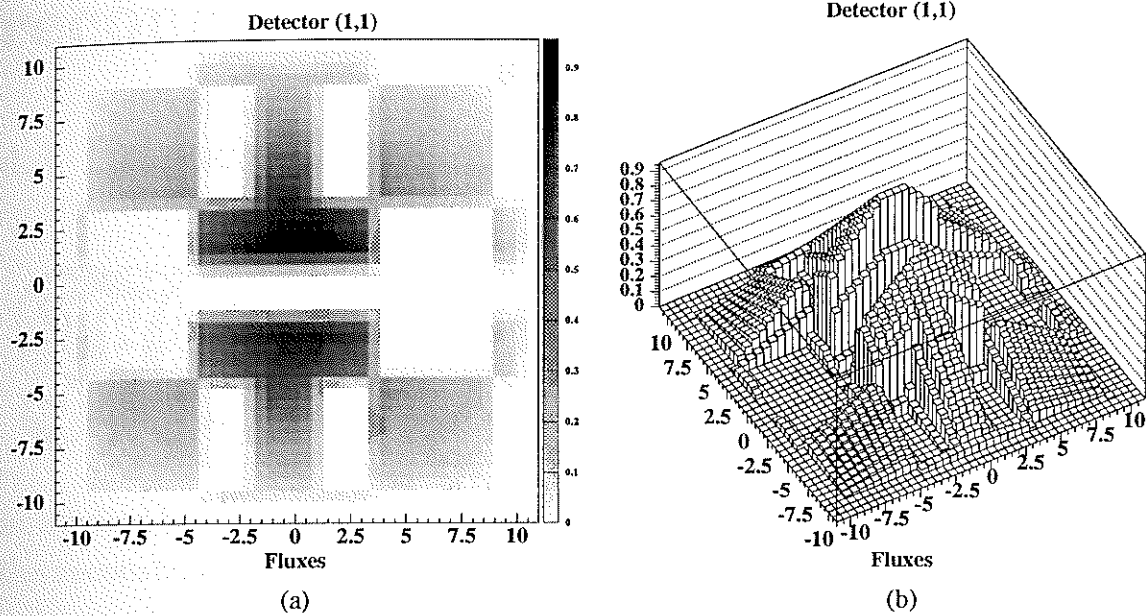


Figure 3.6: Flux factors of the detector (1,1)

As a result of this figures, we can say that the response of a detector plane unit can approximately be described as a pyramidal function (this is the collimator effect, as we have explained in section 2.11.1) as it can be seen more clearly in fig. 3.5 (b) and 3.6 (b), multiplied by the mask pattern that is over the detector unit, as it can be seen more clearly in fig. 3.5 (a) and 3.6 (a).

Chapter 4: Results. Study of the reconstruction methods

4.1 Introduction

Along this chapter we are going to expose the results obtained after the detailed study of the different image reconstruction methods, formerly described, and applied to LEGRI. Here we will study their main characteristics, different considerations and a comparative analysis of those methods will be done, and it will be studied how some phenomena, external to the reconstruction process, affect the reconstruction.

4.2 Convergency criteria

When we generate an image by means of an iterative process, as it is the case of maximum entropy or the EM algorithm, we have to stop the process in a given moment and accept the product of this last iteration as the image generated by the reconstruction process. Therefore, before continuing and beginning to reconstruct images by different methods, we have to study if the iterative methods that we study converge, and if so, know when we must stop them. That is why we are going to carry out a previous study on the convergency of these two methods, and to impose criteria to stop the iterative process.

4.2.1 EM algorithm convergency

As we have said in section 2.12.3, the EM algorithm has an excellent convergency to the desired maximum likelihood estimator. Furthermore, the convergency is monotonous and without oscillations, as we will see soon. We can use this property to choose a stopping criterion for the algorithm. Nevertheless, this is a criterion about the convergency of the process, not about the convergency to the correct result (although in this case it converges to the

correct result). We can impose other criteria to stop the algorithm, for example based on statistics. We are going to use two criteria for the EM algorithm these two criteria are the following.

If we base our criterion on statistics, we can require the algorithm to stop whenever the detector plane data estimation (obtained from the present sky pixels estimation) is indistinguishable from the experimental data, because the value of the estimators is within the error of the experimental data. This means that we can decide to stop the algorithm in the n -th iteration when:

$$\begin{aligned} \tilde{D}_{ij}^n (= \sum_{\alpha\beta} \Phi_{ij}^{\alpha\beta} \tilde{O}_{\alpha\beta}^n) \in (D_{ij} - \sigma_{ij}, D_{ij} + \sigma_{ij}) \\ \text{where } \sigma_{ij} = \sqrt{D_{ij}} \end{aligned} \quad (4.1)$$

This assures us that our reconstruction is a good reconstruction. Nevertheless, this may not happen; the algorithm solution (with infinite iterations) may not fulfil the requirement shown in eq. 4.1 in any case. For these cases, and using the monotonous convergency property of the algorithm, we will impose that the algorithm will stop when the difference between the images of two consecutive iterations is *very* small. One wonders how we can define that *very* and that *difference*.

We are going to define a magnitude that we are going to call δ^n , by:

$$\delta^n = \frac{\left(\sum_{\alpha\beta} \Delta \tilde{O}_{\alpha\beta}^n \right)}{\left(\sum_{\alpha\beta} \tilde{O}_{\alpha\beta}^n \right)} \quad (4.2)$$

$$\text{where } \Delta \tilde{O}_{\alpha\beta}^n = |\tilde{O}_{\alpha\beta}^n - \tilde{O}_{\alpha\beta}^{n-1}|$$

The more similar these two successive images are, the smaller is δ^n . We can impose that the algorithm stops when δ^n is of the order of 10^{-4} (this is more or less its value when the requirement of eq. 4.1 is fulfilled). In practice, we will use as stopping condition the one the algorithm reaches before.

Applied to a particular case, the EM algorithm has been used with the data D obtained when the telescope is illuminated by a source with intensity 100 photons/cm², centred in the field of view, plus a random noise with average value of 30 counts/cm² (it has been used the geometrical simulator described in 3.4).

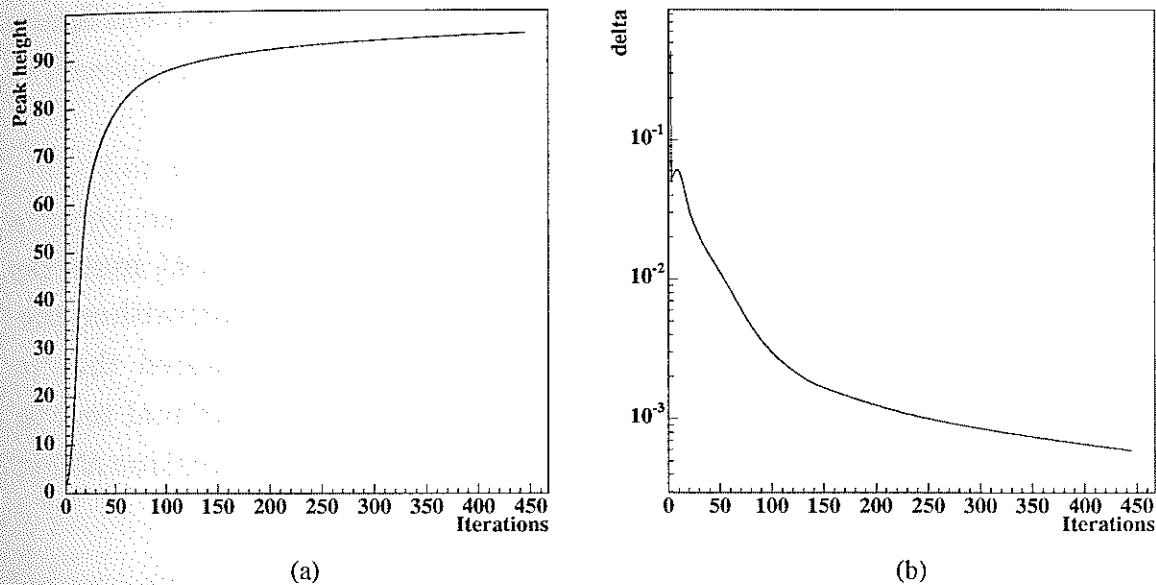


Figure 4.1: EM algorithm convergency

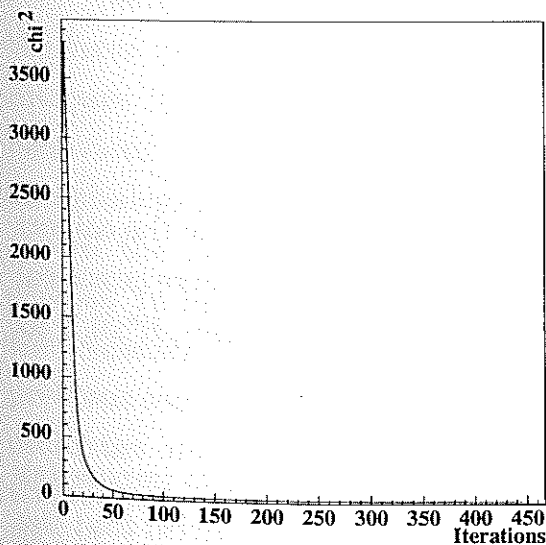


Figure 4.2: χ^2 value

In figure 4.1 (a) the peak height of the central pixel in the reconstructed image (the estimated intensity of the source) is shown, and in figure 4.1 (b) the value of δ^n . The stopping criterion used was the one defined by eq. 3.1. We also show the χ^2 value corresponding to the data estimation in each iteration.

The algorithm stopped at iteration 445. The estimated value of the source intensity is 95.1 photons/cm² and the value of δ^n is $6 \cdot 10^{-4}$. Since

eq. 4.1 was fulfilled and given that χ^2 is defined by:

$$\chi^2 = \sum_{ij} \frac{(D_{ij} - \tilde{D}_{ij})^2}{\sigma_{ij}^2} \quad (4.3)$$

the final χ^2 value can not be bigger than the number of detector units (100 in our case), because each factor in the sum is smaller (or equal) than 1; the final value is 18.4. The execution time was 1 minute and 25 seconds, in a Sun Sparc20 with 120 Megabytes RAM (operating system: Solaris 2.4).

4.2.2 Maximum entropy method convergency

As the maximum entropy solution we have seen in eq. 2.44 must be solved by iterative methods, and given that, contrary to the EM algorithm, the convergency is not assured (and if it converges, it is not assured that it converges to the correct solution), we need to introduce an additional test to estimate the goodness of the solution. Following [31], we define a residue R^n by

$$R^n = \frac{1}{N} \sqrt{\sum_{\alpha\beta} \left[\frac{\left(\tilde{O}_{\alpha\beta}^n - e^{\left(-1 - 2\lambda^n \sum_{ij} \phi_{ij}^{\alpha\beta} \frac{\tilde{D}_{ij}^n - D_{ij}}{\sigma_{ij}^2} \right)} \right)^2}{\tilde{O}_{ij}^{n2}} \right]} \quad (4.4)$$

where both sides of equation 2.44 are compared. The nearer \tilde{O}^n is to the correct solution, the smaller R^n is. In fact, in some cases, it can result more practical to use equation 4.4 as the stopping criterion, imposing, for instance, $R^n \leq 0.1$, as the authors of [31] suggested (or a stricter boundary).

In any iteration method we use to solve eq. 2.44, we have to impose (as it has been said in 2.12.2, and as it is suggested by various authors) that the χ^2 of the data estimation in the next iteration ($n+1$) has to be of the order of the system freedom degrees (100 in our case), choosing the correct λ^n to obtain that requirement. In general this will not be possible, mainly in the first iterations,

and we can find cases where any λ^n we choose will give us χ^2 values bigger even two magnitude orders above the number of freedom degrees. Therefore (and given that the number of freedom degrees in our case is not very high -mainly if we compare LEGRI with other γ -ray telescopes-), in each iteration we will choose that λ^n minimizes χ^2 (seeking in a certain range of λ^n values) in the assumption that a χ^2 value of the order of, for example, 20 (as in the case of the EM algorithm in the previous example) can be considered as *of the order* of freedom degrees.

Let us now study the different iteration methods of the maximum entropy method, in order to seek the solution of eq. 2.44. The first method one can think is just to iterate equation 2.44; this means:

$$\tilde{O}_{\alpha\beta}^{n+1} = e^{-1-2\lambda^n \sum_{ij} \Phi_{ij}^{\alpha\beta} \frac{\tilde{D}_{ij}^n - D_{ij}}{\sigma_{ij}^2}} \quad (4.5)$$

$$y \tilde{D}_{ij}^n = \sum_{\alpha'\beta'} \Phi_{ij}^{\alpha'\beta'} \tilde{O}_{\alpha'\beta'}$$

(one must be careful when $\sigma_{ij}=0$, and has to substitute it, for example, for the mean value of σ_{ij} , in order to avoid divisions by 0).

Sadly, this method does not converge at all, as one can see in figure 4.3. We have iterated the process 445 times (ignoring the δ^n value) in order to compare it to the result obtained with the EM algorithm. Unluckily, the behaviour was so chaotical that the resulting graphic looked as an encephalogram and it was imposible to see anything. That is why we have only shown the last 50 iterations, that are *totally* representative of the whole process. In figure 4.3 (a) it is shown the central pixel intensity estimation in the reconstructed image, for the same celestial source as we used in the previous section for the EM algorithm. We can see that the estimated intensity oscillates alternately between 0 and 100 photons/cm². In figure 4.3 (b) it is shown the χ^2 value for the data estimation in each iteration; as it can be seen, its value is under 1000 only in a few occasions, and this is more true for the 10 first iterations, where values bigger than 10000 can easily be reached. The cause of this unstability is the exponential, that magnifies small fluctuations in the exponent.

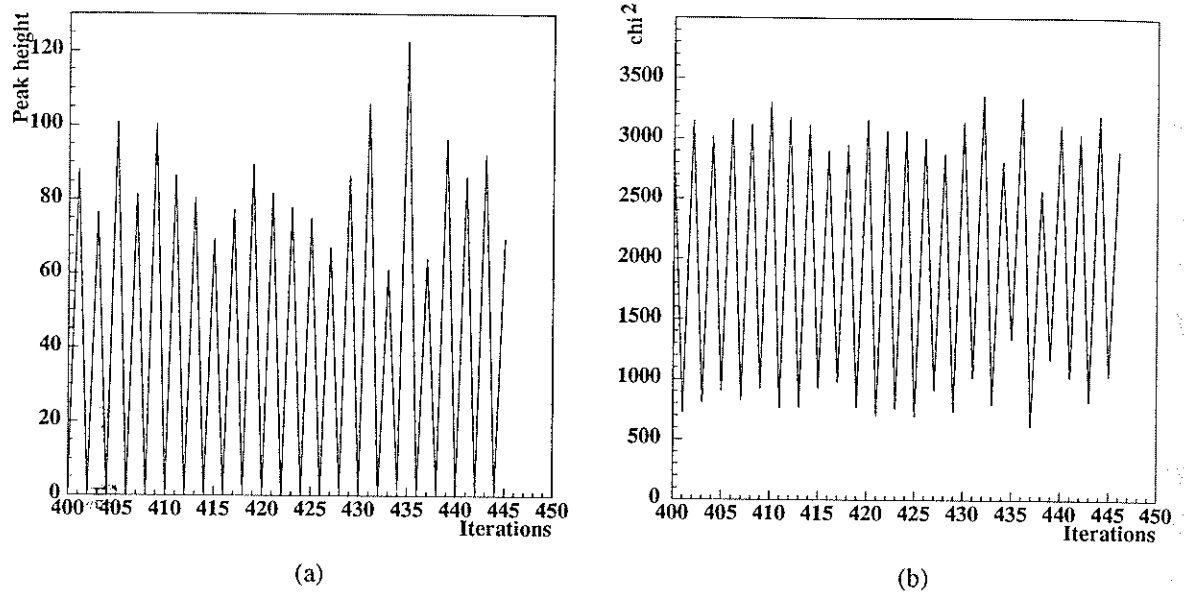


Figure 4.3: Maximum entropy convergency, using eq. 4.5

The execution time for these 445 iterations, due to the need of minimizing χ^2 with respect to λ in each iteration, was 4 hours and 15 minutes.

Some improvement can be obtained if we use the process described by [31], that we have showed in eq. 2.46 and show here again:

$$\tilde{O}_{\alpha\beta}^{n+1} = (1-\gamma)\tilde{O}_{\alpha\beta}^n + \gamma e^{-1-2\lambda^n \sum_{ij} \Phi_{ij}^{\alpha\beta} \frac{(\tilde{D}_{ij}^n - D_{ij})}{\sigma_{ij}^2}} \quad (4.6)$$

where γ is the algorithm "memory" of the result in the previous iteration. It smooths the oscillation of successive iterations. Saying it roughly, summing the result of the previous iteration makes the algorithm to remember the successful previous results, and the exponential acts to "improve" them in the following iteration. The smoothing is bigger as smaller is γ , and so the fluctuation will decrease, but, on the other hand, it can stop the algorithm (even if the iterations carry on) if the value is too small. In [31] it is said that the more suitable value is $\gamma=1/3$. Nevertheless, we can see in figure 4.4 that the behaviour of this algorithm is still very chaotical, and the improvement obtained is quite small. It is again shown, for the last 50 iterations, the intensity of the central pixel in the reconstructed image and the corresponding χ^2 of each iteration.

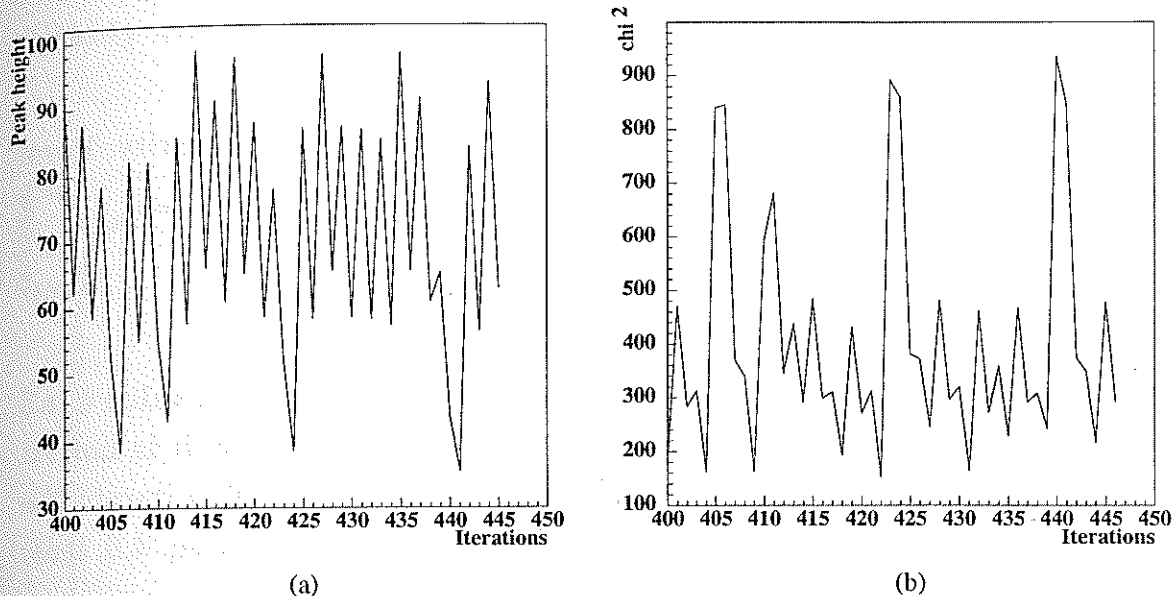


Figure 4.4: Maximum entropy method convergency, using eq. 4.6

Now the algorithm fluctuation is not as big as in the previous case, although is not small either. The intensity value is now mainly included between 60 and 100 photons/cm², with some values arriving at 40 photons/cm². χ^2 is rather small, and its mean value is about 300. On the other hand, although it is not show in any graphic, the residue value (R^n , which behaviour in the previous case was extremely erratic) is now included between 0.5 and 0.05. The execution time is somewhat bigger than in the previous case, but similar: 4 hours and 40 minutes. It is in this method of iteration and in the previous one where using R^n as stopping criterion can be a good idea, in the hope that, in one iteration, R^n fluctuates to a value smaller than a given one, and we have a good estimation of the image. Nevertheless, it would be more comfortable to use some algorithm with a good convergence to the solution of eq. 2.44.

If we base ourselves on the suggestion given in [29] of averaging out successive iterations to get convergency (even though in [29] the exact way to do it is not explained), we have developed a new "smoothing" method in order to improve the convergency. Let us suppose that, taking as input a certain \tilde{O}^{n-1}_{bis} , we use equation 4.5 to obtain \tilde{O}^n . This is:

$$\tilde{O}^n = e^{-1-2\lambda^{n-1}\sum\Phi\frac{\tilde{D}^{n-1}(\tilde{O}_{bis}^{n-1}) - D}{\sigma^2}} \quad (4.7)$$

where we have omitted the pixel and detector indexes for more clarity. From this \tilde{O}^n we generate an \tilde{O}_{bis}^n by:

$$\tilde{O}_{bis}^n = \frac{\tilde{O}^n + \tilde{O}^{n-1} + \dots + \tilde{O}^1}{n} \quad (4.8)$$

This means that our new input to the algorithm will be the mean value of all the previous outputs of eq. 4.5 (we do not consider \tilde{O}^0 , because it is not an algorithm output, but the initial input, and all its values are 1). If we iterate the algorithm, we obtain from this value a new result, \tilde{O}^{n+1} , given by eq. 4.8; it is:

$$\begin{aligned} \tilde{O}_{bis}^{n+1} &= \frac{\tilde{O}^{n+1} + \tilde{O}^n + \dots + \tilde{O}^1}{n+1} = \\ &= \frac{\tilde{O}^{n+1}}{n+1} + \frac{n}{n+1} \cdot \frac{\tilde{O}^n + \tilde{O}^{n-1} + \dots + \tilde{O}^1}{n} = \\ &= \frac{1}{n+1} \tilde{O}^{n+1} + \frac{n}{n+1} \tilde{O}_{bis}^n \end{aligned} \quad (4.9)$$

Let us now substitute \tilde{O} by its value, as given by eq. 4.7, and rename \tilde{O}_{bis} as \tilde{O} , and what we get (writing it in an analogous way to eq. 4.6) is the following iterative equation:

$$\tilde{O}_{\alpha\beta}^{n+1} = \left(\frac{n}{n+1}\right)\tilde{O}_{\alpha\beta}^n + \left(\frac{1}{n+1}\right)e^{-1-2\lambda^n\sum_{ij}\Phi_{ij}^{\alpha\beta}\frac{(\tilde{D}_{ij}^n - D_{ij})}{\sigma_{ij}^2}} \quad (4.10)$$

We can roughly say that here, the "smoothing" factor (γ) of equation 4.6 is not constant, contrary to what Willingale [31] suggested, but decreases with each iteration, being initially 1 (to obtain \tilde{O}^1 , $n=0$ -see eq. 4.10-). This means that, initially, it is more important the current result of the algorithm than the previous ones, but as the iteration number increases, this situation is inverted (we could say that the "memory" of the algorithm grows with the experience).

As we can see in figure 4.5, the convergency capability has increased notably with respect to the previous case.

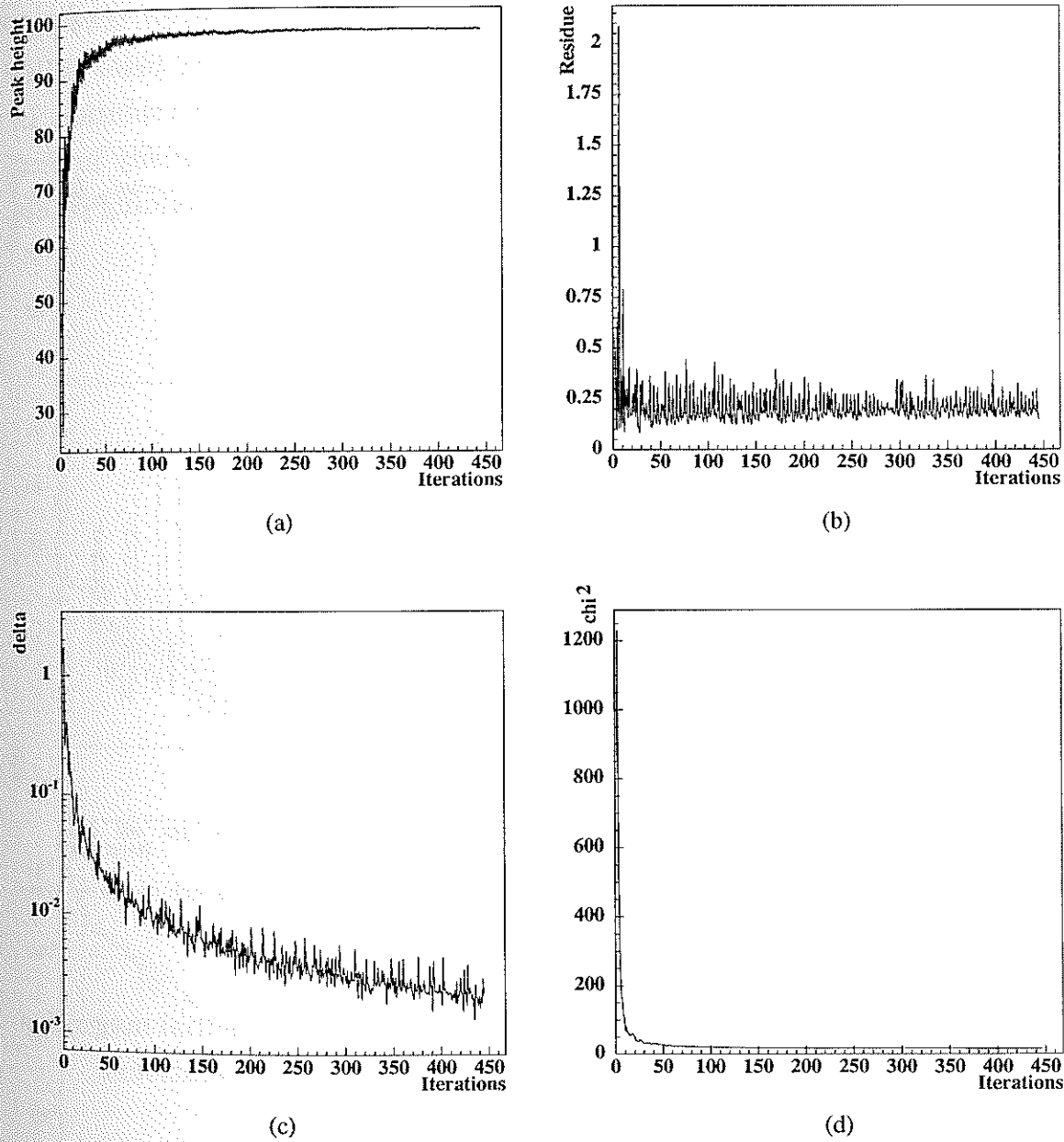


Figure 4.5: Maximum entropy method convergency, using eq. 4.10

Now we really have convergency! Although some small fluctuations still exist. The reconstructed source intensity (fig. 4.5 (a)) is 98.3 photons/cm². The value of R^n (fig. 4.5 (b)) is centred in 0.2. The measurement of the convergence, given by δ^n , as defined in eq. 4.2 (fig. 4.5 (c)), has a value of $2 \cdot 10^{-3}$. The χ^2

value (fig. 4.5 (d)) is now 15.8. The execution time is again 4 hours and 40 minutes. As it can be seen, this is a very good result, comparable to the result obtained with the EM algorithm. Anyway, the residue R^n value (that tells us how close we are to the solution of eq. 2.44), is still high, and this means that although near, the obtained solution is not the correct solution of eq. 2.44 yet. One can observe that in fig. 4.5 (a) we are just looking at a single pixel of the reconstructed image (the central one, where the source is). But the solution, in fact, reconstructs the whole image at once, and although the intensity in that pixel can be more accurate, perhaps it is not the same in the remaining pixels of the image, and fake structures may appear.

Before continuing, let us study the λ^n behaviour along the iterations. In fig. 4.6 it is depicted the λ^n value that minimizes χ^2 in each iteration. The λ^n seeking range in all the explained cases has been from 0 to 1000 (wider enough). As it can be seen, in this case the λ^n value increases more or less linearly with the iteration number, but increase the quantity of fluctuations also. In fig. 4.6 it is shown a linear fit of λ^n . One can be tempted to use this linear fit as values for λ^n in each iteration, and so avoid looking for it.

Unfortunately, this method fails absolutely, because the exponential magnifies the small variations of the parameter λ^n (mainly in the first iterations).

On the other hand, we can see in fig. 4.5 (a) that, from iteration 200, the algorithm has practically converged, and the great oscillations of λ^n that can be seen from iteration 200 in fig. 4.5, almost do not affect the convergency! This means that, as the iteration increases, the algorithm becomes more insensitive to λ^n . This suggest us a method to increase the speed of the algorithm: from a certain moment when the algorithm is more or less near the convergency, we

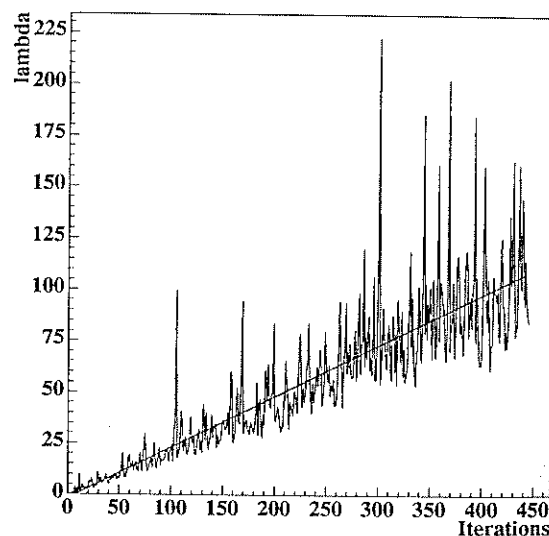


Figure 4.6: λ^n that minimizes χ^2 in each iteration, using eq. 4.10.

can fix the λ^n value. For instance, one can see in fig. 4.5 (a) that the intensity value, from iteration 60, is quite near to its final value. One can also see in fig 4.6, that until the iteration 60, the λ^n value is included between 0 and 10. But, as it is mainly centred in 5, let us do the experiment of allowing λ^n to oscillate only between 0 and 5 during the 60 first iterations, and from iteration 60, we fix its value to 5. The results are shown in figure 4.7:

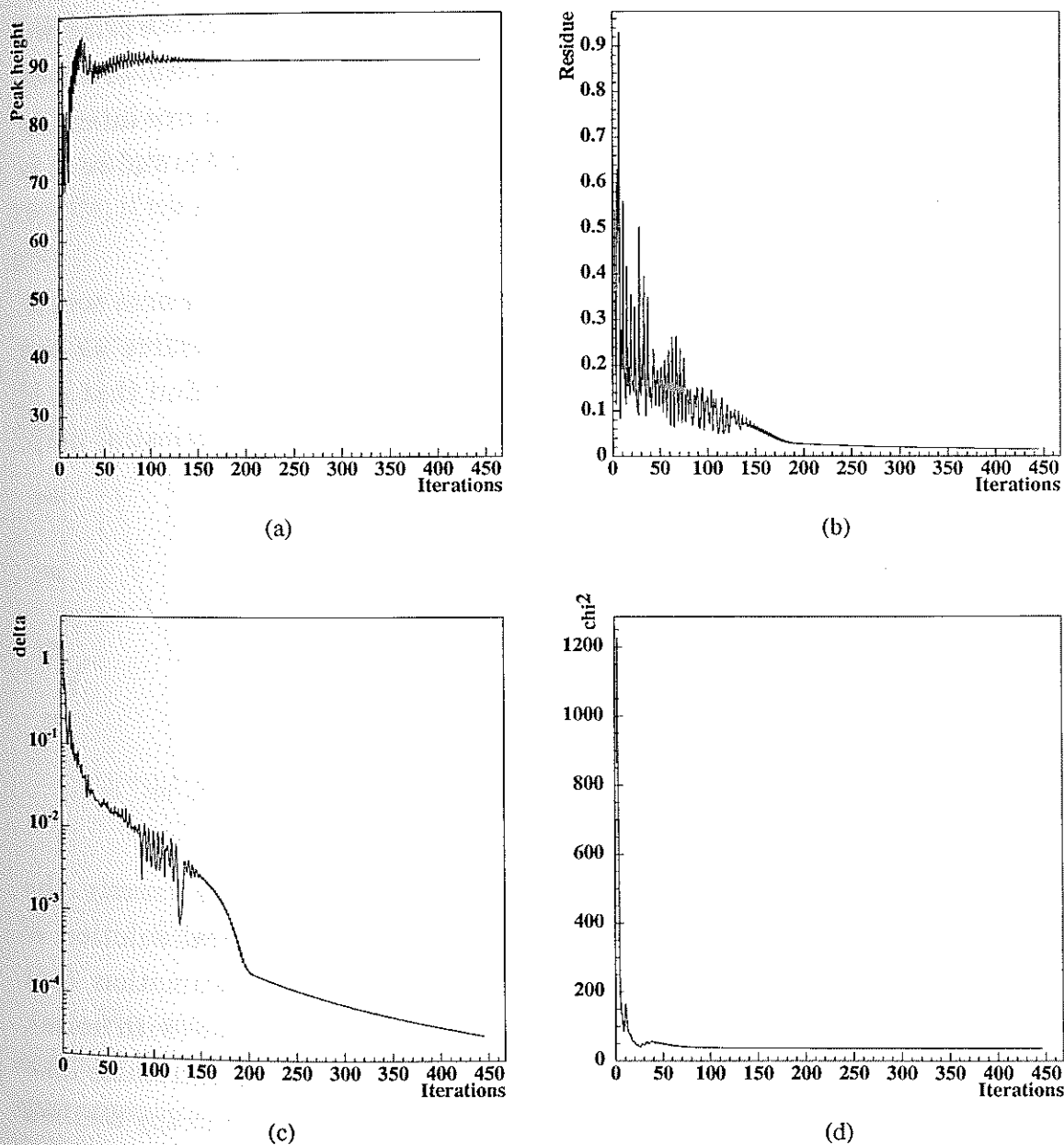


Figure 4.7: Maximum entropy method convergency, using eq. 4.10 and limiting λ^n between 0 and 5

As it can be seen in fig. 4.7 (a), the algorithm now oscillates more at the beginning (because we force λ^n to oscillate between 0 and 5: this would not happen if λ^n oscillated between 0 and 10; but it would take twice the time!). Anyway, the convergency is better; the final δ^n value is now $3 \cdot 10^{-5}$! Contrary to what one could suppose, limiting λ^n between 0 and 5 for the 60-th first iterations (and fix it for the following) has improved the convergency. But, does it converge to the required solution? Now the reconstructed source intensity is 90.0 photons/cm²; it seems a worsening. But it is not! The next surprise we have is that the final value of the residue R^n is now 0.015. An order of magnitude lower than the previous case! Therefore, despite the source intensity is subestimated, this solution is nearer to the solution of eq. 2.44, and so it is more **correct**.

We must not be surprised that this better solution has a worse source intensity reconstruction, because if we use the true celestial source as our parameter estimation (an excellent estimation, indeed!) we will find that it is **not** the solution of eq. 2.44. If we use in eq. 2.44 the true $O_{\alpha\beta}$ celestial map, in absence of noise, as its own $\tilde{O}_{\alpha\beta}$ estimation, we will have:

$$\begin{aligned} \text{if } \tilde{O}_{\alpha\beta} &= O_{\alpha\beta} = \text{true source} \\ &\Rightarrow \tilde{D}_{ij} = D_{ij} \\ &\Rightarrow O_{\alpha\beta} = e^{-1 - 2\lambda \sum_{ij} \Phi_{ij}^{\alpha\beta} \frac{\tilde{D}_{ij} - D_{ij}}{\sigma_{ij}^2}} \\ &= e^{-1} = 0.368 \quad \forall \alpha\beta!! \end{aligned}$$

This means that any map estimation that reproduces *exactly* the measured counts in the detector plane, is not the mathematical solution of equation 2.44. But eq. 2.44 does not pretend to find the estimation that reproduces exactly our experimental data, because in the real case (with noise), a reconstruction that *exactly* fits with our data (with $\chi^2=0$) will introduce fake structures in the image, due only to the noise; the maximum entropy method protects us against that (or it tries to), avoiding a 100% adjustment of the data. Precisely the fact of fixing λ^n in a given moment is what avoids an exact data fitting, and what does not permit the algorithm to approach too much to $\chi^2=0$.

This is why we have a smaller R^n value. Indeed, the χ^2 value we have now is 36.3, bigger than in the previous case. The execution time, as expected, has been reduced to 38 minutes (reducing the seeking range of λ^n accelerates the algorithm); this is another result in favour of fixing the λ^n value in a given moment.

As a preliminary conclusion, and given the results of sections 4.2.1 and 4.2.2, we can say that the EM algorithm does a better reconstruction of the sources intensity than the maximum entropy solution, given by eq. 2.44.

Anyway, it is not convenient to fix λ^n too soon. Let us study the following results; if we repeat the operation fixing the λ^n value from iteration 40, we will get:

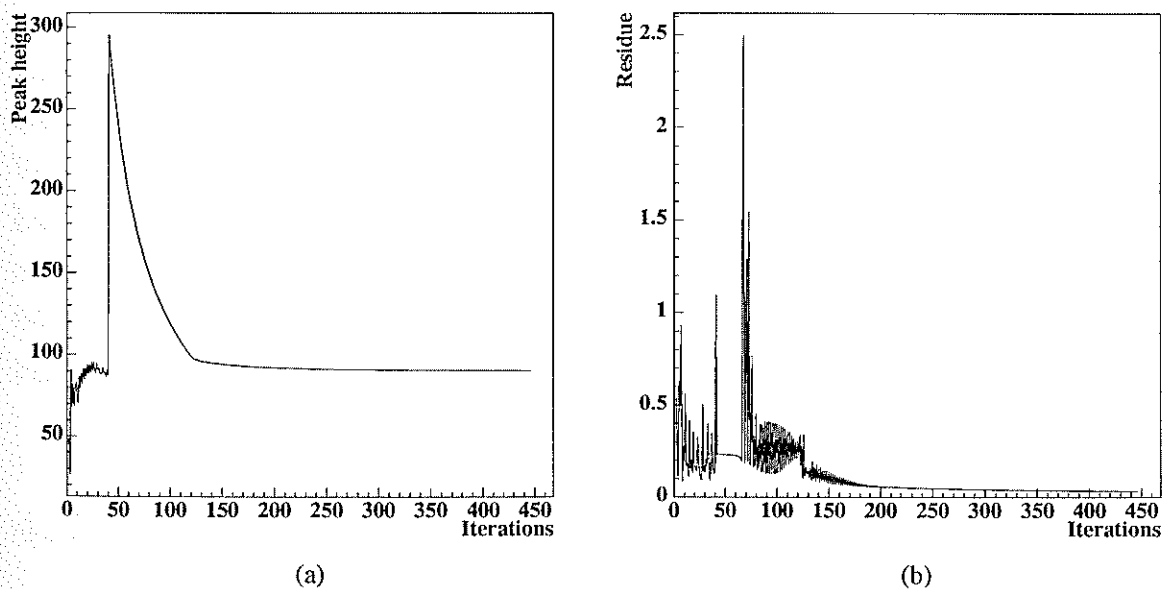


Figure 4.8: The same as in fig. 4.7, but fixing the λ^n value to 5 from iteration 40

We see that, from iteration 40 the convergency is brutally altered, although it slowly returns to convergency until iteration 120, where the convergency is recovered; the δ^n value at the end of the process is $2.5 \cdot 10^{-5}$. The reconstructed source intensity is now 90.6 photons/cm², and the final residue value is 0.032 (somewhat bigger). χ^2 is now 36.4, almost the same as the previous case. The execution time is 25 minutes.

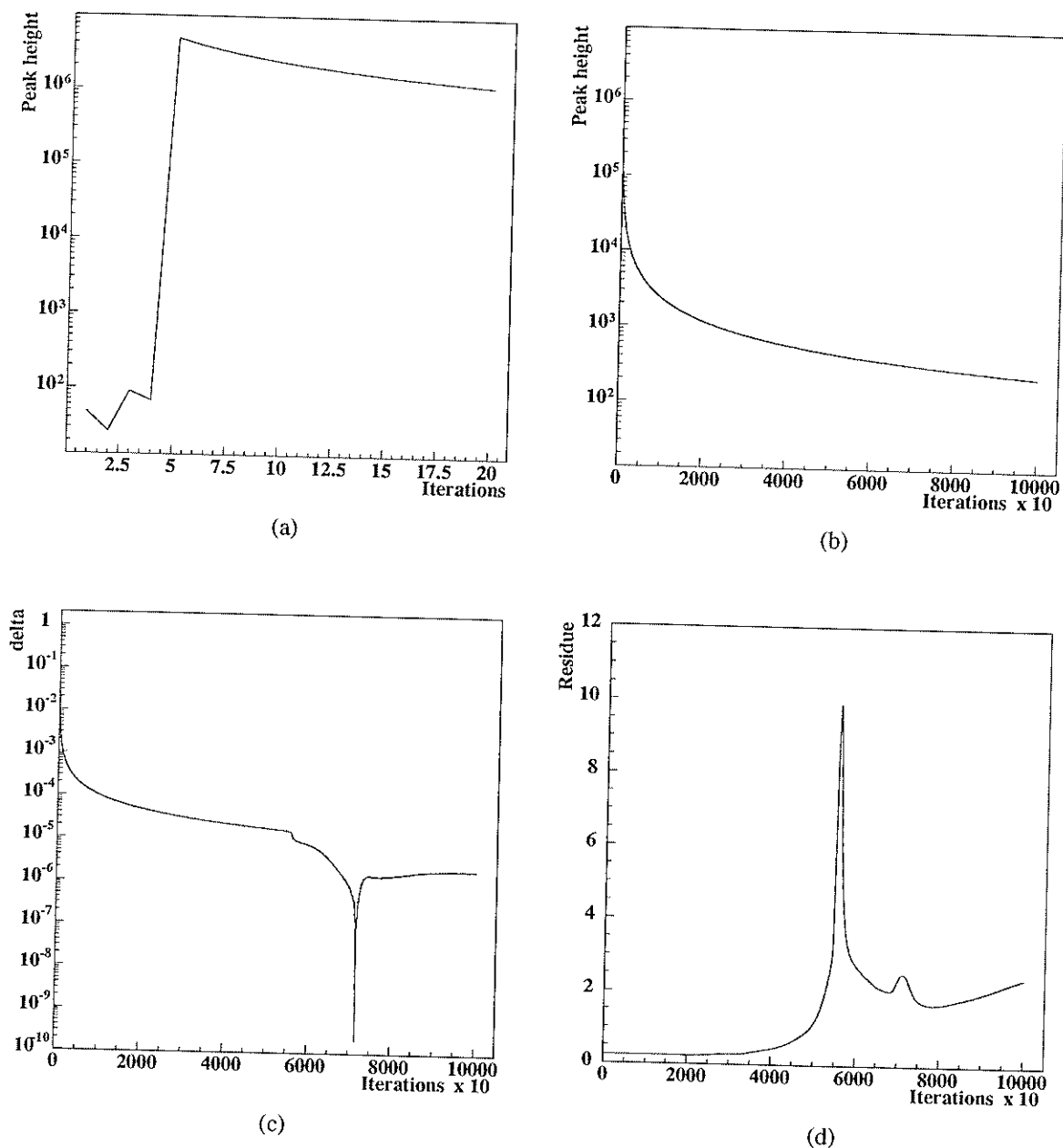


Figure 4.9: The same as in fig. 4.7, but fixing the λ^n value from iteration 5

The sooner we fix the λ^n value, the worse the convergency is. In fact, it is very important that in the first iterations the λ^n value is the one that minimizes χ^2 . In figure 4.9 we have repeated the process, but now we have fixed the λ^n value from iteration 5. In this case we have iterated the process 10^5 times. Fig. 4.9 (a) is an enlargement of fig. 4.9 (b), for the first 20 iterations.

As it can be seen, from iteration 5, where we have fixed the λ^n value, there is a great alteration on the estimated source intensity value, about 5 magnitude orders. It decreases step by step, but in iteration 10^5 , where we stopped the process (after 5 and a half hours), the value was still 230 photons/cm². The convergency process is so slow that from iteration to iteration the image almost does not change, as it can be seen by looking at the small value of δ^n in fig. 4.9 (c), always very close to 0 (its final value is $2.1 \cdot 10^{-6}$, although smaller than 10^{-3} from iteration 200 approx.). **Anyway**, let us observe that now the algorithm does **not** converge to the solution of eq. 2.44 but, on the contrary, it diverges from it, as it can be seen in the odd behaviour of R^n , shown in fig. 4.9 (d). The R^n value at the end of the process was 2.4, and growing. The χ^2 was also very big: 3327 when we stopped the process.

We will choose a compromise between execution **time** and **results**, and calculate the solution of eq. 2.44 using the iterative method described in eq. 4.10, using λ^n between 0 and 5 for the 60 first iteration, and fixing it from iteration 60. These values are, in our case, in the limit of *good behaviour*. Varying λ^n between 0 and 10 or between 0 and 5 for those 60 initial iterations have almost no difference in the final result. But smaller ranges alter the result of those first iterations too much. Equally, fixing its value after iteration 60 does not improve the final result (and takes a longer time) while we already know what happens if we fix it before.

4.3 Reconstruction of a point source

4.3.1 Study of the simulators

Once we have fixed the convergency criteria, we are going to start the reconstruction of images using the explained methods. First of all, we are going to do a study of the simplest case; the reconstruction of a point source (with intensity 100 photons/cm²) in the field of view centre, and in absence of background noise (fig. 4.10). We are going to illuminate the simulators described in section 3.4 with this source and compare both. From this comparison, we are going to study if we can only use the geometrical simulator

(very much faster) to develop the reconstruction software and study the characteristics of the different reconstruction methods considered.

The results can be seen in figure 4.11: in fig. 4.11 (a) it is shown the signal detected in the LEGRI detector plane when using the geometrical simulator, and in fig. 4.11 (b) the detected signal when using the Monte Carlo method, done with GEANT-3, throwing photons with an energy of 100 keV (the energetic range of LEGRI is 20.100 keV).

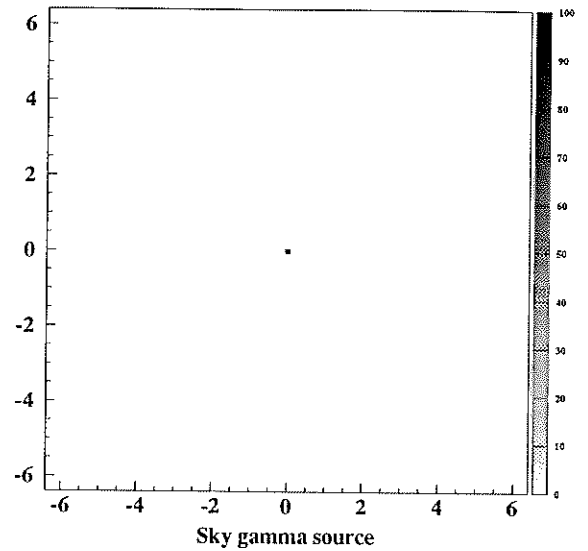


Figure 4.10: Source of 100 photons/cm² in the field of view centre.

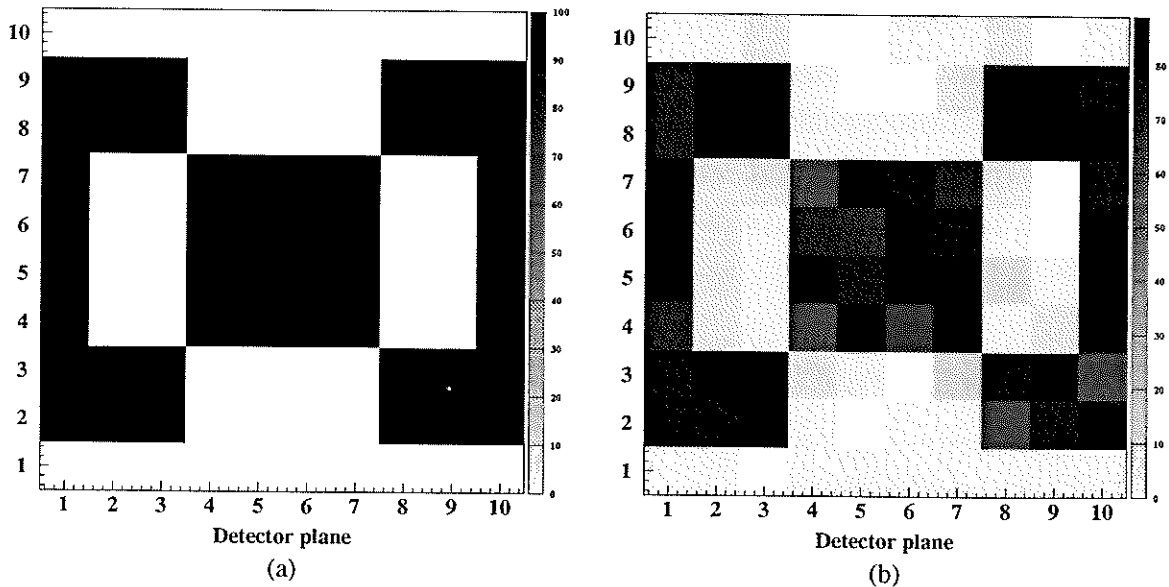


Figure 4.11: Detection of fig. 4.10 using (a) the geometrical simulator and (b) the Monte Carlo method

As it can be seen, the obtained results in both cases is similar. The main difference is that the result obtained with the Monte Carlo method has statistical fluctuations, due to the random nature of the detection process (although the fluctuations will be fewer as the count number increases), and

the measured counts are smaller (about 80 counts/cm² opposite to the 100 exact counts of the geometrical simulator) because the efficiency of the detectors in the Monte Carlo is not 1 (in the geometrical simulator we **do** have considered a value of 1). The detected photons in detector plane units that are covered by opaque mask elements are due to photons scattered about the passive telescope material, and they work as additional noise.

Both the statistical fluctuation and the efficiency smaller than 1 are phenomena easy to implement in the geometrical simulator, and therefore we can work without using the Monte Carlo method. Anyway, although we implement the statistical fluctuation in our geometrical simulator, in all this chapter we will use an efficiency equal to 1, because using one efficiency value or other only acts as a scale factor, and the efficiencies given by the Monte Carlo method do not agree with the true LEGRI efficiencies (due to electronics). We now say that in chapter 5 we will perform simulations using the measured LEGRI efficiencies. But in this chapter the only thing we pretend to do is a comparative analysis of the behaviour of our different reconstruction methods.

4.3.2 Reconstruction

The detected images, shown in fig. 4.11, are the starting point of our reconstructions. We will use them as inputs of our algorithms, and the reconstruction must be as similar as possible to the source image (fig. 4.10). Applying the described reconstruction methods to this detected images, we get the reconstructions shown in figure 4.12. In the (a) column on the left we have the reconstructions obtained from the geometrical simulator; in the (b) column on the right we have the ones obtained from the Monte Carlo model. From top to bottom, the used reconstruction methods have been: Finely Sampled Balanced Correlation (FSBC), δ -decoding, maximum entropy and the EM algorithm, respectively (turning back to section 4.2, the execution time of the reconstruction program using FSBC and δ -decoding was less than 0.2 seconds).

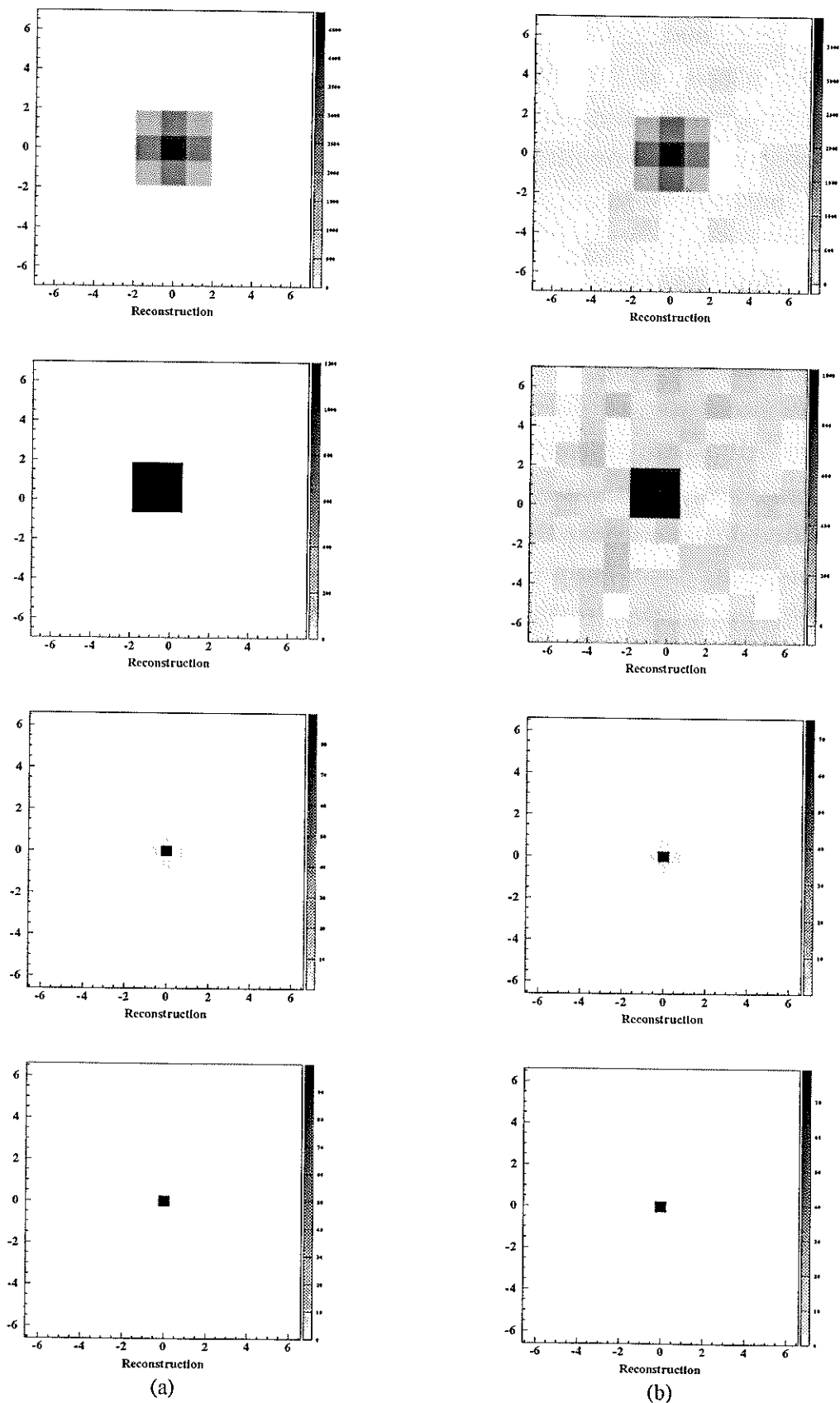


Figure 4.12: Reconstructions of the detected images shown in fig. 4.11

The first point to emphasize is that, using δ -decoding, the reconstructed image is not centred in the field of view, but shifted (to the left and top in this case). As it was said in section 2.9.3, this is because the subdivision different to 0 in each element in the G array (fig. 2.31) is not centred; in our case this is impossible, because we can not subdivide the mask elements in an odd number of subdivisions (so that we would have a central subdivision), but only 2x2 times. Choosing another subdivision different to 0 (but the same for each G element) we have a different reconstruction. See fig. 4.13, where the non-null subdivision is: (a) $\begin{bmatrix} 1 \\ 0 \end{bmatrix} \rightarrow \begin{bmatrix} 1 & 0 \\ 0 & 0 \end{bmatrix}$, (b) $\begin{bmatrix} 1 \\ 0 \end{bmatrix} \rightarrow \begin{bmatrix} 0 & 1 \\ 0 & 0 \end{bmatrix}$, (c) $\begin{bmatrix} 1 \\ 0 \end{bmatrix} \rightarrow \begin{bmatrix} 0 & 0 \\ 1 & 0 \end{bmatrix}$ and (d) $\begin{bmatrix} 1 \\ 0 \end{bmatrix} \rightarrow \begin{bmatrix} 0 & 0 \\ 0 & 1 \end{bmatrix}$ (this is for the case of a hole; for an opaque element, just change 1 by -1).

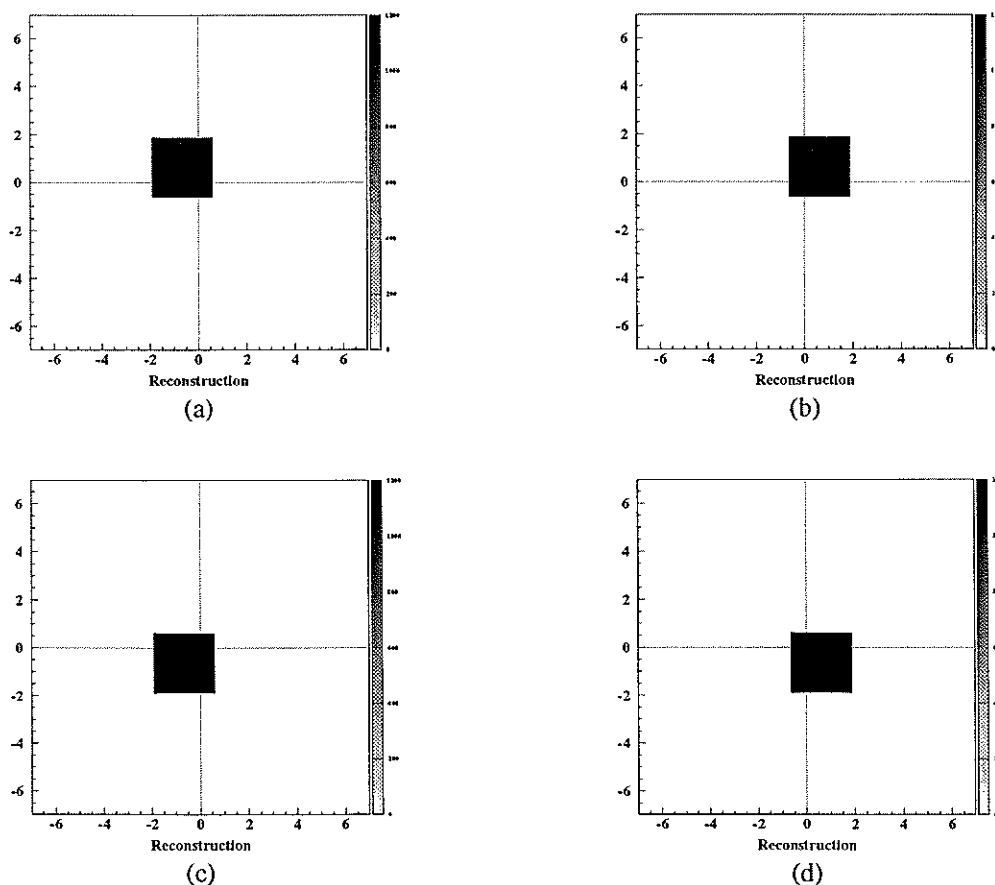


Figure 4.13: Variations of δ -decoding for the detected image shown in fig. 4.11 (a)

These variations of δ -decoding have been applied to the image detected with the geometrical simulator and, of course, the first image coincides with the second image in the (a) column in fig. 4.12. Given the form of eq. 3.1, that

yields the reconstruction when using correlation, and given the definitions of the G array for FSBC and δ -decoding shown in fig. 2.31, we can realize that FSBC is exactly the sum of all the possible choices of δ -decoding and, in fact, if we add all the images in fig. 4.13, we get:

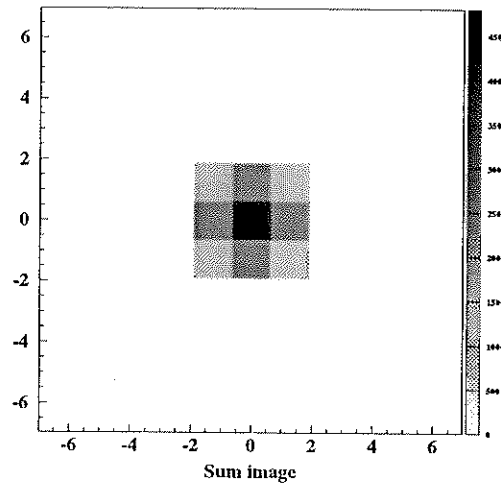


Figure 4.14: Sum of the images in fig. 4.13

which is identical to the image obtained with FSBC (fig. 4.12 (a), image on the top). This means that we can trivially pass from an image done with δ -decoding to the equivalent image with FSBC (and also vice versa, although not so trivially), because they are equivalent.

The next point we are going to consider is the reconstructed source intensity. For images in fig. 4.12 (a) (those obtained from the geometrical simulator), the reconstructed intensities are: 4800 photons/cm² for FSBC in the central pixel (=100 photons/cm² * 48, because there are forty eight 1's in the G array); 1200 photons/cm² for δ -decoding (=100 * 12); 89.73 photons/cm² for maximum entropy and 99.99 photons/cm² for the EM algorithm. For the FSBC and δ -decoding cases we see that the image is multiplied by a number that is the number of 1's in the reconstruction array ($N_U = 12$ for δ -decoding and 48 for FSBC in our case), as it was said in section 2.9, and we only have to divide by it *a posteriori* to get a more realistic estimation of the intensities. In fact, although for clarity in the dissertation it was not mentioned in section 2.9, we can do it implicitly, including that factor in G . That is, each 1 and -1 in the reconstruction array can be substituted by $1/N_U$ and $-1/N_U$ (therefore it is

possible to achieve the "ideal" case of eq. 2.21). The images that will be shown afterwards with this two methods will be corrected by this factor. As for the maximization methods, we can clearly see that the EM algorithm reconstructs better the intensity than the maximum entropy method.

For the images in figure 4.12 (b) (those obtained from the Monte Carlo model), the reconstructed intensities are: 3926 photons/cm² for FSBC (= 81.8 * 48), 1002 photons/cm² for δ -decoding (=83.5 * 12), 75.1 photons/cm² for maximum entropy and 79.2 photons/cm² for the EM algorithm. We can clearly see that the main effect of an efficiency smaller than 1 is a change on the scale; it is as if we detect a source with smaller intensity. This can be easily corrected, dividing the reconstructed intensity by the efficiency or including this factor in the G array; for the maximization methods, the correction can be done including the efficiency in the Φ array (see section 5.3).

The other effect we can see is that the statistical fluctuation worsens the image for the correlation methods (which are analytical methods that do not consider such fluctuation). The image background (where there is not any source) shows a bigger noise than the one observed in the maximization methods (although this is *partly* due to the smaller pixel size chosen in these last two methods); the background oscillates between -110 and 166 for FSBC and between -57 and 85 for δ -decoding. We have pixels with negative intensities, due to the fact that the statistical fluctuation does not allow the total cancellation of the 1's and -1's in the G array. In the correlative methods, the pixel size is fixed, as we have said in section 2.5. In balanced correlation, the pixel size is given by the nominal resolution of the telescope ($\Delta\alpha \times \Delta\alpha$, being $\Delta\alpha = \arctg(c/f) = 2.54^\circ$, where c is the size of a mask element and f the mask-detector plane distance). In FSBC and δ -decoding, when we subdivide the mask, we also subdivide the pixel size (although the resolution, as we saw in 2.9.2 and 2.9.3, is still the same). In our case we divided it by 2, and so the pixel size is given by $(\Delta\alpha/2) \times (\Delta\alpha/2)$. But the maximization methods do not have, in principle, a defined pixel size, and it can be as small as we want.

In the previous paragraph we said that a smaller pixel size decreases partly the level of noise in the rest of the image because the noise counts

assigned to a sky region will be shared out, as in a histogram, among smaller "channels", and so there will be less counts in each channel (the more pixels in a sky zone, the smaller noise counts in each pixel). Nevertheless, the *absolute* noise is smaller too. If we reconstruct the image with the same pixel size (and with the same number of pixels: 11x11) as in the correlation methods, using maximization methods, we get that the noise in the image background oscillates between 0.004 and 0.75 for maximum entropy, and between $8 \cdot 10^{-4}$ and 1.25 for the EM algorithm. Of course, it is a smaller variation than in the correlation methods, and **non**-negative.

The possibility of using a pixel size as small as we want in maximization methods allow us that the reconstructed source in fig. 4.12 could be as "point-like" as we want, so it can be more similar to the real source (fig. 4.10). But this is due to the fact that the source is in a position where projects a shadow that coincides exactly with the detector plane units position, and therefore we can see it properly. If the projected shadow does not coincide so well with the detector plane units position the reconstruction will not be so point-like; it does not matter how small our pixel size will be, as we will see in the next section. This will impose a practical limit to the pixel size.

4.4 Source movement

Let us see next the effect of moving the source with respect to the field of view centre, so that the projected shadow does not coincide exactly with the position of the detector units. The previous source with an intensity of 100 photons/cm², in absence of noise, will be moved from $(\alpha, \beta) = (0, 0)$ to $(\alpha, \beta) = (1.27, 1.27)$ (position where the shadow will coincide again with the detector units position) passing through the intermediate positions (0.32, 0.32), (0.64, 0.64) and (0.95, 0.95), as it can be seen in figure 4.15. We show the results for FSBC, the maximum entropy method and the EM algorithm. We do not show the case $(\alpha, \beta) = (0, 0)$, since it can be seen in fig. 4.12. The simulator used is the geometrical simulator.

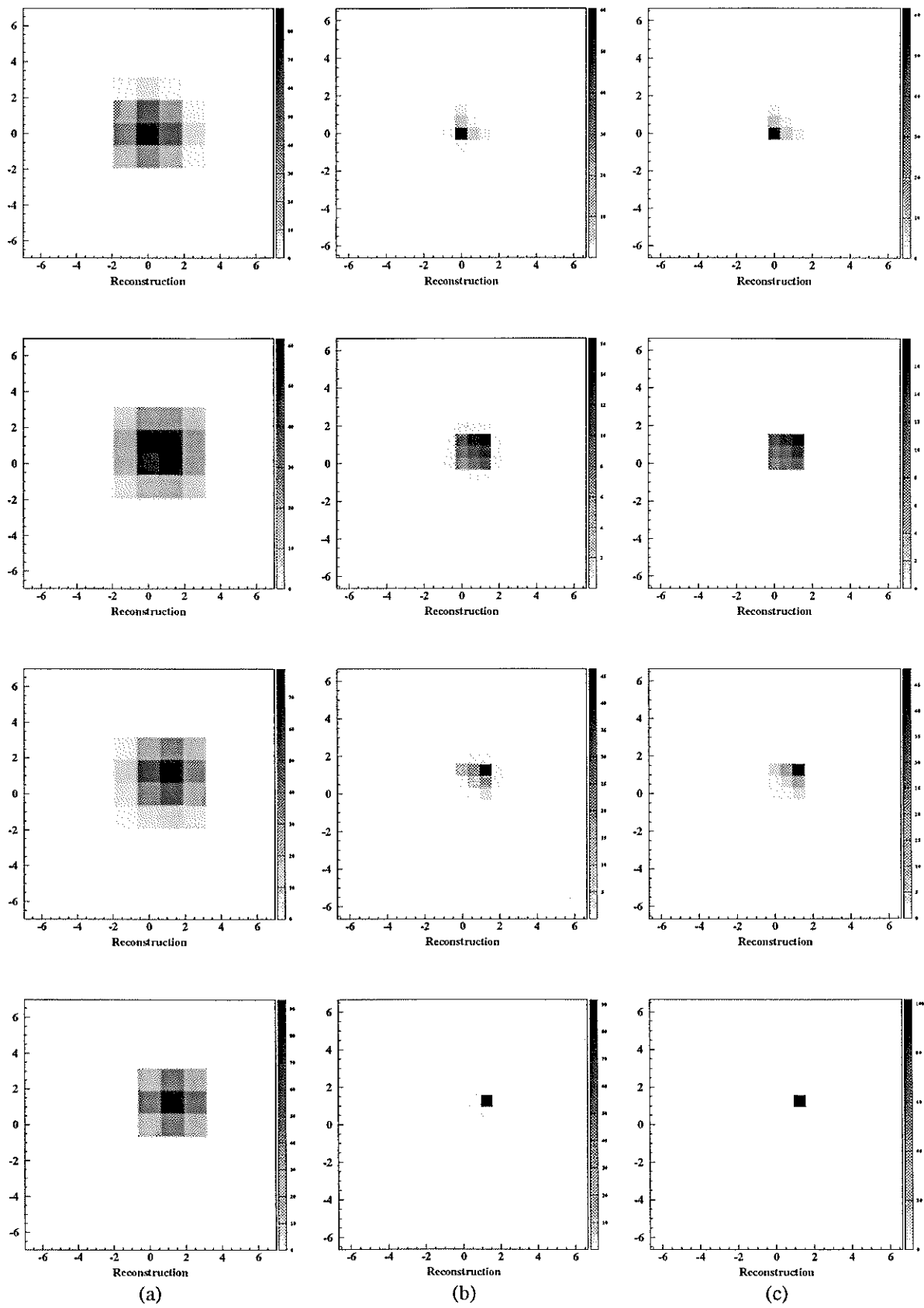


Figure 4.15: Effect of the source movement in the reconstruction.

In the (a) column we see the reconstruction using FSBC; in (b), the reconstruction using maximum entropy and in (c) the reconstruction using the EM algorithm. From top to bottom, the true source positions in degrees are, respectively: (0.32,0.32), (0.64,0.64), (0.95,0.95) and (1.27,1.27), respect to the telescope field of view centre.

When the projected shadow and the detector positions does not coincide, there is an uncertainty in the true sky position of the source, because the detector plane is not able to see clearly the mask pattern. This brings a spread of the reconstructed signal, independently of the reconstruction method used, and so the signal embraces all the zone where the source could be. Given that the signal is shared out in a bigger zone, the reconstructed intensities are also smaller, obtaining the real total intensity by integrating over all the zone (this is a little more difficult with FSBC and δ -decoding, because the reconstructed image, even in the best case, is never limited to a single pixel but occupy some pixels, and then there is an overlapping). When the source is again in a position such that it projects a shadow that coincides with the detectors position, the reconstruction is again the best, as we can see looking at the images on the bottom of figure 4.15.

As it can be seen in fig. 4.15, in the cases (0.32,0.32) and (0.95,0.95), this is when the source is at 0.32° from a position that projects a shadow coinciding with the detectors position, the reconstruction is quite "punctual", and the shadow can induce to think (wrongly) that the true source position is given by the reconstructed source position, by the brightest pixel (when the source is in (0.64,0.64) the source is too spreaded to confuse it with a point source). Therefore we commit an error in positioning a point source of 0.32° , this is $20'$ of arc. This is the point source location capability of our telescope, as we have shown in table II.

An additional point that must be emphasized is that the EM algorithm is the reconstruction method that has less spread in the reconstructed image of all the considered methods.

4.5 Angular resolution

Let us study now the theoretical LEGRI response when our geometrical simulator is illuminated by the sources shown in figure 4.16: they are four sources, all them with an intensity of 100 photons/cm^2 , located in four strategic positions: $(0,0)$, $(0.64,0.64)$, $(-1.27,-1.27)$ and $(2.54,-2.54)$. As we said, the nominal resolution of our telescope, given by the angle that a mask element subtends from the detector plane, is 2.54° . Its half value, that is 1.27° , is the minimum angular distance that we have to move a sky source so that its projected shadow coincides again with the detector units position.

0.64° is again the half of the value of the previous case, and it is a really annoying position, because the shadow that it casts is shared out among various detectors, and it is not possible to solve it properly in the detector plane. The detected image is shown in fig. 4.17.

Since the resolution of our telescope is 2.54° , one can expect that only the source in $(2.54,-2.54)$ can be solved separately while the others are confused, given that their separation is smaller than the resolution power of our telescope; the results are shown in figure 4.18.

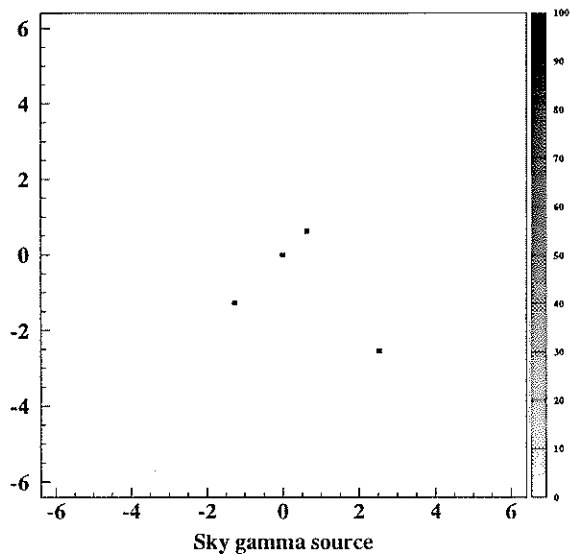


Figure 4.16: Field with four sources, which intensity is 100 photons/cm^2 , positioned at $(0,0)$, $(0.64,0.64)$, $(-1.27,-1.27)$ and $(2.54,-2.54)$.

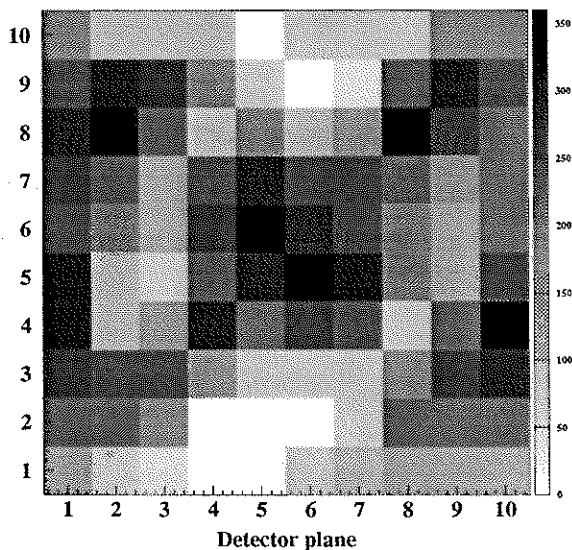


Figure 4.17: Detected image in the detector plane when the telescope is illuminated by the sources in fig. 4.16.

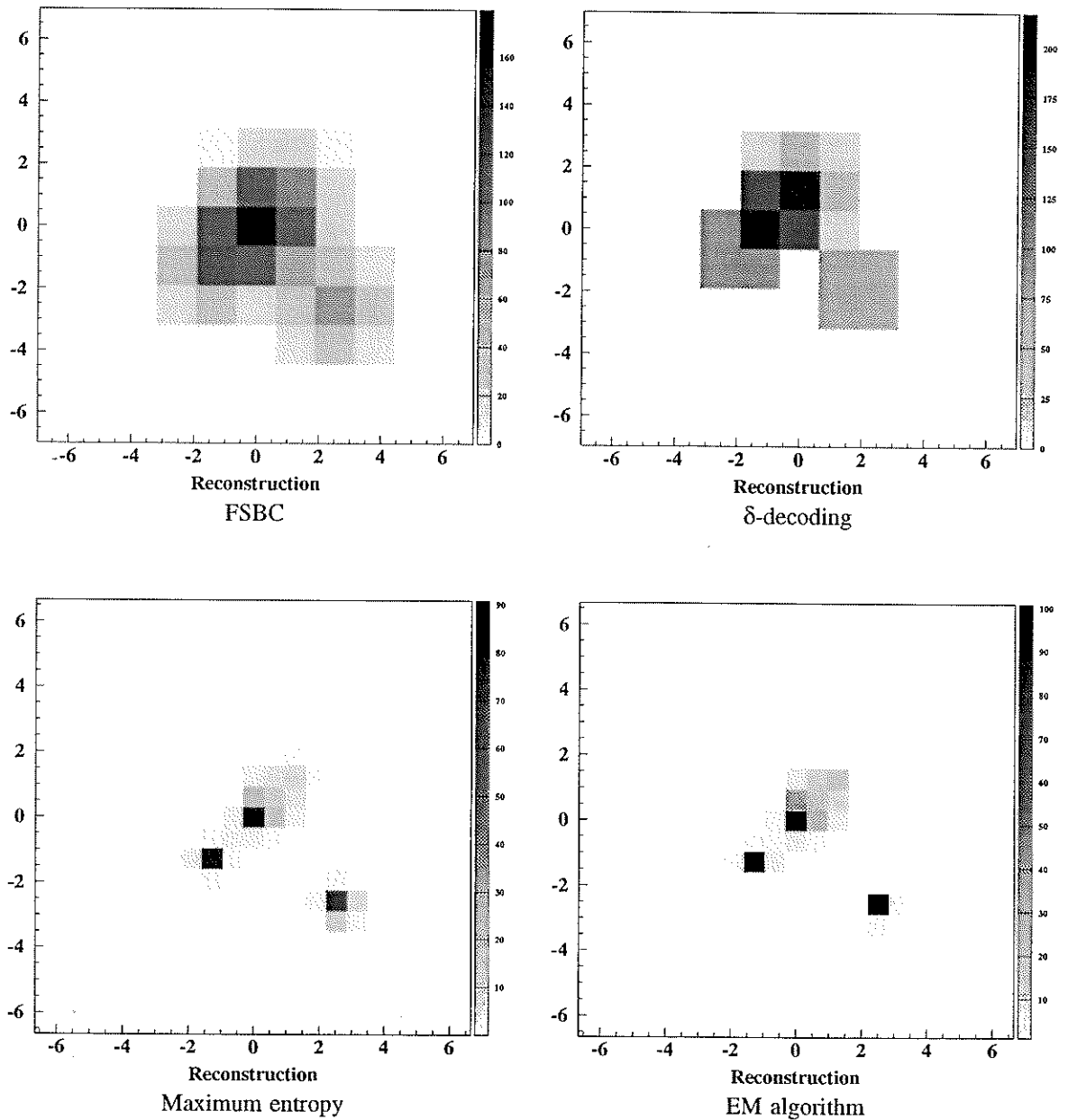


Figure 4.18: Reconstructions from the detected image in fig. 4.17.

We can see that, indeed, with FSBC and δ -decoding, in the central part of the image we only have a mess, difficult to solve, because the reconstructed images at $(0,0)$ and $(-1.27,-1.27)$ are overlapped, and the source at $(0.64,0.64)$ is spreaded, worsening the result. The only source that can be solved separately is the one at $(2.54,-2.54)$, mainly with δ -decoding (using FSBC it is overlapped with the central source).

But when we study the images reconstructed with the maximum entropy method and the EM algorithm, we are surprised as not only the source at (2.54,-2.54) is clearly differenced (more than in the other two methods) but also the one at (-1.27,-1.27), that can be seen clearly! The only source that can not be seen clearly, and which is overlapped in part by the one at (0,0), is the one at (0.64,0.64), which is spreaded (as we have said, this is a particularly annoying position).

We have therefore an important conclusion: the correlation methods obtain an angular resolution which is the nominal one. But the true angular resolution of the telescope is **not** the nominal but, in our case, its half, 1.27°, which is the resolution obtained with maximization methods. In fact, the angular resolution of a coded mask telescope, is **not** given by equation 2.25, which we repeat here:

$$\text{resolution} = \text{arctg}\left(\frac{c}{f}\right)$$

where c is the size of a mask element and f the distance mask - detector plane, but is given by:

$$\text{resolution} = \text{arctg}\left(\frac{d}{f}\right) \quad (4.11)$$

where d is the size of a **detector plane element**. This means that the true angular resolution of a coded mask telescope is given by the spatial resolution of its detector plane, and not by the mask element size.

Therefore, with the reconstruction methods based on the correlation, there is implicit a *loss of information* in the reconstructed image, information which is retrieved when using maximization reconstruction methods. With those methods we can obtain the true angular resolution of the telescope. The only exception will occur when the detector plane elements and the mask elements have the same size; in this case, both resolution will be the same.

The results in section 4.4 and in this section say clearly that, although in maximization methods we can use in the reconstructed image a pixel size as small as we want, there is a practical limit to its size (as it was pointed out in section 2.12.1) because our data are finite and we can not get from them more information than the one they have. Besides, if we have more pixels in the image, the algorithm will take longer time in carrying out the reconstruction. We will use for maximization methods a pixel size of $0.64^\circ \times 0.64^\circ$; this is half the true angular resolution, as it has been done in the images shown so far.

If we compare the images in figure 4.18 (specifically the source at $(-1.27, -1.27)$) with the images of figure 4.15 (specifically those at the bottom) corresponding to a single source at $(1.27, 1.27)$ we have another important conclusion to emphasize: the reconstructed source intensity in a given pixel is rather independent of the presence or absence of other sources inside the field of view. This is a fact implicit in the correlation methods, as it was shown in section 3.2.1; in those methods all pixels are independent of the others. But this was not so clear in the maximization methods. The EM algorithm is the maximization method in which the reconstructed intensity is less affected by the presence of other sources.

In fact, the presence of other sources affects the reconstruction in maximization methods, but not so much the *final image structure* as the *number of iterations* needed to get the image. As the source is more complex, the algorithms are slowed down; this is because it is more difficult to fulfil the stopping requirements that we have explained in section 4.2.

4.6 Ghosts

We have so far limited the field of view in the reconstructed images to a mask cycle; this is the field included in 2×2 times the base pattern of the mask (see fig. 2.15), and it is $(\pm 6.34^\circ) \times (\pm 6.34^\circ)$. But we have to remember that the LEGRI mask is made up of 2.8×2.8 times the base pattern, and the collimator does not limit the detectors field of view to a cycle: this means that

our field of view is bigger, and sources outside these $\pm 6.34^\circ$ will give a modulated signal in the detector plane. This will generate the ghosts mentioned in chapter 2; there will be different source positions that will generate the same shadow on the detector plane, and this will appear in the reconstructed image. We can prove it if we do not limit the field of view on the reconstructed image to a cycle but use the complete field of view, that is given by the collimator height and is equal to $(\pm 10.53^\circ) \times (\pm 10.53^\circ)$ (or also if we limit the field of view on the reconstruction to a cycle but we put a source *outside* it - obtaining, therefore, a reconstructed source *inside* the field of view-). In fact, as we have said in section 2.7, we will have ghosts even if we limit ourselves to a mask cycle, because in this case border of the field of view is degenerated (see fig. 2.17) and any source in its border would appear also on the opposite border (and if it were on a corner, it would appear on the four corners).

Let us work using the complete field of view of our telescope and illuminate it with the field of sources shown in figure 4.19; it consists of three sources with intensities 100 photons/cm², and positions at (0,0), (5.08,0) and (-5.08,-5.08). On this occasion we have added to the detector plane a poissonian noise with a mean value of 30 counts/cm². If we reconstruct the image with FSBC, δ -decoding, maximum entropy and the EM algorithm, using the whole telescope field of view, we get the results shown on the following page. In the last two methods we have used two different representations: tone map (each grey tone is an intensity) and surface map (the intensity is represented by the height).

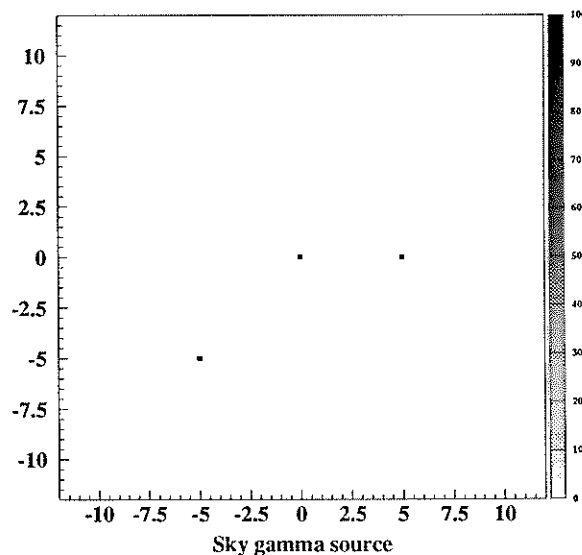


Figura 4.19: Fuente celeste

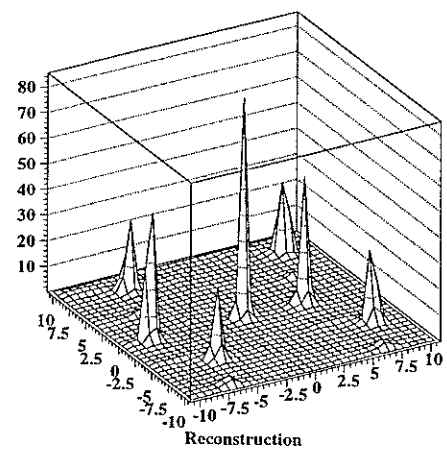
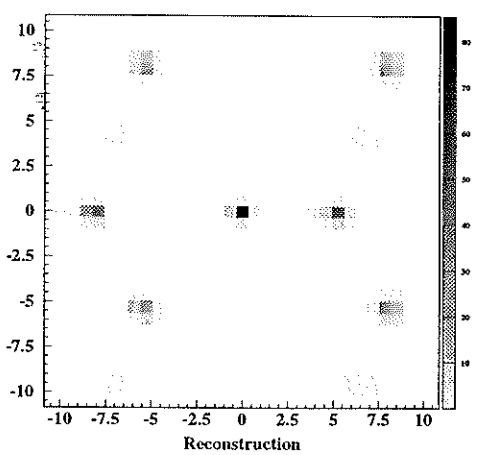
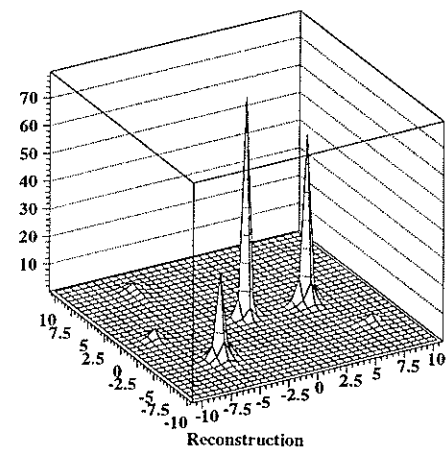
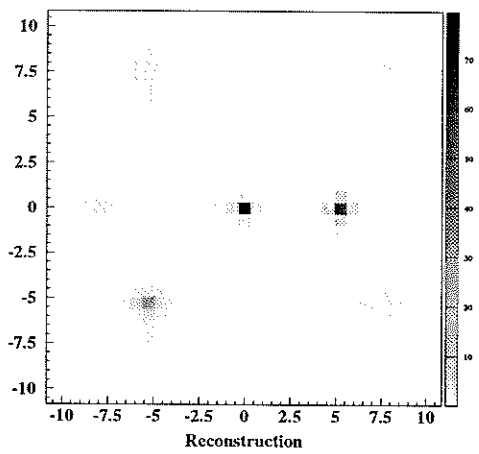
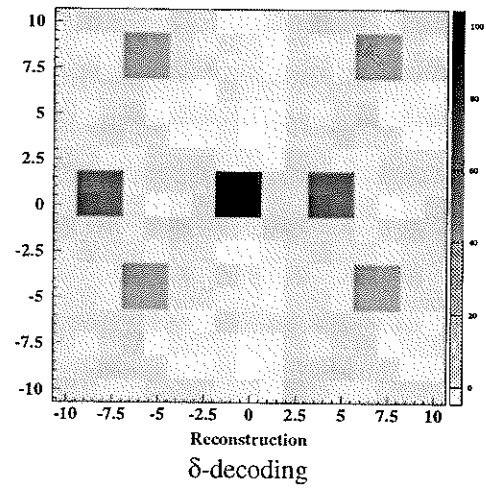
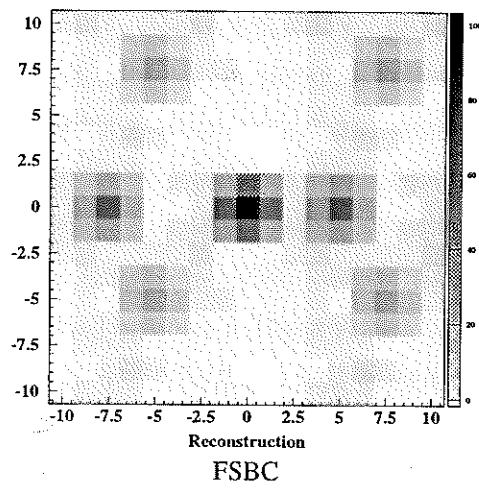


Figure 4.20: Reconstructions from fig. 4.19

As it can be seen, each source not too near to the centre field of view will produce ghosts in the other directions where the same mask pattern could be seen; so, the source at $(5.08,0)$ will produce a ghost at $(-7.59,0)$, and analogously the source at $(-5.08,-5.08)$ will produce three ghosts at $(-5.08,7.59)$, $(7.59,-5.08)$ and $(7.59,7.59)$.

In the methods based on correlation, these ghosts are *exactly* the same, because the correlation is *cyclic*. In these sky pixels, the detector plane data are correlated by the same permutation of the reconstruction array G and therefore what we get is exactly the same. Something similar seems to happen with the EM algorithm, although it is not the same phenomenon, because the EM algorithm (as the maximum entropy method) does not reconstruct the sky pixel by pixel (as we said) but *all* of them at once. One of the most surprising characteristics of our EM algorithm is that it reconstructs all the ghosts practically with the same intensity.

But if we compare the reconstruction by the maximum entropy method (fig. 4.20) with the original source (fig. 4.19) we can see that the three reconstructed sources exactly correspond to the true sky sources! And its ghosts are very suppressed. How is it possible? If all the ghosts project the same mask pattern on the detector plane (except for a difference in the detected intensity due to the collimator), how can the maximum entropy method find the true sources out of all the possible sources? Well, in fact it **can not**. What the maximum entropy algorithm does is to favour the source/ghost nearest to the centre of the field of view, as we can prove if, instead of using the sources field of figure 4.19, we use the one in figure 4.21 (a), where we have subtracted the source at $(5.08,0)$ and we have put instead another (also with an intensity of 100 photons/cm^2) at $(-7.59,0)$; this is, the place where the ghost appears. In figure 4.21 (b) we can see the reconstruction with maximum entropy, represented in surfaces map. As we can see, the source is again reconstructed at $(5.08,0)$ although now the true source now is at $(-7.59,0)$; the maximum entropy algorithm reconstructs the ghost/source nearest to the centre of the field of view.

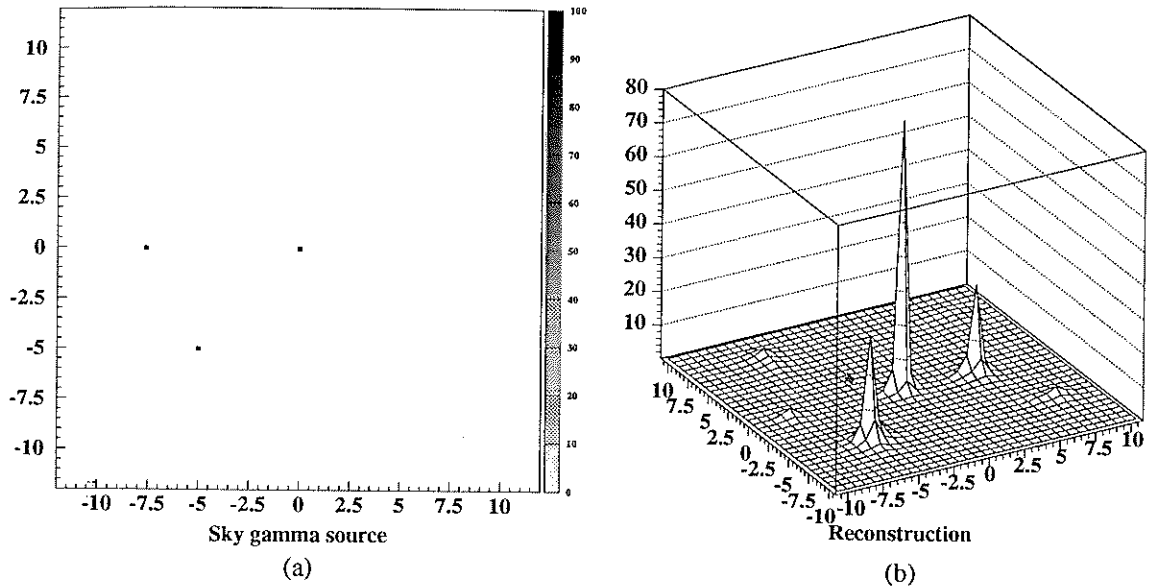


Figure 4.21: Sky source (a) and reconstruction (b) with the maximum entropy method

Of course, with any method we can always determine which ghost is the true source by operative procedures, as it was explained in section 2.7, varying the telescope pointing; although in LEGRI this operative method is somewhat limited by requiring that the LEGRI pointing direction must always be orthogonal to the solar axis. This means that one of the axis (for instance α) varies only as LEGRI turns around the Sun; this is, 360° in 365 days (approx. it varies one degree per day), while all our movement and pointing freedom is in the other axis (β).

Furthermore, as the LEGRI mask is not made up of 2×2 cycles, the ghosts are not limited to the border of the field of view as it was explained in section 2.7, but they come into the telescope field of view: a source near to the border of the total telescope field of view, for example at $\alpha = 10.1^\circ$, will produce a ghost at $\alpha = -2.54^\circ$, because the patterns projected in the detector plane from both directions are the same and so the operational procedure described in section 2.7 needs to be more exhaustive. Nevertheless, this will not be needed as we will see in section 5.5.

4.7 Collimator effect

Let us now study the decrease of the intensity in the reconstructed peaks shown in figure 4.20, as they move away from the field of view centre. Let us begin with the FSBC case and δ -decoding; as can be seen, the sources more remote to the central position are weaker, although the three original sources have the same intensity. This is due to the suppressor effect of the collimator. The reconstructed values of the image are, for FSBM: 103.3 photons/cm² for the central source, 60.7 photons/cm² for the source at (5.08,0) (and its ghost), and 34.8 photons/cm² for the one at (-5.08,-5.08) (and its three ghosts). Similarly, for δ -decoding, these values are: 104.2 photons/cm² for the central source, 59.8 photons/cm² for the source at (5.08,0) and 42.7 photons/cm² for the one at (-5.08,-5.08).

If we subtract the background (that is added to the pixels where the sources are, and whose value -after dividing by the number of *ones* in the *G* array- is about 2.5) and we divide these so corrected intensities by the suppressing factor of the collimator (whose value for the three mentioned positions are 1, 0.565 and 0.32 respectively -see section 2.11.1-) we get that the so corrected reconstructed intensity is about ~ 100 . This is, the suppression we see in the reconstructed peak is due indeed to the collimator.

The shrewd reader could ask why we do not include this collimator correction in the algorithm, so the image already shows the corrected sources. In fact, it is possible (and easy) to do, although we think it is not suitable for several reasons: a) to correct the image by dividing its pixels value by the suppressing collimator factor not only affects those pixels where the sources are but also all the image including the background pixels; b) the background (due to noise in the detector plane, or to statistical fluctuations in the detected counts, or to an incorrect reconstruction -for example, because some detectors do not work, as we will see in section 4.11-) which is usually flat and different to 0, when we correct it by the collimator factor is not so flat but grows as we go away from the centre (in pixels near the border, for example at $(\alpha,\beta)=(10.8,0)$ the suppressing collimator factor is 0.024; therefore its inverse is 42. The background in this zone is 42 times bigger than the one at the centre!). This

means that acting in such a way we introduce a structure in the reconstructed image that could make difficult to see the sources. So we think it is better to do this correction *a posteriori* once the sources are identified.

For the EM algorithm, the observed decreasing in the sources more remote from the centre is not due to the collimator effect, as the algorithm takes into account its effect, looking for the map more coherent with the data, but to the fact that some ghosts appear. Indeed, if we concentrate on the source at (5.08,0), its expected counts in the detector plane are given by its intensity (49.1 photons/cm²) multiplied by the corresponding collimator factor (0.565) **plus** the intensity of the ghosts at (-7.59,0) that is 51.2 photons/cm², multiplied by the corresponding collimator factor (0.305) (we add the intensities of the source to its ghost because the map is reconstructed as a whole; this is not correct for correlation methods because they reconstruct the map pixel by pixel). This procedure gives us an expected count number in the detector plane, corresponding to the source and its ghost, of $49.1 * 0.565 + 51.3 * 0.305 = 43.4$ counts/cm², which is equivalent to a single source at (5.08,0) with intensity 77 photons/cm² ($77 * 0.565 = 43.5$); and in fact this is the reconstructed intensity given by the EM algorithm when limiting the reconstruction to the field of view of one cycle, removing thus the ghosts (or the true source if it is outside the field of view of one cycle).

This means that the collimator has in fact a suppressor effect in the reconstructed intensity, but it is due to the diminution of the Signal to Noise Ratio (SNR). The noise is in proportion bigger for the source at (5.08,0) than for a centred source with the same intensity. In absence of noise, the source is reconstructed with a bigger intensity (~100) (see next section for the noise effect in the peak height). Anyway, the main effect is that the source intensity is shared out among the ghosts (and this is not a collimator effect, but depends on the mask pattern); the more the ghosts, the less the source counts there will be in each ghost. The intensity of the central peak is 87.2 photons/cm², and for the source at (-5.08,-5.08) and its three ghosts, it is ~28 photons/cm² each one.

For the maximum entropy method, the reconstructed intensities are 79.6 photons/cm² for the central pixel, 68.3 photons/cm² for the source at (5.08,0) and 40.7 photons/cm² for the one at (-5.08,-5.08).

We see that it appears a suppression due to the collimator. In part, as with the EM algorithm it is due to the increase of the noise in proportion to the signal that it makes, as in the EM algorithm, the reconstructed peak wider and shorter (see section 4.8); anyway, the suppression is bigger than what one could expect and it is not only due to the increase of the SNR but to the collimator itself too. This suppression appears *even in absence of noise* (this does not happen with the EM algorithm; one can not either associate the suppression to the ghosts presence, because there are not ghosts in the maximum entropy method).

Therefore, although the algorithm indeed takes into account the collimator effect (in Φ , similarly to the EM algorithm), the reconstruction of the pixels more distant to the image centre is affected by the collimator and is, mysteriously, worse than what one could expect; at first sight it seems as if it were not implemented. It is difficult to explain this odd behaviour, unexpected in principle, but it anyway appears when the reconstruction is done; it is as if the maximum entropy method, as it observes less counts corresponding to that sky pixel, were more insecure in its answer and gave a more cautious intensity value. Perhaps this is partly owed to the fact that the method looks for the map compatible with the data that is smoother and with less structure.

About the imaging capability, the maximum entropy method (given that it favours the ghost/source nearest to the image centre -and this happens even if we limit ourselves to a cycle, or if we reconstruct in the whole telescope field of view-) is equivalent to the EM algorithm when we limit it to the field of view of a cycle. Nevertheless, about source intensity reconstruction, the EM algorithm works better.

But on the other hand, if we look at figure 4.20 we can see that, in the EM algorithm reconstruction, the background is more fluctuating than in the maximum entropy method. In the maximum entropy method, except for the ghosts, the background is very flat, while the EM algorithm has generated some small fake sources in zones where there is nothing. These fake sources come from the structure of the noise in the detector plane only. We are going to study, then, the noise effect in the following section.

4.8 Noise effect

As we have just seen, the noise in the detector plane, added to the signal, not only can generate background noise in the reconstructed image but can also alter the shape of the signal and generate fake structures. This is why it is important not to confuse a source due only to the noise structure with a true source. In this section, the simulator is going to undergo a given sky source (always the same) and different noise levels. With it, we will study how sensitive to the noise each reconstruction method is, and how we can improve the image quality. In theory one could expect that the maximum entropy method (because it is a *maximum entropy* method) will be the most insensitive to the noise of all the methods, and would generate the least structures compatible with the data; it should be the flattest image compatible with them and so the background should have almost no fluctuations. We will see that the answer is *yes* and *no*.

4.8.1 Constant noise

Our simulator has undergone a constant noise in the detector plane and a centred source with intensity 100 photons/cm^2 . The results are shown in figure 4.22; from left to right, the reconstruction method used was FSBC, maximum entropy and the EM algorithm. From top to bottom, the noise in the detector plane, constant except for the statistical fluctuation, was 10, 100, 1000 and $10000 \text{ counts/cm}^2$ (the counts were sorted as a gaussian whose width was the square root of the detected counts).

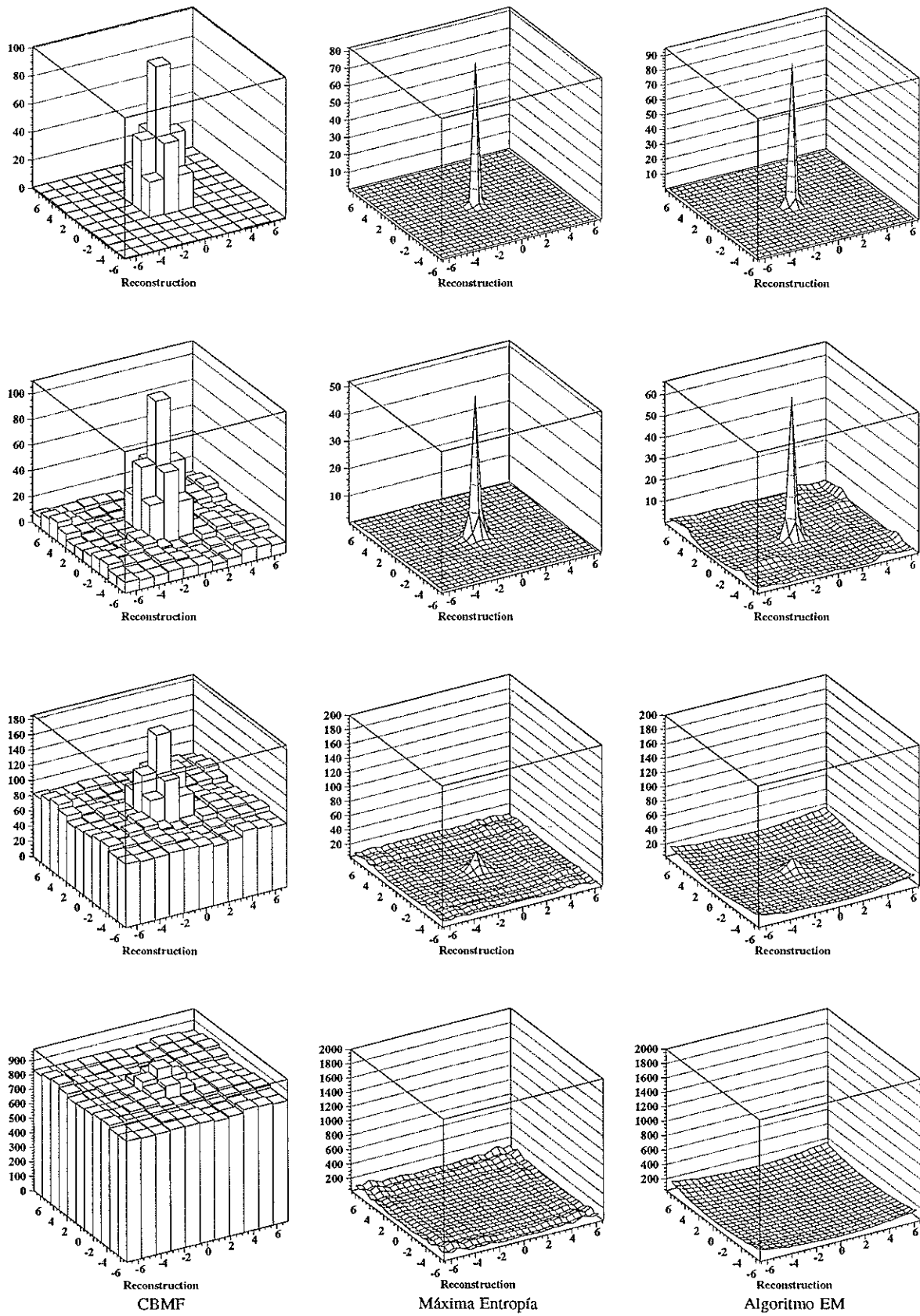


Figure 4.22: Effect of increasing the noise level in the signal.

Using FSBC, the main effect that the noise has in the reconstructed image is that, as the detector plane noise level increases, the reconstructed source (with an intensity of ~ 100 photons/cm²) appears "floating" in a fluctuating background that is bigger each time, as a small floating island in a sea more stormy each time, added to the reconstructed background (even with really big noise levels, one can still see the source in the centre). To emphasize this phenomenon we have used, instead of the surfaces map representation, a variation of it, called *lego* representation (the surfaces map representation assigns a point -a reticle crossing- for each image pixel, while the *lego* representation assigns a whole square; in both cases, the height is proportional to the intensity).

Regarding the maximization methods, the observed phenomenon is that, as the noise level increases (and the statistical significance of the signal decreases), the reconstructed source gets wider and its height decreases. Indeed, for a noise of 10, 100 and 1000 counts/cm², the reconstructed intensity of the central pixel is, for the maximum entropy method, 82.1, 52.1 and 31.5 photons/cm², respectively, and for the EM algorithm, 95.1, 66.4 and 21 photons/cm²; in both cases the signal is widened (it takes more pixels); for a noise of 10000 counts/cm², it is not possible to see any source (**note:** for the cases with 1000 and 10000 noise counts/cm² and only in the case of maximum entropy and the EM algorithm, we have put an upper limit to the height in the representation, of 0.2 times the order of detected counts in the detector plane; that is, 200 and 2000 respectively. If we suppose that the detected counts come from a true sky signal, one expects that its intensity has to be of the order of the detected signal; if with this upper limit does not appear any peak in the reconstruction, it is because the detected signal is mainly noise).

On the whole, the capability for detecting the presence or absence of a source will depend on if the counts coming from the real source are confussed with the noise. The statistical noise fluctuation is given by the square root of the counts due to noise (poissonian statistics); therefore, if the source intensity is slower than this statistical fluctuation, the source will be confussed with the statistical noise fluctuation and will not be possible to detect it. This means that our practical limit to detect a sky source is given by:

$$Intensity \leq \sqrt{Noise} \quad (4.12)$$

The obvious method to improve our detection capability will be, of course, to increase the measurement time, increasing then the count number but improving (decreasing) the statistical data fluctuation (the noise fluctuation increases with \sqrt{B} , but the counts increase with B , therefore the relative fluctuation decreases with $1/\sqrt{B}$). This may allow us to see sources that were hidden by the statistical noise fluctuation and, as the counts increase, they appear (see a more detailed discussion about sensitivity in chapter 5).

As regards to the structures that appear in the background, we see that for a noise of 10 counts/cm², the background is very flat in any case. With a noise of 100 counts/cm², the background is flatter in the maximum entropy method, as it is expected in principle, while in the EM algorithm some structures appear, similarly to the previous section; for FSBC, the background simply oscillates. **But** we observe that as the noise increases (1000, 10000), the situation *is reversed* and unexpected fluctuations appear in the background image in the case of maximum entropy, while the background in the EM algorithm image is smoother (FSBC still simply oscillates).

For the EM algorithm, as the counts increase (decreasing, therefore, the statistical data fluctuation and being more similar to a flat case -without fluctuation-), also the fluctuations in the reconstructed image decrease, and so the fake images; in the case of a 10 counts/cm² noise, the fluctuation is there, but since the background is so weak, it is inconsiderable compared to the reconstructed source of 100 photons/cm², and it can not be observed, while in the case of a noise of 100 counts/cm², both noise and source are similar.

On the contrary, with the maximum entropy method, the structure due to the noise increases as the noise level increases.

4.8.2 Noise with structure

Let us force a little more the reconstruction methods. We have considered in 4.8.1 that the noise in the detector plane, except for the statistical fluctuation, was flat; but this could not be like that. For example, the telescope can become a noise source due to the radiation that will suffer in the space (as it will occur; see section 1.6.1), and the structural elements can become a source that will introduce in the detector plane a non-uniform noise (for example, the armour plating surrounding the detector unit). To

simulate such effect in LEGRI, we have generated with our simulator a noise in the detector plane decreasing from the detector plane borders (nearer to the armour plating) to the centre. We have generated a poissonian noise with mean value of ~ 300 counts/cm² for the most external detectors, ~ 200 counts/cm² for the following detectors, ~ 100 counts/cm² for the next level, and ~ 50 for the four central detectors (this values do not come from any place but are just an exercise). We have added a source in the field of view centre with an intensity of 100 photons/cm². The detected result is shown in figure 4.23.

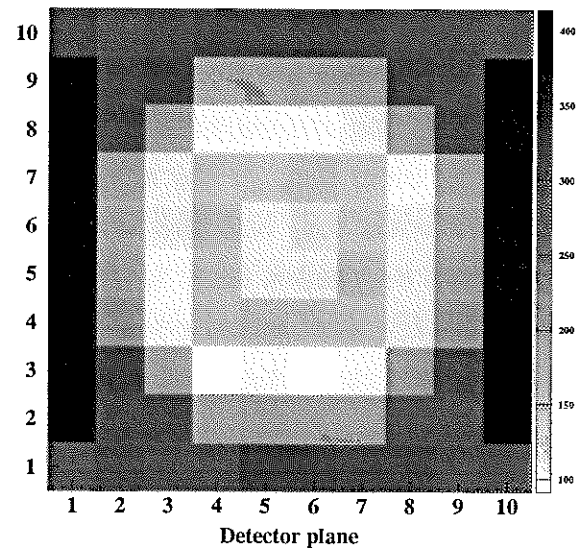


Figura 4.23: Señal en el plano detector con ruido variable más una fuente centrada de 100 fotones/cm².

The reconstruction from this beautiful detector plane, using (from left to right) FSBC, maximum entropy and the EM algorithm, can be seen in figure 4.24. It can be observed in every case the appearance of two simetrical lobes, due to the structure of the detector plane noise, The obvious conclusion is that we can not forget the noise effect, it is very important to know it well and we have to include this information in some way in the reconstruction methods.

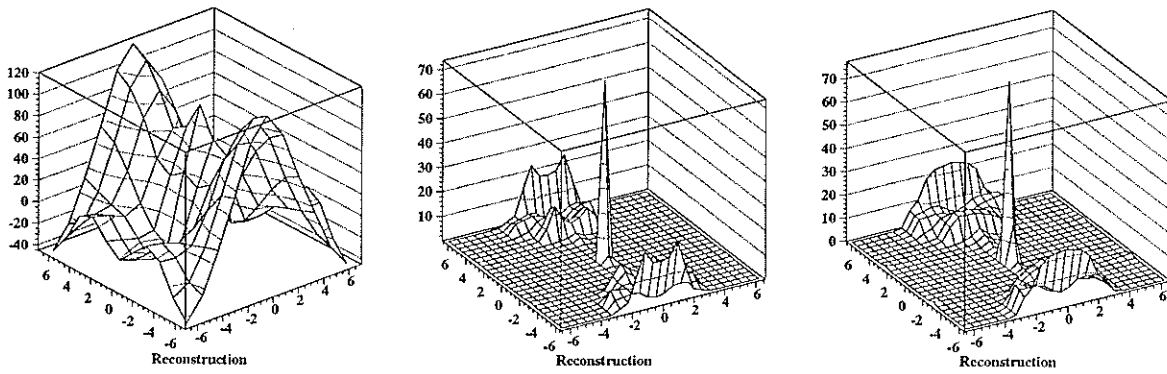


Figure 4.24: Reconstructions with variable noise in the detector plane

4.8.3 Extending the source space

A way of trying to improve the image that one could think if we do not know the noise structure, consists in extending the source space (See section 2.12.1) and including the noise as another parameter to be estimated from the data. We can only do this in the maximization methods.

If we suppose that the noise in the detector plane is constant, we can extend eq. 2.45 to include this noise as another unknown to estimate:

$$\tilde{D}_{ij} = \sum_{\alpha\beta} \tilde{O}_{\alpha\beta} \Phi_{ij}^{\alpha\beta} + B \tag{4.13}$$

The entropy is defined now by:

$$S = -\sum_{\alpha\beta} O_{\alpha\beta} \cdot \log O_{\alpha\beta} - B \cdot \log B \tag{4.14}$$

and the maximum entropy solution is given by equation 4.15.

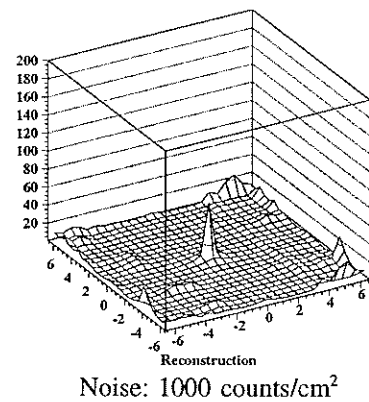
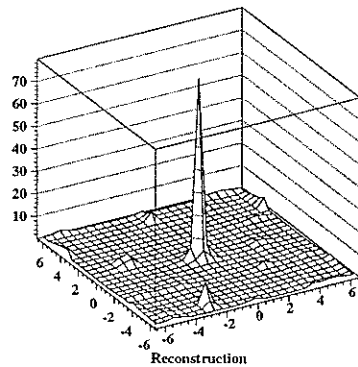
$$\begin{aligned} \tilde{O}_{\alpha\beta} &= e^{-1-2\lambda \sum_{ij} \Phi_{ij}^{\alpha\beta} \frac{(\tilde{D}_{ij}-D_{ij})}{\sigma_{ij}^2}} \\ \tilde{B} &= e^{-1-2\lambda \sum_{ij} \frac{(\tilde{D}_{ij}-D_{ij})}{\sigma_{ij}^2}} \end{aligned} \tag{4.15}$$

Similarly, for the EM algorithm, the iterative solution is shown in equation 4.16.

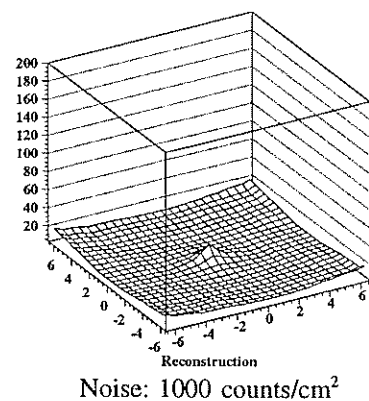
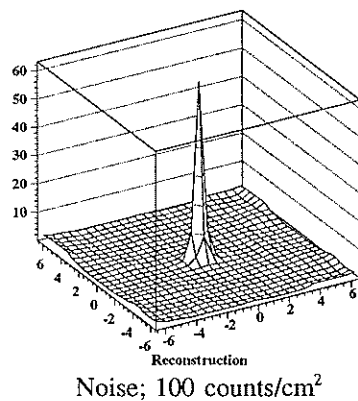
$$\tilde{O}_{\alpha\beta}^{n+1} = \tilde{O}_{\alpha\beta}^n \frac{\sum_{ij} \Phi_{ij}^{\alpha\beta} \left(\frac{D_{ij}}{\tilde{D}_{ij}^n} \right)}{\sum_{ij} \Phi_{ij}^{\alpha\beta}} \quad (4.16)$$

$$\tilde{B}^{n+1} = \tilde{B}^n \frac{\sum_{ij} \left(\frac{D_{ij}}{\tilde{D}_{ij}^n} \right)}{100}$$

where 100 refers to the number of detector plane units. Applying both algorithms to the cases we studied in section 4.8.2, this is, constant noise in the detector plane, with values 100 and 1000 counts/cm², plus a centred source with intensity 100 photons/cm², we get the reconstructions in figure 4.25.



Maximum entropy



EM Algorithm

Figure 4.25: Reconstructions estimating a constant noise B

We can observe that we have now undesired structures in the images obtained with the maximum entropy method that do not correspond to any real source, although the central source intensity reconstruction is, indeed, quite better. The estimation of the central source intensity, when the noise in the detector plane is 100 counts/cm², is now 79.9 photons/cm² (in the previous case, when we did not estimate the noise, it was 52.1) and the estimated detector plane noise is 7 counts/cm² (not very good). In the case when the noise in the detector plane is 1000 counts/cm², the estimation of the central source intensity is now 63.6 photons/cm² (in the previous case it was 31.5) and the estimated noise is 600 counts/cm² (better).

About the EM algorithm, the only result that deserves to be emphasized is that the background fluctuations in the reconstructed image are smaller (in this respect, the image has improved), while the reconstructed intensity is basically the same: when the noise in the detector plane is 100 counts/cm², the estimated intensity of the central source is 63.3 photons/cm² (in the previous case it was 66.4) and the estimated noise is 0.8 counts/cm²; when the noise in the detector plane is 1000 counts/cm², the estimated intensity of the central source is 21.5 photons/cm² (in the previous case it was 21) and the estimated noise is 6.5 counts/cm².

Of course, this method can only be applied if we have good reasons to think that the noise in the detector plane is flat and it can be represented by a single B parameter. For example, in the case where the noise varies and increases from the centre to the border of the detector plane (fig. 4.23) it is no licit to do this approximation.

Therefore we are going to extend equation 4.13 and we are going to consider a variable noise B_{ij} as additional unknowns to be estimated. Then, eq. 4.13 will be now:

$$\tilde{D}_{ij} = \sum_{\alpha\beta} \tilde{O}_{\alpha\beta} \Phi_{ij}^{\alpha\beta} + B_{ij} \quad (4.17)$$

With this extension of the unknowns to be estimated, the entropy is now defined as follows:

$$S = -\sum_{\alpha\beta} O_{\alpha\beta} \cdot \log O_{\alpha\beta} - \sum_{ij} B_{ij} \cdot \log B_{ij} \quad (4.18)$$

and the maximum entropy solution is now given by equation 4.19.

$$\begin{aligned} \tilde{O}_{\alpha\beta} &= e^{-1-2\lambda \sum_{ij} \Phi_{ij}^{\alpha\beta} \frac{(\tilde{D}_{ij} - D_{ij})}{\sigma_{ij}^2}} \\ \tilde{B}_{ij} &= e^{-1-2\lambda \frac{(\tilde{D}_{ij} - D_{ij})}{\sigma_{ij}^2}} \end{aligned} \quad (4.19)$$

Similarly to the previous case, the iterative solution of the EM algorithm will be the following:

$$\begin{aligned} \tilde{O}_{\alpha\beta}^{n+1} &= \tilde{O}_{\alpha\beta}^n \frac{\sum_{ij} \Phi_{ij}^{\alpha\beta} \left(\frac{D_{ij}}{\tilde{D}_{ij}^n} \right)}{\sum_{ij} \Phi_{ij}^{\alpha\beta}} \\ \tilde{B}_{ij}^{n+1} &= \tilde{B}_{ij}^n \left(\frac{D_{ij}}{\tilde{D}_{ij}^n} \right) \end{aligned} \quad (4.20)$$

We are now going to apply these modified algorithms to the cases previously described in sections 4.8.1 and 4.8.2 when the telescope was illuminated by a source with an intensity of 100 photons/cm² and the detector plane had a noise (a) flat of ~100 counts/cm², (b) flat of ~1000 counts/cm² and (c) variable of ~300 counts/cm² in the border and decreasing until ~50 counts/cm² in the centre. In figures 4.26 and 4.27 are shown the results: the column on the left corresponds to the case (a), the one on the middle to the case (b) and the one on the right to the case (c). Figure 4.26 corresponds to the maximum entropy method (the first row shows the sky intensities estimation and the second row shows the detector plane noise estimation); similarly, figure 4.27 corresponds to the EM algorithm.

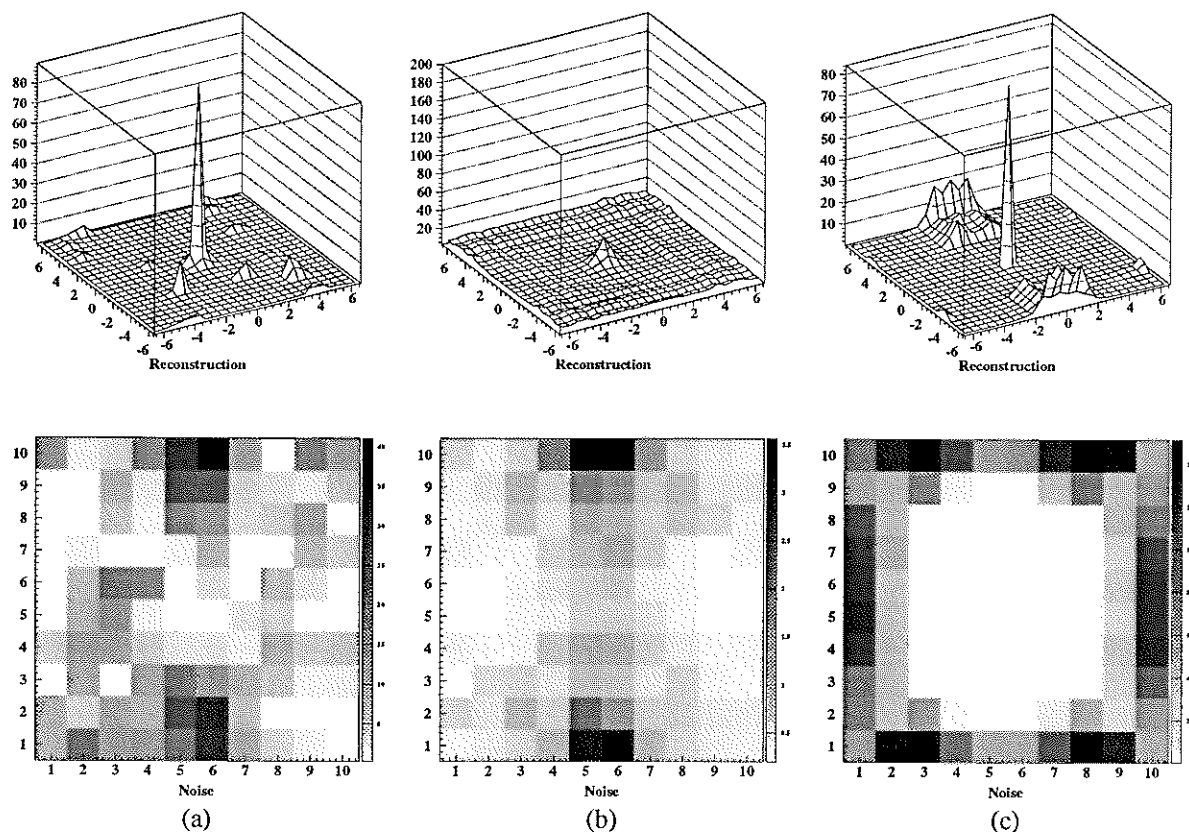


Figure 4.26: Reconstructions estimating a variable noise B_{ij} , and detector plane noise estimations with the maximum entropy method

Beginning with the maximum entropy method, we see that increasing the freedom degrees (by adding the noise estimation as a part of the problem) has a similar effect to the previous case (in which we estimated a constant noise B): we have some undesired structures in the image, but the source intensity estimation on the whole is better (although in case (b) the difference with the original method -without any noise estimation- is not very big). The reconstructed intensities are, for (a) 90 photons/cm², for (b) 32 photons/cm² and for (c) (variable noise) 84.4 photons/cm². We can see that the noise estimation is relatively good, and it *a grosso modo* reproduces the noise structure (although not its magnitude). That is, if we have no way to know the noise structures in our detector plane, this could be a good tool to have a first estimation of it.

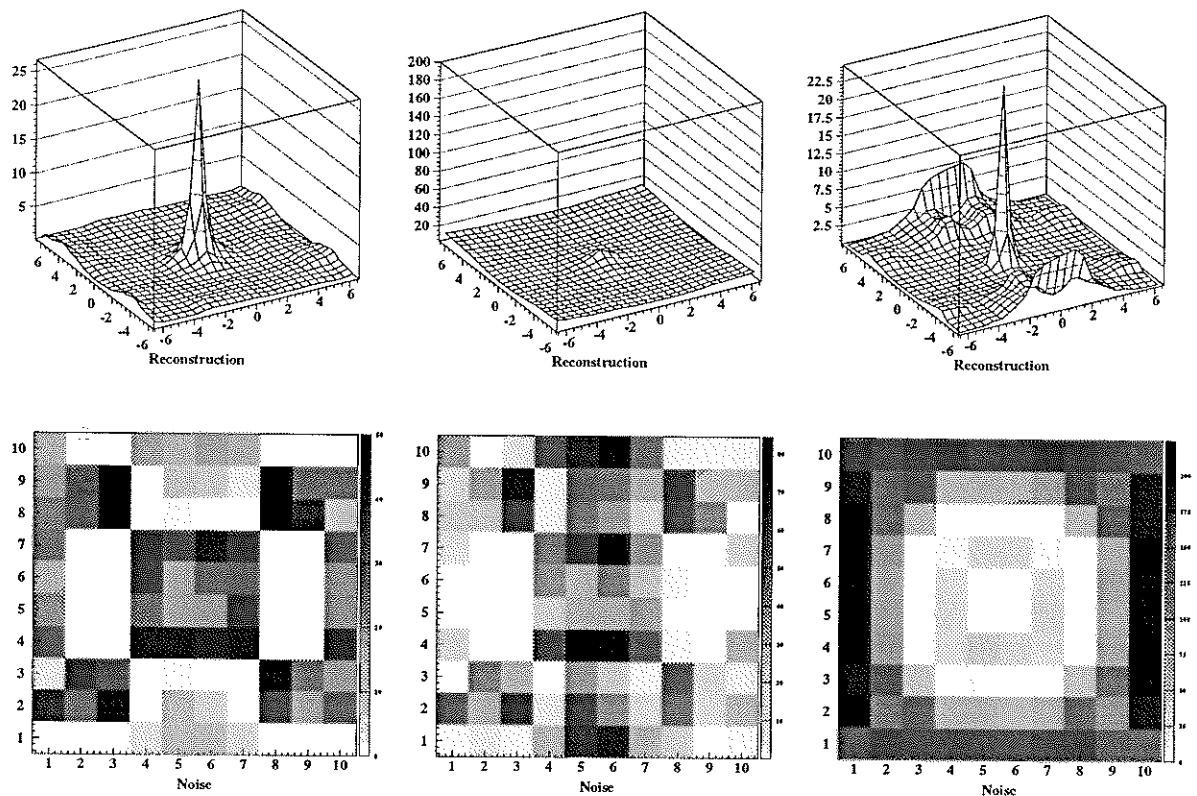


Figure 4.27: Reconstructions estimating a variable noise B_{ij} , and detector plane noise estimations with the EM algorithm

About the EM algorithm, the failure is complete. The peak is more widened, the intensity reconstruction has worsened (for (a) it is 26.7 photons/cm², for (b) 15.8 photons/cm² and for (c) 24.8 photons/cm²) and now there are some new structures in the background. This is because the EM algorithm "thinks" that the best noise estimation in the detector plane is one *which reproduces what is detected in the detector plane*; indeed, if we compare the noise estimations in the cases (a) and (b) with figure 4.11, and the noise estimation in the case (c) with figure 4.23, we see that the noise estimations reproduce the whole **detected signal** and not only the counts due to noise. Introducing these counts in the noise estimation subtracts information to the detected signal for the sources estimation, and so the reconstructed image is worse. We can try to improve the image using as initial value for the noise a more realist noise estimation (for example, the mean value of the detector plane instead of an array of 1's). But this does not alter the result; both methods converge to the same final result.

4.8.4 Improving the results

The methods explained in section 4.8.3 can be useful when we do not know the noise structure. Nevertheless, it is a better way if we can have a good knowledge of the noise structure instead of trying to find it out using these methods. It is possible to study and know the noise structure in our detector plane simply by studying sky zones where there are not gamma sources (or where the sources are too weak for our detector) during enough time. This will give us a good model of the expected noise in the detector plane which will be useful to correct the measurements done with real sky sources. This is possible because, as it was said in section 1.6.1, the prevailing noise in LEGRI will be given by the radiation induced by South Atlantic Anomaly (S.A.A.) which will arrive to a saturation point; therefore from that moment we will have a constant (in time) noise in our detector plane.

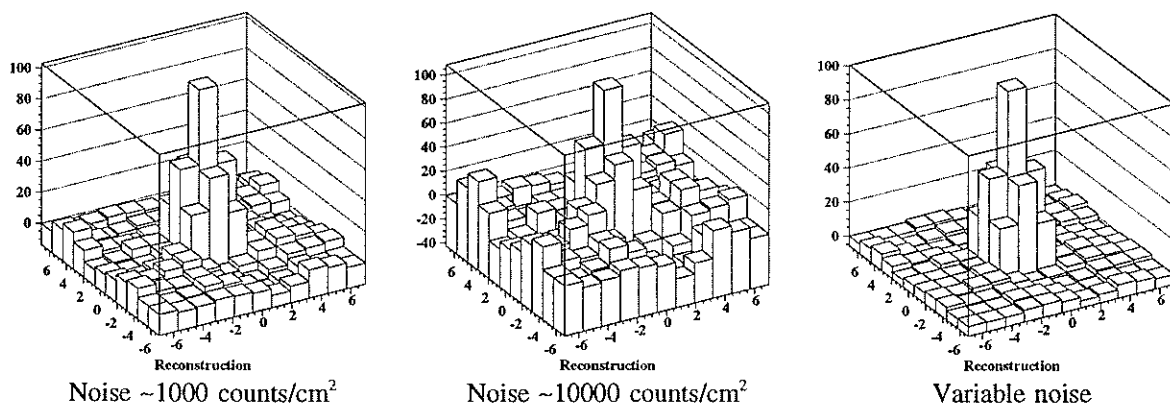


Figure 4.28: Reconstruction with FSBC once subtracted to the detector plane a noise model

Once we have a good detector plane noise model, the first method one could think in order to correct the noise effect in the data is, simply, to subtract the model to the data, and to use this so modified detector plane as input for our reconstruction methods. This will give good results when using correlation methods, but fails when using maximization methods although it is due to different causes. In figure 4.28 it is shown the reconstruction using FSBC for

the cases with a noise of ~ 1000 counts/cm², ~ 10000 counts/cm² and a variable noise (with the structure described in section 4.8.2), but subtracting to the detector plane a noise model, previously to reconstruct. The subtracted model is, respectively, 1000 counts/cm² in the first case, 10000 counts/cm² in the second and from 300 counts/cm² in the external detectors to 50 counts/cm² in the internal detectors; that is, the noise we previously had inserted, but without considering the statistical fluctuation. As it can be seen in figure 4.28, the reconstructed image has really improved. But if we do the same with the maximization methods (this is, we subtract to the detector plane a noise model and use this so corrected data as an input in the algorithm), the method fails as we have said. In the case of the maximum entropy method, this is simply because we are acting wrongly, as now eq. 2.44 is converted in:

$$\tilde{O}_{\alpha\beta} = e^{-1-2\lambda \sum_{ij} \Phi_{ij}^{\alpha\beta} \frac{(D_{ij}-D'_{ij})}{\sigma_{ij}^2}}$$

being $D'_{ij} = D_{ij} - B_{ij}^{model}$

(4.21)

but given that $\sigma_{ij} = \sqrt{D_{ij}}$

then $\sigma'_{ij} = \sqrt{D'_{ij}}$!!

that is, when we use the corrected plane as an input in the algorithm, we are underestimating the experimental errors and (again) we are introducing fake structures in the image [29]. But it is a different (and worse) story for the EM algorithm, because the input D'_{ij} can be now negative! (as it can be seen in the definition in eq. 4.21) and therefore (see eq. 2.56 and 2.57) the non-negativity of the solution is seriously altered; not only that, but even the convergency is damaged! As we can see in figure 4.29, where we show the convergency on the reconstructed intensity and χ^2 , the good convergency of the algorithm that we might see in section 4.2.1 has been totally destroyed, and we can find intensity values that are **negative**. The studied example (shown in figure 4.29) is the case of variable noise in the detector plane, in which we have previously subtracted a noise model.

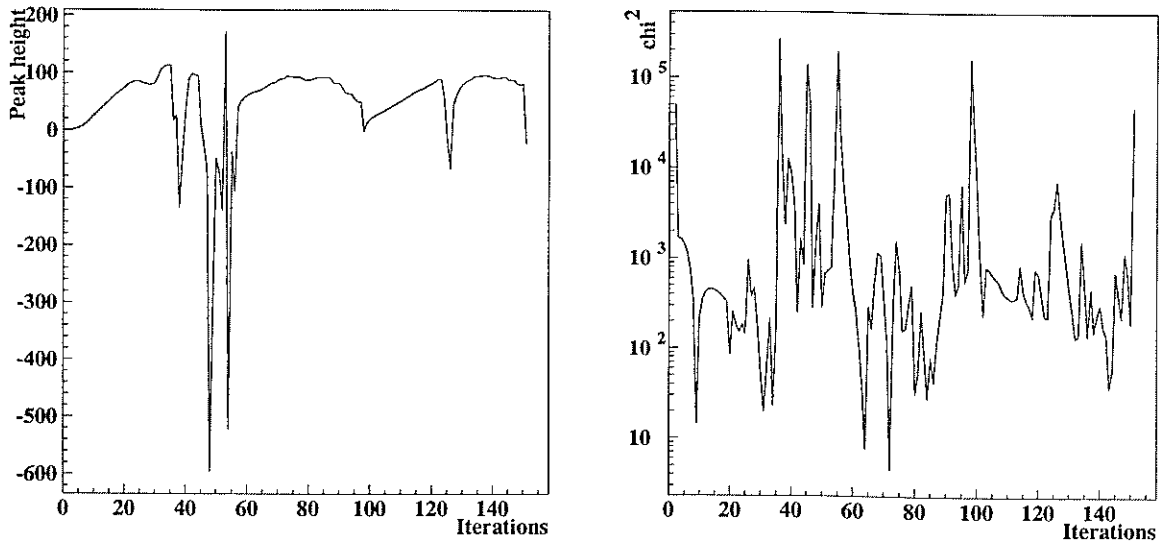


Figure 4.29: EM algorithm convergency of the central pixel intensity and χ^2 when a noise model is subtracted to the experimental data before the reconstruction.

The image reconstructed with the EM algorithm can be seen in figure 4.30. That is, if we previously subtract a noise model from the experimental data (method that gives good results with correlation-based reconstructions), the result is completely catastrophic when applied to the EM algorithm.

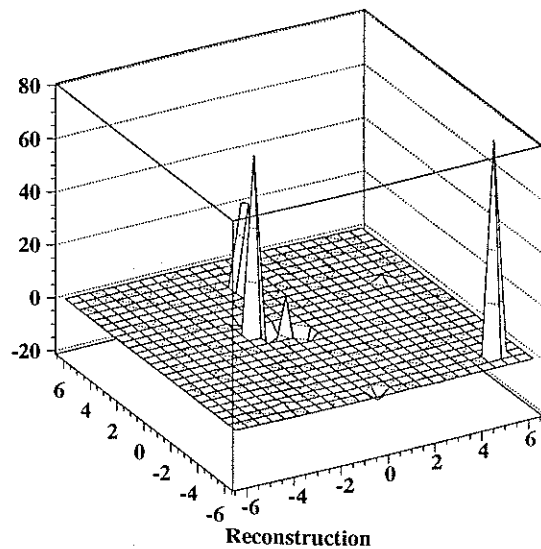


Figure 4.30: Image reconstructed with the EM algorithm when a noise model is subtracted to the data before reconstruction.

Nevertheless, not everything is lost; we can include the noise model in the algorithm but as part of the **detector response**. That is, instead of modifying our experimental data D_{ij} , we modify its estimation (given by eq. 2.45) according to:

$$\tilde{D}_{ij} = \sum_{\alpha\beta} \tilde{O}_{\alpha\beta} \Phi_{ij}^{\alpha\beta} + B_{ij}^{modelo} \tag{4.22}$$

If we implement this in the maximum entropy model, we see that we have corrected the small failure we did in eq. 4.12, because the sum in the exponent is the same as before (then we subtracted the noise from the real data and now we add it to its estimation, but as both are subtracted, the final result is the same). In the denominator we have now the correct error value, because we have not corrected the detector plane counts. About the EM algorithm, now we have again the non-negativity of the solution; everything is again positive, and the algorithm converges again. The results obtained once the noise model has been included as part of the detector response, are shown in figure 4.13; from left to right it is shown the reconstruction for the well known cases with a noise of ~ 100 counts/cm², ~ 1000 counts/cm² and variable noise. At top of the image the results using the maximum entropy method are shown, and at bottom the results using the EM algorithm.

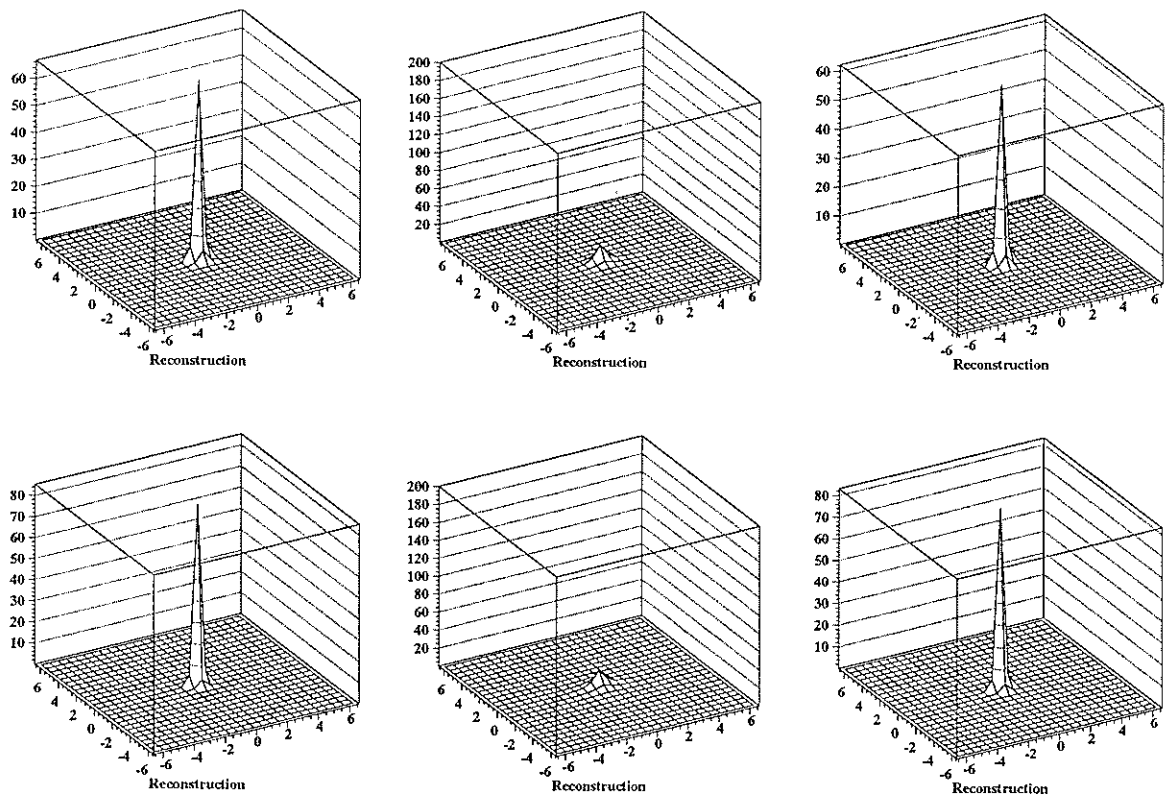


Figure 4.31: Reconstructions including the noise model as a part of the detector response

As it can be seen, now we have eliminated **absolutely** the structures due to the noise, and can clearly be seen a peak in a flat background. The reconstructed intensities for the maximum entropy case are: 66.8 photons/cm² (for a noise of ~100), 19.3 photons/cm² (for a noise of ~1000) and 62.31 photons/cm² (for a variable noise); respectively, for the EM algorithm case, they are: 85.7 photons/cm², 18.9 photons/cm² and 83.22 photons/cm². As it can be seen, for the EM algorithm this is the best way to avoid the noise effect. Although in the maximum entropy method we had a better intensity source reconstruction when estimating B_{ij} , there were anyway undesired structures in the reconstructed image, mainly in the variable noise case (the sidelobes in the image appeared whether we estimate the noise or not, even though if we had quite a good estimation of the noise values).

But have the structures due to noise really disappeared? or are they just so small that when compared with a true signal are negligible? what will happen when we try to reconstruct an image of a sky zone where there are not sources? will we get fake images due to the noise?

To test it, we have put in the detector plane a poissonian noise with a value of ~100 counts/cm² and another of ~1000 counts/cm², both in absence of signa. We have reconstructed the signal *implementing* the correct noise model in the algorithms, and the results can be seen in fig. 4.32; the top of the image shows the results for maximum entropy and the bottom for the EM algorithm; from left to right, the noise value is ~100 and ~10000 counts/cm².

Since a signal must be bigger than the statistical noise fluctuation to be detectable (this fluctuation is given by the square root of the counts), we have used the square root of the noise value as the maximum value for the representation; that is, respectively, 10 and 100. If a signal is detectable, this will be its minimum expected intensity in the reconstruction (this is a stronger constraint than the one we have used before using 0.2 times the mean detected value as upper limit, and more accurate; therefore, if there were some real source it would now be seen clearly).

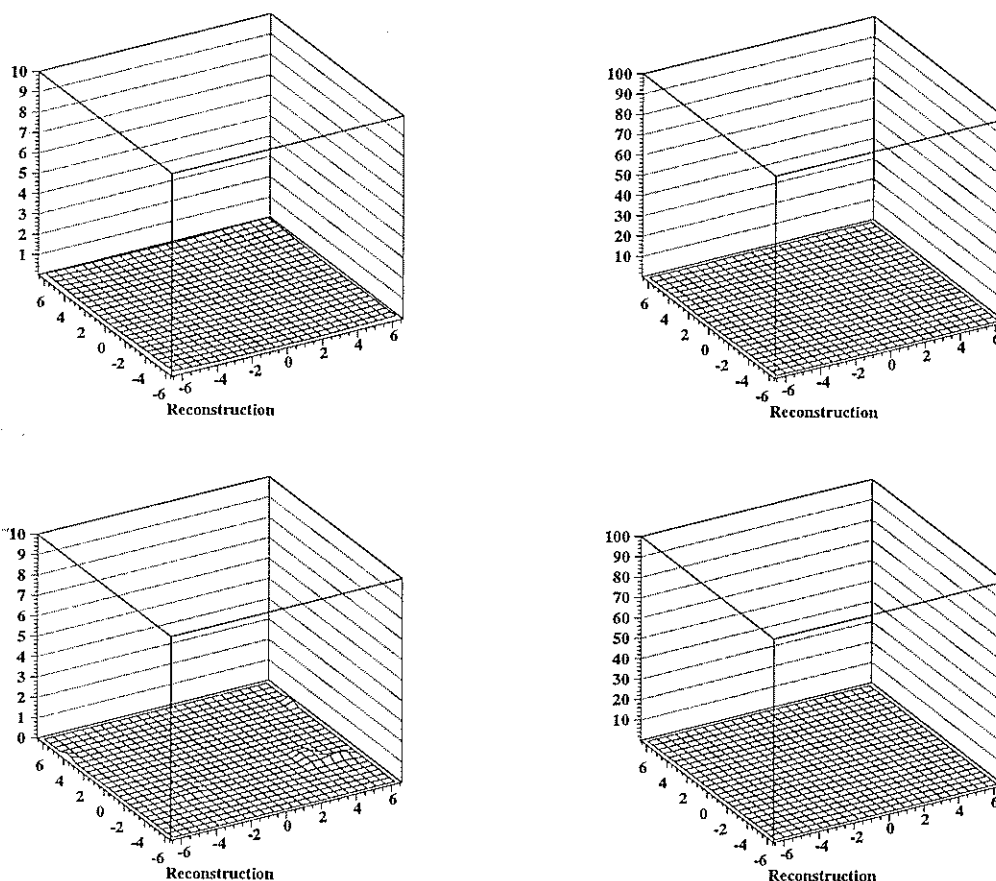


Figure 4.32: Reconstruction in absence of source and in presence of noise, using a model of it

One can see that, for the EM algorithm, in the case of low noise (~ 100 counts/cm²) there are some structures (with an intensity of the order of 0.3 photons/cm²) because of the statistical noise fluctuation; this fluctuation disappears when the noise is stronger and the relative fluctuation is thus smaller (this can be achieved by increasing the measure time). In all the other cases we can not see any structure that could be confused with a real signal; this means that a good knowledge of the noise structure eliminates any ghost source due to it (although any reconstructed source can be identified as a ghost source due to the noise or as a real source simply by varying the pointing direction of the telescope; if it is a true source, it will move in accordance to the pointing change. Anyway, although we could identify true sources by varying the pointing direction, it is better to have an image as good as possible).

Therefore, our conclusion will follow the old maxim "If you can not defeat your enemy, join him", that is, the best way to correct the noise effect and avoid its influence is to know it well (studying sky zones where there are not sources) and afterwards subtract its influence to the data.

What we have done in this section is a particular case of fixing the value of certain pixels and maintaining them invariable in each iteration; in this case, following the idea of section 4.8.3 (in which we included the noise as parameters to be estimated) we have fixed the value of the "pixels" corresponding to noise to a certain value (the one of our noise model). We can always fix some pixels with a given value, so they do not change in each iteration, estimating only the remaining pixels (in fact this is what we do when we limit ourselves to the field of view defined by a mask cycle ($\pm 6.34^\circ$), because we fix to 0 the value of the pixels outside this field of view). This technique can be used to improve the image; for example, if we know with certainty that in a given pixel there is a source of known intensity, we can fix this value and iterate the remaining image to improve it).

4.9 Extended sources

Until now we have studied the behaviour of our telescope to (one or some) point sources. It is true that an extended source can be considered as made up of many point sources (when we use a discrete sky); but it is also true that when the sources are too near they suffer an overlap when reconstructing, or spread when the mask shadow does not match with the detector plane units, as we have checked. So, how will the telescope work when illuminated with an extended source? Could we reconstruct the source shape? And what about the intensities?

Therefore we are going to study the response of LEGRI to an extended source by illuminating it with the sky source that is shown in figure 4.33 (a), in absence of noise. This source we have generated has the shape of an **A**. In figure 4.33 (b) we can see the detected signal in the detector plane, and from

it we have reconstructed the image: figure 4.33 (c) with FSBC, (d) with δ -decoding, (e) maximum entropy methods and (f) the EM algorithm.

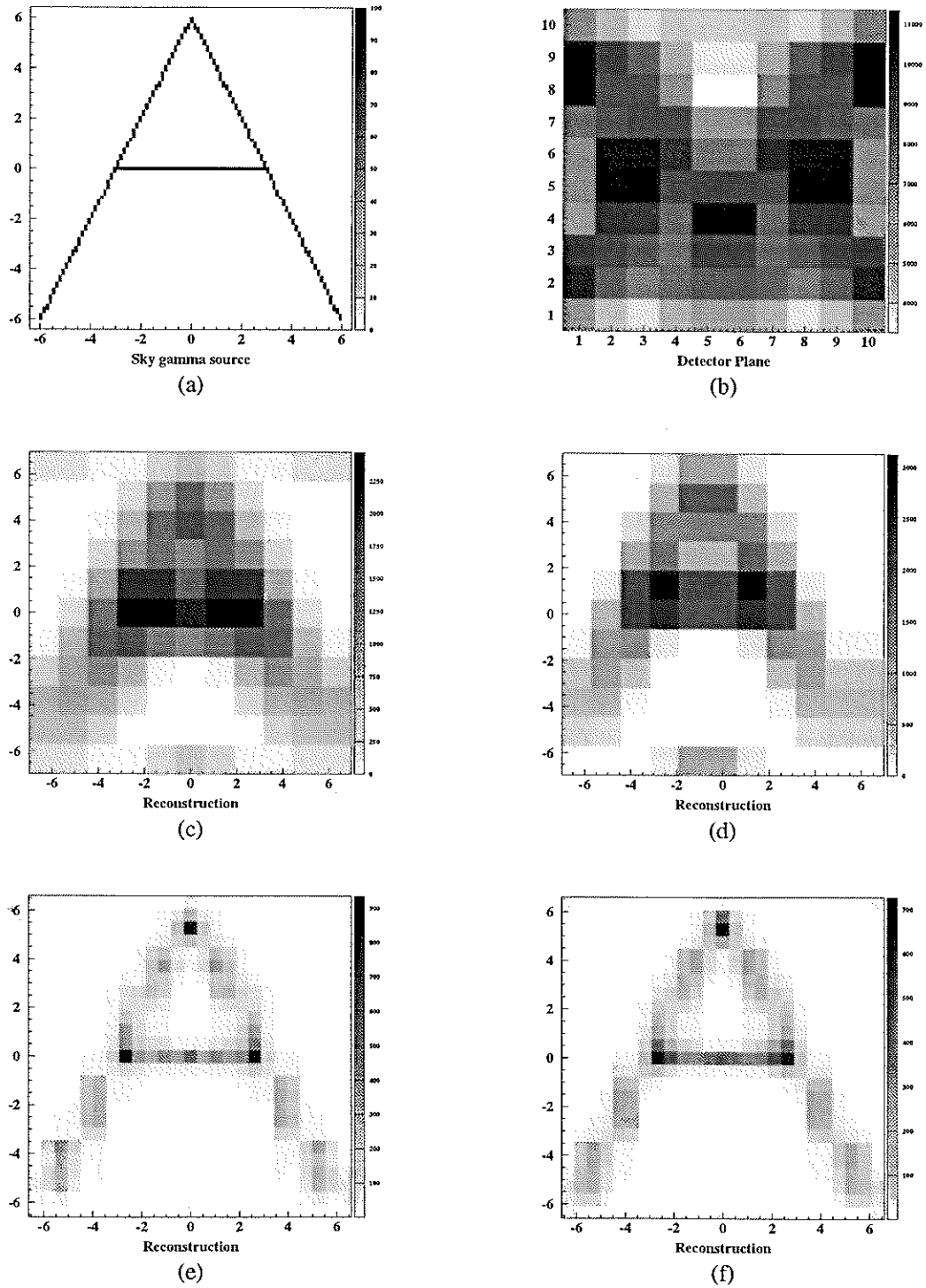


Figure 4.33: Detection and reconstruction of an extended source

These images have been done using the field of view defined by a mask cycle. As we can see, FSBC reconstructs something more or less similar to the source, although it is very blurred; the image is better with δ -decoding, because it has a better contrast. But the best results are obtained with maximization methods.

All the pixels in the source image have the same intensity: 100 photons/cm²; but the intensity in the reconstructed image is not uniform at all, it clearly favours some pixels; specifically, those positions that project a shadow which match with the detector plane units are favored.

4.9.1 Multiple pointing

If we want to improve the results, we need to obtain more information from the source. At the beginning of this work, one might ask oneself why we have not considered more classical methods that work successfully in other fields and problems, as for example the least squares method. In this method we fit some few parameters to a lot of data, all them following in principle the same law; this means that we have very few unknowns and very much data. Here the problem is just the opposite; let us evaluate the unknowns and data we have: our unknowns, that is the sky pixels, will depend on how finely we subdivide the field of view, but for example, in the results we have shown, when we limit ourselves to the field of view of a mask cycle ($\pm 6.34^\circ$) divided into pixels with an angular size of 0.64° , we have $20 \times 20 = 400$ pixels or unknowns (if we also try to evaluate the noise, we will have other 100 unknowns); on the other hand, our data are the measurements in each detector unit, that is 100 data.

Therefore we have 100 data for 400 unknowns to be estimated. Then, in principle we could not apply to our problem a least square method.

But there is a way to do that. We can increase the number of data we have, by doing different pointings in the same sky zone. That is, pointing to a zone, measuring during a certain time, shifting slightly the pointing direction,

measuring again, and so on. So in each pointing we have a different set of data. For example, doing nine pointings in the same zone, we have 900 data for 400 unknowns. The detected counts in detector ij during pointing p are given by equation 4.23.

$$D_{ijp} = \sum_{\alpha\beta} O_{\alpha\beta} \Phi_{ijp}^{\alpha\beta} \quad (4.23)$$

That is, the same old equation, but with an added index. But what are now α and β ? We have so far said that the co-ordinates were given by the telescope and were intrinsic to it; for each pointing we should have a different co-ordinates system. What we have to do is to choose **one** of them as reference pointing and take it as master co-ordinates system, referring the other pointings to this one (see figure 4.34).

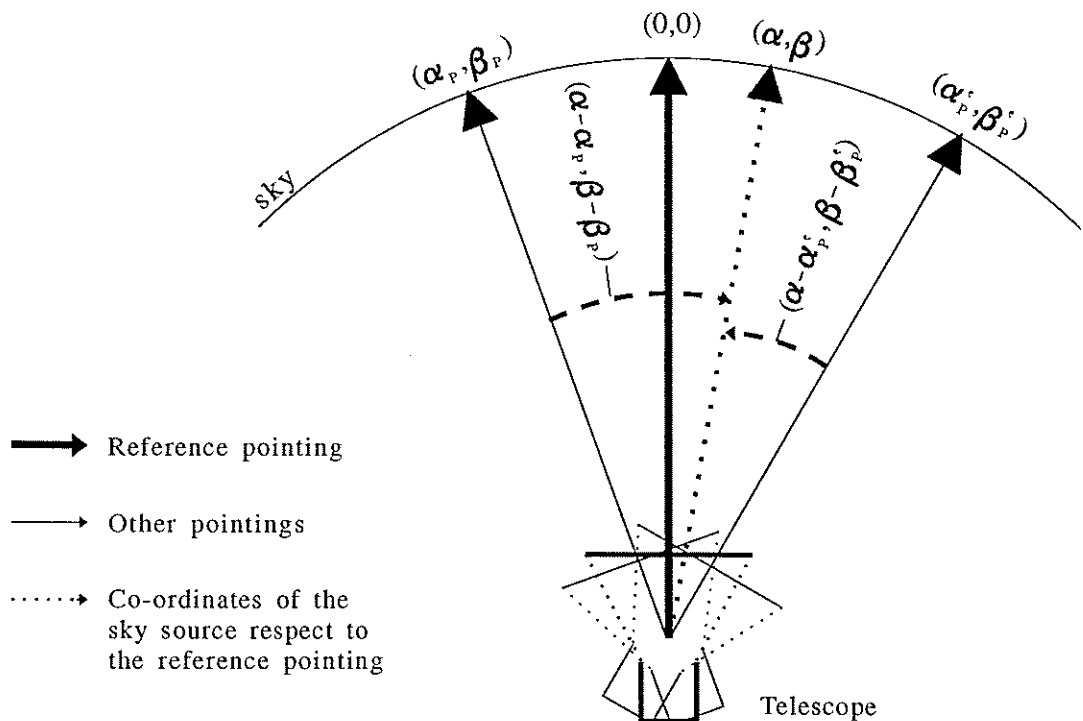


Figure 4.34: Different pointings in the same zone of the sky. We take one of them as master reference system

The sky source co-ordinates (α, β) are measured respect with to the reference pointing co-ordinates system. Likewise, (α_p, β_p) (the field of view centre of another pointing) is also measured with respect to the reference pointing

co-ordinates system. Therefore, the (α, β) coordinates of the sky source, with respect to the pointing p , are given by $(\alpha - \alpha_p, \beta - \beta_p)$ (this is not exactly true, but for pointings that are not rotated very far from the reference pointing -say $\alpha_p, \beta_p < 10^\circ$ -, this is an excellent approximation); that is, by:

$$\Phi_{ijp}^{\alpha\beta} = \Phi_{ij}^{\alpha-\alpha_p, \beta-\beta_p} \tag{4.24}$$

therefore, equation 4.23 is given by:

$$D_{ijp} = \sum_{\alpha\beta} O_{\alpha\beta} \Phi_{ij}^{\alpha-\alpha_p, \beta-\beta_p} \tag{4.25}$$

This equation is equivalent to the following linear equation

$$y^i = \alpha_1 \cdot x_1^i + \dots + \alpha_k \cdot x_k^i \tag{4.26}$$

just doing the equivalence $y=D, x=\Phi$ and $\alpha=O$. Taking several pointings, we can try to estimate the α parameters by means of a least square fitting. Applying it to the problem of the source with the shape of an **A** (figure 4.33 (a)), we have made nine pointings of the sky source, in a 3x3 grid (and without rotations; that is, all the α and β axis are parallel). The central pointing has been taken as reference co-ordinates system. The (α_p, β_p) co-ordinates of the other eight pointings (with respect to the central one) are:

-1, 1	0, 1	1, 1
-1, 0	0, 0 (master system)	1, 0
-1,-1	0,-1	1,-1

For the least square fitting of the so obtained data, we have used an standard mathematical calculation software, very used in physics: the CERN mathematical libraries (or cernlib [41]). Specifically, the used subroutine has been LINSQ, which carries out least squares fittings of linear functions. Previously the subroutine was tested in some typical least squares fitting problems, obtaining good results.

The disappointing result of the fitting for the parameters a (or what is the same, O) is shown in fig. 4.35; anyway it is still possible to glimpse the **A** shape.

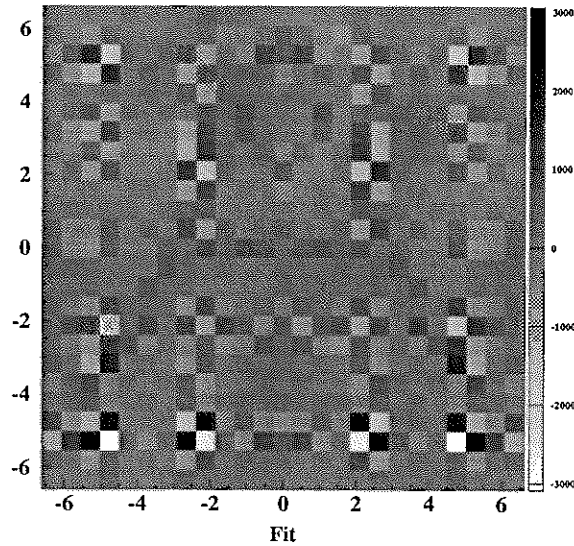


Figure 4.35; Reconstruction of fig. 4.31 (a) using a least squares fitting and nine pointings.

Conclusion: it is possible to apply a least squares fitting method, but with not very good results.

But, anyway, since we have used several pointings of the same zone, we have obtained more information from the source than what we had with a single pointing, and this means that, in principle, we ought to be able to obtain a better reconstruction. Therefore, we are trying to apply the multiple pointing method to our maximization methods, and to generalize them. This generalization will be very easy using equation 4.23, and so, the generalization of the maximum entropy iterative solution (given by eq. 4.10) will be:

$$\tilde{O}_{\alpha\beta}^{n+1} = \left(\frac{n}{n+1} \right) \tilde{O}_{\alpha\beta}^n + \left(\frac{1}{n+1} \right) e^{-1-2\lambda^n \sum_{ijp} \Phi_{ij}^{\alpha-\alpha_p} \cdot \beta-\beta_p} \frac{(\tilde{D}_{ijp}^n - D_{ijp})}{\sigma_{ijp}^2} \quad (4.27)$$

And similarly, the generalization of the EM algorithm solution (given by eq. 2.56) is now:

$$\tilde{O}_{\alpha\beta}^{n+1} = \tilde{O}_{\alpha\beta}^n \frac{\sum_{ijp} \Phi_{ij}^{\alpha-\alpha_p, \beta-\beta_p} \left(\frac{D_{ijp}}{\tilde{D}_{ijp}^n} \right)}{\sum_{ijp} \Phi_{ij}^{\alpha-\alpha_p, \beta-\beta_p}} \tag{4.28}$$

Applying these new algorithms to the nine pointings we have done before, looking at the source in fig. 4.33 (a), we get the results in figure 4.36 (on the left with the maximum entropy method and on the right with the EM algorithm).

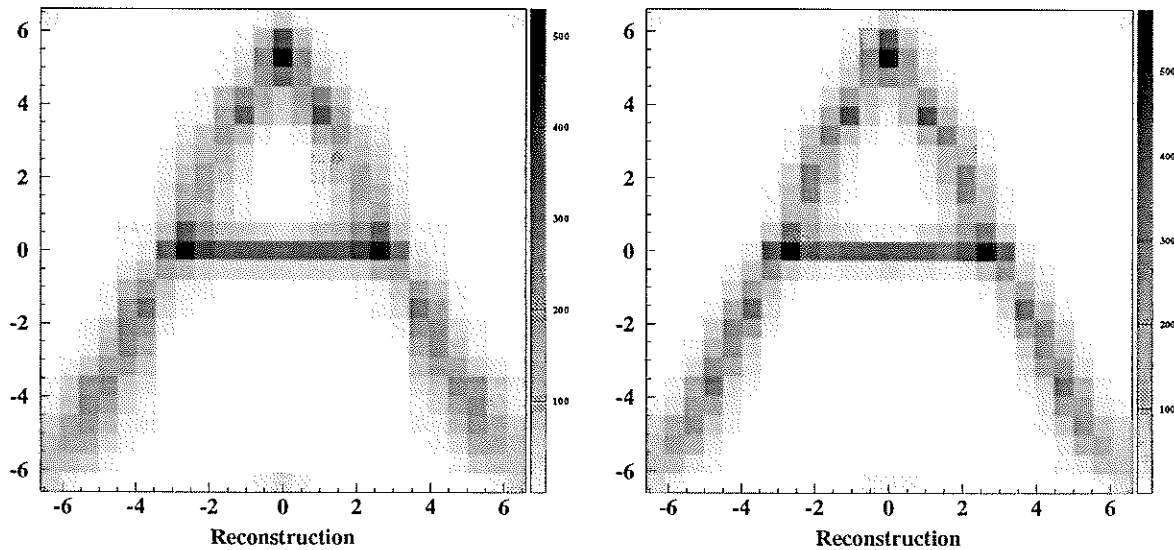


Figure 4.36: Reconstructions with the maximum entropy method and the EM algorithm, using nine pointings of the source in fig. 4.33 (a)

Now we can say "eureka"! The reconstructed image is now much better than when we did a single pointing (see fig. 4.33). As the pointing number increases (increasing therefore the information from the source), we indeed improve the reconstruction. The drawback is that now the reconstruction is slower: in the case of the EM algorithm, it takes nine times more time. But in the maximum entropy method it is worse; the absolute value of the sum in the exponential (that now takes nine times more time than before) is also about nine times bigger, and then, small fluctuations in the λ^n value produce fluctuations bigger than before, due to the magnification power of the

exponential. Therefore, these fluctuations must be counteracted by doing a finely sampling when seeking the correct λ^n value (typically, nine times finer), because otherwise it could not converge. That is, now the maximum entropy method takes $9 \times 9 = 81$ times longer.

As a final remark, let us say that if the pointings grid width were of 1.27° in place of 1° , we would have **not** additional information. We would have the same, but permuted (remember that 1.27° is the angle that a detector plane unit subtends from the mask) and thus the reconstruction obtained would *exactly* be the same we obtained with a single pointing.

4.10 Non-cyclic patterns

We have seen that using a cyclic mask pattern is a good idea when we reconstruct the image using correlation methods, thanks to the autocorrelative properties of the MURA and URA patterns, when the correlation is done cyclically. But, in fact, we have not used the MURA properties when reconstructing with maximization reconstruction methods (we have seen that these last methods give in general better results, and for simple telescopes as LEGRI can be absolutely competitive); in fact we have had more troubles than advantages with a cyclic mask when using maximization methods (mainly the ghosts, that for the EM algorithm means a weakening of the source, as the source intensity is shared out among the ghosts). That is why we are going to prove some non-cyclical masks, to study its behaviour and to check whether they could be preferable for LEGRI. Could this suppose a reappearing of the random masks for simple telescopes?

We have implemented three 14×14 random masks and a 19×19 MURA pattern (from which we have extracted a 14×14 piece) and illuminated the telescope with the sources in fig. 4.19 (but in absence of noise). In figure 4.37 the results are shown: in each row we see, on the left, the implemented pattern (the one on the bottom is the MURA), at the centre the reconstruction with the maximum entropy method, and on the right, the reconstruction using the EM algorithm.

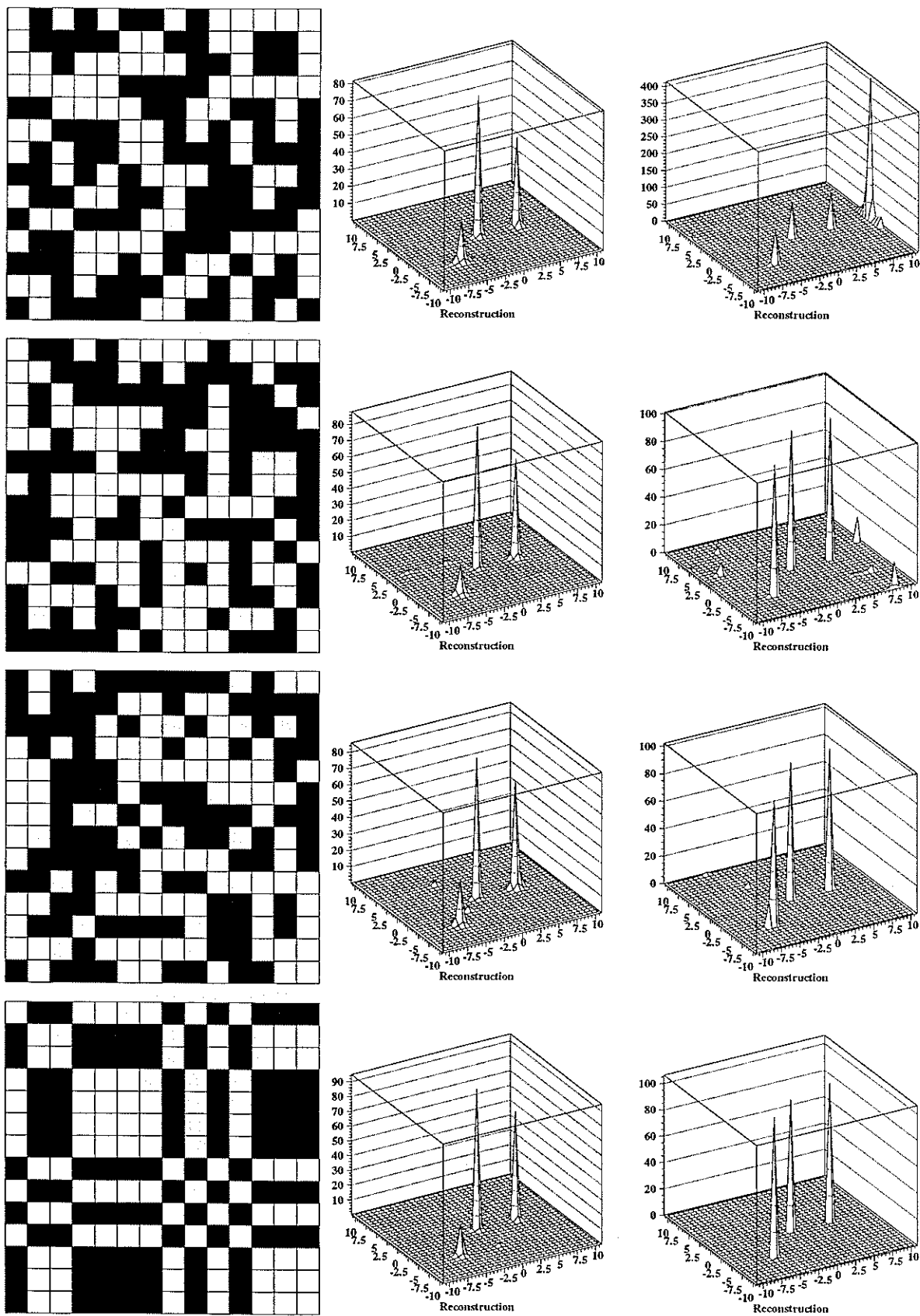


Figure 4.37: Reconstructions using different mask patterns

In this case, as in section 4.6, the image has been reconstructed using the whole field of view. As one can see, comparing these images with those of section 4.6, now we have no ghosts; or almost not. In the EM algorithm (the reconstruction corresponding to the first random mask), one can see an anomalous structure on the right, over the position (10,0); for the second random, the reconstruction has some small structures all over the image; the third mask is the random mask that produces better results. But when we use the MURA pattern we have a marvellous flat background without structures. For all the reconstructions using the EM algorithm, the intensities are properly reconstructed, giving ~ 100 photons/cm².

The maximum entropy method, in reference to ghost structures, has a better behaviour; in all the cases we have a similar image, with small background fluctuations which are smaller in the case of the first random mask (the background is very flat). Nevertheless it is again the MURA pattern the one that has the best results, since it reconstructs the sources intensity better than the other cases (note: contrary to the EM algorithm, the collimator affects the intensities when reconstructing with our maximum entropy method, even in absence of noise -as in this case-, as it was said in section 4.7).

Concluding this section, and as the maximization methods have more advantages than disadvantages in our case, it would be preferable a non-cyclic mask for LEGRI. And, although with a random pattern one can obtain good results, the best results are obtained with URA and MURA patterns, since in a random pattern, in different parts of the mask, subpatterns that are similar (just by pure hazard) can be produced, and they could produce ghosts.

4.11 Damaged detector plane

What would happen if the detector plane suffers some damage and some of the detector units were useless? Would the telescope lose the imaging capacity? To find the answer out, we have simulated this effect by "disconnecting" some detector units in our detector plane. Specifically, and

given that the electronics is common in each row of 10 detectors (in each U of the detector plane), and supposing a damage in the electronics, we have disconnected the U's number 1, 4 and 8. Besides in order to simulate a damage in particular detectors, we have also disconnected the detectors (2,5), (2,9), (3,1), (3,8), (6,4), (7,2), (9,7) and (10,2); that is, 38 detectors altogether (an important loss!). Illuminating the telescope with the sources in fig. 4.16 (those that were used in section 4.5), instead of what we got (see fig. 4.17), now we get what is shown in figure 4.38.

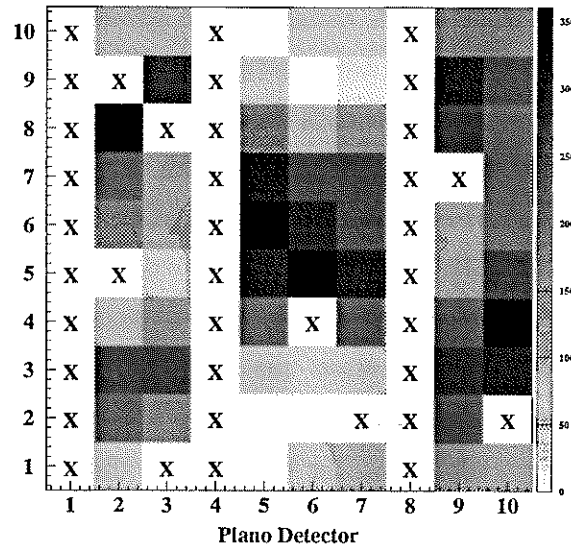


Figure 4.38: Detector plane with 38 detector units disconnected, marked with an X.

If we reconstruct the image from these data, we obtain the images in figure 4.29; from left to right, using FSBC, maximum entropy and the EM algorithm. In this example, as in section 4.5, we have not implemented any noise, so we can compare them with the reconstructions we obtained using a detector plane in perfect conditions.

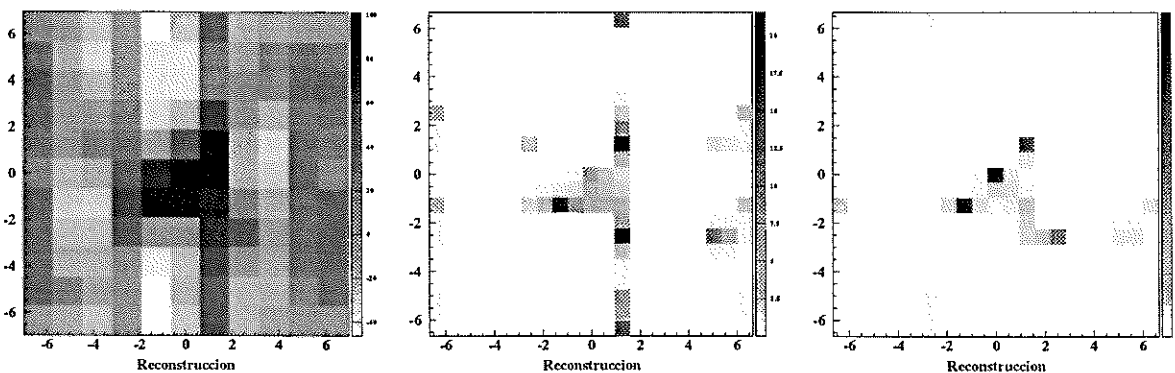


Figure 4.39: Reconstructions from the data obtained with 38 damaged detectors

We can observe that, in the case of FSBC, the autocorrelative properties of the MURA mask (that gave us a flat background where there were not sources) have been totally destroyed (compare this figure with figure 4.18). This is owing to the fact that we can not take into account all the detector units, and thus the 1's and -1's in the G array can not be made up for properly. In the image we obtain we can not make anything out.

The result obtained with the maximum entropy method is better, although anyway we still have fake structures in the image that do not correspond to a source; on the other hand, the reconstructed intensities are somewhat smaller (when all the detector plane worked, the intensities were ~ 90 photons/cm², and now they are ~ 20 photons/cm²). The best result is obtained with the EM algorithm, where we get less structures and the intensities are better reconstructed (before ~ 95 photons/cm² and now ~ 50 photons/cm²).

But we can try to improve this result. Why do these methods give worse results? Because we are taking into account the signal "detected" in the broken detector units (0) as a good value, as valid information; that is, we are deceiving the algorithm and we do not inform to it that the counts (the absence of counts) in those detectors must not be taken into account. Therefore, what we have to do is substituting in equations 2.56 and 4.10 the sum for all the factors with a sum including only the detectors that work properly. That is:

$$\sum_{ij} \rightarrow \sum_{ij \notin \text{damaged detectors}}$$

And what about the correlation? We do not need to do this kind of *bypass*, because it is done *automatically* and the obtained result is exactly the same both if we bypass those detectors or not; if we look at eq. 3.1 we see that, exactly those detector plane units with wrong information that we want to avoid, are avoided by themselves, because D_{kl} has a value of 0 and therefore the product $D_{kl} G_{k+i \ l+j}$ is not added to the sum.

It seems as if the same thing would happen with the EM algorithm in the denominator of eq. 2.56; but if we include the response (the lack of response) of those detectors that do not work, in the Φ array, we will have that all the Φ_{ij} , corresponding to broken detectors ij , will be 0 for all (α, β) and therefore the estimation of D_{ij} (that is dividing D_{ij}) will be 0; this means that we would have 0/0 if we do not do the *bypass*. The obtained result when avoiding the broken detectors can be seen in figure 4.40 (on the left for the maximum entropy method, and on the right for the EM algorithm).

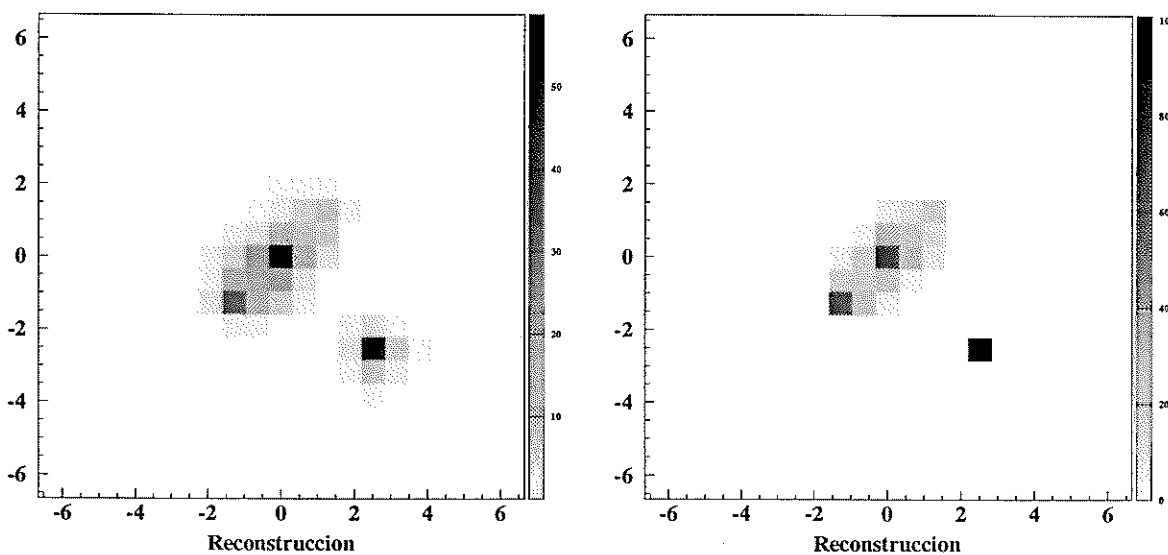


Figure 4.40: Reconstructions, once corrected the effect of the non-operative detector units

As it can be seen, in the case of the maximum entropy method, the image has improved a lot, and the anomalous structures that appeared in the image have been eliminated. The reconstructed intensities have also improved; now they are ~ 60 photons/cm². The same happens with the EM algorithm. The image is now very similar to the one we obtained when the detector plane worked properly (see fig. 4.18); the reconstructed intensities have also improved, being now ~ 100 photons/cm² (although when the detector plane was all right, the sources intensities were more similar among them than now). This is a great success for maximization methods, because one must consider that we have lost almost 40% of the detector area, and we can anyway reconstruct with these methods images with enough quality. The correlation methods have nothing to do in comparison to this case.

On the other hand, as we loose detectors, we are more sensitive to the noise effect and it is easier to generate fake structures, due to the loss of information; the more information is lost, the more possible is that the telescope structure appears in the reconstructed image. Of course, if we loose too much information, there is a moment when it is impossible to work. In an extreme case, if there is only a single detector working, for instance, the (5,6), the obtained "reconstruction" is the one shown in figure 4.41, for maximum entropy on the left and for the EM algorithm on the right.

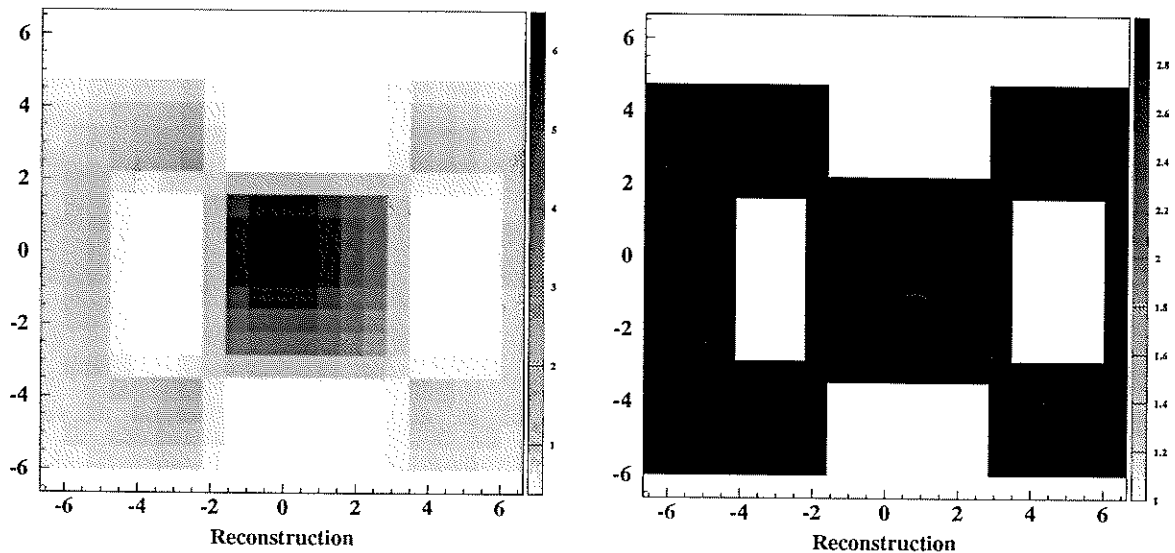


Figure 4.41: Reconstructions with a single operative detector

This means that the presence of counts in the only working detector leads the algorithms to deduce that a source exists in one of the possible sky positions from where light can arrive to the detector; i.e. passing through the mask holes. Therefore, given that all the directions where there are mask holes (seen from the single detector working) can be possible source positions, all of them appear in the reconstructed image. That is, the reconstructed image reproduces the mask pattern over the detector.

Chapter 5: Results. Real response of LEGRI

5.1 Introduction

All the results shown in chapter 4 have been obtained for an idealized LEGRI, with detectors with the same size (1 cm^2) and with an efficiency 1, and being all the non-opaque elements absolutely transparent. Nevertheless, as it was said in chapter 1, LEGRI is mainly an experiment of a new technology demonstration (the technology of HgI_2 and CdZnTe detectors; for the whole experiment, the most important is to study the response and behaviour of the detectors in space conditions).

With this we mean that the HgI_2 detectors were handcrafted detectors (there is not mass production line of detectors at the moment), and therefore there are not two identical detectors; each one has a different size (we do not have this problem with the 20 CdZnTe detectors, because they are commercialized). The response of each detector is also different, mainly due to problems with the flight electronics, which has a response more controversial than the laboratory ground electronics, because it is designed to support the launching and the space conditions at the same time that it must be compact and light. These conditions limit the electronics effectiveness. In fact, there are 15 unworkable detector units: the first detector in each U, due to the fact that the electronics is too noisy in them, and other five detectors that are almost "blind".

Besides, the *honeycomb* or mask tungstens support structure is not completely transparent, but it absorbs part of the γ photons that pass through. In this final chapter we have implemented the real instrument features (the honeycomb transparency, the real size of each detector, its real efficiency, etc...) in the geometrical simulator described in section 3.4, in order to study how the results of chapter 4 are altered; we also will show the real detector response (efficiency, sensitivity, spectral response...).

5.2 Detector response

When we have a discrete array of detectors as detector plane (or even a continuous position detector), the response of different detector plane zones against the same signal is not the same. In a discrete detector this means that two different detector units on the detector plane, with identical source and identical circumstances will measure different counts; this is magnified in our case because we will never have "identical circumstances" since we have not two equal detectors, as it can be seen in figure 5.1, where a picture of the LEGRI detector plane is shown (*a grosso modo*, the HgI_2 have a size about $5 \times 5 \text{ mm}^2$, although they vary quite a lot; the CdZnTe have a size of $10 \times 10 \text{ mm}^2$).

The efficiency is defined as the fraction "measured counts in a detector" / "photons arriving at the detector". In the ideal case, when so many counts as photons arrive at the detector are detected, the efficiency is 1. In the real case, the efficiency is always smaller than 1 mainly for two reasons:

i) The detector (unless it is big and/or masive enough) will not stop all the arriving γ photons, but there will be some of them that will pass through the detector without depositing any energy (and, since in our case the detectors are semiconductors, without producing hole-electron pairs). This implies that the intrinsic detector efficiency is smaller than 1. This is the efficiency one obtains with the Monte Carlo simulation, using the GEANT-3 code we described in section 3.4 (where we considered as *detected event* all those photons that deposit energy in the detector -over a certain threshold-).

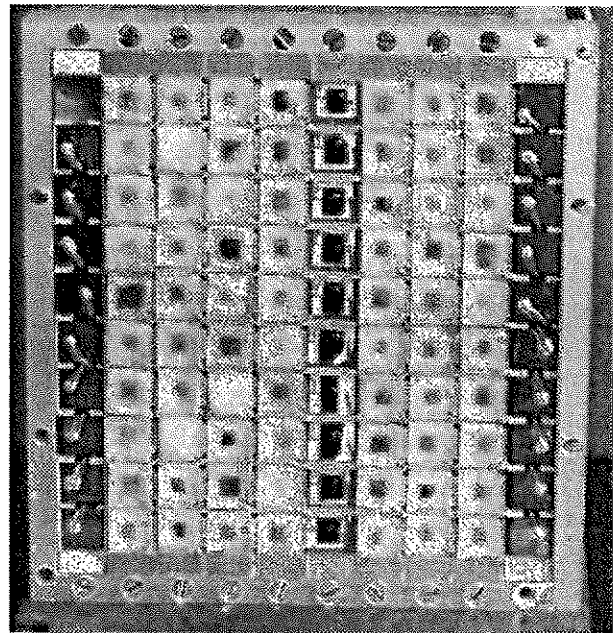


Figure 5.1: A picture of the LEGRI detector plane, without the collimator.

ii) Even so, the real detector will not give a signal for each photon that deposits energy, due to the electronics, which will no process properly **all** the events. This means that two identical detectors, with identical stopping power but different electronics will give a different efficiency depending on the signal processing electronics used. Not only that but also the electronics can produce (and will produce) ghost counts that will not correspond to any real photon (the so called electronic noise), and other things will also happen, as interferences between electronic channels, etc...

In our case we had **very much** better results when using the standard laboratory ground electronics than when using the flight electronics which, as it is compact and light (and resistant to acceleration and radiation) must sacrifice most of the good qualities of the ground electronics, needed for an ideal detection: the GEANT-3 simulations gave us efficiency values of about ~0.8 between 20 and 100 keV for both kinds of detector, results very similar to the obtained

with the laboratory ground electronics. On the other hand, the measured efficiency using the flight electronics is about ~0.3 for HgI_2 and about ~0.5 for CdZnTe, that are clearly worse. In figure 5.2 the measured efficiency in the LEGRI detector plane in the range 20-100 keV for photons is shown; the shown X and Y co-ordinates correspond to the internal co-ordinates of LEGRI; the equivalences with the co-ordinates used in chapter 4 (for example, in figure 4.17) are given by $i=10-Y$, $j=10-X$. One can see that the first detectors in each U (all those with $X=0$) does not work, and the same for other 5 detectors (all of them marked with an X); moreover there are other (as for example $X=7$, $Y=5$) that are almost blind. The 20 CdZnTe correspond to $X=0-9$ $Y=0$ and $X=0-9$ $Y=9$.

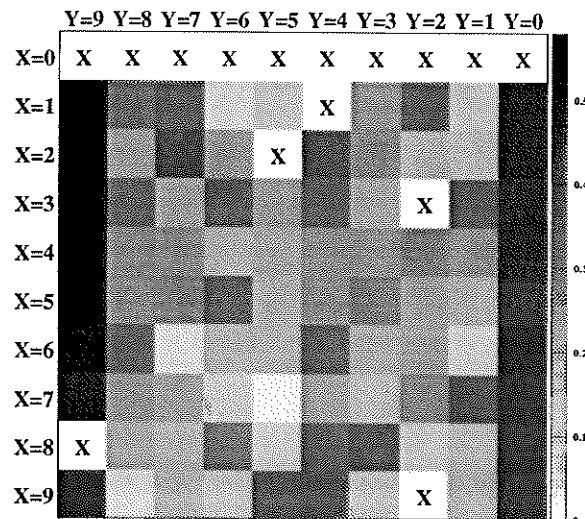


Figure 5.2: LEGRI efficiency

Using the flight electronics does not imply only a worsening in the efficiency, but also in our spectroscopic capability. In figure 5.3 four typical spectra (channel number against counts) taken during the LEGRI calibration are shown (superimposed it is shown the background noise, detected in absence of sources); the two spectra on the top were taken with a CdZnTe detector, and the other two with a HgI₂. The used sources were, from left to right, Cd 109 and Am 241. On the next page, in table V, the emission characteristics of these two sources [42] are shown.

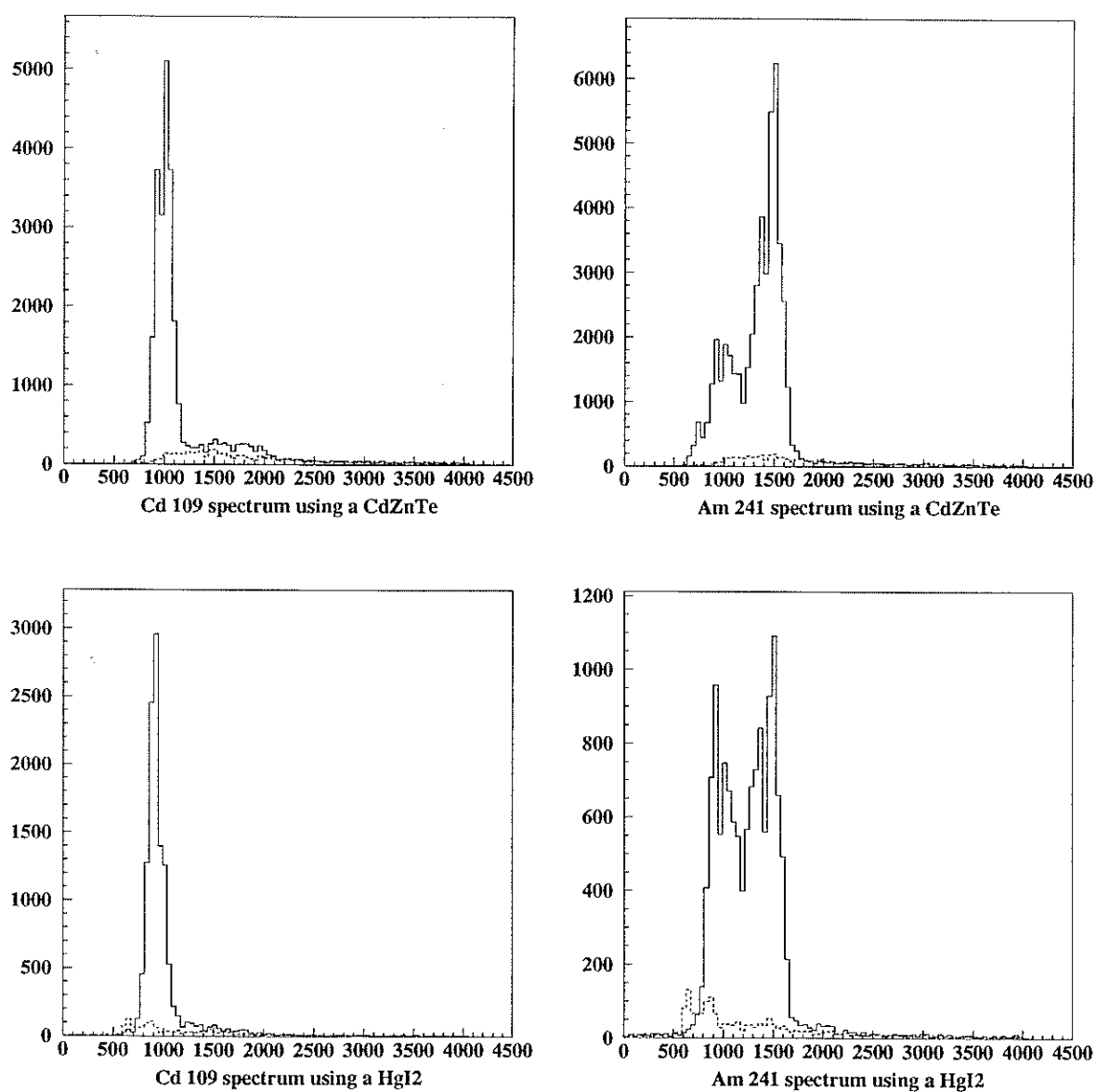


Figure 5.3: Spectra detected with LEGRI.

Source	Desintegr.	Half life	Radiation	Energy	% of emission
Cd 109	Electr. Capture	463 days	γ (X K)	23 keV	102.1
	Electr. Capture		γ	88.0 keV	3.61
Am 241	α	432 years	γ (X L)	16 keV	38.0
	α		γ	59.5 keV	35.9
	α		γ	26.3 keV	2.41

Table V: Radiative sources used during the LEGRI calibration

The 22.6 keV line of Cd 109 and the line of 16 keV of Am 241 correspond to a multiplet of X rays (from the K and L shells respectively) with different energies but very close ones to the others (therefore it is very difficult to solve them), so it is shown an average value of energy and a percentage of emission intensity. We should not be surprised of obtaining percentages bigger than 100, as it refers to the number of photons produced in 100 nuclear desintegrations, and some desintegrations can produce more that one photon.

As it can be seen, the spectral resolution of the LEGRI detectors, with the flight electronics, is not very good; for instance, the 16 and 59.5 keV lines of Am 241 are very close one to each other; the FWHM is about ~ 40 keV, and not all the LEGRI detectors show a peak for each line in the source, but there are others that only show a continuum; in others the electronic noise is dominant (the detectors near $X=0$ are noisier). This fact, plus the lack of time due to problems that appeared during the calibration, which delayed very much the calibration program (when the detectors were subjected to a thermal vacuum that emulates the space conditions, there was an outgassing of the detectors and therefore it was necessary to encapsulate them in order to avoid a direct contact with the vacuum), plus the need of delivering LEGRI to I.N.T.A. (for its assembling with Minisat 01 and the other modules according to the schedule), leded that a detailed study was not possible. Therefore we

do not know the dependence of the LEGRI efficiency as a function of energy (because in principle, the efficiency should be different for photons with different energy) and thus we had to conform to the obtained data and to calculate an efficiency integrated over the nominal range of LEGRI (20 to 100 keV). This is the efficiency shown in fig. 5.2. This array of efficiencies is called the **calibration array**, and it is the starting point of later calibrations that will be done in flight, using well known γ sources (as for example the Crab nebula pulsar); these calibrations will bring successive modifications and improvements on the calibration array (that is, the calibration array will be updated along the mission life).

5.3 Correcting the data

Since the ideal situation would be a detector plane with the same response for each detector unit, we will correct the data in the detector plane to correct its **un**-uniformity, that we know by means of the calibration array. In the case of correlative methods, we can do the following correction:

$$D_{ij}^c = \frac{D_{ij}}{\varepsilon_{ij} Tr} \cdot \frac{1 \text{ cm}^2}{A_{ij}} = \frac{D_{ij}}{\varepsilon'_{ij} Tr} \quad (5.1)$$

where ε_{ij} is the detection efficiency of the detector ij , Tr is the honeycomb transparency (with these two corrections we obtain the photons that have really arrived) and A_{ij} is its area (with it we correct the data in order to have which are the photons that arrive at each cm^2); doing this, we correct all the detectors to obtain D^c , that is a corrected version of the detector plane, and will be our input for the correlation methods. This method is very similar to *flat fielding* [36]; it consists in:

$$D_{ij}^c = D_{ij} \left(\frac{T_c/N}{C_{ij}} \mu \right) \quad (5.2)$$

where C_{ij} is an array that corresponds to the measured counts in detector ij , when all the detector plane is illuminated uniformly by a source, T_c is the total number of the counts measured in the detector plane, N is the total number of detector units (and so T_c/N is the mean count value expected for detector unit) and μ is a normalisation factor that can be introduced to assure flux conservation (that is, the total count number in D is equal to the total count number in D^c).

Using both methods one obtains a uniform detector plane. Indeed, the result with one method is proportional to the other. The problem is that the flat fielding, although it improves the image and eliminates structures, it falsifies the intensity reconstruction, because the detector plane uniformity is related to the remaining detector units, and it is calculated by means of the detected counts, while when we correct using the efficiency, the uniformity is done by means of the really arriving photons (either if they give signal or not). That is to say, the detector plane uniformity is obtained in an **absolute** way while with flat fielding it is obtained in a **relative** way. Nevertheless, if it is impossible or too difficult to measure the detector efficiency, flat fielding is an excellent alternative.

This detector plane corrected by the efficiency, could be used without any problem as an input of our maximization methods (it does not produce negative values; although one must be careful with the experimental error that uses in the maximum entropy method). Anyway it is more useful to include all the information about the detection process in the detector response array Φ such as the efficiencies, the real honeycomb transparency, the different size of the detectors (that entails, for example, that each detector has a different field of view as a function of its size and the collimator height -the total field of view of the telescope is given, then, by the detector with the biggest field of view-), etc... Implementing a size and shape different for each detector is quite easy, as it is a simple generalization of the method explained in section 3.4; now we just have to project the real shape of the detector in the mask pattern (instead of a perfect 10x10 square) and, as it was explained in figure 3.4, to obtain its intersection with the collimator projection (that is exactly the same we did but now the intersection is a different rectangle) and with the mask elements.

Exactly as we did in eq. 5.1 (where we normalized by the area, so all the detectors have the same response to a given flux) now we multiply Φ by $A_{ij}/1\text{cm}^2$ (because for identical illumination, a detector with half the size of other will detect half of the counts!). Therefore, the new detector response array Φ' will be:

$$\Phi'_{ij}{}^{\alpha\beta} = \Phi_{ij}{}^{\alpha\beta} \cdot Tr \cdot \frac{A_{ij}}{1\text{cm}^2} \cdot \varepsilon_{ij} = \Phi_{ij}{}^{\alpha\beta} \cdot Tr \cdot \varepsilon'_{ij} \quad (5.3)$$

being Tr the honeycomb transparency, Φ the flux calculated according to eq. 3.11 (and fig. 3.4) but already taking into account the existence of detectors with different shapes and sizes, and ε'_{ij} the efficiency of detector ij normalized by the area (it was already introduced in eq. 5.1). This new Φ' will be used in our maximization methods exactly in the same way as we used Φ in chapter 4 (and in order to simulate LEGRI with the geometrical simulator so modified).

The transparency values were obtained using Am 241 and Cd 109 collimated sources, and measuring with a Ge type n detector. The measurements were made with honeycomb interposed between the source and the detector and without it. The fraction between both meditions gives us the honeycomb transparency, whose result is given in table VI.

Energy	Transparency
17 keV	62 %
21.5 keV	74 %
26 keV	84 %
31 keV	89 %
35 keV	92 %
60 keV	95 %

Table VI: Honeycomb transparency

Since the LEGRI energy range is between 20 and 100 keV, the value we are going to consider for the following results is the corresponding to ~30 keV (~90%), because we consider that it is representative enough.

5.4 Noise and sensitivity

5.4.1 Noise

As it was said in section 1.6.1 and as it can be seen in [7], the main contribution to the expected noise in the LEGRI detector plane is given by the radioactivity induced in the LEGRI material by the protons trapped in the South Atlantic Anomaly. The desintegrations due to this radioactivity produce γ , β^+ and β^- radiation; the β^+ radiation is invisible for LEGRI because liberates positrons that are desintegrated producing two 511 keV photons, energy that is out of the LEGRI energy range, thus we will only detect the γ and β^- radiation. The radiation induced in the mask does not have a big contribution; the main contribution is due to the armour-plating of LEGRI (from outside to inside, Pb, Ta, Sn and Fe; the main contribution is due to Pb and Ta), to the collimator and to the detector units themselves [7]. In all the cases, except in the detector case, only γ radiation arrives at the detector plane, with the β^- radiation being absorbed by the passive material. The only β^- radiation that is detected is the one produced in the detectors, and it is not predominant but about a quarter of the total radiation generated in the detectors. This means that the counts due to noise induced by the S.A.A. are mainly due to photons coming from desintegrations in the LEGRI material.

E. Porras [7] has calculated by means of Monte Carlo models the noise expected in LEGRI due to the S.A.A. after a year, obtaining that the noise value is about $5 \cdot 10^{-3}$ counts $\text{cm}^{-2} \text{s}^{-1} \text{keV}^{-1}$; specifically, integrating over the range from 20 to 100 keV, it is 0.4 counts $\text{cm}^{-2} \text{s}^{-1}$. But this will not be the noise expected in the **real** LEGRI, since each detector has an area different from 1 cm^2 (this was the area considered in the Monte Carlo model) and an efficiency smaller than the expected one; therefore LEGRI will not detect a noise of 0.4 counts $\text{cm}^{-2} \text{s}^{-1}$, but less: the total detector area of LEGRI is 35.8 cm^2 (far from

the ideal model with 100 cm^2 studied in the Monte Carlo model); the total efficiency for photons (that is: total detected counts versus photons arriving at the whole detector area) is 0.346. Since the greatest part of the noise counts comes from photons (as we have said), we can use the efficiency for photons in order to estimate the expected noise counts, on the whole detector and in the real case:

$$0.4 \text{ counts cm}^{-2} \text{ s}^{-1} \cdot 35.8 \text{ cm}^2 \cdot 0.346 = 4.95 \text{ counts/s} \approx 5 \text{ counts/s}$$

5.4.2 Sensitivity

The sensitivity is defined as the minimum flux coming from a source that can be detected by the detector (it can be made out over the noise and the statistical fluctuation) with some significance level. To develop this section we are going to follow the reasonings in [43] (which are based in [44]).

Let f be the flux (photons $\text{cm}^{-2} \text{ s}^{-1}$) arriving from a sky source. It is defined S as the total detected counts number coming from the source during a certain time. Both magnitudes are related by the exposure, X , as it can be seen in equation 5.4.

$$S = X \cdot f \quad (5.4)$$

Therefore, the exposure is defined as:

$$X = A_{on} \cdot T_{obs} \cdot t \cdot \varepsilon \quad (5.5)$$

where A_{on} is the total detector plane area illuminated by the source (that is, the area in the detector plane where the opaque elements do not project a shadow), T_{obs} is the total observation time, t is the transmission due to residual mass between source and detector (in our case its value come from the honeycomb transparency and the collimator) and ε is the total detector efficiency. Also we define the noise N as the total counts due to background noise. It can be subdivided as:

$$N = N_{on} + N_{off} \quad (5.6)$$

where N_{on} is the count number due to the background measured by the detector plane area illuminated by the source and N_{off} is the count number due to the background in the non-illuminated area. We will call their quotient α :

$$\alpha = \frac{N_{on}}{N_{off}} \quad (5.7)$$

If we have a detector plane where all its units have identical response and the noise is uniform per area unit, it is also equal to:

$$\alpha = \frac{A_{on}}{A_{off}} \quad (5.8)$$

that is, the fraction between illuminated and non-illuminated areas. For detectors with the *same* size it will also be equal to the fraction between open and closed mask elements (it can be similar to 1, depending on the mask; for example, for LEGRI, it *would* be $12/13 = 0.92$).

Let us continue with the definitions: we call C_{on} the counts detected in the area illuminated by the source, and analogously, C_{off} the counts detected in the non-illuminated area. We have, therefore:

$$C_{on} = S + N_{on} \quad (5.9)$$

$$C_{off} = N_{off}$$

An estimation of S is given by:

$$S = C_{on} - \alpha C_{off} \quad (5.10)$$

and, for square error propagation, its error is:

$$\begin{aligned} \sigma^2 &= \left(\frac{\partial S}{\partial C_{on}} \right)^2 \epsilon^2(C_{on}) + \left(\frac{\partial S}{\partial C_{off}} \right)^2 \epsilon^2(C_{off}) = \\ &= \left(\frac{\partial S}{\partial C_{on}} \right)^2 (\sqrt{C_{on}})^2 + \left(\frac{\partial S}{\partial C_{off}} \right)^2 (\sqrt{C_{off}})^2 \\ &\rightarrow \sigma = \sqrt{C_{on} + \alpha^2 C_{off}} \end{aligned} \quad (5.11)$$

If we define now N' as:

$$N' = N_{on} + \alpha^2 N_{off} \quad (5.12)$$

then we have that the S error value is given by:

$$\sigma = \sqrt{S + N'} \quad (5.13)$$

N' is similar to N if α is close to 1. In fact, from equations 5.6, 5.7 and 5.12 we have the following relation between N and N' :

$$\begin{aligned} N' &= N_{on} + \alpha^2 N_{off} = N_{on} + \alpha(\alpha N_{off}) = \\ &= (\alpha N_{off}) + \alpha(N_{on}) = \alpha(N_{on} + N_{off}) \\ N' &= \alpha N \end{aligned} \quad (5.14)$$

therefore, if we know α , it is easy to pass from N to N' .

Finally, the significance n is defined as the fraction between the measurement and its error:

$$n = \frac{S}{\sigma} \quad (5.15)$$

that is, the number of times the signal is greater than its error. Typically, a source can be considered as detected if its significance is greater or equal to 3. From eq. 5.4 and 5.13, we have that the significance is:

$$n = \frac{S}{\sqrt{S + N'}} = \frac{fX}{\sqrt{fX + N'}} \quad (5.16)$$

The minimum detectable flux with a significance n , f_n , is given by the following transcendent equation:

$$f_n = \frac{n\sqrt{f_n X + N'}}{X} \quad (5.17)$$

The solution of eq. 17 is given by the following serial development:

$$f_n = \frac{n\sqrt{N'}}{X} \left[1 + \frac{n}{2\sqrt{N'}} + \frac{1}{2} \left(\frac{n}{2\sqrt{N'}} \right)^2 + O(4) \right] \quad (5.18)$$

The sensitivity is defined as the minimum detectable flux with a significance level n . We will use equation 5.17 with $n=3$ to obtain the LEGRI sensitivity. Unfortunately we do not know N' because the LEGRI detector plane is very uneven, and so the α value (the fraction between the noise in the illuminated area and the non-illuminated area) will depend on the sky position of the source (and therefore on which area it illuminates) and the noise structure. Similarly, in eq. 5.5 (where the exposure is defined), A_{on} will also depend on the source position.

Anyway, let us try to obtain an estimation of the LEGRI sensitivity, calculating it in the case where the source is at (0,0), centred in the field of view, in such a way that the collimator will not affect the transmission t . Therefore, t can be considered equal to the honeycomb transparency (as a value which typifies the whole range, at ~30 keV it is equal to 90% = 0.9). In this case, we have that A_{on} (the illuminated area) is 24.6 cm²; given that the total detector plane area is 35.8 cm², and supposing an uniform noise per area unit, we have $\alpha = A_{on}/A_{off} = 2.21$ (very far from 1! This is due to the fact that, when the source is centred, almost all the CdZnTe -bigger, with an area equal to 1 cm²- are illuminated). Then, we have:

$$A_{on} = 24.6 \text{ cm}^2$$

$$t = 0.9$$

$$T_{ob} = \text{for example } 10^5 \text{ s (somewhat more than one day)}$$

$$\varepsilon = 0.346$$

This gives us an exposure of $X = 7.66 \cdot 10^5 \text{ cm}^2 \text{ s}$ (see eq. 5.5). Given the noise value of 5 counts/s in the whole detector plane which we got in section 5.4.1, for an observing time of 10^5 s , $N = 5 \cdot 10^5 \text{ counts}$, and therefore $N' = \alpha \cdot N = 1.1 \cdot 10^6 \text{ counts}$. With these values of X and N' , and considering $n = 3$, we have that the estimated LEGRI sensitivity, with a significancy of 3σ , during

10^5 seconds of observing time, and integrated over the nominal energy LEGRI range (20 - 100 keV), is:

$$f_3 = 4.12 \cdot 10^{-3} \text{ photons cm}^{-2} \text{ s}^{-1}$$

To obtain the mean value per keV, we divide it by 80 (= 100 - 20), and then we get:

$$f_3 = 5.14 \cdot 10^{-5} \text{ photons cm}^{-2} \text{ s}^{-1} \text{ keV}^{-1}$$

Analogously, for an observation time of 10^6 seconds (approx. a week), $f_3 = 1.3 \cdot 10^{-3}$ photons $\text{cm}^{-2} \text{ s}^{-1}$ (or what is the same, $1.625 \cdot 10^{-5}$ photons $\text{cm}^{-2} \text{ s}^{-1} \text{ keV}^{-1}$). That is, as the observing time increases, the telescope sensitivity increases too (we can see weaker sources). The sensitivity increases (its value decreases!) approximately with the square root of the observing time. This means that to see a source 10 times weaker, we have to observe during a 100 times longer time.

Let us study now a more unfavourable case, in which the CdZnTe are not so well illuminated, for instance, considering the source to be at (2.54,0). The illuminated area is now $A_{on} = 19.14 \text{ cm}^2$; α is now 1.15 (closer to 1!) and therefore, N' (for 10^5 seconds of observing time) is now equal to $5.75 \cdot 10^5$ counts. We already have to include now the collimator effect in the transparency (the collimator effect is different for each detector, because each one has a different size; in fact, in this case, only the CdZnTe are affected by it. This gives an mean value of 0.96). Then, $t = 0.9 \cdot 0.96 = 0.864$. Thus we have an exposure value of $X = 5.72 \cdot 10^5 \text{ cm}^2 \text{ s}$. Using all these values in eq. 5.18, we obtain now the sensitivity value:

$$f_3 = 3.98 \cdot 10^{-3} \text{ photons cm}^{-2} \text{ s}^{-1}$$

and, per keV, it gives a mean value of:

$$f_3 = 4.98 \cdot 10^{-5} \text{ photons cm}^{-2} \text{ s}^{-1} \text{ keV}^{-1}$$

which is not very different to the previous one. That is, with these two results we can conclude that the LEGRI sensitivity, during 10^5 s of observing time, with a significance of 3σ , integrated over the range from 20 to 100 keV is of the order of $\sim 4 \cdot 10^{-3}$ photons $\text{cm}^{-2} \text{s}^{-1}$ (or $\sim 5 \cdot 10^{-5}$ photons $\text{cm}^{-2} \text{s}^{-1} \text{keV}^{-1}$, averaged). As the Crab nebulae pulsar in the range from 20 to 100 keV emits about 0.4 photons $\text{cm}^{-2} \text{s}^{-1}$, we can infer that the LEGRI sensitivity in 10^5 s is equal to 10 mCrab (where 1 mCrab is an intensity 1000 times weaker than the Crab nebulae pulsar emission intensity). This means that LEGRI is able to detect sources 100 times weaker than the Crab nebulae pulsar with a significance of 3σ and during an observing time of 10^5 seconds.

This sensitivity qualifies LEGRI to study a good part of the known X and γ -ray sources. In table VII we show some examples of X and γ -ray sources. The emission shown is the one of the source integrated from 20 to 100 keV, in photons $\text{cm}^{-2} \text{s}^{-1}$.

Black holes candidates		X-Ray binaries		Active Galactic Nuclei	
Name	Emission	Name	Emission	Name	Emission
Cygnus X-1	0.7	0834-430	0.1	NGC 4151	$8.8 \cdot 10^{-3}$
Nova Muscae	0.17	GRO 1948+32	$1.6 \cdot 10^{-2}$	3C273	$5 \cdot 10^{-3}$
SMC X1	$1.3 \cdot 10^{-2}$	0115+63 MISO	$1.6 \cdot 10^{-2}$	IC4329a	$3.6 \cdot 10^{-3}$
1E1740.7-2942	$2.6 \cdot 10^{-2}$	0521+373	$8.1 \cdot 10^{-3}$		

Table VII: Some X and γ -ray sources [45]

As it can be seen, there are some black hole candidates that can be detected by LEGRI, as well as X-ray binaries. In particular 0521+373 is very close to the LEGRI sensitivity value. We are not so lucky with the AGN, whose emission values are very close to the LEGRI sensitivity (as 3C273) or are beneath it, as the case of IC4329a which would be detected with a significance level of $n \sim 2.7$.

5.5 Imaging

We have seen that our real telescope is not exactly the same as we considered in chapter 4; we have detector units with different responses, different efficiencies and different sizes. Does this affect in any way to the conclusion on imaging we have obtained in the previous chapter?

One can expect that if something is affected, one of the effects will be a change in the intensities reconstruction, since the main effect of the efficiency is a reduction in the intensity of the detected signal from the ideal case (although as the efficiency is different in each detector, it is not exactly the same as a scale change). To study it, we have illuminated the detector plane (once the geometrical simulator has been properly modified to include all the effects) with a source with intensity 100 photons/cm^2 (figure 5.4). Comparing this result with fig. 4.11; one clearly sees the effect of different areas and efficiencies, and how the CdZnTe measure more counts than the HgI₂. One can also see (although not so clearly) that there are 15 unworkable detectors (in white).

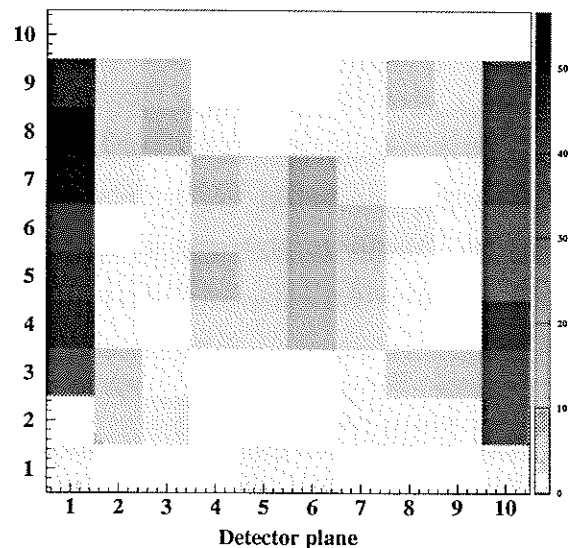


Figure 5.4: Detector plane of LEGRI

If we reconstruct the image, correcting previously the data of fig. 5.4 as it was explained in section 5.3 (see equations 5.1 and 5.3) and bypassing the unworkable detectors, we obtain that the reconstructed intensity of the source has not worsened significantly, as it can be seen in figure 5.5 where, from left to right, the reconstruction with FSBC, the maximum entropy method and the EM algorithm are shown.

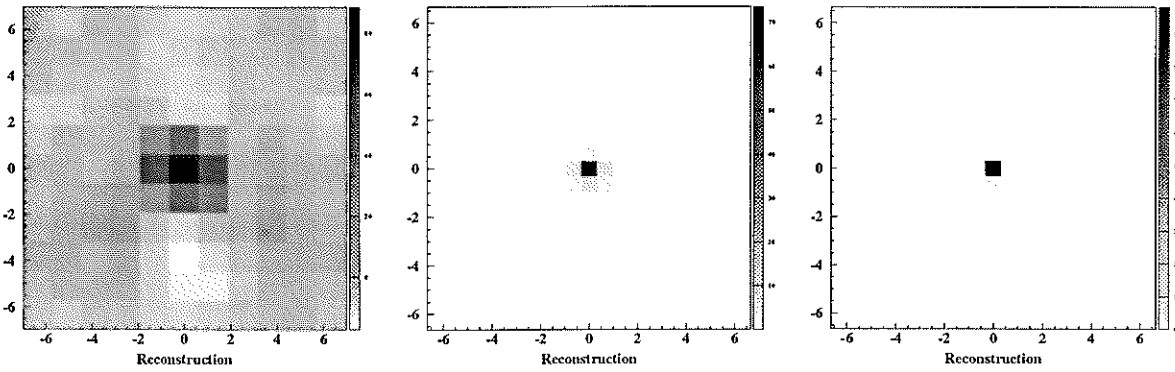


Figure 5.5: Reconstructions from fig. 5.4

In fact, the intensity variation one can observe in the source reconstructed with FSBC is not due to the fact of having different efficiencies (which has been corrected) but to the fact that we can not take into account all the detector plane units; indeed, the detector unit $i=1, j=2$ (fig. 5.4) does not work and its absence makes the estimated intensity to be smaller.

One can consider the example in figure 5.4 (in which the source is centred in the field of view) a lucky case, indeed, because except for one detector, all the illuminated area is operating. Does the result vary in a more unlucky case? To find out the answer, we have now put the same source in a different position: at $(-2.54, -1.27)$. It generates the detector plane shown in figure 5.6. This case is less favourable than the previous one; now the source illuminates 7 unworkable detectors (almost half of them) instead of one. Reconstructing the image now, we obtain the results observed in figure 5.7. Again, from left to right, the reconstruction has been

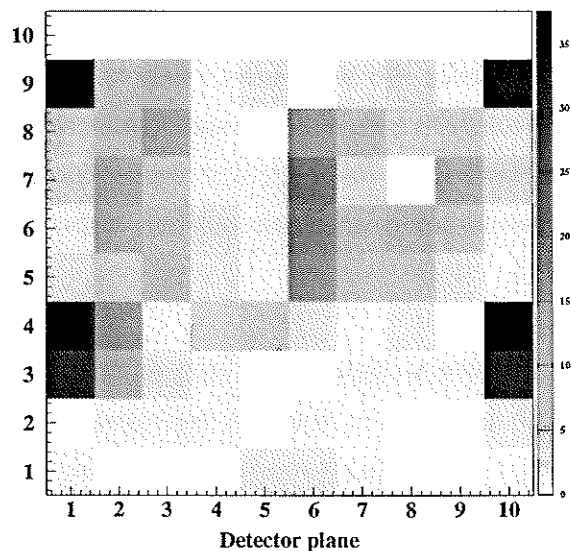


Figura 5.6: Detección de una fuente en $(-2,54,-1,27)$

done with FSBC, maximum entropy and the EM algorithm.

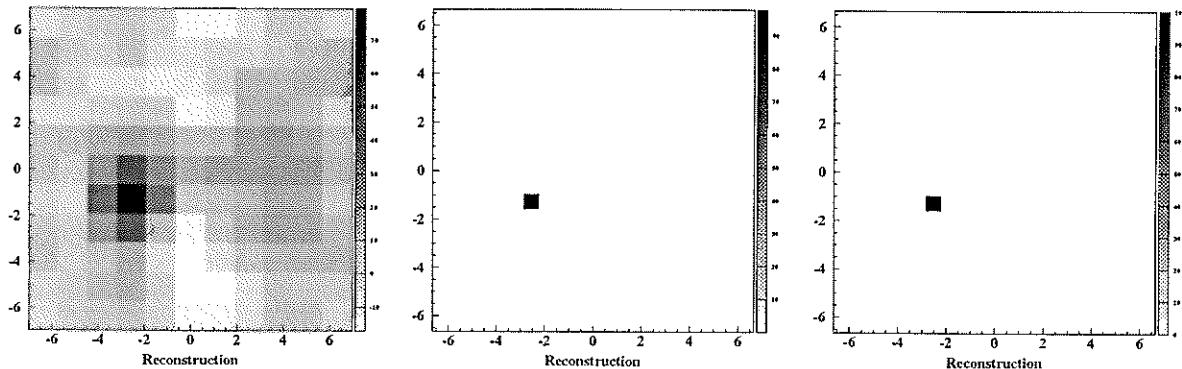


Figure 5.7: Reconstructions from fig. 5.6

We have again good results using maximization methods (it seems that they are even somewhat better than in the previous case!); the result with FSBC is similar, although the background seems to have a little more structure and the source intensity is smaller, in part because of the collimator (in a factor of 0.94), but mainly because we have now 7 detectors that do not contribute to the correlation.

As a conclusion one can say that respect to the results in chapter 4, we practically do not have any worsening in the reconstruction of the source intensity when we use maximization methods, while we can observe a slight worsening in the correlative methods, although it is due to the fact that we can not take into account all the detector units in the detector plane (see section 4.11).

Nevertheless, in this case we have only studied two particular cases with point sources, placed in two strategic positions. A better understanding of the imaging capability can be achieved if we study an extended source. That is why we are going to subject this more realistic LEGRI to the source shown in figure 4.33 (a) (the capital **A**) and compare the result with the one obtained in chapter 4. The results are shown in figure 5.8. From left to right, the method used is δ -decoding (with a better contrast than FSBC), the maximum entropy method and the EM algorithm.

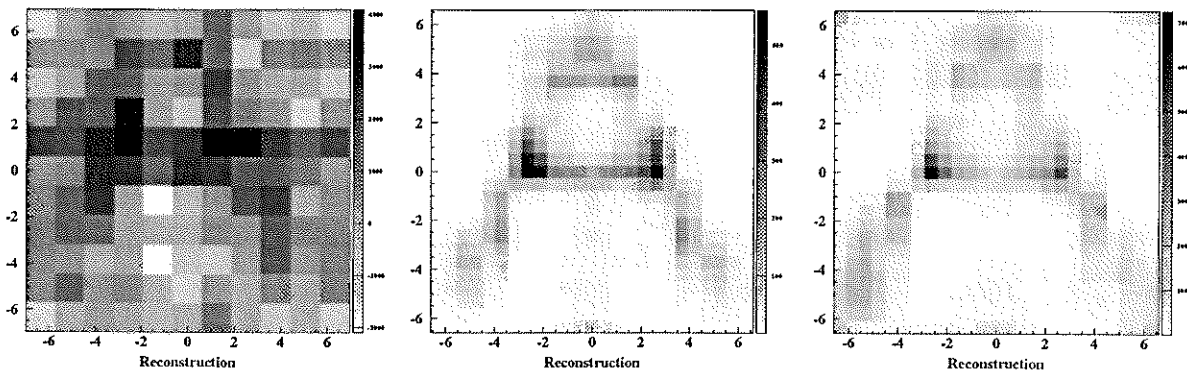


Figure 5.8: Reconstructions of the source shown in fig. 4.33 (a)

It is now clear that there is a worsening in the imaging capability of the real telescope regarding the ideal telescope (fig. 4.33), although it is not critical and the image obtained with the maximization methods is quite good (but not the one obtained with δ -decoding, where one can not recognize the **A**). Anyway, it is possible to improve the image by obtaining more information from it, as we did in chapter 4, using the multiple pointing method. Using the same pointing sequence we used in section 4.9.1, and applying it to the EM algorithm, we obtain the result shown in figure 5.9 (we have not applied this method to the maximum entropy method because it takes too much time to calculate the result, and it is expected a result similar to the EM algorithm result, as it happened in section 4.9.1).

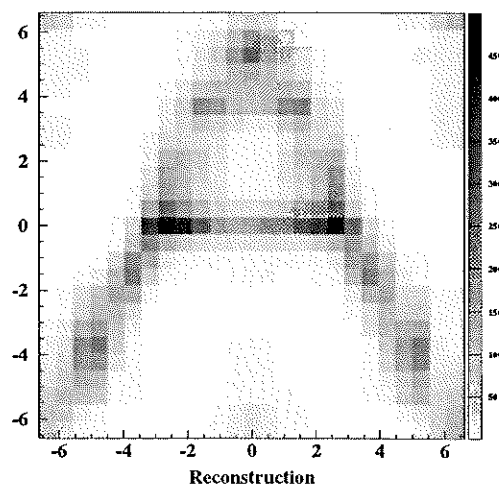


Figure 5.9: Application of the multiple pointing method to the EM algorithm.

The image has improved substantially, indeed, even though it is not so good as in figure 4.35.

Another effect one could expect is related to the ghosts. In chapter 4, all the detectors had the same field of view, limited by the collimator height. Therefore any source in any position inside the field of view affects all the detectors equally (except if mask tungstens cover some of them). It does not happen the same now, because, due to the fact that each detector has a different size, they have also a different field of view (see fig. 5.10), and in most cases they are not square but rectangular (this means a different field of view in each axis). That is, there will be positions inside the field of view where a source could be seen for some detectors but not for the others (forgetting the presence of the mask), while in other positions the source will be seen for all the detectors (the closer to the centre of the field of view, the more the detectors that will see the source, whereas near the field of view, only the greatest detectors will see it).

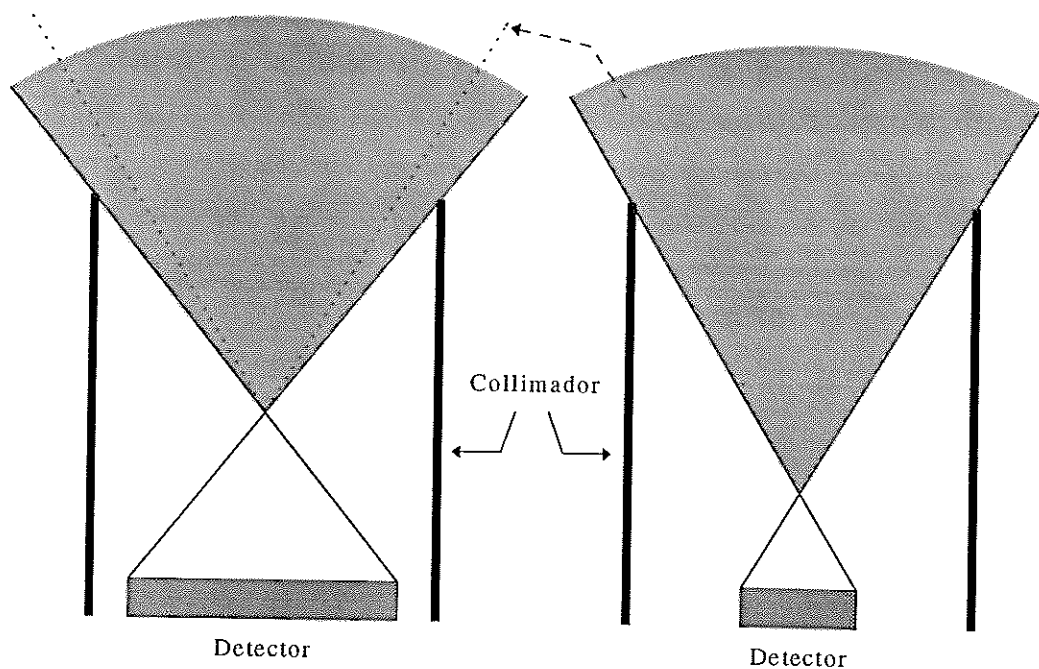


Figure 5.10: Effect of the different detector sizes in the field of view

Will it affect the results about ghosts we obtained in section 4.6? Let us check it by illuminating the telescope with the field of sources shown in figure 4.19, and reconstructing the image using the whole telescope field of view, defined now by the field of view of the biggest detectors (in this case, the CdZnTe). We have also implemented an uniform poissonian noise of 30 counts/cm² in the detector plane (which is multiplied by the real area and efficiency of each detector; this will give us a non uniform noise in counts in each detector, contrary to what had happened in chapter 4). Implementing a good noise model in the reconstruction, the obtained result is shown in figure 5.11, using, from left to right, FSBC, maximum entropy and the EM algorithm. We have used a representation in a surface map for the maximization methods, but not for FSBC because the image obtained with that representation was very confusing; thus we have used a representation in grey tones.

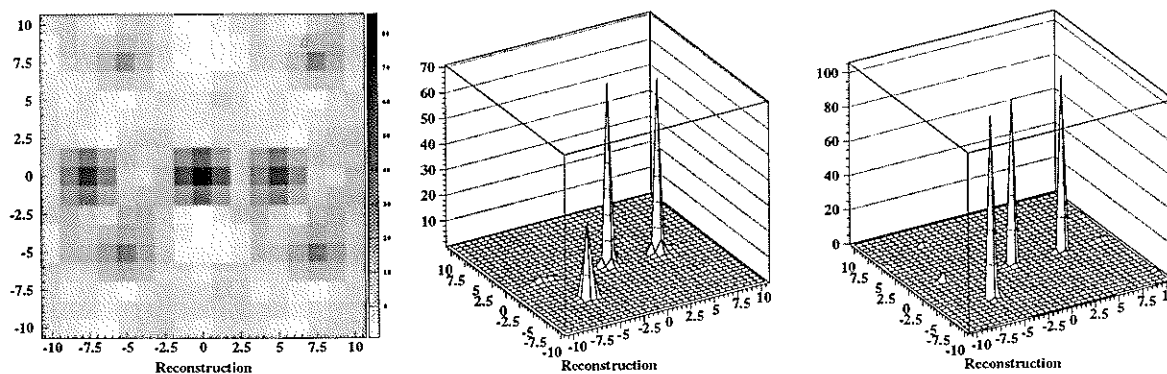


Figure 5.11: Reconstructions of fig. 4.19

The FSBC reconstruction gives nothing surprising, because, as we said in section 4.6, the correlation is cyclic, and then we obtain the ghosts cyclically. They are exactly the same. But we have a great (and nice) surprise when we look at the maximization reconstructions: there are not ghosts! This means that the fact of having different fields of view in each detector, breaks the degeneration we had originally: two different directions that in the ideal telescope give the same shadow, do not give the same shadow in the real telescope, and therefore we can differentiate between both cases. But perhaps what happens is that we are favouring the ghost/source nearer to the field of

view centre, as it has happened in chapter 4 with the maximum entropy method. To demonstrate that this is not what happens, we illuminate now the telescope with the source in figure 4.21 (a). The result is shown in figure 5.12 (from left to right, with FSBC -for completeness-, maximum entropy and the EM algorithm).

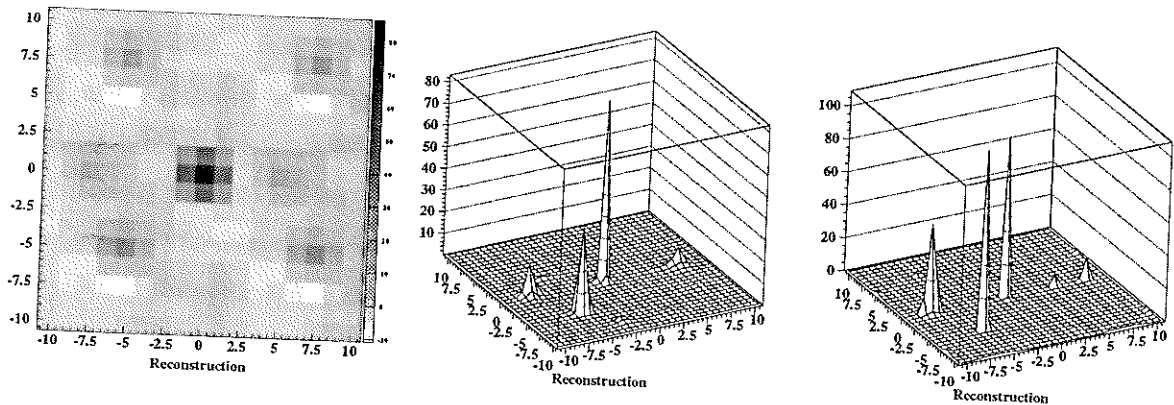


Figure 5.12: Reconstructions of fig. 4.21 (a)

One can see (mainly in the case of the EM algorithm) that now the reconstructed source is in the opposite side, that is, where it really is. Nevertheless, the source reconstruction is worse than before because it is now nearer to the field of view border and therefore there are less detectors which can see it, having then less information.

On the other hand, it is now more necessary to use a good noise model in order to obtain a good reconstruction (see section 4.8.4), because the system is much more sensible now to the noise than before; in the reconstructions we showed in section 4.6, the detector plane was subjected to a noise of 30 counts/cm² plus the source (like now), and even without considering a noise model, the reconstruction was quite good. Now we have had to implement a good noise model to obtain a good result because, otherwise, we get the terrible result shown in figure 5.13, where we can see a lot of structures that are not in the real source.

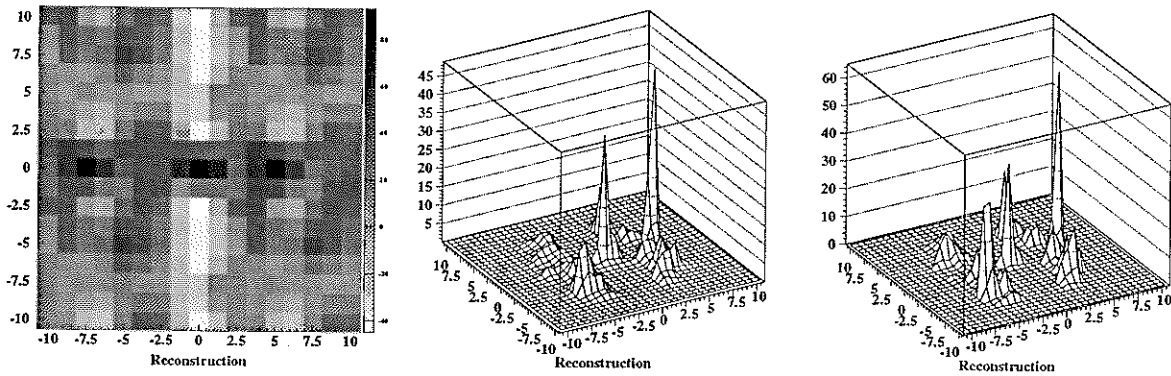


Figure 5.13: Reconstructions of fig. 4.21 (a), ignoring the noise

We therefore conclude that in this more realistic model, including detectors with different shapes, sizes and efficiencies, 15 of them unworkable, and a transparency of the non-opaque elements different from 100%, we can appreciate a worsening of the imaging capability, although it is not critical, mainly if we use maximization methods; we can observe a greater sensitivity to the noise which can be counteracted by including a realistic model of the noise in the reconstruction algorithms. Besides, we have that now there are no ghosts in the reconstruction.

5.6 Errors

Finally and concluding this chapter, we are going to do a study of the errors associated to the reconstructed images. Since this study has only plenty sense in the case of the real LEGRI (given that we will use its data), we present this study in this chapter.

What we have said for the correlative methods in section 3.2.1 is basically still valid; the error in each pixel of the reconstructed image is still **the same for all them**, although now they are not just the square root of the total detected counts, as it can be seen in appendix II, in equation A.16 (there, it is shown the square of the errors).

Applying this error criteria to the examples shown in this chapter, we have that the image obtained with FSBC in fig. 5.5 has an error for each one of its pixels of 5; therefore, the central pixel (where the real source is) has an intensity value of 92 ± 5 photons/cm²; for the image obtained with FSBC in fig. 5.7, each image pixel has an error of 6, and therefore the reconstructed intensity of the source is 79 ± 6 photons/cm² (this value is farther from the real value). For the three sources of the image reconstructed with FSBC in fig. 5.11, the error is ± 9 for all of them. Finally, for the reconstruction of the **A** shown in fig. 5.8 (done with δ -decoding) we have an error of ± 80 in all the pixels. As it happened in the ideal case (see section 3.2.1), the more sources in the field of view, the bigger the error is (although now the relation is not so linear).

About the maximization methods, if we use the error criterion of [38] and use the values in the penultimate iteration to obtain the errors in the last iteration, we can deduce the equations for the error that can be seen in appendix II (eq. A.13 for the EM algorithm and eq. A.14 for the maximum entropy method).

As it can be seen, the error formula for the reconstructed intensity \tilde{O}^{n+1} in the EM algorithm is approximately proportional to the value of \tilde{O}^n which, once has reached the convergency, must be very similar to \tilde{O}^{n+1} , and so, the error value is approximately proportional to \tilde{O}^{n+1} . That is, except for the value included in the brackets of eq. A.13 (the square root), for the EM algorithm, the error of each pixel in the reconstructed image must be approximately proportional to its own value.

On the other hand, as it can be seen in eq. A.14, for the maximum entropy method, the error is approximately proportional to the second addend of the iterative equation 4.10 (used in order to obtain the maximum entropy solution). This means that the error is not proportional to the intensity of the reconstructed image \tilde{O}^{n+1} , but to the difference between two consecutive iterations, $\tilde{O}^{n+1} - \tilde{O}^n$ (since for big values of n , $n/n+1$ is practically 1). In figure 5.14 it is shown the error of the reconstruction in fig. 5.8 for the maximum entropy method (left) and the EM algorithm (right).

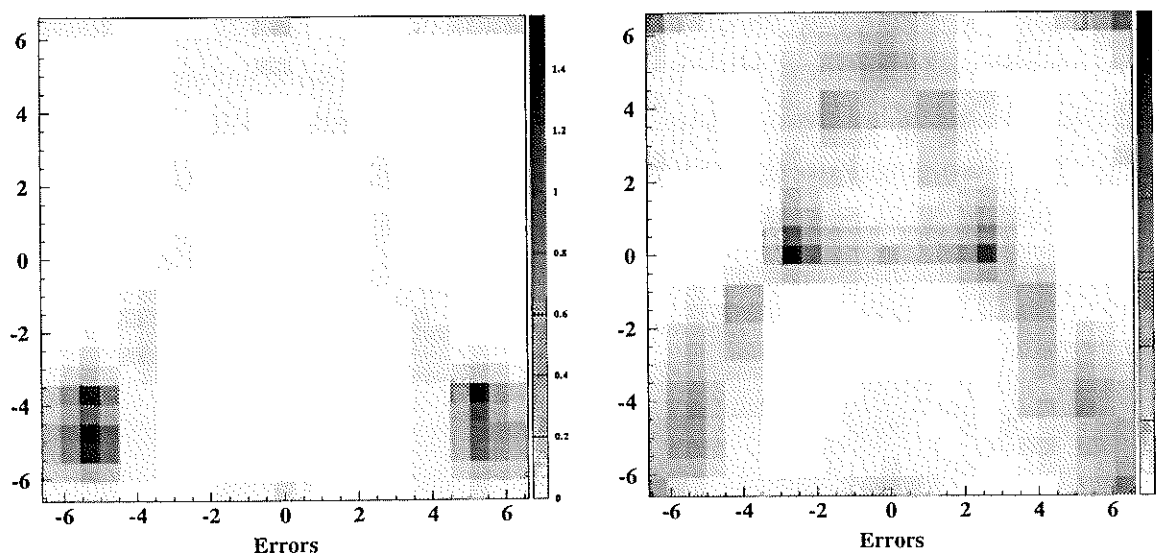


Figure 5.14: Errors associated to the reconstructions in fig. 5.8

As it can be seen, the error associated to the image pixels in the EM algorithm reproduces the shape of the reconstructed image (although they are of course smaller). It does not happen the same with the maximum entropy method; the error does not resemble the final image, but the difference between this and the previous one.

Studying the error we find another argument in favour of fixing the λ^n value in a given moment; as we have said in section 4.2.2, if we leave λ^n fluctuating freely, the image will fluctuate more than if we would fix it in a given moment (compare the final stretch of figures 4.5 (c) and 4.7 (c) where we show the values of δ^n , which indicates the difference between consecutive iterations). Given that the error is approximately proportional to the difference between two consecutive iterations, the error will be smaller if we fix λ^n in a given moment than if we leave it free (even if the final result were the same). For the case of the reconstruction of a centred source with intensity 100 photons/cm² shown in fig. 5.5, the error was ± 3 (casually the same as in the EM algorithm); but when we leave λ^n oscillate freely, since the fluctuation is bigger, the error we obtain is ± 60 !

Nevertheless, we can also find some troubles when fixing λ^n , because the convergency is better, and as the error is proportional to the difference between two consecutive iterations, if our convergency criteria were stricter, the error would also be smaller (and it would also take a longer time). In fact, waiting enough time we could do the error as small as we like, and this is not a very realistic result. This can never happen with the EM algorithm.

Conclusions

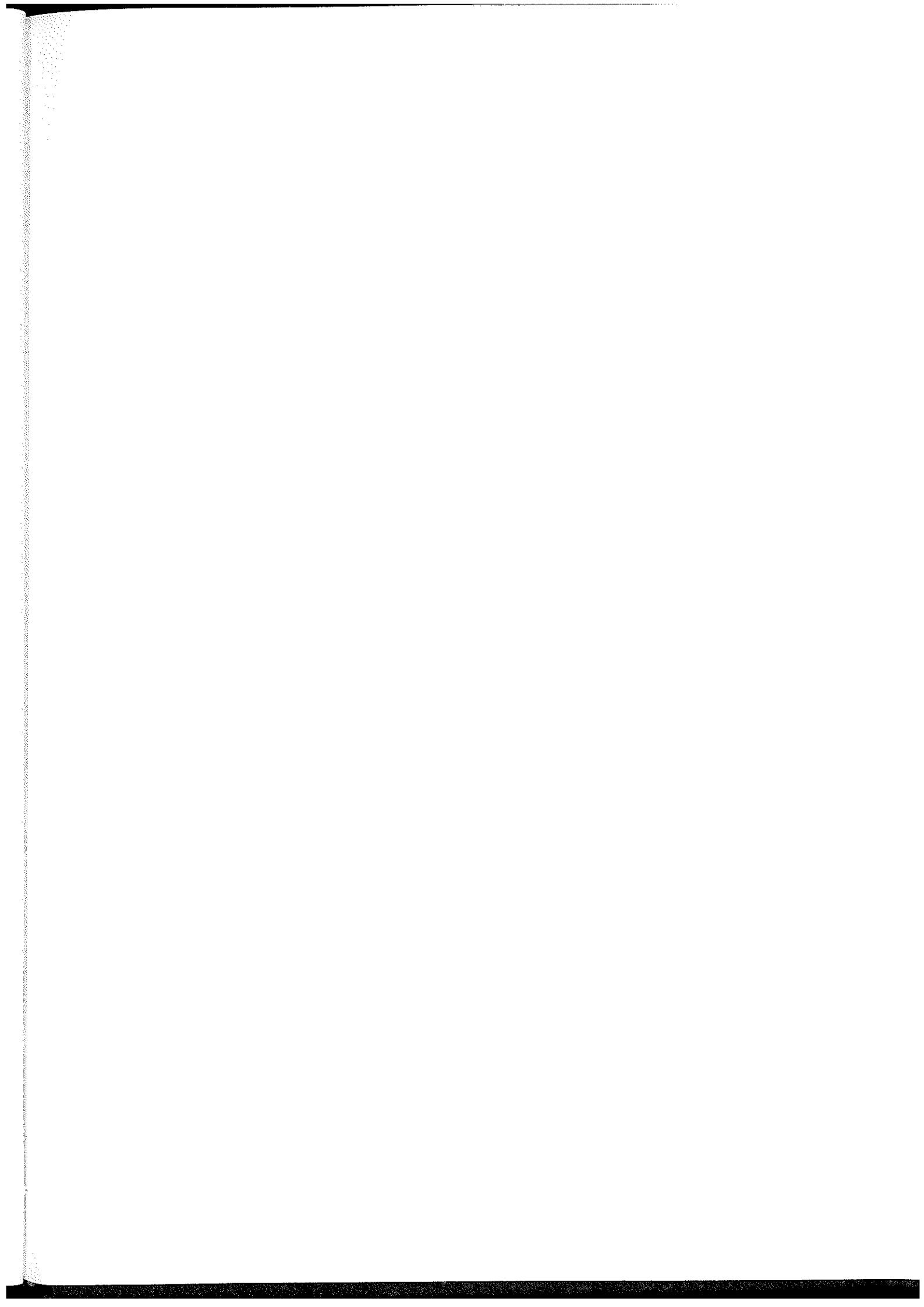
In the carrying out of this work, the main results and conclusions can be summarized in the following points:

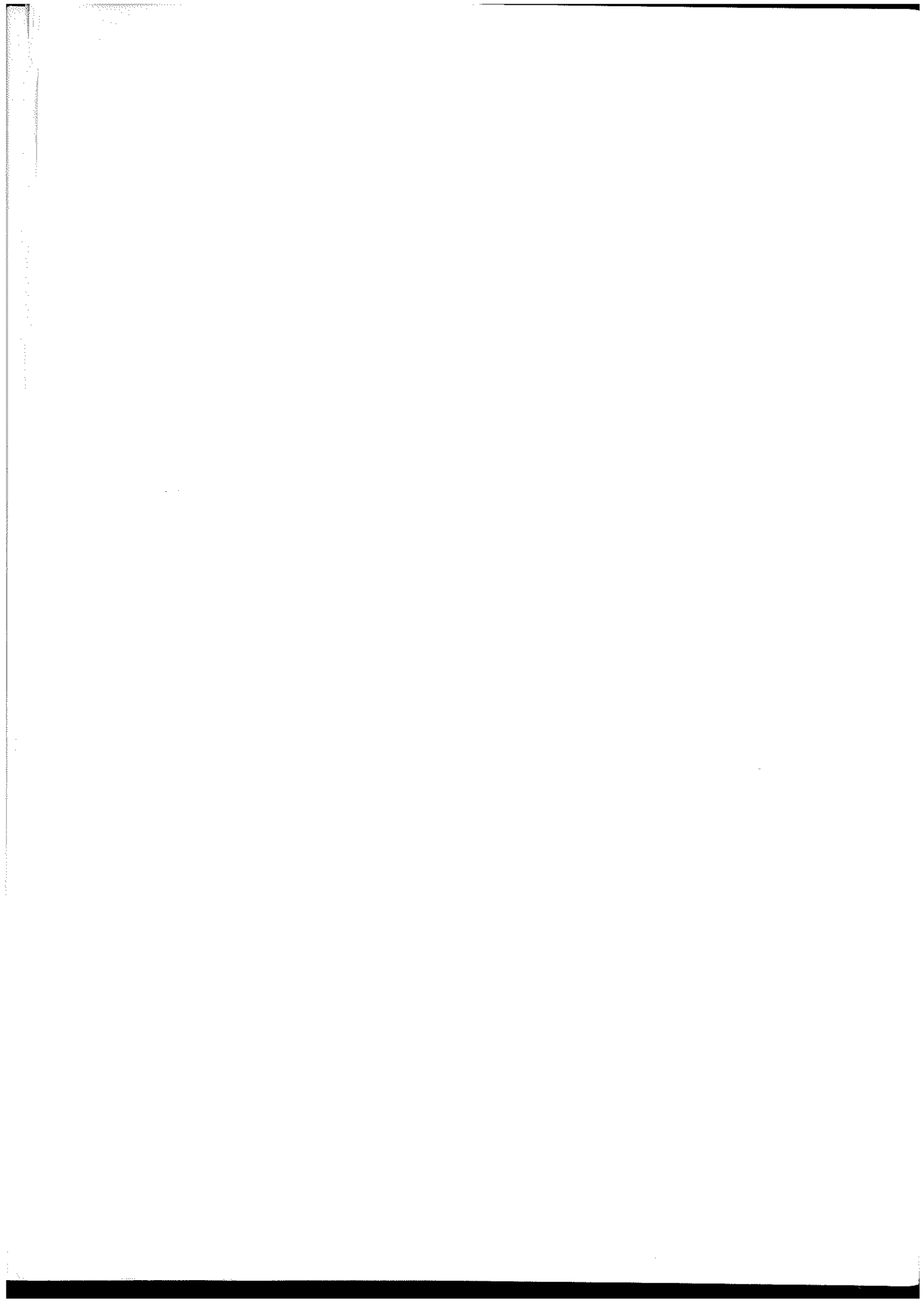
- 1) We have presented the γ -ray telescope LEGRI (Low Energy Gamma Ray Imager), which works in an energy range from 20 to 100 keV and with a field of view of $\pm 10.5^\circ$, describing its structure and objectives, as well as the characteristics of its orbit.
- 2) We have exposed the need of using a coded mask to image while working in energies over 10 keV and we have described the foundations of the theory associated to their use, describing several techniques to reconstruct the image from the coded data.
- 3) We have developed two simulators, a geometrical simulator with two versions (one more idealised and other more similar to the real detector) and a Monte Carlo model. We have studied with them the expected response of the telescope. With these simulators we have generated the flux factors Φ (which indicates the fraction that a certain detector receives from a certain sky direction), needed for the reconstructions using maximization methods.
- 4) We have applied to LEGRI two reconstruction systems based on the balanced correlation, which are the finely sampled balanced correlation (or FSBC) and δ -decoding.
- 5) We have applied to LEGRI a maximum entropy reconstruction method. Given that its solution is a transcendental equation, it is needed to find the solution by an iterative method. We have studied the iterative methods in the literature which find the maximum entropy solution and we have found that the convergency is not the desired one. Therefore, we have developed a new convergency method that produces better results than the previous and that converges to the maximum entropy solution.

- 6) The iterative method that we have developed has a free parameter λ^n . We have found that better results are obtained if λ^n only varies during the first iterations (obtaining a χ^2 of the order of the freedom degrees), and subsequently we fix it.
- 7) We have applied the EM algorithm, which is a maximum likelihood method, to the coded mask telescope context and we have used it as an image reconstruction method. This is the first time the EM algorithm is used in coded mask telescopes. We have seen that its convergency properties in this context are excellent and that it converges to the correct result.
- 8) We have proved that for not very complex telescopes, as the case of LEGRI, the reconstructions with the EM algorithm and the maximum entropy method (which we have generically called maximization methods) are quicker enough to compete with the correlative methods. The fastest of the maximization methods is the EM algorithm, very much faster than the maximum entropy method.
- 9) We have seen that, when the source projects a shadow of the mask on the detector plane which does not match with the position of the detectors, the reconstructed source is spreaded, independently of the reconstruction method used.
- 10) We have checked that the source intensity is better reconstructed with the correlative methods and the EM algorithm, being in general the maximum entropy method the one that gives the worst result in the source intensity reconstruction. Likewise we have seen that the reconstructed intensity of a pixel is independent of the presence or absence of other sources in the image in the correlation methods, and rather independent in the maximization methods. Nevertheless, for a good source reconstruction, correlative methods need all the detector plane working, in order to give optimum results. When it is not possible, the best results are obtained without doubt with the maximization methods.

- 11) We have proved that the maximization methods have better angular resolution than the correlative methods (in which the δ -decoding method has bigger contrast than FSBC). In fact, in the correlative methods there is implicit a loss of information that can be recovered with the maximization methods, obtaining that the telescope angular resolution is directly related to the detector plane spatial resolution. For LEGRI, the angular resolution is 1.27° . The EM algorithm is the maximization method with a better contrast.
- 12) We have seen that a non-cyclic mask is the best option for the maximization methods, since we can therefore avoid the ghosts in the reconstructed image. Besides we have seen that, when we have several ghosts of the same sky source the EM algorithm reconstructs all them with the same intensity whereas the maximum entropy methods favours the closer to the centre of the field of view.
- 13) We have observed that the noise in the detector plane generates fake sources in the reconstructed image, and we need a good knowledge of its structure in order to avoid its influence. Besides we have seen that the noise has the additional effect of widening the reconstructed signal in the maximization methods, doing it wider and weaker.
- 14) We have seen that for correlation methods, the error is the same for all the image pixels. On the other hand, in the EM algorithm the error of a given pixel is roughly proportional to its value. About the maximum entropy method, the error value of a given pixel is related to the difference of values between the final iteration and the previous one. Thus, the closer these two images are, the smaller the error is.
- 15) We have studied the capabilities of the different reconstruction methods to study extended sources, checking that the best results are obtained with the maximization methods. On the other hand, if it is possible to do different pointings of the source, we get more information from it and it is possible to obtain a better reconstruction of the source structure.

- 16) We have applied the studied reconstruction methods to the real LEGRI configuration, which has 15 unworkable detectors and different sizes and efficiencies for each detector. We have seen that the former points are in general still applicable, although a light worsening of the image can be observed (bigger for the correlation methods). The exception is the disappearance of the ghosts in the reconstructed image.
- 17) We have estimated the LEGRI sensitivity with a significance of 3σ , obtaining that it is of the order of $5 \cdot 10^{-5}$ photons $\text{cm}^{-2} \text{s}^{-1} \text{keV}^{-1}$.
- 18) We have seen that the EM algorithm, considering the execution time, robustness, angular resolution, intensity reconstruction capability and ease of adaptation to difficult conditions (unworkable detectors, multiple pointings...) is, in general terms, the method that offers the best results and features of all the studied methods.





Acknowledgements

First of all I want to thank my thesis director, Filomeno Sánchez, for all his help, for his constant attention, for his sharp comments, because I can always rely on him, even when he was ill; and for all the times he paid me the coffee, when I had no coins.

I also want to thanks Victor Reglero for giving me a work theme. I think that working in the LEGRI project is one of those experiences in the life of a person that can not be easily forgotten; thanks for all his help and for all the times he laughed at my bad jokes.

A special place is dedicated to my friends Ana Marín, Amparo Gil and Miguel Ángel G. Jareño. Their help has been vital for me in many times when I was stuck, and this work would not be the same without them. Thanks also to Jesús Ruiz for his help in the English version.

Thanks to G. K. Skinner for his help and for all he taught me in Birmingham. Thanks also to Paul H. Connell for his continual help, for being at the other end of the computer, for all his advices in the masks' world, and for his friendship. Thanks to P. Mandrou for his kind help in Toulouse. And specially to Juan E. Naya for illuminating my way in a dark moment.

Thanks to my parents for all their backing and support, their love, affection, understanding and help.

I want to thank my GACE companions for their company; they make working something almost nice.

Thanks to all my friends, who have cheered me up in my blue hours. And they are: Amelia, Begoña, Belén, Carmen, Cristina, Dani, Dani, Eugenio, Eva, someone, Javi, Jesús, Juan, Juan Carlos, Juan Carlos, Merche, Mónica, Montse, Oscar, Pablo, Santi, Sara, Trino, Waldo and Younis.

Thanks to the mates of ballroom class, who allow me to let off steam every thursday evening and that forget all my stamps.

Appendices

Appendix I: Relation between an area and its orthogonal projection

In section 2.11.1 we have said that the relation between an area and its projection orthogonal to a given direction (α, β) (see fig. 2.35) was given by equation 2.37, which we repeat here:

$$Area = \frac{Area'}{\sqrt{\text{tg}^2\alpha + \text{tg}^2\beta + 1}}$$

where $Area'$ is the considered area and $Area$ the orthogonal projection.

In this appendix we are going to demonstrate this relation. Let us observe figure A.1, which is basically the same as fig. 2.35 but with more legends.

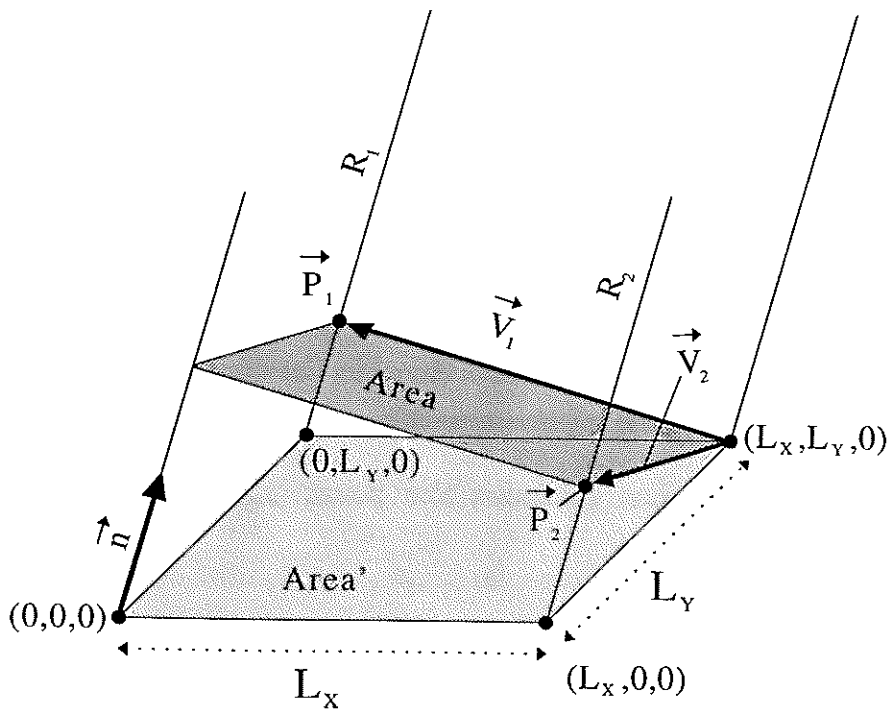


Figure A.1: Orthogonal projection of $Area'$ in a direction (α, β)

The co-ordinates origin in the figure has been taken at the bottom left vertex of *Area'*. L_X and L_Y are the sides of the area whose projection we are going to calculate; therefore we have:

$$Area' = L_X \cdot L_Y. \quad (A.1)$$

\vec{n} is an unitary vector in the direction (α, β) . As it can be deduced from figure 2.1, we have:

$$\frac{x}{z} = \operatorname{tg}\alpha$$

$$\frac{y}{z} = \operatorname{tg}\beta$$

$$\frac{z}{z} = 1$$

Therefore, the unitary vector in that direction will be proportional to the vector $(\operatorname{tg}\alpha, \operatorname{tg}\beta, 1)$, and will be given by:

$$\vec{n} = (\operatorname{tg}\alpha, \operatorname{tg}\beta, 1) \cdot \frac{1}{\sqrt{\operatorname{tg}\alpha + \operatorname{tg}\beta + 1}} \quad (A.2)$$

as it was shown in equation 2.1.

Area is the orthogonal projection of *Area'* in the direction (α, β) ; given that it is orthogonal to that direction, *Area* will be inscribed in a plane P that is perpendicular to \vec{n} and that includes the point $(L_X, L_Y, 0)$. Its equation is, therefore:

$$P: (\operatorname{tg}\alpha)x + (\operatorname{tg}\beta)y + z - (\operatorname{tg}\alpha)L_X - (\operatorname{tg}\beta)L_Y = 0 \quad (A.3)$$

R_1 and R_2 are two straight lines parallel to \vec{n} , and which passes through the points $(0, L_Y, 0)$ and $(L_X, 0, 0)$ respectively. Its equations are given by:

$$\begin{aligned} R_1: & \begin{cases} x = z \operatorname{tg} \alpha \\ y = z \operatorname{tg} \beta + L_Y \end{cases} \\ R_2: & \begin{cases} x = z \operatorname{tg} \alpha + L_X \\ y = z \operatorname{tg} \beta \end{cases} \end{aligned} \quad (\text{A.4})$$

The intersections of R_1 and R_2 with P define the points \vec{P}_1 and \vec{P}_2 :

$$\begin{aligned} \vec{P}_1 &= \left(\frac{\operatorname{tg}^2 \alpha \cdot L_X}{(\operatorname{tg}^2 \alpha + \operatorname{tg}^2 \beta + 1)}, L_Y + \frac{\operatorname{tg} \alpha \cdot \operatorname{tg} \beta \cdot L_X}{(\operatorname{tg}^2 \alpha + \operatorname{tg}^2 \beta + 1)}, \frac{\operatorname{tg} \alpha \cdot L_X}{(\operatorname{tg}^2 \alpha + \operatorname{tg}^2 \beta + 1)} \right) \\ \vec{P}_2 &= \left(L_X + \frac{\operatorname{tg} \alpha \cdot \operatorname{tg} \beta \cdot L_Y}{(\operatorname{tg}^2 \alpha + \operatorname{tg}^2 \beta + 1)}, \frac{\operatorname{tg}^2 \beta \cdot L_Y}{(\operatorname{tg}^2 \alpha + \operatorname{tg}^2 \beta + 1)}, \frac{\operatorname{tg} \beta \cdot L_Y}{(\operatorname{tg}^2 \alpha + \operatorname{tg}^2 \beta + 1)} \right) \end{aligned} \quad (\text{A.5})$$

\vec{V}_1 and \vec{V}_2 are defined as the vectors that go from the point $(L_X, L_Y, 0)$ to the points \vec{P}_1 and \vec{P}_2 , respectively:

$$\begin{aligned} \vec{V}_1 &= \left(\frac{\operatorname{tg}^2 \alpha \cdot L_X}{(\operatorname{tg}^2 \alpha + \operatorname{tg}^2 \beta + 1)} - L_X, \frac{\operatorname{tg} \alpha \cdot \operatorname{tg} \beta \cdot L_X}{(\operatorname{tg}^2 \alpha + \operatorname{tg}^2 \beta + 1)}, \frac{\operatorname{tg} \alpha \cdot L_X}{(\operatorname{tg}^2 \alpha + \operatorname{tg}^2 \beta + 1)} \right) \\ \vec{V}_2 &= \left(\frac{\operatorname{tg} \alpha \cdot \operatorname{tg} \beta \cdot L_Y}{(\operatorname{tg}^2 \alpha + \operatorname{tg}^2 \beta + 1)}, \frac{\operatorname{tg}^2 \beta \cdot L_Y}{(\operatorname{tg}^2 \alpha + \operatorname{tg}^2 \beta + 1)} - L_Y, \frac{\operatorname{tg} \beta \cdot L_Y}{(\operatorname{tg}^2 \alpha + \operatorname{tg}^2 \beta + 1)} \right) \end{aligned} \quad (\text{A.6})$$

As it can be seen in figure A.1, we have that *Area* (the magnitude we want to calculate) will be given by the modulus of the vectorial product of \vec{P}_1 and \vec{P}_2 . That is:

$$\text{Area} = |\vec{V}_1 \times \vec{V}_2| \quad (\text{A.7})$$

Writting $\vec{P}_1 = (x_1, y_1, z_1)$ and $\vec{P}_2 = (x_2, y_2, z_2)$ (the components of the vectors), we have that the square of the vectorial product modulus is given by:

$$\begin{aligned} Area^2 = |\vec{V}_1 \times \vec{V}_2|^2 = & y_1^2 z_2^2 + z_1^2 y_2^2 - 2y_1 z_2 z_1 y_2 \\ & + x_2^2 z_1^2 + z_2^2 x_1^2 - 2x_2 z_1 z_2 x_1 + x_1^2 y_2^2 + y_1^2 x_2^2 - 2x_1 y_2 y_1 x_2 \end{aligned} \quad (A.8)$$

Using the values shown in eq. A.6, we obtain:

$$\begin{aligned} Area^2 = & \frac{\operatorname{tg}^2 \alpha \operatorname{tg}^2 \beta L_X^2}{(\operatorname{tg}^2 \alpha + \operatorname{tg}^2 \beta + 1)^2} \frac{\operatorname{tg}^2 \beta L_Y^2}{(\operatorname{tg}^2 \alpha + \operatorname{tg}^2 \beta + 1)^2} + \\ & \frac{\operatorname{tg}^2 \alpha L_X^2}{(\operatorname{tg}^2 \alpha + \operatorname{tg}^2 \beta + 1)^2} \left(\frac{\operatorname{tg}^4 \beta L_Y^2}{(\operatorname{tg}^2 \alpha + \operatorname{tg}^2 \beta + 1)^2} + L_Y^2 - 2 \frac{\operatorname{tg}^2 \beta L_Y^2}{(\operatorname{tg}^2 \alpha + \operatorname{tg}^2 \beta + 1)} \right) - \\ & 2 \frac{\operatorname{tg} \alpha \operatorname{tg} \beta L_X}{(\operatorname{tg}^2 \alpha + \operatorname{tg}^2 \beta + 1)} \frac{\operatorname{tg} \beta L_Y}{(\operatorname{tg}^2 \alpha + \operatorname{tg}^2 \beta + 1)} \frac{\operatorname{tg} \alpha L_X}{(\operatorname{tg}^2 \alpha + \operatorname{tg}^2 \beta + 1)} \left(\frac{\operatorname{tg}^2 \beta L_Y}{(\operatorname{tg}^2 \alpha + \operatorname{tg}^2 \beta + 1)} - L_Y \right) + \\ & \frac{\operatorname{tg}^2 \alpha \operatorname{tg}^2 \beta L_Y^2}{(\operatorname{tg}^2 \alpha + \operatorname{tg}^2 \beta + 1)^2} \frac{\operatorname{tg}^2 \alpha L_X^2}{(\operatorname{tg}^2 \alpha + \operatorname{tg}^2 \beta + 1)^2} + \\ & \frac{\operatorname{tg}^2 \beta L_Y^2}{(\operatorname{tg}^2 \alpha + \operatorname{tg}^2 \beta + 1)^2} \left(\frac{\operatorname{tg}^4 \alpha L_X^2}{(\operatorname{tg}^2 \alpha + \operatorname{tg}^2 \beta + 1)^2} + L_X^2 - 2 \frac{\operatorname{tg}^2 \alpha L_X^2}{(\operatorname{tg}^2 \alpha + \operatorname{tg}^2 \beta + 1)} \right) - \\ & 2 \frac{\operatorname{tg} \alpha \operatorname{tg} \beta L_Y}{(\operatorname{tg}^2 \alpha + \operatorname{tg}^2 \beta + 1)} \frac{\operatorname{tg} \alpha L_X}{(\operatorname{tg}^2 \alpha + \operatorname{tg}^2 \beta + 1)} \frac{\operatorname{tg} \beta L_Y}{(\operatorname{tg}^2 \alpha + \operatorname{tg}^2 \beta + 1)} \left(\frac{\operatorname{tg}^2 \alpha L_X}{(\operatorname{tg}^2 \alpha + \operatorname{tg}^2 \beta + 1)} - L_X \right) + \\ & \left(\frac{\operatorname{tg}^4 \alpha L_X^2}{(\operatorname{tg}^2 \alpha + \operatorname{tg}^2 \beta + 1)^2} + L_X^2 - \frac{2 \operatorname{tg}^2 \alpha L_X^2}{(\operatorname{tg}^2 \alpha + \operatorname{tg}^2 \beta + 1)} \right) \left(\frac{\operatorname{tg}^4 \beta L_Y^2}{(\operatorname{tg}^2 \alpha + \operatorname{tg}^2 \beta + 1)^2} + L_Y^2 - \frac{2 \operatorname{tg}^2 \beta L_Y^2}{(\operatorname{tg}^2 \alpha + \operatorname{tg}^2 \beta + 1)} \right) + \\ & \frac{\operatorname{tg}^2 \alpha \operatorname{tg}^2 \beta L_X^2}{(\operatorname{tg}^2 \alpha + \operatorname{tg}^2 \beta + 1)^2} \frac{\operatorname{tg}^2 \alpha \operatorname{tg}^2 \beta L_Y^2}{(\operatorname{tg}^2 \alpha + \operatorname{tg}^2 \beta + 1)^2} - \\ & 2 \left(\frac{\operatorname{tg}^2 \alpha L_X}{(\operatorname{tg}^2 \alpha + \operatorname{tg}^2 \beta + 1)} - L_X \right) \left(\frac{\operatorname{tg}^2 \beta L_Y}{(\operatorname{tg}^2 \alpha + \operatorname{tg}^2 \beta + 1)} - L_Y \right) \frac{\operatorname{tg} \alpha \operatorname{tg} \beta L_X}{(\operatorname{tg}^2 \alpha + \operatorname{tg}^2 \beta + 1)} \frac{\operatorname{tg} \alpha \operatorname{tg} \beta L_Y}{(\operatorname{tg}^2 \alpha + \operatorname{tg}^2 \beta + 1)} \end{aligned}$$

Developing this expression, we have the following:

$$\begin{aligned}
Area^2 = & \frac{tg^2\alpha tg^4\beta L_X^2 L_Y^2}{(tg^2\alpha + tg^2\beta + 1)^4} + \frac{tg^2\alpha tg^4\beta L_X^2 L_Y^2}{(tg^2\alpha + tg^2\beta + 1)^4} + \frac{tg^2\alpha L_X^2 L_Y^2}{(tg^2\alpha + tg^2\beta + 1)^2} - \\
& 2 \frac{tg^2\alpha tg^2\beta L_X^2 L_Y^2}{(tg^2\alpha + tg^2\beta + 1)^3} - 2 \frac{tg^2\alpha tg^4\beta L_X^2 L_Y^2}{(tg^2\alpha + tg^2\beta + 1)^4} + 2 \frac{tg^2\alpha tg^2\beta L_X^2 L_Y^2}{(tg^2\alpha + tg^2\beta + 1)^3} + \\
& \frac{tg^4\alpha tg^2 L_X^2 L_Y^2}{(tg^2\alpha + tg^2\beta + 1)^4} + \frac{tg^4\alpha tg^2\beta L_X^2 L_Y^2}{(tg^2\alpha + tg^2\beta + 1)^4} + \frac{tg^2\beta L_X^2 L_Y^2}{(tg^2\alpha + tg^2\beta + 1)^2} - \\
& 2 \frac{tg^2\alpha tg^2\beta L_X^2 L_Y^2}{(tg^2\alpha + tg^2\beta + 1)^3} - 2 \frac{tg^4\alpha tg^2\beta L_X^2 L_Y^2}{(tg^2\alpha + tg^2\beta + 1)^4} + 2 \frac{tg^2\alpha tg^2\beta L_X^2 L_Y^2}{(tg^2\alpha + tg^2\beta + 1)^3} + \\
& \frac{tg^4\alpha tg^4\beta L_X^2 L_Y^2}{(tg^2\alpha + tg^2\beta + 1)^4} + \frac{tg^4\alpha L_X^2 L_Y^2}{(tg^2\alpha + tg^2\beta + 1)^2} - 2 \frac{tg^4\alpha tg^2\beta L_X^2 L_Y^2}{(tg^2\alpha + tg^2\beta + 1)^3} + \frac{tg^4\beta L_X^2 L_Y^2}{(tg^2\alpha + tg^2\beta + 1)^2} + \\
& L_X^2 L_Y^2 - 2 \frac{tg^2\beta L_X^2 L_Y^2}{(tg^2\alpha + tg^2\beta + 1)} - 2 \frac{tg^2\alpha tg^4\beta L_X^2 L_Y^2}{(tg^2\alpha + tg^2\beta + 1)^3} - 2 \frac{tg^2\alpha L_X^2 L_Y^2}{(tg^2\alpha + tg^2\beta + 1)} + \\
& 4 \frac{tg^2\alpha tg^2\beta L_X^2 L_Y^2}{(tg^2\alpha + tg^2\beta + 1)^2} + \frac{tg^4\alpha tg^4\beta L_X^2 L_Y^2}{(tg^2\alpha + tg^2\beta + 1)^4} - 2 \frac{tg^4\alpha tg^4\beta L_X^2 L_Y^2}{(tg^2\alpha + tg^2\beta + 1)^4} + \\
& 2 \frac{tg^4\alpha tg^2\beta L_X^2 L_Y^2}{(tg^2\alpha + tg^2\beta + 1)^3} + 2 \frac{tg^2\alpha tg^4\beta L_X^2 L_Y^2}{(tg^2\alpha + tg^2\beta + 1)^3} - 2 \frac{tg^2\alpha tg^2\beta L_X^2 L_Y^2}{(tg^2\alpha + tg^2\beta + 1)^2}
\end{aligned}$$

Simplifying terms and regrouping, we have:

$$\begin{aligned}
Area^2 = & \frac{(tg^2\alpha + tg^2\beta)L_X^2 L_Y^2}{(tg^2\alpha + tg^2\beta + 1)^2} + \frac{(tg^4\alpha + tg^4\beta)L_X^2 L_Y^2}{(tg^2\alpha + tg^2\beta + 1)^2} + L_X^2 L_Y^2 - \\
& 2 \frac{(tg^2\alpha + tg^2\beta)L_X^2 L_Y^2}{(tg^2\alpha + tg^2\beta + 1)} + 2 \frac{tg^2\alpha tg^2\beta L_X^2 L_Y^2}{(tg^2\alpha + tg^2\beta + 1)^2}
\end{aligned}$$

and factorizing, we get:

$$\begin{aligned}
Area^2 = & \frac{L_X^2 L_Y^2}{(tg^2\alpha + tg^2\beta + 1)^2} \cdot [tg^2\alpha + tg^2\beta + tg^4\alpha + tg^4\beta + (tg^2\alpha + tg^2\beta + 1)^2 - \\
& 2(tg^2\alpha + tg^2\beta) \cdot (tg^2\alpha + tg^2\beta + 1) + 2tg^2\alpha tg^2\beta] =
\end{aligned}$$

$$\begin{aligned}
&= \frac{L_X^2 L_Y^2}{(\operatorname{tg}^2 \alpha + \operatorname{tg}^2 \beta + 1)^2} \cdot [\operatorname{tg}^2 \alpha + \operatorname{tg}^2 \beta + \operatorname{tg}^4 \alpha + \operatorname{tg}^4 \beta + \operatorname{tg}^4 \alpha + \operatorname{tg}^4 \beta + 1 + \\
&\quad 2 \operatorname{tg}^2 \alpha \operatorname{tg}^2 \beta + 2 \operatorname{tg}^2 \alpha + 2 \operatorname{tg}^2 \beta - 2 \operatorname{tg}^4 \alpha - 2 \operatorname{tg}^2 \alpha \operatorname{tg}^2 \beta - 2 \operatorname{tg}^2 \alpha - \\
&\quad 2 \operatorname{tg}^2 \alpha \operatorname{tg}^2 \beta - 2 \operatorname{tg}^4 \beta - 2 \operatorname{tg}^2 \beta + 2 \operatorname{tg}^2 \alpha \operatorname{tg}^2 \beta] = \\
&= \frac{L_X^2 L_Y^2}{(\operatorname{tg}^2 \alpha + \operatorname{tg}^2 \beta + 1)^2} \cdot [\operatorname{tg}^2 \alpha + \operatorname{tg}^2 \beta + 1] = \frac{L_X^2 L_Y^2}{(\operatorname{tg}^2 \alpha + \operatorname{tg}^2 \beta + 1)}
\end{aligned}$$

Given that $Area'$ is equal to $L_X \cdot L_Y$, we have, therefore:

$$Area^2 = \frac{Area'^2}{(\operatorname{tg}^2 \alpha + \operatorname{tg}^2 \beta + 1)} \quad (A.9)$$

or what is the same:

$$Area = \frac{Area'}{\sqrt{\operatorname{tg}^2 \alpha + \operatorname{tg}^2 \beta + 1}} \quad (A.10)$$

as we wanted to demonstrate.

This relation, applied here to a rectangular area of the form $L_X \cdot L_Y$, is also valid in its differential form; that is, one can apply it to a differential area $dL_X \cdot dL_Y$. Therefore, we can subdivide an area with any shape in differential rectangular (or square) areas and apply eq. A.10 to each differential; when integrating over the whole area, we have that equation A.10 is still valid.

Appendix II: Errors

In section 3.2.2 we have said that the error criterion for the iterative maximization methods is the one given in [38]; once the algorithm has reached the desired result (at iteration $n+1$) the errors of the image pixels are estimated by square error propagation from the iterative formula estimated at the iteration n .

Doing this, we obtain that the (square of the) error in the intensity estimation of pixel (α, β) (considering as magnitudes with error the detected counts D_{ij} , and the detector response array Φ) is given by equation 3.7 that we show here again:

$$\varepsilon^2(\tilde{O}_{\alpha\beta}^{n+1}) = \sum_{kl} \left[\left(\frac{\partial \tilde{O}_{\alpha\beta}^{n+1}}{\partial D_{kl}} \right)_n^2 \cdot \varepsilon^2(D_{kl}) + \left(\frac{\partial \tilde{O}_{\alpha\beta}^{n+1}}{\partial \Phi_{kl}^{\alpha\beta}} \right)_n^2 \cdot \varepsilon^2(\Phi_{kl}^{\alpha\beta}) + \sum_{\gamma\delta \neq \alpha\beta} \left(\frac{\partial \tilde{O}_{\alpha\beta}^{n+1}}{\partial \Phi_{kl}^{\gamma\delta}} \right)_n^2 \cdot \varepsilon^2(\Phi_{kl}^{\gamma\delta}) \right]$$

where the subindex n means that the partial derivatives are estimated with the values of iteration n .

In the case of the EM algorithm (eq. 2.56) we have that the partial derivatives are:

$$\begin{aligned} \left(\frac{\partial \tilde{O}_{\alpha\beta}^{n+1}}{\partial D_{kl}} \right)_n &= \tilde{O}_{\alpha\beta}^n \frac{\Phi_{kl}^{\alpha\beta} \frac{1}{\tilde{D}_{kl}^n}}{\sum_{ij} \Phi_{ij}^{\alpha\beta}} \\ \left(\frac{\partial \tilde{O}_{\alpha\beta}^{n+1}}{\partial \Phi_{kl}^{\gamma\delta}} \right)_n &= -\tilde{O}_{\alpha\beta}^n \cdot \tilde{O}_{\gamma\delta}^n \frac{\Phi_{kl}^{\alpha\beta} \frac{D_{kl}}{(\tilde{D}_{kl}^n)^2}}{\sum_{ij} \Phi_{ij}^{\alpha\beta}} \\ \left(\frac{\partial \tilde{O}_{\alpha\beta}^{n+1}}{\partial \Phi_{kl}^{\alpha\beta}} \right)_n &= \tilde{O}_{\alpha\beta}^n \left(\frac{\frac{D_{kl}}{\tilde{D}_{kl}^n} - \tilde{O}_{\alpha\beta}^n \Phi_{kl}^{\alpha\beta} \frac{D_{kl}}{(\tilde{D}_{kl}^n)^2}}{\sum_{ij} \Phi_{ij}^{\alpha\beta}} - \frac{\sum_{ij} \Phi_{ij}^{\alpha\beta} \frac{D_{ij}}{\tilde{D}_{ij}^n}}{\left(\sum_{ij} \Phi_{ij}^{\alpha\beta} \right)^2} \right) \end{aligned} \tag{A.11}$$

Similarly, for the maximum entropy method (eq. 4.10), we have that the partial derivatives are:

$$\begin{aligned}
\left(\frac{\partial \tilde{O}_{\alpha\beta}^{n+1}}{\partial D_{kl}}\right)_n &= \left(\frac{1}{n+1}\right) \left[e^{-1-2\lambda^n \sum_{ij} \Phi_{ij}^{\alpha\beta} \left(\frac{\tilde{D}_{ij}^n - D_{ij}}{\sigma_{ij}^2}\right)} \right] \frac{(2\lambda^n)}{\sigma_{kl}^2} \Phi_{kl}^{\alpha\beta} \\
\left(\frac{\partial \tilde{O}_{\alpha\beta}^{n+1}}{\partial \Phi_{kl}^{\gamma\delta}}\right)_n &= \left(\frac{1}{n+1}\right) \left[e^{-1-2\lambda^n \sum_{ij} \Phi_{ij}^{\alpha\beta} \left(\frac{\tilde{D}_{ij}^n - D_{ij}}{\sigma_{ij}^2}\right)} \right] \frac{(-2\lambda^n)}{\sigma_{kl}^2} \Phi_{kl}^{\alpha\beta} \tilde{O}_{\gamma\delta}^n \\
\left(\frac{\partial \tilde{O}_{\alpha\beta}^{n+1}}{\partial \Phi_{kl}^{\alpha\beta}}\right)_n &= \left(\frac{1}{n+1}\right) \left[e^{-1-2\lambda^n \sum_{ij} \Phi_{ij}^{\alpha\beta} \left(\frac{\tilde{D}_{ij}^n - D_{ij}}{\sigma_{ij}^2}\right)} \right] \frac{(-2\lambda^n)}{\sigma_{kl}^2} (\tilde{D}_{kl}^n + \Phi_{kl\alpha\beta} \tilde{O}_{\alpha\beta}^n)
\end{aligned} \tag{A.12}$$

Applying A.11 and A.12 to eq. 3.7, factorizing and defining σ_{kl} as the error of D_{kl} , we have for the EM algorithm:

$$\begin{aligned}
\varepsilon(\tilde{O}_{\alpha\beta}^{n+1}) &= \frac{\tilde{O}_{\alpha\beta}^n}{\sum_{ij} \Phi_{ij}^{\alpha\beta}} \left[\sum_{kl} \left(\frac{\Phi_{kl}^{\alpha\beta}}{\tilde{D}_{kl}^n} \right)^2 \sigma_{kl}^2 + \right. \\
&\quad \left. \sum_{kl} \left(\frac{D_{kl}}{\tilde{D}_{kl}^n} - \tilde{O}_{\alpha\beta}^n \Phi_{kl}^{\alpha\beta} \frac{D_{kl}}{(\tilde{D}_{kl}^n)^2} - \frac{\sum_{ij} \Phi_{ij}^{\alpha\beta} \frac{D_{ij}}{\tilde{D}_{ij}^n}}{\sum_{ij} \Phi_{ij}^{\alpha\beta}} \right)^2 \varepsilon^2(\Phi_{kl}^{\alpha\beta}) + \right. \\
&\quad \left. \sum_{kl} \sum_{\gamma\delta \neq \alpha\beta} \left(\tilde{O}_{\gamma\delta}^n \Phi_{kl}^{\alpha\beta} \frac{D_{kl}}{(\tilde{D}_{kl}^n)^2} \right)^2 \varepsilon^2(\Phi_{kl}^{\gamma\delta}) \right]^{1/2}
\end{aligned} \tag{A.13}$$

and for the maximum entropy method:

$$\begin{aligned} \varepsilon(\tilde{O}_{\alpha\beta}^{n+1}) = & \left(\frac{1}{n+1} \right) \left[e^{-1-2\lambda^n \sum_{ij} \Phi_{ij}^{\alpha\beta} \left(\frac{\tilde{D}_{ij}^n - D_{ij}}{\sigma_{ij}^2} \right)} \right] (2\lambda^n) \left[\sum_{kl} \left(\frac{\Phi_{kl}^{\alpha\beta}}{\sigma_{kl}^2} \right)^2 \sigma_{kl}^2 + \right. \\ & \sum_{kl} \left(\frac{\tilde{D}_{kl}^n}{\sigma_{kl}^2} + \tilde{O}_{\alpha\beta}^n \Phi_{kl}^{\alpha\beta} \frac{1}{\sigma_{kl}^2} \right)^2 \varepsilon^2(\Phi_{kl}^{\alpha\beta}) + \\ & \left. \sum_{kl} \sum_{\gamma\delta \neq \alpha\beta} \left(\tilde{O}_{\gamma\delta}^n \Phi_{kl}^{\alpha\beta} \frac{1}{\sigma_{kl}^2} \right)^2 \varepsilon^2(\Phi_{kl}^{\gamma\delta}) \right]^{1/2} \end{aligned} \tag{A.14}$$

Regarding the correlative methods, and expanding what we said in section 3.2.1, we obtain that a reconstruction, once corrected by the number of 1's in the G array (N_U), by the efficiency and area of the detectors, and the mask transparency, is given by:

$$\tilde{O}_{ij} = \frac{1}{N_U} \sum_{kl} \frac{D_{kl}}{\varepsilon_{kl} Tr A_{kl}} \cdot G_{k+i, l+j} \tag{A.15}$$

Both N_U as G are numerical constants and, therefore, without error. Since G is equal to ± 1 (or also 0 in δ -decoding), when in the error formula we use its square, we will lose all the information about the mask pattern (that is included in the ± 1 values), and therefore, the same as in section 3.2.1, the error for all the pixels of the reconstructed image will be exactly the same; although it will not now correspond exactly to the square root of the total detected counts, but it will be given (by square error propagation) by:

$$\begin{aligned} \varepsilon^2(\tilde{O}_{ij}) = & \frac{1}{N_U^2} \sum_{kl} G_{k+i, l+j}^2 \left[\left(\frac{\varepsilon(D_{kl})}{\varepsilon_{kl} Tr A_{kl}} \right)^2 + \left(\frac{D_{kl}}{Tr A_{kl}} \cdot \frac{\varepsilon(\varepsilon_{kl})}{\varepsilon_{kl}^2} \right)^2 + \right. \\ & \left. \left(\frac{D_{kl}}{\varepsilon_{kl} A_{kl}} \cdot \frac{\varepsilon(Tr)}{Tr^2} \right)^2 + \left(\frac{D_{kl}}{\varepsilon_{kl} Tr} \cdot \frac{\varepsilon(A_{kl})}{A_{kl}^2} \right)^2 \right] \end{aligned} \tag{A.16}$$

References

- [1] "Recent Advances in High Energy Astronomy. Proceedings. Toulouse International Colloquium on Recent Advances in High Energy Astronomy. Toulouse (France), 17-20 Mar 1992". P. Mandrou et al. *Astron. Astr. Suppl.* 97 (1993) 1.
- [2] "Future Goals for Imaging". A. J. Dean. *Exp. Astr.* vol. 6 no. 4 (1995) 77.
- [3] "Gamma-Ray Astronomy - A status report". S. S. Holt. *Astroph. Jour. Suppl. Series* 92 (1994) 693.
- [4] "Low Energy Gamma Ray Imager (LEGRI)". F. J. Ballesteros et al. *Exp. Astr.* vol. 6 no. 4 (1995) 183.
- [5] "Empleo de HgI_2 como detector de radiación γ ". J. M. Perez. Tesis doctoral. Director P. Olmos. Facultad de C. Físicas, U. Complutense de Madrid.
- [6] "9th International Workshop on Room Temperature Semiconductors X and gamma-ray Detectors, Associated Electronics and Applications". September 18-22th (1995) Grenoble (France), abstracts of the proceedings.
- [7] "Proton induced background in LEGRI". E. Porrás et al. Accepted for publication in *N.I.M. B.*
- [8] "Background in Space-Born Low-Energy Gamma-Ray Telescopes". A. J. Dean, F. Lei & P. T. Knight. *Space Sci. Rev.* 57 (1991) 109.
- [9] "X-Ray Imaging with Coded Mask". G. K. Skinner, *Scientific American.* August (1988).
- [10] "Design Parameters of Paraboloid-Hyperboloid Telescopes for X-Ray Astronomy". L. P. Van Speybroeck, R. C. Chase. *Appl. Opt.* Vol 11 (1972) 440.
- [11] "Fresnel Zone Plate Imaging of Gamma Rays; Theory". H. H. Barrett & F. A. Horrigan. *Appl. Opt.* Vol 12 (1973) 2686.
- [12] "Optica". J. Casas. Ed. Librería Pons (Zaragoza) (1985) 243.
- [13] "Coded Aperture Imaging with Uniformly Redundant Arrays" E. E. Fenimore & T. M. Cannon. *Appl. Opt.* Vol 17 (1978) 337.
- [14] "Techniques for the Analysis of Data from Coded-Mask X-Ray Telescopes". G. K. Skinner et al. *Astroph. & Space Science* 136 (1987) 337.
- [15] "Imaging with Coded Aperture Mask" G. K. Skinner. *N.I.M.* 221 (1984) 33.
- [16] "Point Arrays Having Compact, Nonredundant Autocorrelations". M. J. E. Golay. *J. Opt. Soc. Amer.* 61 (1971) 272.

-
- [17] "On the Properties of Images from Coded-Masks Telescopes". G. K. Skinner & T. J. Ponman. *Mon. Not. R. Astron. Soc.* 267 (1994) 518.
- [18] "New Family of Binary Arrays for Coded Aperture Imaging". S. R. Gottesman & E. E. Fenimore. *Appl. Opt.* Vol 28 (1989) 4344.
- [19] "Infinite Families of Perfect Binary Arrays". P. Wild. *Electron. Let.* Vol 24 No 14 (1988) 845.
- [20] "Constructing New Perfect Binary Arrays". J. Jedwab & C. Mitchell. *Electron. Let.* Vol 24 No 11 (1988) 650.
- [21] "Synthesis of Coded Masks for Gamma-Ray and X-Ray Telescopes". L. E. Kopilovich & L. G. Sodin. *Mon. Not. R. Astron. Soc.* 266 (1994) 357.
- [22] "Synthesis of Binary Arrays with Perfect Correlation Properties - Coded Aperture Imaging". K. Byard. *N.I.M. A* 336 (1993) 262.
- [23] "Uniformly Redundant Arrays: Digital Reconstruction Methods". E. E. Fenimore & T. M. Cannon. *Appl. Opt.* Vol 20 (1981) 1858.
- [24] "Numerical Recipes: the Art of Scientific Computing". W. H. Press et al. Ed. Cambridge University Press (1986) 389 y ss.
- [25] "Statistical Analysis for Coded Aperture γ -Ray Telescopes". G. Ducros & R. Ducros. *N.I.M.* 221 (1984) 49.
- [26] "Image Restoration and Processing Methods". G. J. Daniell. *N.I.M.* 221 (1984) 67.
- [27] "Maximum Entropy Image Processing in Gamma-Ray Astronomy". J. Skilling et al. *Mon. Not. R. Astr. Soc.* 187 (1979) 145.
- [28] "Maximum Entropy Image Reconstruction: General Algorithm". J. Skilling & R. K. Bryan. *Mon. Not. R. Astr. Soc.* 211 (1984) 111.
- [29] "Image Reconstruction from Incomplete and Noisy Data". S. F. Gull & G. J. Daniell. *Nature* Vol 272 (1978) 686.
- [30] "Maximum Entropy Methods". T. J. Ponman. *N.I.M.* 221 (1984) 72.
- [31] "Use of the Maximum Entropy Method in X-Ray Astronomy". R. Willingale. *Mon. Not. R. Astr. Soc.* 194 (1981) 359.
- [32] "EM Reconstruction Algorithms for Emission and Transmission Tomography". K. Lange & R. Carson. *J. Comput. Assist. Tomogr.* Vol 8 No 2 (1984) 306.
- [33] "Maximum Likelihood from Incomplete Data via the EM Algorithm". A. P. Dempster et al. *J. R. Statist. Soc. B* 39 (1977) 1.
- [34] "On the Convergence Properties of the EM Algorithm". C. F. J. Wu. *Ann.*

- Statist. Vol 11 No 1 (1983) 95.
- [35] "On the Convergence of the EM Algorithm". R. A. Boyles. J. R. Statist. Soc. B 45 (1983) 47.
- [36] "Correction for Detector Uniformity of a Gamma-Ray Telescope using Coded Aperture Imaging" Ph. Laudet & J. P. Roques. N.I.M. A 267 (1988) 212.
- [37] "Techniques for Nuclear and Particle Physics Experiments". W. R. Leo. Ed. Spriger-Verlag Berlin Heidelberg (1987) 94.
- [38] "Probability and Statistics in Particle Physics". A. G. Frodesen et al. Ed. Reklametrakk A.S. Bergen, Norway (1979) 314-315.
- [39] "Monte Carlo Theory & Practice". F. James. Rep. Prog. Phys. 43 (1980) 1145.
- [40] "GEANT-Detector Description and Simulation Tool". Application Software Group. Computing and Network Division. CERN, Geneve, Suiza (1994).
- [41] "CERN Program Library". Varios. CERN computer centre, CH-1211 Geneve 23, Suiza (1988).
- [42] "Table of Isotopes". C. M. Lederer & V. S. Shirley. Ed. John Wiley & sons, Inc. New York (1978).
- [43] "Science Performance Report". P. Mandrou. Internal Report for INTEGRAL Spectrometer, CESR, Centre National de la Recherche Scientifique-Université Paul Sabatier, Ref: SPI-NS-0-9758-CSCI, 23/05/96.
- [44] "Proceedings of the 19th ICRC, La Jolla". R. Staubert. Vol 3, OG 9.5-10 (1985) 477.
- [45] V. Reglero, Internal Report on the LEGRI scientific team.